



KATHOLIEKE UNIVERSITEIT LEUVEN

FACULTEIT TOEGEPESTE WETENSCHAPPEN

DEPARTEMENT WERKTUIGKUNDE

AFDELING TOEGEPESTE MECHANICA

EN ENERGIEKONVERSIE

Celestijnenlaan 300 A B-3030 Heverlee

EXPERIMENTAL AND THEORETICAL STUDY OF FILM COOLING ON A GAS TURBINE BLADE

Promotor :
DR. ir. J. BERGHMANS , DOCENT.

Proefschrift voorgedragen tot
het behalen van het doctoraat
in de toegepaste wetenschappen
door

Cengiz CAMCI

Mei 1985

von KARMAN INSTITUTE FOR FLUID DYNAMICS

TABLE OF CONTENTS

ACKNOWLEDGEMENTS	iv
SAMENVATTING	v
ABSTRACT	vii
NOMENCLATURE	x
LIST OF FIGURES	xv
LIST OF TABLES	xxi
LIST OF APPENDICES	xxvi

CHAPTER 1 INTRODUCTION

CHAPTER 2 LITERATURE REVIEW

2.1 CYCLE CONSIDERATIONS	4
2.2 BLADE COOLING METHODS	7
2.3 CONTRIBUTION OF FILM COOLING ON THE COOLING EFFICIENCY OF A GAS TURBINE BLADE	10
2.4 AERODYNAMIC LOSSES DUE TO COOLANT EJECTION IN A TURBINE STAGE	13
2.5 HOT MAINSTREAM FLOW OVER A TURBINE AIRFOIL	15
2.6 AVAILABLE HEAT TRANSFER DATA ON GAS TURBINE BLADES WITHOUT FILM COOLING	17
2.7 FILM COOLING HYDRODYNAMICS AND HEAT TRANSFER ON A GAS TURBINE BLADE	23
2.7.1 FILM COOLING ON THE LEADING EDGE OF A TURBINE BLADE	23
2.7.2 FILM COOLING ON THE SUCTION SIDE AND ON THE PRESSURE SIDE	25
2.8 SIMILARITY CONSIDERATIONS	31
2.9 STATE OF THE ART	35

CHAPTER 3 EXPERIMENTAL TECHNIQUE AND MODEL DESCRIPTION

3.1 THE ISENTROPIC LIGHT PISTON COMPRESSION TUBE FACILITY	37
3.2 WALL HEAT FLUX MEASUREMENTS	41
3.2.1 DETAILS OF THE ASSUMPTIONS	42
3.2.1.1 ONE DIMENSIONAL HEAT TRANSFER	42
3.2.1.2 SUBSTRATE THICKNESS	42
3.2.1.3 THIN FILM GAUGE THICKNESS	44
3.2.2 ANALOGUE CIRCUIT DESCRIPTION	45
3.2.3 THIN FILM HEAT FLUX SENSORS	47
3.2.3.1 THIN FILM GAUGE CONSTRUCTION DETAILS	47
3.2.3.1.1 PREPARATION OF THE SUBSTRATE SURFACE	47
3.2.3.1.2 APPLICATION OF THE GAUGE MATERIAL	48
3.2.3.1.3 ELECTRICAL CONNECTIONS	52
3.2.3.2 TEMPERATURE COEFFICIENT OF THIN FILMS	53
3.2.3.3 SUBSTRATE THERMAL PRODUCT	54
3.3 PRESSURE AND TEMPERATURE MEASUREMENTS	55
3.4 COOLANT FLUID CONDITIONING	59
3.5 TURBULENCE GENERATION	60
3.6 MEASUREMENT CHAIN AND DATA PROCESSING	61
3.7 UNCERTAINTY ANALYSIS	63
3.8 MODEL DESCRIPTION	67

CHAPTER 4	EXPERIMENTAL RESULTS AND DISCUSSION	
4.1	RESULTS IN THE ABSENCE OF COOLANT EJECTION	71
4.1.1	INVISCID MAINSTREAM FLOW AT ZERO INCIDENCE	71
4.1.2	HEAT TRANSFER AT ZERO INCIDENCE	73
4.1.3	INVISCID MAINSTREAM FLOW AND HEAT TRANSFER AT OTHER INCIDENCES, ($i = -10, +10, +15$)	77
4.2	RESULTS IN THE PRESENCE OF COOLANT EJECTION	79
4.2.1	LEADING EDGE HEAT TRANSFER WITH FILM COOLING	79
4.2.1.1	RESULTS AT ZERO INCIDENCE	79
4.2.1.2	RESULTS AT OTHER INCIDENCES, ($i = -10, +10$)	82
4.2.2	SUCTION SIDE HEAT TRANSFER WITH FILM COOLING	84
4.2.3	PRESSURE SIDE HEAT TRANSFER WITH FILM COOLING	86
4.2.4	SIMULTANEOUS COOLANT EJECTION THROUGH THE LEADING EDGE, SUCTION SIDE AND PRESSURE SIDE	88
4.2.4.1	COOLANT HYDRODYNAMICS	88
4.2.4.1.1	Total Coolant Mass Flow Versus Local Plenum Chamber Pressure	88
4.2.4.1.2	Local Discharge Coefficients	89
4.2.4.1.3	Coolant Split Between Plenum Chambers	90
4.2.4.1.4	Local Blowing Rates	90
4.2.4.1.5	Verification Of The Estimated Hydrodynamic Data	90
4.2.4.2	FILM COOLING HEAT TRANSFER, LOCAL INVESTIGATIONS	92
4.2.4.2.1	Stagnation Region Film Cooling Behaviour-downstream Of Row (LS)	92
4.2.4.2.2	Stagnation Region Film Cooling Behaviour-downstream Of Row (LP)	92
4.2.4.2.3	Heat Transfer-downstream Of Row (P)	93
4.2.4.2.4	Heat Transfer-downstream Of Row (S)	93
4.2.4.2.5	Influence Of Coolant Temperature	94
4.2.4.2.6	Heat Transfer In The Absence Of Stagnation Region Ejection	95
4.2.4.2.7	Influence Of Free Stream Turbulence Intensity On Film Cooling Heat Transfer	95
4.2.4.2.8	Influence Of Incidence On Film Cooling Heat Transfer, ($ s/C > 1/3$)	96
4.2.5	CONCLUSIONS	97
CHAPTER 5	HEAT TRANSFER PREDICTIONS	
5.1	HEAT TRANSFER PREDICTIONS IN THE ABSENCE OF COOLANT EJECTION	100
5.1.1	DESCRIPTION OF THE NUMERICAL METHOD	100
5.1.2	DETAILS OF THE REQUIRED PHYSICAL INPUTS	102
5.1.2.1	MIXING LENGTH VARIATION ACROSS THE BOUNDARY LAYER	103
5.1.2.2	VARIABLE TURBULENT PRANDTL NUMBER	105
5.1.2.3	LAMINAR TO TURBULENT TRANSITION	106
5.1.2.4	FLUID PROPERTIES (AIR)	106
5.1.3	CALCULATIONS AND COMPARISON WITH THE MEASURED DATA ALONG THE SUCTION SIDE	107

5.1.4	CALCULATIONS AND COMPARISON WITH THE MEASURED DATA ALONG THE PRESSURE SIDE	110
5.2	NUMERICAL SIMULATION OF FILM COOLING HEAT TRANSFER	113
5.2.1	SIMULATIONS ON THE SUCTION SIDE AND COMPARISONS WITH THE MEASURED DATA	113
5.3	FINITE ELEMENT ANALYSIS OF THERMAL CONDUCTION IN THE FILM COOLED TURBINE BLADE	121
5.3.1	DISCRETIZATION OF THE BLADE AND BOUNDARY CONDITIONS	121
5.3.2	THE METHOD OF ANALYSIS	123
5.3.3	COMPUTATIONAL RESULTS	129
5.3.3.1	ONLY INTERNAL CONVECTION COOLING	129
5.3.3.2	FILM COOLING RESULTS	131
5.3.3.3	THE INFLUENCE OF THE COOLING HOLE	132
 CHAPTER 6 CONCLUSIONS		
6.1	HEAT TRANSFER IN THE ABSENCE OF COOLANT EJECTION .	134
6.2	FILM COOLING HEAT TRANSFER ON THE LEADING EDGE . .	136
6.3	FILM COOLING HEAT TRANSFER ON THE SUCTION SIDE . .	138
6.4	FILM COOLING HEAT TRANSFER ON THE PRESSURE SIDE . .	139
6.5	FILM COOLING HEAT TRANSFER FROM SIMULTANEOUS EJECTION	139
6.6	CONVECTIVE HEAT TRANSFER PREDICTIONS IN BOUNDARY LAYERS IN THE ABSENCE AND PRESENCE OF COOLANT EJECTION	141
6.7	FINITE ELEMENT ANALYSIS OF THERMAL CONDUCTION IN THE FILM COOLED TURBINE BLADE	142
 REFERENCE LIST		143

ACKNOWLEDGEMENTS

The author would like to express his sincere gratitude and appreciation to his advisor Professor J.Berghmans of the Katholieke Universiteit Leuven for his guidance and encouragement, and helpful suggestions in the course of this research.

Several people have helped considerably in the development of this thesis .The author wishes especially to thank Professor T.Arts of the Von Karman Institute for fluid dynamics for his invaluable help and encouragement ,and for his extremely constructive criticism. He also expresses his gratitude to Professor F.A.E. Breugelmans, the head of the turbomachinery department at the VKI,for the research assistantship which was granted in 1980 and for his suggestions in every aspect of this work.

He acknowledges the other members of his thesis reading committee,Professor W. Dutre and Professor P.Monnens of the Katholieke Universiteit Leuven for their useful comments and criticism .This acknowledgement is extended to Professor D.Schultz of the Oxford University for his interest and comments in the final development of this thesis. Thanks are also due to Professor P.M.Ligrani of the U.S. Naval Postgraduate School in Monterey ,for his interest in the initial phase of the research.

The help of the VKI technical personnel is very much appreciated. Mr.J.P. Biebuyck is acknowledged for his extremely careful work in constructing the thin film heat flux gauges. Mrs.N. Toubeau is also thanked for her skilful typing of the equations in this thesis.

He is indebted to his friends at the VKI ,Ali Anaturk ,Elias Boletis and Constantinos Mathioudakis for many fruitful discussions.

He also wishes to express his gratitude to his parents ,who always had faith in the dreams of their son.

Finally ,the author wishes to dedicate this work to his best friend Esin who did everything possible to help him to complete this work.

SAMENVATTING

Het is wel bekend dat gasturbines werken met een hoger rendement wanneer de turbine inlaattemperatuur toeneemt bij een gegeven drukverhouding van de kringloop. De hoge inlaattemperaturen zijn een algemeen aanvaard verschijnsel wegens de constante vraag naar zuinige en kompakte luchtvaartmotoren. De maximum toelaatbare inlaattemperatuur wordt beperkt door de materialen. Daarom is koeling van de turbineschoep door inwendige uitwendige middelen noodzakelijk om de levensduur van de schoepen te verlengen in deze uitzonderlijke omstandigheden in een gasturbine.

Filmkoeling door afzonderlijke gaatjes werd in een recent verleden bestudeerd op vlakke adiabatische wanden bij relatief lage snelheden vergeleken met de voorwaarden in een motor. Meestal werd de lokale temperatuursverandering bestudeerd op een adiabatische wand stroomafwaarts van de injectie plaats, of de warmteoverdrachtscoefficient wanneer de koeling wordt ingebracht op dezelfde temperatuur als de hoofdstroming langs een isotherme wand. Nochtans zijn de lokale warmtefluxen naar de buitenoppervlakken van de schoep niet verwarloosbaar wegens de grote lokale temperatuursgradienten in een hoge temperatuurmotor. Daarbij komt dat de koelinglucht nooit wordt geïnjecteerd op dezelfde temperatuur als de hoofdstroming, zoals in vele adiabatische wand experimenten waar de dichtheid van de koeling en hoofdstroming gelijk zijn. De temperatuur van de koeling is typisch gelijk aan de helft van deze van de hoofdstroming. Een suksesvol ontwerp van een gekoelde schoep kan alleen maar bekomen worden door de kennis van de externe warmtebelasting te wijten aan de ingewikkelde viskeuze stroming rond het profiel. De externe warmtestroming naar een door film gekoelde schoep kan voorgesteld worden door een konvektieve warmteoverdrachtscoefficient. Deze wordt bepaald met de rekuperatie temperatuur van de vrije stroming en de lokale wandtemperatuur op de voorgeschreven koelingstemperatuur.

Het hoofddoel van deze studie is het onderzoeken van de gedwongen konvektieve warmteoverdracht doorheen de filmgekoelde lagen van een turbulente grenslaag die aanwezig is rond een schoep van een hoge druk gasturbine trap. De verschillende koelingsmethoden, warmteoverdracht zonder koeling, filmkoeling over een vlakke plaat en over turbine schoepen met adiabatische en niet adiabatische wandvoorwaarden worden besproken aan de hand van de litteratuur. De techniek voor de meting van de warmtestroming aan de wand,

druk- en temperatuursmetingen, het koeling injectie systeem en het test model worden in detail besproken in hoofdstuk 3. De schoep, geïnstrumenteerd voor warmteoverdrachtmetingen, werd gefreesd uit een blok keramisch materiaal. Drie onafhankelijke suskamers werden geboord voor de toevoer van de koeling, één in de neus van de schoep, één aan de zuigzijde op $s/\bar{c} = 1/5$ en één aan de drukzijde op $s/\bar{c} = 1/3$. Het materiaal heeft een zeer kleine thermische geleidbaarheid en diffusieviteit, dit is belangrijk om een isotherme wandtoestand te bekomen tijdens de tests in de kompressiebuis. Een schoep uit een stuk is zeer belangrijk om kleine storingen te vermijden in de dunne grenslaag stroomafwaarts van de injectie. Het is een alternatieve voor de metallieke schoep met inzetstukken en vermindert de sterke warmtegeleiding die kan ontstaan bij de overgang metaal-inzetstuk. De techniek van de dunne platinumfilm en de electrische analogie van een eendimensionale warmtestroming in een half oneindig lichaam werden gebruikt om de directe metingen uit te voeren.

Het hoofdstuk 4 bevat de experimentele resultaten van de warmteoverdracht op een rotorschoep met en zonder filmkoeling uit gaatjes op verschillende plaatsen op het profiel. Verschillende debieten en temperaturen van de koelstroming werden onderzocht tijdens de testen in de CT-2 kompressiebuis van het VKI waarin gasturbine voorwaarden kunnen nagebootst worden. De invloed van het lokale Reynoldsgetal, de invalshoek, de turbulentie van de vrije stroming en koelingsparameters op de warmteoverdracht werden onderzocht.

De voorspelling van de warmteoverdracht met en zonder filmkoeling wordt bestudeerd in hoofdstuk 5 door gebruik te maken van een twee dimensionale eindige differensen grenslaag berekening. Een model voor de konvekse krommingen en de invloed van de kromming op de turbulente schuifspanningen werd aan het programma toegevoegd. Een betere overeenstemming met de metingen wordt bekomen dan met een model dat steunt op de vlakke plaat "mixing length". Een tweede "mixing length" model werd ingevoerd om de kromming van de konkave drukzijde in rekening te brengen. De voorspelling van de warmteoverdracht langs de drukzijde blijft nochtans moeilijk wegens de versnelling-vertraging van de stroming, de verhoging van de turbulentie door het konkave oppervlakte. In het geval van de filmkoeling wordt een verbeterde "mixing length" voorgesteld om verhoogde turbulentie

in de nabijheid van de injectie te kunnen behandelen in de vorm van een Prandtl "mixing length". De verhoogde "mixing length" werd experimenteel bepaald als functie van het koeldebiet. De koeling werd verondersteld verspreid te zijn op een afstand gelijk aan 80% van de grenslaagdikte, gemeten loodrecht op de wand stroomafwaarts van de injectierij. Deze specifieke benadering was zeer suksesvol om filmkoeling warmteoverdracht na te bootsen vooral wanneer de diameter van de koelgaatjes veel groter is (4.75 keer) dan de grenslaagdikte.

De gemeten externe warmteoverdrachtscoefficienten werden gebruikt om de interne warmtestromingen in het schoepenmateriaal te berekenen. Het probleem van de warmtegeleiding werd opgelost met een eindige elementen methode. De neus van de schoep is de meest kritische plaats wanneer alleen interne konvektieve koeling aanwezig is. De wandtemperatuur werd nochtans sterk verminderd in deze zone wegens de zeer effektieve koeling door de inwendige koelkanalen in de aanvalsboord. De resultaten van de filmkoeling-tests tonen aan dat de wand stroomafwaarts van de koelinginjectie verre van adiabatisch en verre van isotherm is. De inbreng van de konvektieve warmteoverdrachtbijdrage van de injectiegaatjes op de warmtegeleiding werd onderzocht. Er werd aangetoond dat de richting en groote van de warmtestromen in de nabijheid van injectiegaatjes sterk bepaald wordt door het konvektieve gedrag. De wandtemperatuur juist stroomafwaarts van het gaatje is gelijk aan de koelingstemperatuur in de plenumkamer wat een zeer efficiënte filmkoeling betekent in deze zone. De vaste wanden tussen de koelkanalen brengen een belangrijk hoeveelheid warmte naar de interne koelstroming en grote temperatuursgradienten werden opgemerkt in de hoeken van deze kanalen.

ABSTRACT

An experimental and theoretical investigation of forced convection heat transfer in the film cooled boundary layers of a high pressure gas turbine rotor blade is discussed in detail. A literature review on gas turbine cycle considerations, turbine blade heat transfer and blade cooling methods are given. The technique used for the measurement of wall heat flux, transient temperature, transient pressure, the model and the coolant ejection system are described. Experimental results from convective heat transfer measurements on the rotor blade are presented at different ejection sites such as the leading edge, the suction side and the pressure side. The local Reynolds number, incidence angle, free stream turbulence intensity, blowing rate, coolant temperature and coolant ejection site are the main experimental parameters varied in the investigation. The theoretical study consists of the prediction of both convection heat transfer through the boundary layers and conduction heat transfer in a realistic cooled blade configuration. The convection heat transfer study includes a curvature modification and a proposed method to determine the Prandtl mixing length for the case of coolant ejection from discrete holes. The mixing lengths are especially evaluated for realistic gas turbine conditions where the ejected coolant layer thickness is in the order of the approaching

boundary layer thickness or larger. The computed results of convection heat transfer are compared with the measurements in the absence and presence of film cooling ejection. The molecular conduction field is predicted by means of a finite element method using the measured heat transfer coefficients as external boundary conditions.

KEYWORDS

Film cooling
Heat transfer
Turbomachinery
High temperature engines
Turbine blade
Boundary layers
Convection
Molecular conduction

NOMENCLATURE

The widely used symbols are given below. One should remember that a few of the symbols defined below may have more than one meaning. Only the most frequently used symbol is listed in the nomenclature. Others are explained in the text.

AREA	total film cooling area at the exit of the holes(perpendicular to the axis),[m ²]
a	speed of sound,[m/sec] $a = (\gamma \cdot R T_{\infty})^{1/2}$
A*/B	analogue circuit calibration constant $\sqrt{V}/(\text{units } \sqrt{\text{sec}})$
A ⁺	effective thickness of the viscous sublayer,[m]
[A]	global matrix of the finite element analysis
≈	
[B]	the matrix containing the shape function
≈	derivatives
̄c	chord length,[m]
c _p	specific heat of air at constant pressure [kJ/kgK]
c'	capacitance per unit length
C _d	discharge coefficient
d	ejection hole diameter,[m]
̄d	exit hole diameter of the shaped hole,[m]

dS	infinitesimal surface area [m ²]
dL	infinitesimal curvilinear length,[m]
D	Van Driest's damping parameter
E	Eckert number $E = \frac{U_\infty}{c_p} (T_{0\infty} - T_w)$
G	Grashof number $G = \frac{g \beta s^3 (T_{0\infty} - T_w)}{v^2}$
h_0 , h	convective heat transfer coefficient without,with film cooling, $h = \frac{q_s}{T_{0\infty} - T_w}$ [kw/m ² K]
i	incidence angle,[deg]
	positive in the counter clockwise direction
I	momentum flux ratio $I = \frac{\rho_c U_c^2}{\rho_\infty U_\infty^2}$
I^*	total enthalpy,[kJ/kg]
\bar{k}	thermal conductivity of air,[kW/mK]
λ	Prandtl's mixing length,[m]
$\bar{\lambda}_{max}$	maximum of the mixing length augmentation for film cooling on the turbine blade,[m]
m	blowing rate $m = \frac{\rho_c U_c}{\rho_\infty U_\infty}$
\dot{m}_c	coolant mass flow rate,[kgf/sec]
$\dot{m}_c / \dot{m}_\infty$	coolant to free stream mass weight ratio
$\delta\dot{m}$	coolant mass flow rate,shed into a stream-tube [kgf/sec]
\dot{m}_{old}	mass flow rate per unit depth in a stream-tube [kgf/sec]
Ma	local Mach number $Ma = \frac{U_\infty}{\sqrt{\gamma R T_\infty}}$
N	shape function
Nu	local Nusselt number , ($Nu = h \cdot s / \bar{k}$)
n	unit normal vector
Pr	molecular Prandtl number , ($Pr = \mu \cdot C_p / \bar{k}$)

P0	penetration depth,[m]
\overline{PD}	constant penetration depth , $\overline{PD} = 0.86$
Pe_t	turbulent Peclet number $Pe_t = \frac{\epsilon_m}{v} Pr$
p	pressure,[bar]
\dot{q}_s	wall heat flux rate,[W/cm ²]
[R] ~	right hand side vector in finite element solution
Ri	Richardson number,see page 122
R	thin film resistance,[ohms]
R_0	thin film resistance at ambient temperature [ohms]
r_j	coolant jet radius of curvature,[m]
r_w	wall radius of curvature,[m]
Re	local Reynolds number , $Re = \frac{\rho_\infty U_\infty s}{\mu_\infty}$
Re_θ	Reynolds number based on momentum thickness $Re_\theta = \frac{\rho_\infty U_\infty \theta}{\mu_\infty}$
Re	Reynolds number at which the transition onsets
1/R	curvature,[1/m]
s	curvilinear distance on the blade surfaces (negative on the pressure side) [m]
S	internal coolant passage area,[m ²]
S	gas side area,[m ²]
St_0, St	Stanton number
	without,with film cooling , $St = \frac{h}{\rho_\infty U_\infty C_p}$
t	time,[sec]
[t] ~	8 component temperature vector for a given finite element
T	temperature,[K]

T_{ref}	a reference temperature for the coolant,(290 K .
T_{u_∞}	turbulence intensity , $T_{u_\infty} = \frac{\sqrt{U'^2}}{U_\infty}$
U	velocity,[m/sec]
u', v'	fluctuating velocity components,[m/sec]
\bar{U}_{new}	average velocity in the boundary layer after coolant ejection,[m/sec]
\bar{U}_{old}	average velocity in the boundary layer before coolant ejection,[m/sec]
\bar{U}_j	coolant velocity at the exit of a hole,[m/sec]
V_0	thin film voltage at ambient temperature,[V]
x, y, z	cartesian coordinates
y	distance from the wall in a boundary layer,[m]
ρ	density,[kg/m ³]
μ	absolute viscosity of air,[kg/m]
δ	boundary layer thickness , ($\delta_{.99}$), [m]
$\frac{d}{R}$	strength of curvature parameter
δ	displacement thickness,[m]
$\bar{\theta}$	momentum thickness,[m]
k	von Karman constant , ($k = 0.41$)
θ	nondimensional coolant temperature, $\theta = \frac{T_{0\infty}-T_c}{T_{0\infty}-T_w}$
α	coolant ejection angle,[deg]
η	adiabatic wall effectiveness $\eta = \frac{T_{0\infty}-T_{av}}{T_{0\infty}-T_c}$
(ϵ, η)	local coordinates
η_{C0}	convective cooling efficiency $\eta_{C0} = \frac{T_{c_2}-T_c}{\bar{T}_m-T_c}$
η_f	film efficiency $\eta_f = \frac{T_{0\infty}-T_f}{T_{0\infty}-\bar{T}_m}$
ν	kinematic viscosity,[m ² /sec]
ϵ_m	eddy diffusivity of momentum,[m ³ /sec] $\epsilon_m = \frac{l^2}{\frac{\partial U}{\partial y}}$

μ_{eff}	effective viscosity,[kg/m] $\mu_{\text{eff}} = \mu + \mu_t = \rho(\gamma + \epsilon_m)$
μ_t	turbulent viscosity,[kg/m]
γ	specific heat ratio $\gamma = \frac{c_p}{c_v}$
α	thermal diffusivity,[m ² /sec] $\alpha = \frac{k}{\rho c}$
Γ	circulation
β_1, β_2	inlet,exit flow angle measured from the axial direction,[deg]
λ	outer layer constant
$\sqrt{\rho ck}$	density,specific heat and thermal conductivity triple product of a solid material W·√sec/(cm ² ·K)
α_R	temperature coefficient of a thin film,[K]
π	pressure ratio , $\pi = \frac{P_2}{P_1}$

SUBSCRIPTS

a_w	adiabatic wall
\bar{c}	based on chord length
c	relative to coolant
ex	exit
in	inlet
o	total condition
0^∞	free stream total condition
r	recovery
$\bar{\theta}$	based on momentum thickness

LIST OF FIGURES

- Fig.1 Enthalpy-entropy diagram of a simple gas turbine cycle
- Fig.2 Variation of thermal efficiency with respect to pressure ratio and temperature ratio
- Fig.3 Internal convection cooling through a hollow blade,HALLS,[5]
- Fig.4 Steam cooling on the leading edge of a rotor blade,RICE,[8]
- Fig.5 Internal convection cooling
- Fig.6 Extended surfaces used in convection cooling
- Fig.7 Impingement cooling+film cooling+trailing edge ejection, METZGER,[9]
- Fig.8 Impingement cooling+trailing edge ejection,HALLS,[5]
- Fig.9 Transpiration cooling,HALLS,[5]
- Fig.10 A film cooled turbine blade
- Fig.11 A film cooled turbine blade,double rows only
- Fig.12 Coolant jet-mainstream interaction,GOLDSTEIN et al.,[91]
- Fig.13 Full coverage film cooling,MEINER,[17]
- Fig.14 Thermal energy balance in a cooled turbine blade
- Fig.15 ϵ as a function of mass flow function
- Fig.16 A turbine rotor blade and free stream Ma number distribution,CONSIGNY,[62]
- Fig.17.a Radial temperature variation in front of a nozzle guide vane,MUKHERJEE,[19]
- Fig.17.b Radial temperature variation in front of a nozzle guide vane,HENNECKE,[14]
- Fig.18 Heat transfer and free stream static pressure distribution around a turbine blade,WILSON and POPE,[80]

- Fig.19 Heat transfer coefficients and comparisons with theory around a turbine blade, TURNER,[60].
- Fig.20 Effect of frequency of turbulence on heat transfer coefficient
- Fig.21.a Local heat transfer coefficients on a nozzle guide vane for a range of exit Re numbers,[65]
- Fig.21.b Effect of intensity and frequency of turbulence on heat transfer at different locations on a turbine blade,[65]
- Fig.22 Effect of inlet Re number without turbulence grid,DANIELS,[34]
- Fig.23 Effect of inlet Re number with turbulence grid,DANIELS,[34]
- Fig.24 Comparison of TURNER's [83] heat transfer coefficients around a turbine blade with PRIDDIN's predictions,[84]
- Fig.25 Effect of TU_∞ on heat transfer coefficients on a turbine blade,BAYLEY et al.,[65]
- Fig.26 Comparison of k- ϵ predictions and heat transfer coefficients on a turbine blade,CONSIGNY,[62],i=0 deg
- Fig.27 Comparison of k- ϵ predictions and heat transfer coefficients on a turbine blade,CONSIGNY,[62],i=15 deg.
- Fig.28 Influence of TU_∞ on measured mean Nu number on a turbine blade and comparisons,CONSIGNY,[62]
- Fig.29 Heat transfer on the suction side and on the pressure side of a nozzle guide vane,KERCHER et al.,[89]
- Fig.31 Discrete hole film cooling, isothermal wall effectiveness on a flat wall,[92]
- Fig.32 Static pressure variations around a film cooling hole,[94]
- Fig.33 Velocity profiles just after double row of ejection holes,[95]
- Fig.34 Comparison of adiabatic wall effectiveness from single row of holes and double row of holes,GOLDSTEIN et al.,[97]
- Fig.36 Adiabatic wall effectiveness distribution over a flat plate with three sets of injection rows,with and without a favourable pressure gradient,[105]
- Fig.35 Influence of approaching boundary layer type,with a laminar and turbulent coolant jet on n ,single row of holes,[102]
- Fig.37 Film cooling geometry on the leading edge of a turbine blade compound angled ejection,LUCKEY et al.,[108]

- Fig.38 A turbine airfoil leading edge for film cooling studies ,KRUSE,[12]
- Fig.39.a Variation of the stagnation line position with film cooling ,KRUSE,[12]
- Fig.40 Three film cooling configurations on a turbine blade,[106]
- Fig.41 Superposition of cooling fields and effect of exit Re on adiabatic wall effectiveness,[106]
- Fig.42 Curvature effects on film cooling layers,[114]
- Fig.43.a Averaged adiabatic wall effectiveness on the surfaces of a gas turbine blade,[114]. $\rho_c/\rho_\infty=0.95$
- Fig.43.b Averaged adiabatic wall effectivenesses on the surfaces of a gas turbine blade, $\rho_c/\rho_\infty=2.00$
- Fig.44 Film cooling geometry of [34]
- Fig.45 Breakdown of turbine efficiency loss associated with rotor cooling flows,BARRY,[18]
- Fig.46 The thermal efficiency reductions due to coolant ejection MC DONEL,[123]
- Fig.47 VKI/CT-2 compression tube facility
- Fig.48 A schematic view of the compression tube
- Fig.49 Timing of the events
- Fig.50 The fast opening valve
- Fig.51 Compression tube pressure and piston velocity,time history
- Fig.52 Measured total pressure fluctuations in the test section of CT-2
- Fig.53 Heat conduction in a metallic film on semi-infinite insulating substrate
- Fig.54 Electrical analogue using equal sections representing a homogeneous heat conductor
- Fig.55 Parabola input signal for calibration of analog circuits
- Fig.56 Step output signal from a calibration of analogue circuits
- Fig.57 Penetration of thermal pulse into substrate from step function in surface heat flux,from [125]
- Fig.58 Penetration of thermal pulse into substrate due to step function in surface heat flux

- Fig.59 Effect of surface metallic film on calculated heat transfer rate. q_0 =amplitude of actual step function in heat transfer rate
- Fig.60 Time response of a thin film platinum gauge with $\alpha^{1/2}=0.10$ and $\alpha=0.25 \text{ cm}^2/\text{s}$
 $(\rho_1 C_1 k_1 / \rho_2 C_2 k_2)$
- Fig.61 Response time from thin platinum film, time for the heat flow to reach 94 % of step input value with $\alpha=0.25 \text{ cm}^2/\text{s}$
 $\alpha^{1/2}=0.10$
 $(\rho_1 C_1 k_1 / \rho_2 C_2 k_2)$
- Fig.62 Sketch illustrating response criteria for electrical analogue circuits
- Fig.63 Typical calibration graph of a thin film gauge
- Fig.64 Typical α_R calibration results
- Fig.65 Measured pressure in the compression tube
- Fig.66 Measured free stream total pressure
- Fig.67 Inlet static pressure
- Fig.68 Measured coolant pressures
- Fig.69 Temperature measurement in the free stream and in the compression tube
- Fig.70 Measured coolant temperatures
- Fig.71 A typical sonic orifice and measurement locations
- Fig.72 Coolant air supply
- Fig.73 High speed data acquisition system and analogue circuits used for processing signals from thin-film gauges
- Fig.74 Measurement chain
- Fig.75 A flow chart for the software developed for CT-2
- Fig.76 A typical cascade exit static pressure trace
- Fig.77 Typical wall heat flux traces
- Fig.78 Temperature dependency of the thermal conductivity and the thermal diffusivity for machinable glass ceramic,[128]
- Fig.79 External profile of the blade
- Fig.80 Coordinates of the HP turbine rotor blade
- Fig.81 The cascade geometry
- Fig.82 The cascade

- Fig.83 Heat flux gauge locations
 Fig.84 Thin film heat flux gauges mounted on the film cooled blade
 Fig.85 The three film cooling ejection sites
 Fig.86 The geometrical details of the LEADING EDGE ejection site
 Fig.87 The geometrical details of the SUCTION SIDE ejection site
 Fig.88 The geometrical details of the PRESSURE SIDE ejection site
 Fig.89 The fully assembled heat transfer instrumented blade
 Fig.90 Plenum chamber and side-wall connection details
 Fig.91 Plenum chamber and side-wall connection details
 Fig.92 Blade velocity distribution
 Fig.93 Calculated iso-Mach number lines in the turbine passage
 Fig.94 Leading edge heat transfer without cooling , effect of T_{∞}
 Fig.95 Influence of unblocked leading edge holes ($\dot{m}_e/\dot{m}_{\infty} = 1.4 \%$ and $U_{\infty}^{inlet} = 7.7 \text{ m/sec}$)
 a. Leading edge holes are not blocked
 b. Leading edge holes are blocked
 Fig.96 Leading edge heat transfer without cooling , effect of holes existence
 Fig.97.a Wall heat flux signals ($0.01 < s/\bar{c} < 0.27$)
 Fig.97.b Wall heat flux signals ($0.12 < s/\bar{c} < 0.27$)
 Fig.97.c Wall heat flux signal ($s/\bar{c} = 0.31$)
 Fig.98 Heat flux gauge locations on the suction side
 Fig.99 Effect of local Re number on heat transfer
 Fig.100 Suction side heat transfer without cooling
 Fig.101 Heat transfer at different T_{∞} levels, (no coolant ejection)
 Fig.102 Effect of inlet flow direction on Mach number distribution around the leading edge

Fig.103 Leading edge velocity distribution,
effect of incidence
(calculations with a singularity method)

Fig.104 Leading edge heat transfer without cooling,
effect of incidence

Fig.105 Influence of incidence angle on heat transfer
without ejection

Fig.106 Cooling holes discharge coefficients

Fig.107 Oil flow vizualisation
leading edge ejection
 $\dot{m}_e/\dot{m}_\infty = 1.4 \%$ and $U_{\infty, \text{inlet}} = 7.7 \text{ m/sec}$

Fig.108 Leading edge heat transfer with film cooling,
effect of temperature ratio

Fig.109 Effect of wall temperature deviations from an
isothermal value on h

Fig.110 Leading edge heat transfer with film cooling,
effect of mass weight ratio

Fig.111 Leading edge heat transfer with film cooling,
effect of coolant temperature

Fig.112 Averaged leading edge heat transfer

Fig.113 Leading edge heat transfer with film cooling,
effect of incidence, ($T_U = 0.8 \%$)

Fig.114 Oil flow vizualisation
suction side ejection
 $\dot{m}_e/\dot{m}_\infty = 1.4 \%$ and $U_{\infty, \text{inlet}} = 7.7 \text{ m/sec}$

Fig.115 Suction side heat transfer with film cooling,
effect of blowing rate
($i=0, T_U = 5.2 \%, Re_g = 8.42 \times 10^5, T_w/T_\infty = 0.72, T_\infty = 408 \text{ K}$)

Fig.116 Typical velocity profiles,
downstream of double rows of cooling holes

Fig.117 Jet penetration into the mainstream at high
blowing rates

Fig.118 Suction side heat transfer with film cooling,
low blowing rate

Fig.119 Suction side heat transfer with film cooling,
medium blowing rate

Fig.120 Suction side heat transfer with film cooling,
high blowing rate

- Fig.121 Oil flow vizualisation
pressure side ejection
 $\dot{m}_e / \dot{m}_{\infty} = 1.1 \%$ and $U_{\infty, \text{inlet}} = 7.7 \text{ m/sec}$
- Fig.122 Heat transfer coefficient, h , no coolant ejection
($i=0$, $T_{U\infty}=5.2 \%$, $Re_{\infty}=8.4 \times 10^5$, $T_w/T_{\infty}=0.70$, $T_{\text{cool}}=409 \text{ K}$)
- Fig.123 Film cooling on the pressure side,
coolant at wall temperature, ($T_e/T_{\infty}=0.70$)
- Fig.124 Film cooling on the pressure side
 h/h_0 reductions due to lowered coolant temperature level
($T_e=0.5 \times T_{\infty}$)
- Fig.125 Total normalized coolant mass weight ratio
versus plenum chamber pressure
- Fig.126 Discharge coefficients of ejection sites
- Fig.127 Coolant split in between plenum chambers
($i=P, S$ or L)
- Fig.128 Local blowing rates of the ejection sites
- Fig.129 Leading edge film cooling heat transfer,
a verification of the evaluated hydrodynamic data
- Fig.130 Simultaneous coolant ejection from L,P and S
($T_e/T_{\infty}=T_w/T_{\infty}=0.71$)
- Fig.131.a Effect of blowing rate on film cooling heat transfer
- Fig.131.b Effect of coolant temperature on film cooling
heat transfer
- Fig.132 Influence of leading edge ejection on downstream
coolant layers (P and S)
- Fig.133 Effect of free stream turbulence intensity on
film cooling heat transfer
- Fig.134 Effect of incidence angle on film cooling heat transfer
- Fig.135 Effect of incidence angle on film cooling heat transfer, $i=+10$
- Fig.136 Effect of incidence angle on film cooling heat transfer, $i=-10$
- Fig.137 Comparison of film cooling heat transfer data taken at various
incidences, ($i=0 +10, -10$)
- Fig.138 Outer layer mixing length, curvature and
boundary layer thickness on the suction side
- Fig.139 Momentum thickness Reynolds number, with and without
curvature effect

Fig.140 Measured St_{∞} number distribution and predictions without cooling

Fig.141 Curvature and outer layer mixing length variation on the pressure side

Fig.142 Free stream velocity profile on the pressure side

Fig.143 Measured St distribution and comparison with predictions on the pressure side,

($i=0.., Ma_{inlet} = 0.25, Ma_{exit,i} = 0.908, TU_{\infty} = 5.2 \%, Re_{\infty} = 8.4 \times 10^5, T_{\infty} = 410 \text{ K}, T_w = 300 \text{ K}$)

Fig.144 Momentum thickness Re variation on the pressure side and comparison with the suction side data

Fig.145 St_{∞} predictions on the pressure side

Fig.146 Coolant boundary layer interaction in a typical control volume

Fig.147 Boundary layer scaling in the presence of film cooling

Fig.148 Mass shed ratio versus blowing rate

Fig.149 Boundary layer thickness variation on the suction side with film cooling

Fig.150 Finite difference mesh near suction side ejection rows

Fig.151 Mixing length augmentation due to coolant ejection on the suction side

Fig.152 Augmented mixing length versus blowing rate

Fig.153 Film cooling heat transfer,predictions, $m < 0.69$

Fig.154 Film cooling heat transfer,predictions

Fig.155 Film cooling heat transfer,predictions, $m > 0.76$

Fig.156 Film cooling heat transfer,predictions

Fig.157 Comparison of \bar{x}_{max} with ref.[133]'s slant angle ejection data

Fig.158 A solution domain and the boundaries for the heat conduction problem

Fig.159 Second order curved and isoparametric finite elements

Fig.160 The shape functions

Fig.161 The discretization of the film cooled blade

Fig.162 The external convective heat transfer coefficients used in the heat conduction analysis

Fig.163 Isothermal contours in the blade
only internal convection cooling,CASE-1

Fig.164 Heat flux vectors
only internal convection cooling,CASE-1

Fig.165 Isothermal contours in the blade
Internal convection + film cooling
film cooling hole effect is not included,CASE-2

Fig.166 Heat flux vectors
Internal convection + film cooling
film cooling hole effect is not included,CASE-2

Fig.167 Isothermal contours in the blade
Internal convection + film cooling
film cooling hole effect is included,CASE-3

Fig.168 Heat flux vectors
Internal convection + film cooling
film cooling hole effect is included,CASE-3

Fig.169 Computed surface temperature distribution on the suction side;comparison of CASE-1 , CASE-2 and CASE-3

LIST OF TABLES

- | | |
|----------|---|
| Table 1. | A tabulation of film cooling hole sizes
on the leading edge of gas turbine blades |
| Table 2. | A review of injection hole diameter for
film cooling studies on gas turbine blades |
| Table 3. | Uncertainties on the basic experimental
parameters |
| Table 4. | Main experimental parameters of the leading
edge film cooling study |

LIST OF APPENDICES

- Appendix 1. Boundary layers and heat transfer on a turbine airfoil,a literature review
- Appendix 2. Discrete hole film cooling on flat walls, a literature review
- Appendix 3. Wall heat flux measurement technique
- Appendix 4. Turbulent shear stresses and heat fluxes
- Appendix 5. Viscous sublayer thickness versus p^+
- Appendix 6. Turbulent Prandtl number variation
- Appendix 7. Input data for heat transfer predictions (suction side)
- Appendix 8. Input data for heat transfer predictions (pressure side)

CHAPTER 1

INTRODUCTION

It is a well known fact that gas turbine engines operate more efficiently when their entry temperatures are elevated ,for a given pressure ratio of the cycle.Due to sharply increasing demands to fuel efficient or compact aeroengines;in recent years,high temperature operation became a widely accepted mode of operation.The maximum permissible turbine entry temperature is limited due to materials considerations.Therefore,cooling of a turbine blade by internal and external means is necessary to prolong the life of the blading in the extremely harsh medium of a gas turbine engine.

In recent years discrete hole film cooling has most of the time been studied on flat adiabatic walls in relatively low speed environments compared to aeroengine conditions.The most frequently reported quantities were either the local temperature variation downstream of the ejection site on a perfectly adiabatic wall or the heat transfer coefficient when the coolant

is ejected at the same temperature as the mainstream. However, in a high temperature engine due to very strong local temperature gradients, local wall heat flux levels on the external surfaces of the blade are not negligible. Furthermore, coolant fluid is never ejected at the temperature of the main gas stream, like many adiabatic wall experiments performed in the past with a coolant to mainstream density ratio of unity. A typical coolant temperature level of a high temperature engine is about half of the mainstream level. A successful design of a cooled airfoil can only be achieved by knowing external heat loads which are mainly determined by very complex flows of viscous nature surrounding the airfoil. External heat flow to a film cooled airfoil can be represented by a convective heat transfer coefficient defined between the free stream recovery temperature and the local temperature of the wall at a prescribed coolant temperature.

The major aim of this study is to investigate forced convection heat transfer through the film cooled layers of turbulent boundary layers existing on a high pressure gas turbine rotor blade. After a literature review on gas turbine cycle considerations, blade cooling methods, gas side heat transfer without cooling; film cooling on flat walls and on turbine blades with adiabatic and non-adiabatic walls are discussed from available literature. In chapter-3, the technique for the quantitative measurement of wall heat flux, transient pressure and temperature measurements; the coolant ejection system and the heat transfer model are described in detail.

Experimental results of convective heat transfer measurements on the rotor blade in the presence and absence of discrete hole film cooling are given in chapter-4, at various locations on the blade, in a range of blowing rates and coolant temperatures. Measurements are taken in the CT-2 compression tube facility of the VKI under realistically simulated gas turbine conditions. Coolant hydrodynamics is also discussed. In chapter-5, the predictability of heat transfer measurements is searched using a two dimensional differential boundary layer code on the suction side of the blade without and with film cooling. An already existing boundary layer code is modified in

order to take the influence of the strong longitudinal curvature on the turbine blade heat transfer into account. For the case of film cooling, a modified mixing length is proposed from quantitative heat flux measurements, in order to handle near ejection site turbulence augmentations in the form of Prandtl's mixing length. Numerical calculations of heat transfer with film cooling are compared with the measured data. Measured external heat transfer coefficients are used in the predictions of internal local wall heat flux patterns in the rotor blade. A numerical approach based on a finite element method to solve the heat conduction equation is employed for this purpose and the results are used in the interpretation of local heat flow behaviour in the blade under realistic gas turbine conditions

CHAPTER 2

LITERATURE REVIEW

2.1 CYCLE CONSIDERATIONS

The enthalpy entropy diagram of a simple gas turbine cycle is shown in fig.1. The air is first compressed in a compressor with a pressure ratio of,

$$\pi = \frac{P_2}{P_1} \quad (1)$$

Combustion of fuel in a combustor generates the hot mainstream fluid, just before the nozzle guide vanes of the high pressure turbine stage. The ratio of the maximum cycle temperature to compressor inlet temperature is defined as follows :

$$\theta = \frac{T_3}{T_1} \quad (2)$$

The thermal energy of the hot mainstream gases is converted into kinetic energy through a turbine .The ratio of obtained net work to consumed fuel thermal energy is the thermal efficiency of the cycle.For the simple gas turbine cycle shown in fig.1 , the thermal efficiency may be written as :

$$\eta_{th} = \left(1 - \left(\frac{1}{\pi} \right)^{\frac{\gamma-1}{\gamma}} \right) \cdot \left[\frac{\eta_t \cdot \theta^{\frac{\gamma-1}{\gamma}} / \eta_c}{\theta - 1 - \frac{\pi^{\frac{\gamma-1}{\gamma}} - 1}{\eta_c}} \right] \quad (3)$$

where η_t is the adiabatic efficiency of the turbine and η_c is the adiabatic efficiency of the compressor .Eq. (3) is valid under the following assumptions :

-- negligible pressure drop in the combustion chamber.

-- constant specific heat ratio.

The variation of thermal efficiency as a function of pressure ratio π and temperature ratio θ is given in fig.2 for $\eta_t = \eta_c = .85$.The figure shows that,at a pressure ratio of 25,increasing θ from 4 to 8 may almost double the thermal efficiency of the gas turbine cycle, indicating the marked influence of turbine entry temperature on the thermal efficiency of the cycle.

During the 1960's the first cooled commercial engine became operational with a turbine entry temperature of 1300 K .From that time on, continuous improvements in aero engine technology led to turbine entry temperatures of 1650 K in the 1980's,HOLLAND and THAKE , [1].The latest commercial transport engines such as JT 9-D ,CF-6,RB-211 have turbine entry

temperatures during take off conditions close to 1550 K, KERREBROCK , [2].Entry temperatures during cruise are somewhat lower. There are also experimental engines operating in the range of 2000 K to 2500 K ,according to OLSSON , [3].In a typical high temperature engine,a pressure ratio of 25 and a maximum cycle temperature of 1800 K are possible.The maximum permissible turbine entry temperature is however limited by material considerations.

When the blade temperature rises above 1250 K,material properties such as creep strength,fatigue and oxidation resistance fall rapidly.A composite material of tungsten reinforced superalloy may endure a temperature of 1350 K OLSSON ,[3] being superior to ordinary superalloys which may withstand up to 1250 K.From a materials point of view,a 20 K increase in metal temperature may halve the life of a blade, over a certain specified temperature limit.As it was discussed earlier,thermodynamic cycle considerations suggest that,increasing the amount of useful power from a given amount of fuel is only possible by an increase in cycle temperature ratio Θ ,at a given pressure ratio.High pressure turbine components,especially nozzle guide vanes and rotor blades must be cooled effectively because of weak material behaviour at elevated turbine entry temperatures.Another important alternative is to continue to develop high temperature resistant materials such as ceramics, thermal barrier coatings,LIEBERT and STEPKA ,[4] ,directionally solidified materials,radially stacked (diffusion bonded) laminates etc..The introduction of unidirectional solidification has brought improvements,especially in fatigue life of materials,HOLLAND and THAKE ,[1].It is hoped that the future use of single crystal blades,rapid solidification,powder metallurgy,directionally solidified eutectics and oxide dispersion strengthened alloys will permit further increases in engine temperatures.In the future,higher temperatures over 1800 K may easily be feasible by adding efficient cooling systems to turbine components manufactured from advanced high temperature resistant materials.

2.2 BLADE COOLING METHODS

Historically blade cooling applications started during world war II. One of the first cooled rotor blades is shown in fig.3,HALLS ,[5]. Up to now many types of cooling systems such as liquid cooling, steam cooling, water spray cooling, liquid metal cooling, internal convection cooling with air, impingement cooling, film cooling, full coverage film cooling, transpiration cooling were developed .

Liquid cooling systems are almost always closed circuits. A closed circuit is necessary to avoid a waste of coolant fluid. The coolant liquid can flow radially inward and outward through one or more passages in the blade . In gas turbine practice, water cooled turbines have been operated in the U.S. and Europe because of the excellent heat transfer characteristics of water, ESGAR ,[6]. However, water used as a turbine blade coolant has a very serious disadvantage. The boiling point of water is very low unless the entire coolant system is under very high pressures. At elevated coolant pressures, the turbine is overcooled and the heat ejection rates are excessive. Development of a three stage liquid cooled gas turbine is reported by ALPERT et al., [7]. The turbine, made of nonstrategic low alloy components is aimed to operate at a 1230 K TET with the help of a closed liquid cooling system.

Steam cooling of a reheat gas turbine cycle is shown schematically in fig.4. According to RICE ,[8], the leading edge of nozzle guide vanes or rotor blades may be cooled using steam as a coolant fluid. In order to improve the heat exchange, turbulence ribs are used internally in the leading edge . In addition to cooling, the vane shown in fig.4 is coated with a ceramic thermal barrier.

Water spray cooling is accomplished by spraying water on to the blade external surface. Water is sprayed from a few stationary circumferential locations and impinges on the blades in the leading edge area. Such a method is disadvantageous

particularly because of noncooled trailing edge. Thermal shock to the blades when the water spray is introduced is a major drawback.

Internal convection cooling of gas turbine blades through forced convection by circulating compressor extraction air inside the blade is one of the most commonly used methods. The air flows in a hollow interior or cooling passages inside the blade, fig.5. Most internally cooled rotor blades have their cooling air supplied into passages starting within the blade root and developing in the spanwise direction towards the blade tip, fig.6. The air is usually discharged through the tip which often carries a shroud and a sealing system or through a film cooling configuration across the external surfaces of the blade. Aeroengine cooling air supply systems suffer from heat pick up and pressure losses between the high pressure compressor exit and the cooled blade root. Such losses and heat pick up reduce the thermal efficiency of the total process. At the root of a cooled blade, coolant temperatures may be e.g. around 100 K hotter than their isentropic values, HOLLAND and THAKE , [1].

An impingement cooled turbine blade equipped with a coolant insert is shown in fig.7. It is generally accepted that, impingement of the cooling air normal onto a hot surface is advantageous, HALLS , [5]. On the leading edge of gas turbine blades, a combination of internal jet impingement cooling and film cooling is often used, METZGER , [9]. Fig.8 shows the cross section of a blade incorporating such a cooling scheme. A two dimensional array of coolant jets cools the inner skin of the blade in the region where the effectiveness of the leading edge film decays to very low values. Part of the impingement cooling fluid is discharged through the trailing edge of the blade. Extensive studies of impingement cooling are reported by FLORSCHUETZ et al. , [10].

Transpiration cooling of a gas turbine blade is also known as effusion cooling. The cooling air is introduced inside the blades made of porous or permeable material as shown in

fig.9,MOSKOWITZ et al.,[11].The air passes into the mainstream through the very fine holes or cavities of the porous wall.The mixing of coolant jets with the hot mainstream gas strongly depends on the size and the arrangement of the holes,KRUSE,[12].The highest cooling effectiveness can be achieved by blowing the coolant through porous blade materials into the boundary layer.However the thermal and mechanical strength of the present day porous materials are quite limited.MOSKOWITZ and LOMBARDO ,[11] report a maximum allowable porous blade material temperature of 1260 K.The difficulties in the production of materials with uniform porosity and the possibility of local clogging due to harsh environment of a gas turbine engine limit the extensive use of such a cooling scheme.

Discrete hole film cooling may be considered as a particular case of transpiration cooling. Coolant air is ejected into the boundary layer through a finite number of rows of holes inclined at a certain angle. The highest cooling protection is observed just downstream of the ejection holes and the protection dies away with increasing downstream distance.Typical examples of film cooled nozzle guide vanes are given in fig.10 and fig.11. The hole spacing is usually several hole diameters,the latter being of the order of 0.5 1.0 mm. or even larger.Since the boundary layer thickness is generally of this order or even smaller,discrete jets, penetrating into the boundary layer are turned by the free stream and then flow along the surface,mixing with the boundary layer fluid.A qualitative description of coolant jet/free stream interaction is given by ABRAMOWITCH [15], KEFFER et al. [16].As the secondary fluid jets leave the ejection holes,they retard the main flow along the upstream side of the jet.This phenomenon causes a pressure increase on the upstream side of the jet.The pressure difference between the upstream and downstream side deforms the jet,fig.12.Circulatory motions are caused by the intensive intermixing of the two flows.The deformation of the jet is strongly affected by the blowing rate.

Full coverage film cooling is a variation of film cooling. In order to obtain a maximum effectiveness, most of the time the compressor discharge air first impinges on the inner surface of the vane or blade shell to remove heat through forced convection. The cooling air is then bled out through a large number of evenly distributed holes in the shell ,fig.13,[17]. The coolant forms a continuous, cool insulating layer between the outer surface of the shell and the hot gas stream.

2.3 CONTRIBUTION OF FILM COOLING ON THE COOLING EFFICIENCY OF A GAS TURBINE BLADE

A simple heat exchange model is a very useful tool in explaining the important contribution of film cooling on the total cooling efficiency of a gas turbine blade. The following discussion is based on the model suggested by BARRY ,[18].

The total cooling efficiency of a gas turbine blade including hot gas side and internal heat exchange phenomena can be expressed as follows,

$$\epsilon = \frac{T_{0\infty} - \bar{T}_m}{T_{0\infty} - T_{C1}} \quad (4)$$

where $T_{0\infty}$, \bar{T}_m , and T_{C1} are respectively the total free stream, mean blade and inlet coolant temperatures.

Such a quantity is mainly related to the hot gas side heat transfer ,in addition to all cooling processes applied internally.In order to insulate the internal cooling activities from the gas side heat transfer with film cooling,the internal convective cooling efficiency is defined as follows,

$$\eta_{C_0} = \frac{T_{C_2} - T_{C_1}}{\bar{T}_m - T_{C_1}} \quad (5)$$

where T_{C_2} is the coolant exit temperature from the blade. Conservation of energy in the region shown in fig. 14, leads to the following expression of internal convective cooling efficiency.

$$\eta_{C_0} = 1 - \exp\left(-\frac{1}{m^*} \cdot \frac{h_i S_i}{h_o S_0}\right) \quad (6)$$

$$m^* = \frac{\dot{m}_c C_p c}{S_0 L h_0} \quad (6a)$$

- \dot{m}_c being the coolant mass flow rate, h_i the internal convective heat transfer coefficient, S_i the internal area, h_o the gas side mean heat transfer coefficient, S_0 the gas side total surface area, L the blade length and C_p the coolant specific heat.

Using equations (4), (5), (6) and (6.a), the total blade cooling efficiency can be related to the internal convective cooling efficiency, as follows :

$$\epsilon = \frac{\eta_{C_0} \cdot m^*}{1 + \eta_{C_0} \cdot m^*} \quad (7)$$

Fig.(15) shows the relation between ϵ and m^* in terms of η_{C_0} and $h_i S_i / h_o S_0$, which is a measure of the ability of the internal cooling system to remove the heat introduced across the hot gas side. In order to maximize $h_i S_i / h_o S_0$, extended surfaces and fins are widely used in internal convective cooling

systems. Turbulence augmentors and complicated internal geometry of the coolant channels inside the blade may augment h resulting in higher internal convective cooling efficiency, as given in eq.(6). Fig.15 shows that, as the convective efficiency rises, it becomes difficult to achieve increases in cooling effectiveness by increasing the product $h_i S_i$ alone. This is the starting point where internal convective cooling has to be complemented by film cooling. In order to clarify the beneficial effect of film cooling on the total blade cooling efficiency, a film efficiency based on mean film temperature is defined as follows,

$$\eta_f = \frac{T_{0\infty} - T_f}{T_{0\infty} - \bar{T}_m} \quad (8)$$

Eq.(4) may be splitted into two parts

$$\varepsilon = \frac{T_{0\infty} - \bar{T}_m}{T_{c_2} - T_{c_1}} \cdot \frac{T_{c_2} - T_{c_1}}{T_{0\infty} - T_{c_1}} \quad (9)$$

and arranging eq.(9),

$$\varepsilon = \left[\frac{(T_f - \bar{T}_m) + (T_{0\infty} - T_f)}{(T_{c_2} - T_{c_1})} \right] \cdot \begin{bmatrix} (T_{c_2} - T_{c_1}) & (\bar{T}_m - T_{c_1}) \\ (\bar{T}_m - T_{c_1}) & (T_{0\infty} - T_{c_1}) \end{bmatrix} \quad (10)$$

eq.(10) yields to,

$$\varepsilon = \left[m^* + \frac{T_{0\infty} - T_f}{T_{c_2} - T_{c_1}} \right] \cdot \eta_{c_0} (1-\varepsilon) \quad (11)$$

and,

$$\epsilon = \frac{m^* \cdot n_{c_0}}{1 + m^* \cdot n_{c_0} - n_f} \quad (12)$$

Eq.(12) shows the possible contribution of film cooling to the total blade cooling efficiency. If a high pressure turbine blade for which $m^* = 1.0$ and $h_i S_i / h_o S_o = 1.5$ is considered; a 100 % rise of the $h_i S_i / h_o S_o$ value is needed for a 10 % gain of the ϵ value. However, such an increase in ϵ can be gained by only applying film cooling on the hot gas side having a mean film effectiveness equal to 0.2 and keeping $h_i S_i / h_o S_o$ equal to 1.5. Such an argument supports the idea that film cooling is an extremely efficient way of supplementing internal convective cooling on a gas turbine blade.

2.4 AERODYNAMIC LOSSES DUE TO COOLANT EJECTION IN A TURBINE STAGE

Film cooling is known to improve the thermal efficiency of a gas turbine cycle through important increases in turbine entry temperature. There are however situations in which film cooling may show a detrimental aerodynamic behaviour when excessive amounts of coolant are introduced in a turbine stage. In recent years, aerodynamic penalties associated with the coolant film ejection in a stage have been studied by a number of investigators. According to HARTSEL's constant pressure mixing model,[109], the blading efficiency penalty is,

--proportional to the coolant to free stream mass weight ratio,

--a strong function of mixing Mach number and ejection angle ,

--a weaker function of T_e / T_{∞}

Different coolant ejection sites in a stage result in different aerodynamic penalties.A breakdown of turbine efficiency losses associated with rotor cooling flows is given in fig.45,BARRY,[18].It may be noted that the ejection of the suction surface coolant has an extremely important negative effect on efficiency. ITO,ECKERT and GOLDSTEIN,[120] predicted the aerodynamic losses based on HARTSEL's constant pressure mixing approach. The model developed by TABAKOFF and HAMED [121] is based on the assumption that all the coolant stays in the mainstream boundary layer.However,most of the time,in turbine blade cooling applications,the coolant layers penetrate into the free stream.

Another approach dealing with the aerodynamic loss problem due to cooling was the elimination of external film cooling using very efficient internal cooling schemes especially on the suction side,[122].HESS reports a reduction in the aerodynamic losses of approximately 30 % less than the design point which was achieved with the externally film cooled airfoil.

The thermal efficiency of an experimental turbine is given in fig.46 ,by McDONEL,[123] as a function of stator and rotor coolant mass weight ratio.When only the stator blade was cooled with a discrete hole cooling scheme, a 1.1 % thermodynamic efficiency drop is reported.When the stator and the rotor are simultaneously cooled,the total reduction is about 3.35 %.The high detrimental influence of rotor blade cooling may be related to the influence of enormous centrifugal forces acting on high density ($\rho_e / \rho_{\infty} = 2$) coolant layers in a rotating frame.

The trailing edge of an HP rotor blade is slender and difficult to cool.This region must be well cooled by substantial film ejection or by internal air cooling.This may result in

relatively thick trailing edges. Due to the blockage effect ,the trailing edge losses of a typical high pressure turbine,having a transonic exit Mach number can be as high as 3 % of turbine efficiency,[18].The trailing edge losses are caused by two different effects.The first is the unsteady wake mixing and the second is the shock formation in the external passage flow.A detailed hydrodynamic investigation of the trailing edge configuration is given by SIEVERDING ,[124].An experimental investigation of trailing edge geometry on thermodynamic efficiency is reported by BARRY,[18]

2.5 HOT MAINSTREAM FLOW OVER A TURBINE AIRFOIL

During the flow of hot and accelerated combustion gases through a blade passage ,a certain amount of external moment is exerted on the rotor disk,because of the rate of change of angular momentum. Because of the specific flow phenomena occurring in a turbine passage ,the convex and concave sides of the rotor blade naturally experience different static pressure distributions in the streamwise direction.In fig.16,a typical turbine rotor blade geometry and its associated inviscid free stream velocity distribution at zero incidence are given,[62].The mainstream fluid enters the turbine passage at a given angle,defining univocally the stagnation point position.

The hot mainstream fluid in front of the first nozzle guide vanes has usually a nonuniform total temperature distribution in the radial direction.A typical example of such a total temperature distribution is presented in fig.17.a ,MUKHERJEE and FREI ,[19] .The maximum temperature is observed close to the mean radius. Another gas temperature distribution is shown in fig.17.b,[14].

Near the stagnation zone,the turbulence intensity of the gas is amplified and a 3D flow structure exists,creating the highest local wall heating rates on the blade.Streamwise

vortices existing on both sides of the stagnation line start getting amplified in the downstream direction. The laminar boundary layer instabilities occurring around the leading edge have a very complicated nature. The critical Re number for instability is defined as the position where small disturbances become amplified in the laminar boundary layer.

Along the suction side, the influence of a strong favourable pressure gradient, amplification of the instabilities created on the leading edge, formation of very high local shear stresses, vortex breakdown and hairpin eddy formation are possible related phases of a laminar to turbulent transition.

Along the pressure side, the mainstream fluid first strongly accelerates, farther, an adverse pressure gradient may be observed, almost at the curvature inversion location. The strength of this velocity peak depends however on the blade design. A very early breakdown of streamwise vortices originating from the leading edge and a very quick laminar to turbulent transition may then occur very close to the stagnation region. The transitional behaviour in this region is also strongly influenced by the free stream turbulence intensity and the local Reynolds number distribution.

Very strong variations of the radius of curvature around a turbine blade cause important modifications in local boundary layer behaviour. The suction side boundary layer is influenced by a convex curvature. On the pressure side, a strong concave curvature takes place following a highly convex leading edge.

A strong favourable pressure gradient existing along the surfaces of a turbine blade may force a turbulent boundary layer to undergo laminarization through a process related to the increasing thickness of the viscous sublayer. Such a phenomena should be expected when acceleration parameter $K = \frac{v}{U_\infty^2} \frac{dU_\infty}{dx}$ exceeds a certain critical value ($K > 2 \times 10^{-6}$). .

When a high pressure ratio is imposed on the rotor,a shock wave boundary layer interaction may occur on the suction side where the shock wave originating from the adjacent trailing edge interacts with the boundary layer fluid.As a result of such an interaction,a boundary layer separation and reattachment may take place on the aft portion of the suction side.

In front of the nozzle guide vanes,very wild root mean square velocity oscillations up to 20 % are possible. The leading edge of a rotor blade also sees the wakes of the nozzle guide vanes at a frequency of the order of about 10 KHz .The amplitude of these fluctuations is a strong function of the clearance between the nozzle guide vane trailing edge plane and the leading edge plane of the rotor.Quantities characterizing the turbulence in a turbine passage have also local variations when they are passing through the channels and at present,no information is available on the local variations of turbulence quantities in a gas turbine. A detailed review of the topics related to "Hot Mainstream Flow over a Turbine Airfoil" is presented in appendix-1 .

2.6 AVAILABLE HEAT TRANSFER DATA ON GAS TURBINE BLADES WITHOUT FILM COOLING

WILSON and POPE,[80] investigated the heat transfer on a blade profile designed using circular arcs of different radii for an inlet Re number ranging from 1.8×10^5 to 7.0×10^5 .

Experiments have been carried out in a low speed cascade facility with a wooden heat transfer model for incidences varying from -30 deg. to +20 deg.A typical result from their measurements is given in fig.18 for zero incidence .Even though the experiments were run in a realistic Re range,the blade Ma distributions and the wall to free stream temperature ratio were not adequately simulated.

AINLEY,[81] reports on full scale tests performed on an experimental turbine operating at temperatures over 1370 K with air cooled blades. He demonstrated that gas side heat transfer coefficients obtained in experimental turbines are substantially higher than in stationary cascades. He pointed out that the free stream turbulence, the centrifugal effects on the boundary layer and the secondary flows may all contribute to this situation. WALKER and MARKLAND [82], studied the effects of secondary flows on heat transfer across a turbine blade using the same facility and model as WILSON and POPE. They showed the contribution of the spanwise velocities, produced by the secondary flows, along the blade surface, providing an augmentation of skin friction and heat transfer.

TURNER , [60] made measurements of local heat transfer coefficients on a gas turbine blade at representative local Re and Ma numbers . However the wall to free stream temperature ratio was not adequately simulated. The wall heat transfer coefficients were obtained by introducing the accurately measured wall temperature distribution into a finite element code, solving the 2 D heat conduction equation on the turbine blade. A typical example of heat transfer coefficients obtained with this method is shown in fig.19, for different $T_{w,s}$ values, the exit Ma number being equal to 0.750. Comparisons with the theory of SPALDING and PATANKAR , [84] are also provided in fig.19 .

BAYLEY and MILLIGAN,[86] studied the effect of free stream turbulence upon heat transfer to turbine blades in a cascade facility producing correctly simulated Re and Ma numbers. The finite element technique of TURNER , [60] was used to generate wall heat transfer coefficients from measured wall temperature data. The free stream turbulence was generated using a squirrel cage in order to simulate as well the intensity of turbulence as the frequency of the velocity fluctuations. The variation of the normalized mean heat transfer coefficient as a function of bar passing frequency and intensity of turbulence is given in fig.20. The blade pressure surface heat transfer was found to be mostly affected by the changes in both turbulence intensity and

frequency. The second half of the suction side responded less to frequency or intensity of the turbulence compared to all other portions of the blade. The heat transfer coefficient averaged around the blade was found to increase with turbulence intensity and especially at higher intensities, with the dominant frequency.

Studies of turbulence characteristics and their effects upon the distribution of heat transfer to turbine blades have been performed by BAYLEY and PRIDDY,[65] in the experimental facility used by , [86]. The blade was made of a hollow shell, cooled internally by air. During a steady state heat transfer test, thermocouples located in the inner and outer surfaces of the shell, provided external heat transfer coefficients after a simple data reduction procedure. Fig.21.a shows a typical heat transfer coefficient distribution around a turbine nozzle guide vane at different local Re numbers. The effect of intensity and frequency of turbulence on heat transfer at different locations on the blade is also shown in fig.21.b,[65]. This demonstrates how important turbulence frequency and intensity parameters are with respect to turbine blade heat transfer.

DANIELS ,[34] carried out experiments on a high pressure turbine rotor blade in the Oxford university free piston tunnel. A number of data sets measured on a ceramic blade using thin film heat transfer gauges are given in a range of inlet Re numbers from 4.1×10^5 to 13.5×10^5 . The effect of inlet Re number and turbulence on wall heat flux is shown in fig.22 and 23. The measurements were taken in a facility providing realistic simulation of gas turbine mean flow conditions. The turbulence intensities were generated with an upstream bar grid. DANIELS found almost no influence of the exit Ma number on the pressure side heat transfer. His explanation is the very small variations in the pressure surface Ma number distribution, caused by the exit Ma number variations. Along the suction side, increasing Ma number moved the onset of transition point forward to the leading edge on the suction side. Tests run at higher TU_{∞} levels

resulted in considerable enhancement of the heat transfer rates in the laminar and transitional boundary layer regions. At low Re numbers, pressure side heat transfer is virtually uniform from $s/\bar{C} = -0.2$ up to the trailing edge. At higher Re numbers, the pressure side heat transfer increases monotonically towards the trailing edge. The pressure side heat transfer, at a given turbulence level, depends strongly upon two counteracting phenomena; the free stream acceleration tending to suppress transition and the instability generating mechanism of the concave curvature tending to promote transition and augment wall heating rates.

DANIELS and BROWNE, [88] published a set of heat transfer measurements performed on a gas turbine rotor blade. Short duration measurements of wall heat flux were compared with a number of 2 D differential boundary layer calculation methods. Good agreement for the laminar leading edge and for the fully turbulent region on the suction side was reported. There were difficulties in predicting the suction side transitional region. They found no further improvement in the prediction of the suction side heat transfer behaviour by incorporating more complicated turbulence models than a zero equation model. On the pressure side a two equation turbulence model resulted in better qualitative heat transfer predictions. However, the quantitative agreement was poor.

In fig.24, the variation of heat transfer coefficient around the suction surface of a turbine blade measured by TURNER, [83] is presented. The predictions of the heat transfer behaviour by PRIDDIN, [84] is also presented. The turbulence model was a

$k-\epsilon$ Boussinesq viscosity model incorporating low Reynolds number effects as suggested by JONES and LAUNDER, [85]. Results are given for three turbulence levels.

BAYLEY and PRIDDY, [65] used a squirrel cage turbulence generator in the university of Sussex. The squirrel cage can be rotated at varying speeds. The speed of the cage and the number of bars in the cage control the frequency of the

perturbations. The intensity of the turbulence is closely related with the bar diameter and the distance between the squirrel cage and the leading edge of the cascade is another controlling parameter , [65]. Using this squirrel cage,a turbulence intensity of 15-32 % and bar passing frequencies between 4 10 KHz were reported.Fig.25 shows the effect of free stream turbulence intensity on the heat transfer coefficient for a turbine rotor blade using this turbulence generator.TU_∞ has a particularly strong effect on the pressure side heat transfer coefficient.According to the results of this experimental program, the blade passing frequency has a less important effect on the heat transfer coefficient compared to the turbulence intensity.Increasing the bar passing frequency augmented slightly the heat transfer coefficient ,[65].

Short duration measurements of heat transfer rates to a gas turbine rotor blade have been made by CONSIGNY and RICHARDS,[62]. They used the VKI short duration isentropic light piston tunnel and the measurements were provided by thin film heat transfer gauges painted on a machinable ceramic blade.The tests were performed for three cascade exit Ma numbers 0.62 , 0.92 and 1.15; inlet Re_{∞} was varied from 2.4×10^5 to 9.6×10^5 ,the incidence angle from 0 deg. to 15 deg. and the turbulence intensity level from 0.8 to 5.2 %.The effect of changing these parameters on transition and separation of the boundary layer, on leading edge and on average heat transfer to the blade was studied.The cascade geometry is described in fig.16. A comparison of the heat transfer measurements with a $k-\epsilon$ two equation model is given in fig.26 and 27.The influence of turbulence on the blade mean Nusselt number is presented in fig.28 . CONSIGNY and RICHARDS's main conclusions were : the strong influence of free stream turbulence intensity on stagnation point laminar and transitional heating;the unaffected turbulent heating with increased TU_∞ level;the advance of the onset of transition with increase in Re and TU_∞;the initiation of laminarization in the regions of high favourable pressure gradient; the transition initiated under the presence of shock waves in transonic flow; the high heating rate found at the

trailing edge of finite thickness ;the poor numerical predictions for transitional region heat transfer and turbulent boundary layer downstream of a separation bubble.

DUNN,[87] reports measurements of heat flux and pressure in a turbine stage located downstream of a shock tube.Thin film measurements at the stator endwall and at the tip are presented.A significant influence of the presence of the rotor on full stage stator airfoil heat flux data is reported.The stator only heat transfer results showed a ~ 20 % reduction from the corresponding full stage test results.

KERCHER,[89] investigated wall heating rates on the surfaces of a gas turbine nozzle guide vane in a short duration facility adapted from a shock tube.His measurements were focused on the effects of wall to free stream temperature ratio and local Reynolds number.Eckert's reference temperature method,[89] is reported as a very useful base to present heat transfer information from such facilities.The author observed important influence of the wall to free stream temperature ratio on heat transfer coefficients. A Nu number versus local Re evolution along the blade is presented in fig.29 and 30.

Effect of Ma number,Re number, T_{U_∞} and T_w/T_∞ on local heat transfer coefficients around two nozzle guide vanes were studied by NEALY et al..The tests were performed in a 3 vane hot cascade facility (811 K) under realistic gas turbine conditions.They observed that the suction side heat transfer behaviour in the vicinity of the adverse pressure spike(occurring only for one of the vanes tested) was strongly dependent on the local Ma number distribution in this region. Transitional heat transfer pattern on the suction side showed a very pronounced Re dependency.The effect of exit Ma number on pressure surface heat transfer was negligible .This observation is in accordance with DANIELS's observations,[34] .Heat transfer downstream part of the suction surfaces exhibited some response to pressure gradient history.

2.7 FILM COOLING HYDRODYNAMICS AND HEAT TRANSFER ON A GAS TURBINE BLADE

In recent years because of the ever increasing number of applications of discrete hole film cooling on gas turbine blades, many investigators attempted to study this subject. However, most of the data generated was about film cooling on flat walls using low speed wind tunnels, although actual applications are more related to highly curved surfaces operating in compressible flow with very large temperature differences between the free stream and the wall. A review of discrete hole film cooling studies on flat walls is presented in appendix 2.

2.7.1 FILM COOLING ON THE LEADING EDGE OF A TURBINE BLADE

The available information on the leading edge heat transfer of a film cooled turbine blade is very scarce. A film cooled leading edge configuration on a turbine vane has been reported by LANDER,FISH and SUO,[106]. However, the heat transfer behaviour just downstream of injection locations was not mentioned. The study was mainly focused on the adiabatic effectiveness contribution of the leading edge film on the far downstream part of the suction side coolant film. MIRHUSSEINI,BARROW,[107] and LUCKEY,WINSTANLEY,HANUS,[108] studied the leading edge of a film cooled blade using a cylinder in cross flow. They report heat transfer information from a single row of holes at different angular ejection locations relative to the stagnation point. Their ejection holes were angled in the spanwise direction as shown in fig.37. The wall heat flux measurements using thin foil Gardon gauges were performed in a blowdown facility equipped with a combustor. Cooling effectiveness dropped very quickly as the injection row moved to the stagnation point. Spanwise angled ejection gave a better cooling scheme compared to streamwise angled ejection. GOLDSTEIN,ECKERT,ERIKSEN and RAMSEY,[109] presented the results

of spanwise angled ejection on a flat plate and they found a wider field of film coverage, resulting in a better cooling effectiveness compared to a streamwise angled ejection. [109] 's conclusions on a flat plate and [108]'s results on a cylinder confirmed the beneficial situation gained through the application of spanwise angled ejection. A three times scaled film cooled turbine vane leading edge was studied by HANUS and L'ECUYER , [111]. They found that the influence of spanwise angled ejection is very pronounced on cooling effectiveness around the stagnation line. They quoted more than 20 % cooling effectiveness gain by decreasing the injection angle from 35 deg to 18 deg in spanwise direction and a drop in cooling effectiveness as the injection site moved through the stagnation line. [108] explained such an effectiveness drop by the detrimental effect of increasing the free stream acceleration parameter near the stagnation line. However, it is a well known fact that, very complex three dimensional flow structures and an augmentation of the free stream turbulence intensity in this zone are known to be responsible for high heating rates making the wall cooling very difficult to perform; BOLDMAN and BRINICH, [21] ; KESTIN and WOOD, [20]. An adiabatic heat transfer model of a film cooled turbine airfoil leading edge has been investigated by KRUSE, [12]. Cooling effectiveness downstream of various film cooling configurations were studied for a coolant to free stream temperature ratio equal to 0.75. Although inlet Ma and Re numbers were correctly simulated , the measurements were taken on an isolated airfoil rather than on a cascade as shown in fig.38. Furthermore when compared with a coolant to free stream temperature ratio of ~ 0.5, as encountered in current high temperature engines, a coolant to free stream temperature ratio of 0.75 [12] is quite high. KRUSE pointed out that an effective film formation just downstream of the leading edge rows is quite difficult to achieve at high blowing rates, mainly because of the high curvature of the walls . He also reported that small variations of the stagnation line position may change the trajectory of the coolant film, located very close to this line, fig.39 . The coolant film may follow a path on the suction side or due to changes in stagnation line position, may turn to the

pressure side. In order to avoid hot spots around the leading edge, closely spaced multirow of holes are suggested by [12]. A tabulation of film cooling hole sizes and other basic geometries on the leading edge of gas turbine blades from available literature is given in table-1. A review of the injection hole diameters on gas turbine rotor blades is given in table-2.

2.7.2 FILM COOLING ON THE SUCTION SIDE AND ON THE PRESSURE SIDE

Two different film cooled turbine vanes with different solidities were investigated experimentally,(fig.40), by LANDER ,FISH and SUO ,[106]. Film cooling through double row of holes was applied on the suction side at different s/c locations for the two blades .The test rig comprised a combustor,a transition duct and a shuttling cascade holder,providing very realistic aero-engine flow conditions .Adiabatic wall effectivenesses were determined from wall temperature measurements under steady state conditions and the coefficient h_f was obtained from the transient measurements of the wall temperature.The definition of h_f is as follows,

$$h_f = \frac{\dot{q}_s}{T_{aw} - T_w} \quad (13)$$

for a given time interval,where T_{aw} is the adiabatic wall temperature and T_w is the instantaneous temperature of the wall.Film cooling through a double row of holes on the suction side provided lower effectiveness values than the values for slots obtained from low speed wind tunnel tests,[106].The investigators observed no apparent effect of local Re number on adiabatic wall effectiveness η , as given in fig.41.The presence of cooling holes,no blowing being applied increased locally the heat transfer .The authors mentioned an important influence of the injection hole diameter to length ratio on the

deviation of the ejection angle from the drilling angle.

MUSKA,FISH and SUO ,[113] carried out an experimental heat transfer program on a film cooled nozzle guide vane,in a hot cascade facility.They evaluated adiabatic wall effectivenesses through adiabatic wall temperature measurements.Sellers's superposition hypothesis was proven to be valid ,for an exit Ma number ranging from 0.65 to 0.82 . One of the most detailed studies on film cooling of a gas turbine blade has been published by ITO,GOLDSTEIN and ECKERT,[114]. The pressure and suction side coolant jets of a turbine blade show different behaviours. Effects of injection angle,momentum flux ratio, and surface curvature on film cooling effectiveness may be explained qualitatively using a simplified form of the equation of motion under a number of assumptions.The discussion given in the following paragraph is originally based on the work published by [114].

Assuming a wall with a constant radius of curvature r , using the momentum conservation equation in transversal direction and neglecting the terms related with unsteady flow,viscosity,gravity and external force fields,eq.(14) may be evaluated.Asssuming that there is no static pressure gradient in the transversal direction, one can write:

$$\frac{dp}{dr} = \rho_{\infty} \frac{U_{\infty}^2}{r} \quad (14)$$

Eq.(14) represents the balance between the centrifugal forces and pressure gradient for a chosen control volume (8) shown in fig.42.a .Fig.42.b shows the situation where a jet enters in the free stream at an injection angle α , r being the mean radius of the coolant jet and $\rho_j U_j$ being the coolant mass flux rate. It may be assumed that the coolant mass flow rate is very small compared to that of the free stream.Thus,the coolant fluid influence on the free stream static pressure distribution can be ignored.For the coolant jet one gets,

$$\frac{dp}{dr} = \rho_j \frac{U_j^2}{r_j} \quad (15)$$

In eq.(14), r may be replaced by r_w for the layers very close to the solid wall,to obtain:

$$\frac{dp}{dr} = \rho_\infty \frac{U_\infty^2}{r_w} \quad (16)$$

Due to the unchanged free stream static pressure in the normal direction, equating eq.(15) and (16),

$$\frac{r_j}{r_w} = \frac{\rho_j U_j^2}{\rho_\infty U_\infty^2} \quad (17)$$

The average momentum flux rate of the coolant,at the exit of the coolant hole is as follows,

$$\rho_j (U_2 \cdot \cos \alpha) (U_2 \cdot \cos \alpha) \quad (18)$$

In the control volume ,the local momentum flux of a fluid element should be between the film entering value $\rho_2 U_2 \cos^2 \alpha$ and the free stream value $\rho_\infty U_\infty^2$. One defines:

$$\phi = \frac{\rho_j U_j^2 - \rho_\infty U_\infty^2}{\rho_2 U_2 \cos^2 \alpha - \rho_\infty U_\infty^2} \quad (19)$$

The coolant momentum flux ratio is defined as:

$$I = \frac{\rho_2 U_2^2}{\rho_\infty U_\infty^2} \quad (20)$$

Substituting eq.(19) into eq(20),yields:

$$\frac{\rho_j U_j^2}{\rho_\infty U_\infty^2} = 1 + \phi(I \cdot \cos^2 \alpha - 1) \quad (21)$$

Equation (17), leads to,

$$\frac{r_j}{r_w} = 1 + \tilde{\Phi}(I \cdot \cos^2 \alpha - 1) \quad (22)$$

The latter relation expresses the radius of curvature of the cooling jet in terms of coolant exit momentum flux rate, injection angle and $\tilde{\Phi}$. As consequences of eq.(22) ,

$I \cdot \cos^2 \alpha > 1$	$ r_j > r_w $	[
$I \cdot \cos^2 \alpha = 1$	$ r_j = r_w $	
$I \cdot \cos^2 \alpha < 1$	$ r_j < r_w $	

(23)

When the absolute value of the coolant jet radius of curvature is smaller than that of the surface,(fig.42.b), the jet comes closer to a convex wall;but moves away from a concave wall. This is a pure geometrical reasoning. It is a well known fact that for higher film cooling effectivenesses, the ejected film layer should be as close as possible to the wall. In order to increase the film cooling effectiveness on the suction side of a turbine blade, the following condition has to be satisfied :

$$|r_j| < |r_w| \quad (24)$$

Considering eq.(23), eq.(24) is satisfied only when $I \cdot \cos^2 \alpha < 1$. Along the pressure side,decreasing the radius of curvature of the coolant film will lower the film cooling

effectiveness,because the film moves away from the pressure side: $|I \cos^2\alpha|$ should be maintained to keep the film close to the pressure surface. The authors, [114] experimentally confirmed the results of the above mentioned injection model both on the pressure side and on the suction side of the turbine blade.Typical local adiabatic wall effectiveness distributions at a density ratio of 0.95 are shown in fig.43.a. At the same blowing rate, the suction side adiabatic wall effectiveness has been found to be greater than the pressure side effectiveness ,mainly because of curvature effects.The authors also reported substantial curvature effects on adiabatic effectiveness just downstream of the injection holes,[114]. η values measured at $\beta_c/\beta_\infty = 2.0$ are presented in fig.43.b . DRING,BLAIR and JOSLYN [115] carried out an experimental investigation of film cooling on a turbine rotor blade,using a large scale,low speed model of the first stage of a high pressure turbine. Local flow visualizations and local adiabatic wall effectivenesses on both sides of the rotor blade have been obtained under the influence of rotational effects in a blowing rate range from 0.5 to 1.5 . The density ratio was varied from 1.0 to 4.0.Along the suction side,the coolant film had a very small radial displacement under the influence of rotation and the effectiveness data were almost identical to those taken by [114] on a plane cascade airfoil of similar geometry.Along the pressure side a very large radial displacement of the coolant field was observed during flow visualizations , because of the radial component of the free stream flow over the blowing region.The pressure surface results showed a much faster decay of the effectiveness than did the flat wall data because of the curvature effects and rotation. The effect of film cooling on the pressure side of a turbine vane has been studied by GAUNTNER and GLADDEN ,[116].It has been reported that,a turbine vane is more effectively cooled by a combination of film and convection cooling alone for blowing rates greater than 0.23.Effects of film ejection angle on turbine vane cooling have been studied on the suction side by GAUNTNER,[117].The cooling effectiveness for compound angled ejection was found to be greater than that of slanted in line ejection for blowing rates up to 1.2.A flow vizualisation study

showed that ,ejection from compound angle holes results in a strong vortex motion keeping the boundary layer close to the surface even at high blowing rates.[117].A short duration study of film cooling on a gas turbine rotor blade has been performed in a free piston tunnel by DANIELS ,[34] , in the Oxford university engineering laboratory.The film cooling geometry used in this study is shown in fig.44. Direct wall heat flux measurements have been taken under correctly simulated gas turbine conditions in a linear turbine cascade, with TU_{∞} levels,generated with a bar grid, of up to ~ 4 %.He reported almost negligible influence of suction side injection on the local Ma distribution.The ejection reduced the dynamic head in the free stream resulting in a static pressure rise along the ejection site.This slight increase caused a slight drop in Ma after the ejection location,[70].Discharge coefficient of a film cooling jet in cross flow and in still air is different due to the above mentioned reduction in the dynamic head of the free stream.DANIELS found very little effect of TU_{∞} on \dot{q}_c/\dot{q}_{t_0} which is the ratio of heat flux with film cooling to the one without film cooling.He reported a maximum film cooling effect occurring 10-12 hole diameter downstream of the ejection location.Suction side film produced very similar trends to those on a flat plate.However,the suction side film was much more efficient than a flat plate with the same injection parameters.DANIELS reported a detrimental effect, because of film ejection on the pressure surface heat transfer rate,at low TU_{∞} levels.He attributed such effect, to the coolant film acting as a boundary layer trip and forcing transition of the pressure surface boundary layer.As a matter of fact,very close to the ejection point,the coolant film may separate and the free stream may penetrate beneath it.At high TU_{∞} level ,the pressure side film achieved a small amount of cooling at large blowing rates ,(m = 1.38 ,at $x/d < 10.0$).Again the separation of the film,coupled with the penetration of the free stream seems to be likely the cause.DANIELS found a poorer performance of the pressure side film cooling than that of a flat wall.The poor film cooling behaviour was connected to the concave curvature of the pressure side, [34] .

2.8 SIMILARITY CONSIDERATIONS

An experimental investigation of forced convection heat transfer across the boundary layers of a gas turbine blade with and without film cooling should be carried out under well simulated conditions of the real phenomenon. Using similarity rules, SCHMIDTH,[119]; SCHLICHTING,[120] evaluate the Navier Stokes and energy equations in the mean flow direction in a nondimensionalized form, for a constant property compressible fluid. The form of the governing differential equations suggests that, their solution depends on the following dimensionless groups :

$$\frac{\rho_{\infty} U_{\infty} S}{\mu}$$

$$\frac{g \cdot \beta (T_{0\infty} - T_w) S}{U_{\infty}^2}$$

$$\frac{\bar{k}}{\rho_{\infty} C_p U_{\infty} S}$$

$$\frac{U_{\infty}^2}{C_p (T_{0\infty} - T_w)}$$

$$\frac{\mu U_{\infty}}{\rho_{\infty} C_p (T_{0\infty} - T_w) S}$$

(25)

Since, the fourth and fifth groups are dependent by the factor of $\rho_\infty U_\infty S / \mu_\infty$, only four nondimensional quantities govern the similarity. The second group can be arranged as follows,

$$\frac{g \cdot \beta (T_{0\infty} - T_w) S}{U_\infty^2} = \frac{g \cdot \beta S^3 (T_{0\infty} - T_w)}{\nu^2} \quad \frac{\nu^2}{U_\infty^2 S^2} = \frac{G}{Re^2} \quad (26)$$

where G is the Grashof number

$G = g \cdot \beta \cdot S^3 \cdot (T_{0\infty} - T_w) / \gamma^2$ representing the ratio of inertia forces to buoyancy forces. For most of the forced convection problems, such as heat transfer on a gas turbine blade, buoyancy forces are negligible compared to inertia forces. The third nondimensional group can be rearranged as follows,

$$\frac{\bar{k}}{\rho_\infty U_\infty C_p S} = \frac{\bar{k}}{\mu C_p} \cdot \frac{\mu}{\rho_\infty U_\infty S} = \frac{1}{Pr} \cdot \frac{1}{Re} \quad (27)$$

The fourth nondimensional quantity is known as the Eckert number.

$$E = \frac{U_\infty^2}{C_p (T_{0\infty} - T_w)} \quad (28)$$

The Eckert number can be evaluated in terms of free stream Mach number, wall to free stream temperature ratio and specific heat ratio. The velocity of sound is,

$$a = (\gamma \cdot R T_\infty)^{1/2} \quad (29)$$

and,

$$a^2 = \gamma \cdot \frac{p_\infty}{\rho_\infty} = C_p \cdot (\gamma - 1) \cdot T_\infty \quad (30)$$

substituting eq.30 into eq.28 yields,

$$\begin{aligned} E &= C_p(\gamma-1) \cdot \frac{U_\infty^2}{a^2} \cdot \frac{T_\infty}{C_p(T_{0\infty}-T_w)} \\ E &= (\gamma-1) \cdot Ma^2 \cdot \frac{T_\infty/T_{0\infty}}{1-T_w/T_{0\infty}} \quad (31) \\ E &= (\gamma-1) \cdot Ma^2 \cdot \frac{\left[\frac{1}{1 + \frac{\gamma-1}{2} Ma^2} \right]}{\left[1 - \frac{T_w}{T_{0\infty}} \right]} \end{aligned}$$

As a result of equations 25 to 31, a forced convection heat transfer investigation across the boundary layers developing on the surfaces of a gas turbine blade requires the similarity of

the following nondimensional numbers.

$$\text{Re}, \quad \text{Pr}, \quad \text{Ma}, \quad T_w/T_{\infty}, \quad C_p/C_v \quad (32)$$

In recent years, most of the experimental heat transfer research aiming at the understanding of gas turbine blade heat transfer has been performed in low speed facilities with large scale models. Although detailed boundary layer measurements of high quality and resolution were obtained, all these investigations suffered from a lack of Ma, Re and especially wall to free stream temperature ratio simulation. Recently, very realistic simulation of gas turbine conditions has been achieved, using light piston compression tube facilities and shock tubes adapted for heat transfer research, SCHULTZ [61], RICHARDS [83], KERCHER [89], LOUIS [93], DUNN [87], LOFTUS and JONES, [103]. Such facilities provided the full simulation of T_w/T_{∞} , Pr and specific heat ratio, making them very valuable devices in producing high quality heat transfer data.

When film cooling is applied, local heat transfer coefficients downstream of an injection hole are strongly affected by:

- coolant to free stream temperature ratio,
- coolant to free stream mass flux rate ratio,
- injection geometry,
 - exit hole shape,
 - hole cross section (circular or rectangular),
 - coolant trajectory in the hole,
 - straight hole axis
 - curvilinear hole axis
- injection angle,
 - slanted
 - compound angled

hole diameter to length ratio,
hole spacing,
number of rows,
row configuration,
 in-line rows
 staggered rows
--pressure gradient along the injection site,
--longitudinal curvature
--surface roughness,
--approaching boundary layer situation,
 displacement thickness to hole diameter ratio

Another very important parameter to be simulated is the free stream turbulence of a gas turbine engine. Up to now, this parameter has been simulated using upstream bar grids and rotating squirrel cages in order to produce well defined turbulence intensities and frequencies. However a full simulation of the engine turbulence seems to be very difficult to generate, unless the measurements are performed in an experimental engine.

In order to provide a realistic simulation of a turbine blade film cooling situation, all of the previously mentioned geometric parameters and flow conditions should be simulated accurately under laboratory conditions.

2.9 STATE OF THE ART

Up to this point different blade cooling methods have been reviewed. Liquid cooling systems have not been widely used because of heat removal from the mainstream and low boiling point of the coolants. Thermal shock has been the major problem with water spray cooling. The highest turbine entry temperatures may be achieved when transpiration cooling is applied. However, clogging of porous material, aerodynamic penalties resulting from the protective cold fluid layer around the

blade,difficulties in manufacturing a blade with uniform porosity,mechanical problems and materials costs are still important disadvantages of this method. Transpiration cooling has not been used extensively in aeroengine practice;only a few laboratory conditions were investigated.As a result, film cooling and combinations with internal convective cooling and impingement cooling arrangements became very popular in aeroengine applications in recent years.Film cooling applications on the surfaces of coated (thermal barrier coating) blades are also expected to become popular in the future.Research on shell/spar technology has also resulted in successful results under laboratory conditions.In this method,cooling air flows through channels between a thin metallic external sheet (shell) and a hollow cast internal support member (spar) which are joined by diffusion bonding,as described by LEVARI et al. in [153].A combination of film cooling with this configuration may also be a useful alternative in the future. Cooling hole geometries other than a circular cross section and longitudinally curved cooling holes may find applications in this area.Reductions in the temperature of the coolant air are also expected to take place in blade cooling applications.

CHAPTER 3

EXPERIMENTAL TECHNIQUE AND MODEL DESCRIPTION

3.1 THE ISENTROPIC LIGHT PISTON COMPRESSION TUBE FACILITY

The high speed, compressible flow conditions simulating the mainstream flow behaviour of a gas turbine engine have been generated in an isentropic light piston compression tube tunnel. Such a short duration tunnel is most advantageous to experimental engines in terms of capital cost and direct operating costs. The isentropic light piston compression tube facilities are operated in such a way that they run at full scale (mean) engine conditions but in a transient mode so that although the power flow is correctly simulated, the total energy consumption is tremendously reduced. This feature is especially advantageous to the laboratories where the initial costs and running costs of continuous heat transfer test rigs effectively limit research under real flow conditions. However, in a compression tube, engine turbulence, thermal radiation and other

phenomena related to the combustion and blade to blade interaction are difficult to simulate adequately with the present day techniques.

The VKI short duration compression tube facility CT-2 uses the isentropic light piston tunnel concept developed by JONES et al.,[126]. The tube is 5 m long and has an internal diameter of 1m,(fig.47).It was designed to withstand a maximum pressure of 40 bars.The test section measures 0.25X0.10 m² and allows the study of models of complex shapes such as full scale cascades.Since the measurements are taken with a finite number of blades considerable attention should be given to the uniformity of the flow upstream of the cascade as well as to its downstream periodicity. Wall static pressure distributions downstream of the blade row,oil flow visualization and Schlieren observations are the standard tools to check the periodicity of the flowfield in the tunnel.The model tested in this transient facility can also be tested in an ambient temperature blowdown tunnel (VKI-C3) for further aerodynamic investigations.

The compression tube is driven by means of the VKI high pressure (250 bar) air supply. The downstream dump tank has a capacity of approximately 3 m³ and pressure adjustments ranging between 0.1 to 3 bar can be made during the test program.Total pressure and temperature of the air inside the tube before and after compression can range between 0.5 and 7 bar and 290 and 600 K respectively.

The operating principle is based on the isentropic compression heating of a test gas in a tube by a light weight piston ,the model itself remaining at ambient temperature. If the wall to gas temperature ratio is taken as the similarity parameter to model the heat transfer processes across the boundary layer.A free stream gas temperature and a model temperature respectively equal to 420 K and 288 K simulate a wall to gas temperature ratio of 0.68. A gas temperature of this magnitude can easily be reached by single stroke of the piston with a compression ratio of 3.74.Operating with models initially

at ambient temperature also provides a definite advantage on unit Re number. For example, a decrease in total temperature from 1620 K to 450 K (at $Ma=0.2$) increases the unit Reynolds number more than 4 times.

The operation of the compression tube shown in fig.47 may be explained by looking at figures 48 and 49. The high pressure air reservoir is connected to the tube through an orifice which is always choked. A piston moves freely in the tube; the latter is bored and honed to provide a smooth passage for the piston. A fast opening valve isolates the compression tube from the test section during the compression, (fig.50). When valve A is opened (fig.48), high pressure air from the reservoir flows through the choked orifice and drives the piston down the tube and compressing the enclosed air almost isentropically. When the preset pressure level is reached, the fast opening valve (B) is actuated and this heated air stream flows through the test section. If the volumetric flow rate through sonic orifice (A) is equal to the one through the test section, then the test section free stream conditions remain constant until the piston reaches the end of the tube. This equilibrium condition can be controlled by varying the sonic orifice (A) area as a function of the upstream reservoir pressure. A comprehensive theory about the flow in a compression tube is given in [126].

The weight of the piston plays a major part in the compression tube flow behaviour. Ideally, a weightless piston should be used, acting as a barrier between the reservoir air and the compressed test air. The piston should move almost frictionless in the tube and the leakages between the upstream and downstream sides of the piston should be avoided. The piston should also withstand to stresses during acceleration and when it strikes the end of the tube. All these structural requirements result in a piston with a non-negligible weight.

The piston velocity and tube pressure time histories in a compression tube are given in fig.49 and fig.51. Just before the end of the compression, the piston velocity is quite low. As soon

as the fast opening valve opens, the heated air ahead of the piston accelerates to a high velocity. The acceleration ratio is a function of the (tube/test section) area ratio. Immediately after the acceleration, the velocity of the piston can not instantaneously adjust itself to the velocity of the heated air because of the finite mass of the piston. The pressure ahead of the latter suddenly drops and the piston starts oscillating with a certain frequency and amplitude. The period of these oscillations can be calculated as follows [126]:

$$T = \frac{2\pi}{\gamma^{1/2}} \cdot \left(\frac{P_0}{\bar{P}} \right)^{1/2\gamma} \cdot \left[1 - \left(\frac{P_0}{\bar{P}} \right)^{1/\gamma} \right]^{1/2} \cdot \left[\frac{L \cdot Ma}{A \cdot \bar{P}} \right]^{1/2} \quad (33)$$

where P_0 being the initial tube pressure, \bar{P} the final tube pressure, L the tube length, A the piston area, Ma the Mach number and γ the specific heat ratio. The amplitude of the pressure fluctuations is a function of $(\text{piston mass})^{1/2}/(\text{total pressure})^{1/2}$.

The weight of the piston is about 27 kg. The pressure oscillations become more serious either at lower operating pressures or at higher stagnation temperatures. Measured total pressure fluctuations in the test section of the CT-2 facility are shown in fig. 52, under the nominal operating conditions of the present experimental program.

3.2 WALL HEAT FLUX MEASUREMENTS

The wall heat flux measurements in the VKI CT-2 compression tube facility are performed using thin film heat transfer gauges. Most often, the model is initially at ambient temperature. The fast opening of the shutter valve allows the compressed hot gas to pass over the model and provides, in the ideal case, a step like variation in heat flux. The real heat flux variation is not an exact step : the heat flow across the model surfaces actually decreases with time as the substrate thermal properties change because of the increasing model temperature. However, in spite of this fact, the step like behaviour of the heat flux across the substrate surface corresponds to a nearly parabolic temperature rise.

The principles of transient heat conduction in a semi-infinite body are discussed in appendix-3. The main assumptions of this analysis are as follows:

- the thin film has a negligible effect on heat conduction
- the substrate is semi-infinite
- the heat flow into the substrate is one dimensional

An electrical analogy was used in the solution of the governing differential equations. A semi-infinite body was represented by means of capacitances and resistances. The details of this analogy and its implementation in direct wall heat flux measurements are also given in appendix-3. A more detailed analysis of this technique can be found in [126] by SCHULTZ and JONES.

3.2.1 DETAILS OF THE ASSUMPTIONS

In section 3.2 ,three assumptions have been listed;they need to be satisfied if a correct measurement of wall heat flux using thin film gauges is to be made correctly.These assumptions will now be considered individually.

3.2.1.1 ONE DIMENSIONAL HEAT TRANSFER -

The heat transfer into the substrate must be one dimensional.Most of the time, this assumption is verified provided that the gauges are not placed near the edges of the model. A good rule-of-thumb is to place gauges away from substrate discontinuities at a distance at least equivalent to that required for a semi-infinite substrate behaviour, LIGRANI et al. [128].

3.2.1.2 SUBSTRATE THICKNESS -

The substrates on which the thin film gauges are deposited must be thick enough so the heat transfer across these substrates is similar to i. to a semi-infinite solid.Therefore,at the end of a test θ_x/θ_s should be negligible at the base of the substrate.Ideally, θ_x should be equal to zero; the temperature at the base of the substrate should remain constant equal to ambient temperature.

To consider this problem quantitatively,we will express $\bar{\theta}_x$ by means of the following equation,(appendix-3) :

$$\bar{\theta}_x = \frac{1}{\sqrt{\rho ck}} \cdot \frac{\dot{q}_s}{\sqrt{s}} \cdot \exp\left(-x \sqrt{\frac{s}{\alpha}}\right) \quad (34)$$

If the surface is submitted to a step variation in heat flux (\dot{q}_s = constant), one gets:

$$f(\dot{q}_s) = \frac{\dot{q}_s}{s} \quad (35)$$

and,

$$\bar{\theta}_x = \frac{1}{\sqrt{\rho ck}} \cdot \frac{\dot{q}_s}{s^{3/2}} \cdot \exp\left(-x \sqrt{\frac{s}{\alpha}}\right) \quad (36)$$

or, alternatively,

$$\theta_x = \frac{\dot{q}_s}{\sqrt{\rho ck}} \cdot \left[\frac{2\sqrt{t}}{\sqrt{\pi}} \cdot \exp\left(-\frac{x^2}{4at}\right) - \frac{x}{\sqrt{\alpha}} \operatorname{erfc} \sqrt{\frac{x^2}{4at}} \right] \quad (37)$$

And hence,

$$\frac{\theta_x}{\theta_s} = \exp\left(-x^*{}^2\right) - \sqrt{\pi} \cdot x^* \cdot \operatorname{erfc} x^* \quad (38)$$

where $x^* = \frac{x}{\sqrt{4at}}$. and θ_s is the temperature at the base of the substrate.

Equation (38) has been plotted in fig.57 and redrawn in fig.58 for a pyrex substrate (0.3, 0.5 and 0.7s testing time) and for a fused silica substrate (0.5s testing time). For both materials, considering a 0.5s testing time, the substrate thickness must be about 1.6 mm to maintain the θ_x/θ_s ratio below 5 % at the base of the substrate.

3.2.1.3 THIN FILM GAUGE THICKNESS -

The thin film gauges must not disturb the surface heat flux. This is generally the case due to the fact that films are usually about 10^{-6} or 10^{-7} meters thick and have a high thermal conductivity. According to Schultz and Jones [126], the ratio of the heat flux through the film to the actual heat flux is given by

$$\frac{\dot{q}}{\dot{q}_0} = 2a \cdot \frac{\sqrt{\alpha_1 t}}{\epsilon} \cdot \left[\frac{1}{\sqrt{\pi}} - \frac{2a}{1+a} \cdot \sum_{n=0}^{\infty} \left(\frac{1-a}{1+a} \right)^n \cdot i \cdot \operatorname{erfc} \left(\frac{\frac{n+1}{2}}{\sqrt{\alpha_1 t}} \right) \right] \quad (39)$$

where $i = \sqrt{-t}$ and $a = \sqrt{\frac{R C_1 k_1}{R C_1 k_1}}$. Fig. 59 shows this function plotted as \dot{q}/\dot{q}_0 versus $\sqrt{\alpha_1 t}/\epsilon$. This is redrawn in fig. 60 to compare the response times of platinum films being respectively 1 μm and 2 μm thick. From this figure, it can be seen that it takes a 1 μm film .4 ms to reach 95 % \dot{q}/\dot{q}_0 compared to 1.6 ms for the 2 μm film. This illustrates the effect of increased film thickness on the gauge response time. A further illustration of this point may be made using fig. 61. The time for the heat flow to reach 94 % of a step input of heat transfer is plotted against the film thickness for platinum material.

3.2.2 ANALOGUE CIRCUIT DESCRIPTION

The actual values of r' and c' (equation (A.49) and (A.50)) required in analogue circuits are difficult to define. Any arrangement of resistive and capacitive components represents a semi-infinite heat transfer behaviour provided that the product $\sqrt{r'c'}$ (analogous to $\sqrt{\rho c k}$) is constant with time. The criteria by which alternative circuits may be evaluated are related to the speed and duration of their response to inputs or changes in heat flux. Two characteristic times are then important:

(a) the response time is the time required for the analog output to fully account for an alteration in the voltage input signal.

(b) the operation time is the time after the first input to the analogue that the output signal represents a particular heat transfer profile to a stated accuracy. Namely, for a constant heat flux situation the operation time is over when the output of the analogue drops more than 1.4 % of the constant heat flux level.

These characteristic times are illustrated in fig.62, where a step input of heat transfer has been considered ; the response time was exaggerated for clarity. The aim in analogue circuit design is to minimize the response time and to maximize the operation time, at least for the duration of one complete test.

The T-section analogue illustrated in fig.54 proved to have a short response time. The response time of this circuit is equal to RC , provided that all stages are made of identical components. The operation time during which this circuit reproduces a step input in heat transfer to within 1.4 % is calculated as follows:

$$0.2 \times n^2 \times (RC) \quad (40)$$

where n is the number of equivalently designed stages. The operating time is specified as the testing time and then the number of identical stages required can be calculated from equation (40), RC being specified as the necessary response time needed. When long operating times or high measurement accuracy are required corresponding to a large number of identical stages, then arithmetically increasing component values are suggested by SCHULTZ,[125]. When using arithmetically increasing components, the first two stages must be identical to provide an acceptable frequency response. When the analog circuit is consisting of "L" stages and the resistance-capacitance values are arithmetically increasing, then eq.(40) may be rearranged as,

$$0.2 \times [1 + (L-1)L/2]^2 \times RC \quad (41)$$

Fig.56 illustrates the termination of a T-section analogue circuit, with $R_i = R/2$.

3.2.3 THIN FILM HEAT FLUX SENSORS

3.2.3.1 THIN FILM GAUGE CONSTRUCTION DETAILS -

The procedure used to deposit the platinum thin film heat transfer gauges on ceramic substrates will now be described. The process may be divided into three parts:

- (1) substrate surface preparation
- (2) application and baking of the gauge material
- (3) electrical connections to the gauges.

Each of these steps will be discussed in detail.

3.2.3.1.1 PREPARATION OF THE SUBSTRATE SURFACE -

The type of ceramic we used as substrate material is referred to as MACOR, or machinable glass ceramic from Corning Glass Works (1980). Some properties of it are presented in LIGRANI et al. [128]. It allows to place gauges on complex geometrical shapes. It may also be machined quite easily using standard machine tools. If quartz is used as a substrate material instead of ceramic, inserts contained in a metallic model are required. Using such an approach lies in the possibility that surface discontinuities may exist at quartz/metal interfaces where the quartz and metal are adjacent. Such discontinuities actually disturb the boundary layers developing over the blade surfaces. A heat transfer instrumented blade manufactured using this approach is shown in fig.44 by DANIELS,[44].

MACOR is an ideal thin-film gauge substrate material because it has a low thermal conductivity (12.93×10^{-3} (W/cm.K) at room temperature) making it a good thermal insulator. Good

insulation properties are required if heat transfer to the gauges mounted on the substrates is to be one dimensional and similar to that into a semi-infinite solid. MACOR may also be heated to 1000 C without significant geometrical deformation. Temperatures near this value are indeed required during the preparation of thin film gauges.

In order to apply the gauges, the surface of the substrate material must be smooth and highly polished. In order to smooth and polish the surface, 600 grain wet or dry silicon carbide sandpaper is first used for a period of 4 to 7 minutes. In such cases, a rotating wheel may be used for polishing, however, for complicated geometric shapes such as a turbine blade, hand polishing is required.

At the end of the polishing process, the ceramic piece is cleaned with warm water and eventually a liquid detergent. After cleaning, the substrate should be heated just above 100 C to remove any remaining water. If a long time passes between cleaning and gauge application, the substrate should be cleaned again before the gauge material is applied.

Geometric non-uniformities in the substrate material such as fine cracks on the surface may have a detrimental effect on the gauge quality. A close look at the surface using a microscope is then recommended to check for such problems before gauge material is applied.

3.2.3.1.2 APPLICATION OF THE GAUGE MATERIAL -

One of the best materials to produce thin-film gauges is platinum. For electrical connections, gold has many advantages even though silver has sometimes been used at VKI in the past, [128]. In order to apply liquid gold and liquid platinum the following materials are needed:

- (1) Liquid bright platinum 05-x (Englehard ind.ltd.)
- (2) Liquid bright gold FL-8.....(Englehard ind.ltd.)
- (3) Thinning essence 730.....(Englehard ind.ltd.)
- (4) a Rowneys series 56 size 3 brush or a 0.3 mm graphos refillable ink pen
- (5) 3 mm diameter glass stirring rods and small mixing pots.

The liquid platinum and liquid gold containers should be shaken well before use of the liquids. Also, glass stirring rods, glass mixing pots and brushes should be cleaned using acetone before and between use. The first step in applying the platinum to the ceramic substrate is to prepare a mixture of thinning essence and platinum. This is done by using separate glass rods to place droplets of material from each bottle into a small mixing bowl. The relative concentration of the platinum and thinner depends on the preference of the user. A mixture of 100 % platinum liquid may be used for painting, however, many users find that a mixture of 50 % of each compound allows an easier application. If too small quantity of platinum is used in the mixture, non uniform thin film gauge boundaries may result. The mixing of the two materials, must be performed in a clean environment. Impurities in the bottles of platinum or thinner as well as impurities in the glass pot during mixing may result in faulty gauges.

The final resistances of the gauges depend strongly on the relative concentrations of the platinum and thinner, and also on the geometry of the gauge. For a 1x5 mm² gauge, a 50/50 mixture (on a volume basis) of platinum and thinner will provide a resistance of approximately 250 ohms after one coat. The application of 5 or 6 coats of pure platinum will give gauges with a resistance between 30 and 50 ohms.

The brush or other application device used to apply the gauge material also depends on the preference of the user. If a brush is used , a fine instrument with only a few coarse hairs is most suitable. The present gauges were applied using a single brush stroke.

Immediately after the gauge application on the substrate, the entire piece should be placed under a high power lamp for drying. Ideally the total drying time should range between 5 and 20 minutes. Again, care should be taken to avoid the collection of dust or other impurities on the surfaces.

After each layer of platinum has been placed on the substrate and dried, the piece must be baked. This baking process will be described shortly. After each baking cycle , the resistances have to be measured to determine if they are within acceptable limits(45-150 ohms). The procedure may then be repeated depending on whether any changes in gauge resistance are required. If several applications of platinum have to be made, polishing with Cerium oxide between the application/baking cycles may be advisable to further control the resistance values and the ceramic surface quality.

Once acceptable platinum gauges are obtained, the gold material may be applied using the same procedure . For the gold connections, only one coat is usually necessary ; the same thinning essence 730 may be used . Gold connections may also be used to lower the resistance of a platinum film by shortening its effective length. The gold should therefore always be applied after the platinum. If platinum is applied after gold, the resistance of the platinum will be adopted at the application point instead of that of the gold. Gold is a convenient connection material for thin film platinum gauges because the same baking temperatures and times may be used as for platinum. It should also be noted that gold forms thin film connections,in contrast to other materials such as silver which gives thick film connections with possible surface discontinuities.

As indicated earlier, after application of each layer of platinum or gold material, baking is required. The baking is done using an electrical furnace. The oven should be cleaned and purged of foreign gases and other impurities by heating to about 1000 C. After the oven has cooled down to room temperature, the baking procedure for platinum or gold may begin.

The first step in the baking process is to set the oven temperature controller between 670 C and 690 C with the oven door open. The temperature will then begin to rise and the substrate should be inserted into the oven before a temperature of 100 C and 150 C is reached. As long as the furnace temperature is less than 250 C to 300 C the door should be left open for ventilation. This ventilation period may last 10 to 15 minutes and allows residual moisture or thinning essence to evaporate from the oven. After the oven door is closed, the oven used at the von Karman Institute requires another 20 to 25 minutes to reach a 670 to 690 C temperature. The substrate is maintained at this temperature for 30 minutes. The furnace is then switched off. Some users, however, recommend a one hour baking time at maximum temperature. Cooling down the furnace to ambient temperature with a closed door then requires more than 4 or 5 hours. Ideally, this cooling process should take place overnight. In any case, rapid cooling must be avoided. Quenching of the substrate may result in the formation of thermal stresses and possibly cracks.

The baking cycle must be repeated as new layers of platinum are applied to the substrate. As ceramic substrate material is baked, its thermal properties such as $\sqrt{\rho c k}$ will change. Thus, one must produce a thin film gauge on an additional piece of ceramic which may be later calibrated to determine $\sqrt{\rho c k}$. This calibration piece should then undergo the same painting and thermal processing procedures as the pieces to be used for an actual measurement.

3.2.3.1.3 ELECTRICAL CONNECTIONS -

Electrical connections to the thin film gauges may be made directly to the platinum or to the gold connections which lead to the platinum. If the gauges are closely spaced ,the electrical wiring may be made through holes across the ceramic substrate.

The wire used for connections should be flexible and easily solderable ; stranded wire is often suggested. For the connections, the outer diameter of the wire insulation is 0.3 mm with 5 electrical strands within. For the connection, the wire insulation was first removed over a length equivalent to the length of the thick silver film deposited at both ends of the gold films, (fig.84). The wire was then soldered in place on this thick film.

After the connections to the thin film heat transfer gauges are completed, the gauges and connections must be annealed. This process is necessary to eliminate the possibility that the resistance of a gauge could drift at a given temperature. To anneal a set of heat transfer gauges, the instrumented substrate is placed in an oven or bath and heated to a temperature between 80 C and 100 C . The resistances of gauges should be measured both before and after heating. The process should be continued until the resistances of the gauges are the same after one heating sequence as they were before. In most cases, the annealing heating process must be repeated 4 to 5 times . A typical resistance versus temperature relation for a completed platinum gauge placed on a ceramic substrate is shown in fig.63. The linear dependence of resistance on temperature is evident from the figure.

3.2.3.2 TEMPERATURE COEFFICIENT OF THIN FILMS -

The temperature resistance coefficient of a thin film gauge α_R depends on a variety of factors including the film material, the size of the deposit , and its shape. Each gauge must therefore be calibrated independently .

The temperature coefficient of resistance α_R has been defined by equation (A.58)

$$R = R_0 \left[1 + \alpha_R(T-T_0) \right] \quad (42)$$

As indicated in appendix-3, reference temperature T_o , and hence:

$$\frac{R-R_0}{T-T_0} = \alpha_R \cdot R_0 \quad (43)$$

The magnitude of $(R-R_0)/(T-T_0)$ is found from a resistance versus temperature plot for a given gauge . R_0 is determined by measuring the resistance of the gauge and its connecting wires just before input to an analogue circuit .If the measured ambient temperature is different from T_o ,the correction $(1+ \alpha_R(T_\infty-T_o))$ must be applied.Typically this correction term may account for 1 % of \dot{q}_s if $(T_\infty-T_o)$ is about 5 to 10 C .

The thin film resistances are measured in a range of constant temperatures between ambient and 80 C.A graphical result of such a calibration is shown in fig.63.The value of α_R may be obtained using a linear regression analysis.Typical examples of results are tabulated in fig.64.

3.2.3.3 SUBSTRATE THERMAL PRODUCT -

The substrate thermal product is defined as $\sqrt{\rho c k}$. For quartz substrates, the value of the thermal product is known for the temperature range encountered in the CT-2 facility, between ambient and 140 C. Although the free stream air temperature may be as high as 140 C, the corresponding wall temperature rise is less than 50 C. $\sqrt{\rho c k}$ for quartz increases almost linearly from .153 to .175 ($\frac{W}{cm^2 \cdot K} \cdot \frac{\sqrt{sec}}{K}$) between 20 and 100 C.

However, machinable ceramic substrates cannot be generalized. Their value of the thermal product depends on the history of the gauge construction and also on the firing details of the ceramic production processes. Therefore all new batches of ceramic must be calibrated for $\sqrt{\rho c k}$.

As for quartz, the ceramic thermal product will vary with temperature. This variation cannot be predicted and must therefore be calibrated. A suitable arrangement for such a calibration could consist of quartz and ceramic gauges mounted on a flat test plate. The heat flow is calculated from the quartz gauge measurements. The value of \dot{q}_s obtained is substituted into equation (A.70) applied to the ceramic gauge readings to give,

$$\left(\sqrt{\rho c k} \right) = \dot{q}_s \frac{V_0}{V_{out}} \cdot \frac{\alpha_R}{\frac{A^*}{\beta}} \cdot \frac{1}{(1 + \alpha_R(T_\infty - T_0))} \quad (44)$$

A typical value of $\sqrt{\rho c k}$ for ceramic was measured to be 0.205 ($\frac{W}{cm^2 \cdot K} \cdot \frac{\sqrt{sec}}{K}$) at 20 C. For the present model, between 20 C and 40 C this value of $\sqrt{\rho c k}$ for one particular piece tested was found to vary about 1 per cent. A 3.5 % uncertainty on $\sqrt{\rho c k}$ was also expected with the present method of measurement, being one of the main uncertainty contributions to wall heat flux measurement.

3.3 PRESSURE AND TEMPERATURE MEASUREMENTS

The pressure in the compression tube was measured with a validyne type DP15TL variable reluctance differential transducer. This type of transducer provides a sufficient stability and accuracy to be a reliable input into the control system of the tunnel. A typical measured tube pressure under nominal operating conditions is shown in fig.65. A least squares line fit determines the tube total pressure at the shutter valve opening time (approximately 60 msec later than the start of data sampling for the present testing conditions). The initial pressure in the compression tube was set by means of a mercury manometer. A precise adjustment of the initial tube pressure was useful in obtaining a well defined compression ratio.

National semiconductor differential transducers with built-in integrated circuit amplifiers were used to measure free stream and discharge tank pressures. The free stream total pressure was measured by means of a total pressure probe located about one chord length upstream of the cascade. A typical free stream total pressure trace is given in fig.66. Because of the existence of a turbulence grid, a total pressure drop of about 2.5 % was observed. The total pressure loss was 1.0 % when the grid was removed from the tunnel. The wall static pressures at the inlet of the cascade were measured at two stations and the inlet Mach number was evaluated from an averaged value, (fig.67). Downstream static pressures were also recorded using semiconductor differential transducers. The measurements recorded through 13 static holes in the exit plane were averaged along a pitch. The exit static hole locations are indicated in fig.81.

The coolant plenum chamber pressure measured using a variable reluctance differential transducer showed a slight transient just after the establishment of the free stream flow, as it is given in fig.68. This pressure rise was attributed to the sudden deceleration of the plenum flow due to

instantaneous static pressure increase in the free stream. However, the total pressure upstream of the orifice was quite uniform in time, because of sonic flow conditions through the orifice.

Compression tube total temperature and free stream total temperature measurements were attempted using two Cr-Al fast response thermocouples, (20 μ m), during a test cycle. The solid line in fig. 69 shows the tube temperature and a comparison with the instantaneously measured test section free stream temperature (dashed line) is given. In evaluating the total temperature drop, the data measured at the end of the test (~500 msec after shutter valve opening time) were used because of decreasing influence of heat conduction losses through the stem of the free stream thermocouple. This sensor was inserted into the mainstream with a 40 mm long stem, normal to the flow direction. A recovery factor of 0.67 was taken into account. As a result, a ~2 % total temperature drop between the compression tube and the free stream was recorded, in the presence of the turbulence grid. In the absence of the grid, no temperature drop in the tunnel was observed.

The determination of free stream total temperature has been important for each test because of its continuous use in the evaluation of heat transfer coefficient from measured heat flux data. The final compression tube total temperature was computed from measured initial temperature and compression ratio. Using the total temperature drop values with and without the turbulence grid, the total temperature in the free stream was evaluated and used in the determination of convective heat transfer coefficient defined as follows:

$$h = \frac{\dot{q}_s}{(T_{0\infty} - T_w)} \quad (45)$$

where T_{∞} is the total recovery temperature in the free stream and T_w is the model wall temperature. A recovery factor of 0.89 was used in the evaluation of the recovery temperature as suggested by SCHLICHTING,[120].This is a typical value when the boundary layer is fully turbulent.

Temperature measurements in the coolant plenum chambers and upstream of the sonic orifice were measured using Cr-Al thermocouples with cold junctions immersed in a melting ice bath.The temperature in the heat exchanger supplying the conditioned cooling air was also monitored.

Typical coolant plenum chamber and sonic orifice temperatures are shown in fig.70.The plenum chamber temperature rise (2-3 K) after the establishment of the free stream flow is related to the pressure rise observed in fig.68.This temperature rise ,compared to the quite high temperature of the free stream (~420 K),corresponds to a coolant to free stream temperature ratio variation which is less than half a per cent.The actual order of magnitude of the coolant to free stream temperature ratio is between 0.4 to 0.6 for realistic situations.Therefore, this transient in the plenum chamber is negligible.

The coolant mass flow rates were evaluated from the measured upstream total pressure and temperatures of choked orifices.However,when $d/d^* \gg 1$,the static conditions may also be applied,especially with the very high pressure ratios of the present coolant flow.Typical measurement locations are shown in fig.71.The actual mass flow rate passing through a choked orifice can be computed through FLEIGNER's approach, as explained by SHAPIRO, [143]:

$$\dot{m}_c = C_d \cdot A_c \cdot \frac{\pi}{4} \cdot d^2 \cdot \frac{P_{\text{inlet}}}{\sqrt{T_{\text{inlet}}}} \quad (\text{kg/s}) \quad (46)$$

where $A_c = 4.0424$ and

P_{inlet} and T_{inlet} are in the units of (bar) and (K) respectively. The discharge coefficient C_d was evaluated as unity because of choking conditions. However, even with choked flow conditions, due to viscous action, the discharge coefficient is always less than unity. This difference was neglected, since it always remained less than one percent. The necessary condition for an orifice to be sonic is,

$$\frac{P_{oc}}{P_{inlet}} < \left(\frac{2}{\gamma + 1} \right)^{\frac{\gamma}{\gamma+1}} = 0.528 \quad (47)$$

The blowing rate m is defined as follows:

$$m = \frac{\dot{m}_c / \text{AREA}}{\rho_\infty U_\infty} \quad (48)$$

where AREA is the total exit area of film cooling holes and,

$$\rho_\infty U_\infty = \frac{P_\infty}{RT_\infty} \cdot Ma \cdot \sqrt{\frac{C_p}{C_v} R T_\infty} \cdot 10^5 \quad (\text{kg/m}^2\text{s}) \quad (49)$$

where P_∞ , T_∞ and Ma are the free stream static pressure (bar), temperature (K) and Mach number at the film cooling location.

3.4 COOLANT FLUID CONDITIONING

For film cooling experiments, the coolant air is obtained from a 50 lt reservoir which can be pressurized up to 40 bar. The temperature of the coolant is then adjusted to the desired level by means of a regenerative heat exchanger and the mass flow is controlled by a choked orifice close to the test section.

The regenerative heat exchanger is made of a stack of brass screen matrices in a 40 cm long and 25 mm diameter steel tube. It was designed to heat or cool the secondary gas at the maximum coolant mass flow rate with a temperature variation of less than 1 % during the test, provided that the pressure losses remain minimal. The heat exchanger temperature can be adjusted between -150 and +120 C by a low pressure secondary open loop system having an electrical heater in an oil bath or a cooler made of an alcohol bath whose temperature can be decreased down to -70 C by addition of dry ice.

Using dry ice in an alcohol bath is obtained typical plenum chamber temperatures of about - 20 C. With a free stream total temperature of 420 K, a coolant to free stream temperature ratio of $T_c/T_\infty=0.60$ is obtained. As a matter of fact, in film cooled turbine blade research T_c/T_∞ ratios ranging between 0.4 and 0.6 are more representative. For this purpose, the low pressure secondary open loop air is passed through a coil immersed in a cryogenic fluid (liquid Nitrogen) in addition to the alcohol/dry ice bath. This configuration allows heat exchanger temperatures as low as -150 C and, T_c/T_∞ values as low as 0.4 (or a plenum chamber temperature of about -70 C) can be achieved without any difficulty.

After a period of heating or cooling, when the required temperature is reached, the heat exchanger is isolated from the low pressure loop and connected to the high pressure reservoir, ready for a test, (fig.72).

The sonic orifice, used for coolant mass flow rate measurements is located between the heat exchanger and the plenum chamber, to minimize the volume up to the test section. The coolant pressure can then adjust itself to the free stream pressure and can follow even a very small pressure fluctuation within a delay of a few milliseconds. Smaller plenum chamber volumes result in smaller flushing times of the ejection system. The latter allows the user a better timing of the coolant flow during a short duration test.

3.5 TURBULENCE GENERATION

The external free stream turbulence has been generated by means of a grid of parallel horizontal bars located upstream of the cascade. The bar diameter is 3 mm and the bars are 9 mm apart from each other. These values have been chosen using classical correlations available in the literature,[129],[130]. By placing the turbulence grid at different streamwise positions upstream of the cascade, different turbulence intensities may be generated. The turbulence intensity has been measured using a constant temperature anemometer with a frequency response of about 15 Khz,[67]. The probe consisted of a 9 μ m diameter tungsten wire with an active length of 1 mm. The hot wire probe was placed in the same position as the total pressure probe as shown in fig.81, one chord length upstream of the cascade. At a Mach number of 0.2 and total temperature of 420 K, the signals were analyzed using 1500 data points over a test period of 100 msec (25 Khz). Temperature fluctuations evaluated by varying the overheat ratio were found to be of the order of 0.2 %. The analysis of the velocity fluctuations showed that, in the absence of the grid the turbulence level was found

to be between 0.9 % and 1.2 %. Turbulence intensity levels ranging between 2 % and 5.2 % were observed, in the presence of the grid, depending on the grid-model distance. A maximum value of 5.2 % was obtained and considered as the nominal condition for the present tests.

3.6 MEASUREMENT CHAIN AND DATA PROCESSING

In a short duration facility, a precise synchronization of all measurement devices with the tunnel operating conditions is required. In the CT-2 facility, although the data sampling through 48 channels is computerized, the main control of the whole system is achieved by a purpose built electronic control unit. This unit also serves as a safety device against failures resulting from hardware and human mistakes. A schematic of the measurement chain is given in fig.73.

Once the compression tube is pressurized, the electronic control unit monitors continuously the pressure evolution and triggers the opening of the fast acting valve when the preset pressure is reached. This unit also triggers the computer to start the data acquisition about (100-200) millisecond before the shutter valve opening time. The details of the VKI built high speed data acquisition system is given by OLIVARI,[131]. The system ,(fig.74) ,consists of three 250 kHz data rate modules placed in parallel by analog devices. When multiple channels are sampled, channel signals go to DAC units 1,2 and 3 in sequences of 3,(i.e.,channel 1 to DAC 1,channel 2 to DAC 2,etc.). The three outputs are then multiplexed digitally and stored in a temporary buffer before transmission to an on-line PDP 11/34 computer. The entire system is capable of a maximum sampling rate of 500 kHz for 48 channels of data. The signal resolution of the analog-digital converter is 12 bits, however, words are sent by means of a 16 bit parallel line to the computer memory operated in a direct access mode. The extra 4 bits exceeding the data are available for control

signals.

The sampled data (with 1000 Hz for the present program) may be wall heat flux, thin film temperature output, pressure, temperature(thermocouple output), hot wire output or displacement. The sampling is terminated after 512 data points per channel were accumulated in the computer, giving 511 msec of total data acquisition time . By means of the control unit, the start up time of the coolant ejection can also be adjusted with respect to the mainstream flow establishment time. This is especially significant in minimizing the time duration between the cooling start-up and mainstream flow establishment. The model surfaces which are of a low thermal conductivity substrate material are far from being isothermal when a very early coolant start-up occurs. The time duration between the start-up and mainstream establishment(shutter opening time) should not exceed 300-400 msec. This phenomenon is especially important when the coolant temperature is less than ($0.60 \times T_{\text{crit}}$).

For each test a PDP 11/34 computer stores a raw data file of 103 blocks ,consisting of 103×256 integer words of information. The raw data is in the form of 12 bit information, varying between -2048 to +2048 corresponding to an analogue range from -5 V to +5 V . In order to evaluate quantitative results of the tests,a number of computer programs were installed on both PDP and VAX computers.A flow chart of the specifically developed software is shown in fig.75.

Transient variation of the inlet total pressure and static pressure in the test section were shown in fig.66 and 67. The least squares line fit to the signals were almost horizontal lines with respect to time. However in the exit plane of the cascade the static pressures slightly rised in time,(after the first 100 msec following the shutter valve opening time),as a result of the finite size of the discharge tank.An exit static pressure trace is given in fig.76.The pressure rise causes a drop in exit Reynolds and Mach numbers in time. The hydrodynamic and heat transfer data were processed on least squares lines

only for the first 100 msec of the tests ,during which the averaged exit Reynolds number remained constant,as shown in fig.77.Using the first 100 msec is also significant from the fact that more than 50 % of the wall temperature rise occurs in this time interval.

3.7 UNCERTAINTY ANALYSIS

In the following paragraphs,estimated uncertainty values for wall heat flux,pressure,temperature and blowing rate are given for a confidence level of 95 %.The analysis is based on the method developed by KLINE et al. [132].

Wall heat flux from an electrical circuit can be computed quantitatively as a result of the theory described in appendix-3

$$\dot{q}_S = \frac{A^*}{\beta} \cdot \frac{N_{out}}{V_0} \cdot \frac{\sqrt{\rho c k}}{\alpha_R} \cdot \left[1 + \alpha_R (T_0 - T_\infty) \right] \quad (50)$$

where N_{out} is the digitized analogue circuit output,proportional to V_{out} .The uncertainty on wall heat flux can be evaluated from equation (50) as follows:

$$\begin{aligned} \delta \dot{q}_S = & \left\{ \left[\frac{\partial \dot{q}_S}{\partial A^*} \cdot \delta \left(\frac{A^*}{\beta} \right) \right]^2 + \left[\frac{\partial \dot{q}_S}{\partial N_{out}} \cdot \delta (N_{out}) \right]^2 + \left[\frac{\partial \dot{q}_S}{\partial V_0} \cdot \delta V_0 \right]^2 \right. \\ & \left. + \left[\frac{\partial \dot{q}_S}{\partial \sqrt{\rho c k}} \cdot \delta \sqrt{\rho c k} \right]^2 + \left[\frac{\partial \dot{q}_S}{\partial \alpha_R} \cdot \delta \alpha_R \right]^2 \right\}^{1/2} \end{aligned} \quad (51)$$

where

$$\frac{\partial \dot{q}_S}{\partial \frac{A^*}{\beta}} = \frac{N_{out}}{V_0} \cdot \frac{\sqrt{\rho ck}}{\alpha_R} \quad (52)$$

$$\frac{\partial \dot{q}_S}{\partial N_{out}} = \frac{A^*}{\beta} \cdot \frac{1}{V_0} \cdot \frac{\sqrt{\rho ck}}{\alpha_R} \quad (53)$$

$$\frac{\partial \dot{q}_S}{\partial V_0} = \frac{A^*}{\beta} \cdot \frac{N_{out}}{\alpha_R} \cdot \sqrt{\rho ck} \cdot \left(-\frac{1}{V_0^2} \right) \quad (54)$$

$$\frac{\partial \dot{q}_S}{\partial \sqrt{\rho ck}} = \frac{A^*}{\beta} \cdot \frac{N_{out}}{V_0} \cdot \frac{1}{\alpha_R} \quad (55)$$

$$\frac{\partial \dot{q}_S}{\partial \alpha_R} = -\frac{A^*}{\beta} \cdot \frac{N_{out}}{V_0} \cdot \frac{\sqrt{\rho ck}}{\alpha_R^2} \quad (56)$$

A typical wall heat flux uncertainty was computed using the experimental conditions of a representative test, summarized as follows:

$\dot{q}_s = 13.44$	W/cm^2
$V_0 = 1.000$	V
$\alpha_R = 1.21 \times 10^{-3}$	1/K
$N_{\text{out}} = 1000$	data units
$A^*/B = 1.063 \times 10^{-4}$	V/(units $\sqrt{\text{sec}}$)
$\sqrt{pck} = 0.215$	$\text{W}\cdot\sqrt{\text{sec}}/(\text{cm}^2\cdot\text{K})$

(56a)

The estimated uncertainties of the different terms in equation (98) are:

$\delta V_0 = \pm 0.0005$	V
$\delta \alpha_R = \pm 4.0 \times 10^{-5}$	1/K
$\delta N_0 = \pm 10$	data units
$\delta \frac{A^*}{B} = \pm 2.5 \times 10^{-6}$	V/(units $\sqrt{\text{sec}}$)
$\delta \sqrt{pck} = \pm 7.0 \times 10^{-3}$	$\text{W}\cdot\sqrt{\text{sec}}/(\text{cm}^2\cdot\text{K})$

(56b)

By substituting the data given in equations (56.a) and (56.b) into equation 51, a wall heat flux uncertainty of about $\delta \dot{q}_s = \pm 7.5 \%$ was found. In evaluating $\delta \dot{q}_s / \dot{q}_s$, the main uncertainty contributions were occurring due to $\delta \sqrt{pck}$ and $\delta \alpha_R$. The corresponding heat transfer coefficient uncertainty was found to be $\pm 7.6 \%$ when $T_{\infty} = 417$ K and $T_w = 293$ K. An estimated uncertainty on $\delta(T_{\infty} - T_w) = \pm 2 \%$ was used in the calculation. The uncertainty on the pressure measurements was estimated to be $\pm 0.4 \%$ for a full scale reading of 3 bars with a semiconductor differential transducer. The variable reluctance transducer exhibited an

uncertainty of $\pm 0.6\%$ because of the relatively noisy signal when compared to the signal from a semiconductor transducer. In all pressure measurements, special care was taken to minimize the transducer cavity volume and connection pipe volume in order to improve its response time .

Temperature measurements using Cr-Al thermocouples (20 μm) carried an uncertainty of $\pm 2\text{ K}$ when full scale reading was 417 K, corresponding to a δT of $\pm 0.5\%$.

The blowing rate uncertainty δm determined from (equation (48)) , (from the measured coolant mass flow rate, the measured free stream mass flux rate and total exit area of coolant holes) was estimated to be $\pm 4\%$, when the full scale blowing rate was 2.

A summary of the uncertainties on the basic experimental parameters of the present tests are summarized in table 3-1.

3.8 MODEL DESCRIPTION

The heat transfer investigations were carried out on a high pressure rotor blade made of machinable glass ceramic. This specific material has a very low thermal conductivity and diffusivity, as shown in fig.78. These properties were extremely useful in obtaining a nearly isothermal test surface during a compression tube test.

The external profile of the blade is shown in fig.79 and the corresponding list of blade coordinates are given in fig.80. The linear cascade is made of 6 blades and its main characteristics are described in fig.81. An overall view of the cascade is given in fig.82 with an aluminum blade installed instead of the heat transfer instrumented blade.

45 platinum thin film heat transfer gauges were deposited on the ceramic blade using the method described in section 3.2.5.1. The gauge locations are shown in fig.83. A special attention was given to obtain a good gauge resolution near downstream of the ejection sites. The final completed model is shown in fig.84. The two gauges were intentionally located in the showerhead region (in between the rows) of the leading edge, fig.84.a. The dimensions of the active portion of the thin film gauges are 0.8 mm x 20.0 mm. The passive thin film (gold) connectors and thick silver films for external connections are also shown in fig.84.

Three independent circular plenum chambers were drilled in the blade machined from a single block of ceramic. Using a single block was significant in order to avoid any disturbance of the very thin boundary layers especially downstream of the ejection sites. This approach also eliminates the strong conduction heat flow paths which may occur near substrate/metal interfaces.

Three rows of spanwise angled ejection holes on the leading edge, double rows of shaped holes on the suction side and a single row of shaped holes on the pressure side were manufactured, (fig.85). The geometrical details of the leading

edge, the suction side and the pressure side coolant ejection sites are respectively described in figs.(86),(87) and (88). The heat transfer instrumented blade is shown in fig.89 after completion of electrical connectors, plenum chambers and epoxy side wall positioning pieces

The pressure and temperatures in the three plenum chambers were continuously and independently monitored using Cr-Al (20 μ m) thermocouples and pressure transducers. Fig.90 shows the plenum chamber measurement details.

CHAPTER 4

EXPERIMENTAL RESULTS AND DISCUSSION

In this chapter, an experimental investigation of convective heat transfer around a film cooled high pressure turbine rotor blade is presented in detail. The model has been described in section 3.2 .

After a discussion of the mainstream hydrodynamic characteristics , the heat transfer results in the absence of coolant ejection are given. The main parameters investigated are local Reynolds number, longitudinal curvature, free stream turbulence intensity, incidence angle ($i=-10, 0, +10$ and $+15$) and disturbance effect due to the presence of a cooling hole.

The heat flux measurements in the presence of discrete hole film cooling were independently performed around the leading edge and along the suction and pressure sides,in order to provide baseline data sets for further investigations and

numerical predictions. As was described in section 3.2, the data was generated under correctly simulated gas turbine conditions.

The film cooling heat transfer data was produced in a range of realistic coolant temperatures and blowing rates. The discharge coefficients of the three independent ejection sites were also evaluated from coolant hydrodynamic measurements. The final section of this chapter deals with the simultaneous coolant ejection through three ejection sites. These measurements, representing a close simulation of an actual film cooled blade were interpreted with the aid of independent ejection data.

4.1 RESULTS IN THE ABSENCE OF COOLANT EJECTION

4.1.1 INVISCID MAINSTREAM FLOW AT ZERO INCIDENCE

The measured isentropic Mach number distributions along the blade surfaces at zero incidence are shown in fig.92. The cascade inlet Mach number under nominal testing conditions was measured to be 0.25 ,at one chord length upstream of the passage.Because of the relatively small leading edge radius ,detailed static pressure measurements around the stagnation point could not be performed.On the suction side, between the stagnation point and $s/\bar{c}=0.05$,the mainstream accelerates to $Ma=0.35$. This favourable pressure gradient region continues up to $s/\bar{c}=0.30$ and between $s/\bar{c}=0.30$ and 0.45,a flat region is observed. Further downstream,the mainstream continues to accelerate and almost sonic velocities occur near the trailing edge.On the pressure side,following the strong acceleration around the leading edge,a maximum velocity takes place around $s/\bar{c}=-0.05$. A diffusion region is observed along a very short distance between $s/\bar{c}=-0.08$ and -0.12.The position where the curvature changes from convex to concave and the onset of the deceleration appear to be almost at the same position.Starting from $s/\bar{c}=-.30$,a favourable pressure gradient accelerates the mainstream up to nearly sonic velocities near the trailing edge.

The nominal mainstream conditions chosen for this experimental program are listed as follows:

$$Ma_{inlet} = 0.25 \quad (57)$$

$$Ma_{exit,s} = 0.92$$

$$Re_{C_{inlet}} = 8.42 \times 10^5$$

$$i = 0^\circ$$

$$TU_\infty = \sim 5.2\%$$

$$T_C/T_{0\infty} = \sim 0.71$$

(58)

A two dimensional, finite area, time marching method, developed by ARTS,[148] has been applied to predict the inviscid free stream flow in the cascade. The predictions at zero incidence shown in fig.92 agree well with the measured data. The dashed lines drawn in fig.93 indicate the sonic velocity locus. Such regions occur locally near the trailing edge along the suction side. However, a sonic throat does not exist under nominal operating conditions ($Ma_{exit,s} = 0.92$). Since this method does not accurately model the leading edge flow, a singularity method (Martensen) was found to be more eligible for the computation of the inviscid free stream velocities around the leading edge and for an accurate determination of the stagnation point position,[149]. Martensen predictions near the leading edge asymptotically approach the finite area computations and the measured Ma number data,(fig.92). As a result of these calculations, the stagnation point at zero incidence has been found to be at $s/\bar{c}=-0.019$, very close to the mid row of holes, as shown in fig.103. This result suggests that,in the absence of coolant ejection, the suction side boundary layer sees both of the cooling rows LM and LS as roughness elements. (fig.103) .The pressure side boundary layer starts to grow along a smooth surface between the stagnation point and the cooling row LP. At $s/\bar{c}=-0.026$,it is only disturbed by the cooling row LP.

4.1.2 HEAT TRANSFER AT ZERO INCIDENCE

The heat transfer coefficient distributions in the absence of coolant ejection are shown in fig.94 for the near stagnation region, ($-0.10 < s/\bar{c} < 0.10$). In order to avoid any undesirable free stream air circulation between rows LM,LP and LS, the coolant plenum chamber was filled with a flexible insert. In the absence of the latter, as was demonstrated from surface oil flow visualizations, (fig.95), the free stream air penetrates in to the plenum through row LM and depending on the local static pressures, is ejected through rows LP and LS, affecting the local heat flux measurements.

From a heat transfer point of view, the leading edge of a turbine blade can be modelled by a cylinder in cross flow. Stagnation heat transfer on such a configuration is mainly dominated by a three dimensional vortical structure, KESTIN and WOOD, [22]. These vortices have their vorticity axes parallel to the main flow, as visualized by SADEH et al., [23]. The amount of heat transfer is proportional to the quantity $TU_\infty \frac{V_2}{Re}$. Any increase of this product decreases the spacing of the vortices and, hence, enhances the heat transfer rate. Looking at the results from the gauges located at $s/\bar{c}= \pm 0.01$, (fig.94), enhancement of heat flux is clearly observed when TU_∞ is increased from 0.8 % to 5.2 %. KESTIN and WOOD's cylinder in cross flow correlation [22] provides similar trends. For $TU_\infty = 0.8$ %, the present data are also compared with TURNER and COLLADAY's cylinder in cross flow correlation [24]. However even at zero incidence, a cylinder in cross flow is not an exact simulation of a turbine blade leading edge, because different inviscid flow characteristics exist on both sides of the stagnation line. A circulation also exists around the blade (because of lift production). The circulation around the profile is defined as,

$$\Gamma = \oint V_\theta \cdot dS = (\operatorname{tg}\beta_1 - \operatorname{tg}\beta_2) \cdot \cos\beta_1 \quad (59)$$

around the
profile

where v_θ is the local tangential component of the inviscid velocity and ds is a differential length measured along the external contour and β_1, β_2 are respectively flow inlet and exit angle measured from the axial direction as shown in fig.81. This quantity indicates the rotational character of the fluid motion around the blade. When compared with a cylinder in cross flow with zero circulation; the streamlines around the circular leading edge of a turbine blade follow different directions. This rotational character results in a deviation of the stagnation streamline from the approaching mainstream direction. Such changes in the streamline pattern definitely influence the stagnation region heat transfer. Moreover, the present model displays three rows of holes acting as roughness elements.

The influence of the existence of the leading edge film cooling holes on heat transfer has been investigated by comparing the data measured along a smooth uncooled blade having the same contour and the data measured along the present model, no coolant being ejected. For comparison purposes, almost the same free stream conditions were generated in the facility. The smooth blade and the blade with cooling holes did not show significant differences along the pressure side, when $TU_\infty = 5.2\%$, as far as heat transfer coefficients are concerned, (fig.96). On the smooth blade, the pressure side laminar boundary layer is expected to transit very quickly to a turbulent state near the curvature inversion location, at about $s/C = -0.08$, [62]. Most of the time such a quick transition is attributed to the amplification of the 3D vortices originating from the stagnation region when the flow is accelerating around the initially convex part of the pressure side. Finally, a vortex breakdown near the curvature inversion point may cause a highly turbulent boundary layer configuration, as stated by RICHARDS, [33]. For the present model, although the pressure side boundary layer is disturbed by row LP, the contribution of this surface roughness to the pressure side transitional heat transfer is not very pronounced, at least within the experimental accuracy of the present tests, (fig.96).

Along the suction side, the boundary layer development appears to be strongly influenced by the existence of cooling rows LM and LS, even without ejection, (fig.96). The comparison of $TU_{\infty}=5.2\%$ heat transfer data along the present model with the smooth blade data, suggest a very early transition along the suction side of the cooled blade model. The suction side boundary layer appears to be fully turbulent at $s/\bar{c}=0.25$, mainly because of cooling hole induced transition process taking place between the stagnation point and $s/\bar{c}=0.25$. The existence of a fully turbulent boundary layer is confirmed by examining the timewise variation and the order of magnitude of the heat flux signal traces. A series of wall heat flux signals measured between the stagnation point and $s/\bar{c}=0.31$ are presented in fig.97. The heat flux gauge locations in this part of the blade are shown in fig.98. The traces from location B to H are all of the type of turbulent boundary layer heat flux signals. No significant qualitative differences between the signals D, E, F and G were observed, (fig.97). This fact allows to asses the already turbulent structure of the boundary layer, even before the double rows of cooling holes on the suction side, ($s/\bar{c}<0.21$). However, on the smooth blade, as a result of natural transition, a much longer transitional state is observed. The boundary layer becomes fully turbulent at almost $s/\bar{c}=0.40$. When TU_{∞} is reduced to 3 % on the smooth blade, the transitional boundary layer is extended up to $s/\bar{c}=0.8$, indicating the definite influence of TU_{∞} on laminar and transitional boundary layers, (fig.96).

The boundary layers developing along the suction and pressure side are extremely thin compared to the cooling hole diameter. Typically, the computed boundary layer thickness near the ejection site S was about 5 times thinner than the hole diameter; this corresponds to an hole diameter to momentum thickness ratio of 43. The computations were based on a two dimensional boundary layer code developed by CRAWFORD et al.[133] and on a modified Prandtl's mixing length turbulence model taking into account the streamwise convex curvature effects. As a matter of fact, relatively thin boundary layers may easily undergo local separation and reattachment downstream of

the ejection sites S and P even without ejection. Such viscous flow behaviour resulting from the interaction of the boundary layer with a hole which is almost 4-5 times larger than the approaching boundary layer thickness may be considered as the prime cause of some data scatter observed locally, just downstream of injection sites S and P, (fig.99). A very strong influence of local Re number on the heat transfer coefficients is also shown in (fig.99), where the inlet $Re_{\bar{c}}$ number values range from 7.4×10^5 to 9.65×10^5 .

The Nusselt number measurements performed at various locations along the suction side for different local Re number levels fit along a straight line in between the turbulent [150] and the laminar [150] flat plate correlations (fig.100). The fluid properties were evaluated using the local free stream static temperature. The line A fitted to the measured Nu number data provided somewhat lower values than the turbulent flat plate correlation. This effect is primarily due to convex curvature stabilization. The reductions of the turbulent kinetic energy and turbulent shear stress levels, especially in the outer layers of the turbulent boundary layer developing along a convexly curved surface are closely related to the reductions in wall heating rates,[52]. The largest deviations from the turbulent flat plate correlation are observed where the boundary layer is expected to be highly transitional ($0.05 < s/\bar{c} < 0.20$ or $Re < 1.5 \times 10^5$). The line A asymptotically converges to the turbulent flat plate correlation near the trailing edge, where the streamwise curvature effects disappear. A full recovery to a flat wall boundary layer is however not expected ,[52].

In order to obtain the response of a boundary layer to changes in free stream turbulence intensity, this quantity was raised from 2 % to 3.5 % and finally to 5.2 % , (fig.101). The only region influenced by this change was the stagnation area, between $s/\bar{c} = -0.01$ and $s/\bar{c} = +0.20$. Almost, no heat transfer coefficient enhancement was observed in all other regions of the blade . It is indeed a well documented fact [151],[152] that TU_{∞}

only significantly affects laminar or transitional boundary layers ,in the presence of a favourable pressure gradient,as far as wall heating rates are concerned.Therefore, except for the region between $s/\bar{C}=-0.01$ and 0.20,the remainder of the blade surface seems to experience local heating rates of fully turbulent boundary layers ,(fig.101).

4.1.3 INVISCID MAINSTREAM FLOW AND HEAT TRANSFER AT OTHER INCIDENCES,($i=-10,+10,+15$)

Iso-Mach lines computed by a finite area method [148] at $i=0,+10$ and -10 are presented in fig.102. A qualitative description of the flow around the leading edge is obtained at various incidences, (fig.102).For a positive incidence variation, the stagnation point moves towards the pressure side,with respect to the zero incidence position.At negative incidences , the stagnation point moves towards the suction side.

As shown in fig.102.b,positive incidences create excesses in local Mach numbers along the suction side ($s/\bar{C}<0.4$) ,whereas negative incidences induce local Ma number deficits . The incidence angle effect on the local Ma number occurs in a reversed way along the pressure side.The influence of incidence angle almost disappears along the regions where $|s/\bar{C}|>0.4$,on both suction and pressure sides.

A more precise determination of the stagnation point location and the near leading edge velocity distribution was computed at different incidences using a Martensen method ,(fig.103).The corresponding measured heat transfer evolutions are presented in fig.104.At zero incidence,as a result of the tripping effect of rows LM and LS,the onset of the suction side boundary layer transition is observed at $s/\bar{C} \sim 0.08$.In this study, the onset of transition location is defined as the first measurement point where the heat transfer coefficient h increases in a pronounced way.Increasing the incidence to +10 and +15 moves the stagnation point respectively to points A and

D whereas the transition onset is displaced to $s/\bar{c}=0.065$ and 0.050 , (fig.104). At $i=-10$, the stagnation point is located in C and only row LS disturbs the suction side boundary layer. Along the pressure side, at $i=0$ and $i=-10$, transition is observed to occur at $s/\bar{c}=-0.08$, because of the effect of the adverse pressure gradient. In the latter case, a higher local free stream velocity level, enhancing local Re number as well as the disturbing effect of rows LM and LP, are responsible for slightly higher heat transfer coefficient values. At $i=+15$, the stagnation point D nearly coincides with row LP and the unfavourable pressure gradient almost disappears; hence larger laminar and transitional regimes are expected. This behaviour has been confirmed by the measurements, (fig.104).

The heat transfer coefficients measured at various incidences have been non dimensionalized with respect to those obtained at zero incidence, (fig.105). The displacement of the transition onset point around the leading edge along the suction side with increasing positive incidences (fig.105.a and fig.105.b) as well as larger laminar and transitional zones along the pressure side (fig.105.a) are shown. Fig.105 also demonstrates that the wall heating rates are not strongly influenced by changes in incidence angle in the stagnation region where $-0.02 < s/\bar{c} < 0.02$. When the incidence angle is changed from $i=-15$ to $+15$, the total displacement of the stagnation point is about 6 % of the chord length, (4.8 mm). The computed stagnation point always remains in between row LP and LS within this incidence range, (fig.103). The two thin film gauges at ($s/\bar{c}=\pm 0.01$) cover an important part of this zone. The width of these thin films is about 1.2 % of the chord length, (~1.0 mm). Therefore the averaging property of the gauges may be a reason for the wall heating rates which are quite close to each other.

4.2 RESULTS IN THE PRESENCE OF COOLANT EJECTION

4.2.1 LEADING EDGE HEAT TRANSFER WITH FILM COOLING

4.2.1.1 RESULTS AT ZERO INCIDENCE -

Because of different free stream conditions around the leading edge, as well as because of different internal flows (or loss patterns) in the cooling holes of different rows, the local discharge coefficients of the three rows differ from each other. Since local mass flow rate measurements around each row were not possible, a mean discharge coefficient \bar{C}_d was evaluated from the total measured coolant mass flow rate, the coolant plenum total pressure and an averaged free stream static pressure. The discharge coefficient was defined as,

$$\bar{C}_d = \frac{\dot{m}_c / \text{AREA}}{(\rho_c U_c)_i} = \frac{(\rho_c U_c)}{(\rho_c U_c)_i} \quad (59a)$$

where

$$(\rho_c U_c)_i = P_\infty \left(\frac{P_{0c}}{P_\infty} \right)^{\frac{\gamma-1}{\gamma+1}} \left[\frac{2 \frac{\gamma+1}{\gamma-1}}{RT_{0c}} \left(1 - \frac{P_{0c}}{P_\infty} \right)^{-\frac{\gamma-1}{\gamma}} \right]^{1/2} \quad (59b)$$

The \bar{C}_d distribution, obtained for a mass weight ratio range of 0.48 % to 1.01 % is shown in fig.106. The present data show qualitative agreement with the measurements obtained by TILLMAN et al., [153], in a water tunnel on a cylinder equipped with three cooling rows.

The effect of coolant temperature on the convective heat transfer coefficient distribution is shown in fig.108. The coolant to free stream temperature ratio was varied from 0.5 to 0.7 for a constant mass weight ratio equal to 0.48 %. From stagnation point location predictions, (fig.103) as well as from qualitative (low speed) oil flow visualizations, (fig.107), it appears that the suction side wall heating is affected by the coolant jets from rows LM and LS whereas the pressure side heat

flux is only affected by row LP.

The blowing rate m has been the most documented parameter in film cooling research because of its governing role in the distribution of coolant fluid inside the viscous layers, normal to the wall. A given coolant distribution establishes its specific mean velocity gradients and the associated turbulent shear stress and turbulent kinetic energy distributions. Unfortunately, because of a lack of detailed static pressure measurements, a very accurate determination of local m values was not obtained. An attempt to calculate local m values was made using the calculated local isentropic coolant mass flux rate, the averaged \bar{C}_d and the predicted free stream mass flux rate. Looking at fig. 108, local blowing rate values of 4.17, 1.26 and 0.85 were respectively obtained for the rows LM, LP and LS. On the suction side, highly penetrating jets from row LM disturb the approaching mainstream boundary layer; downstream of this row, a separated coolant layer zone is observed ($s/\bar{C} = -0.01$), where a poor cooling efficiency is achieved. Reattachment is expected near row S due to the free stream acceleration and strong streamwise convex curvature. The gauge located at $s/\bar{C} = -0.01$ provides a quite low heat transfer coefficient measurement, although this region does not seem to be submitted to the influence of a coolant film. This observation may be attributed to the fact that, even with this low conductivity material and short running times, local wall temperature measurements could be affected by conduction in between closely spaced ejection rows ($-0.01 < s/\bar{C} < +0.01$). This influence is mainly related with the local wall temperature measurement, rather than the wall heat flux measurement which is only sensitive to time rate of change of wall temperature. The comparison of heat transfer coefficients evaluated with an isothermal wall temperature and with the locally measured wall temperatures, displayed a quite negligible difference 3 hole diameters downstream of rows LP and LS, fig. 109-a. In the showerhead region ($s/\bar{C} = \mp 0.01$), the heat transfer coefficient measurement is affected by some additional uncertainty because of the inter-row heat conduction. The deviations from the isothermal wall temperature and the resulting heat transfer

coefficient uncertainty is presented in fig.109-b, for $T_c/T_{\infty}=0.52$, $\dot{m}_c/\dot{m}_{\infty}=0.48 \%$. The row spacing and the hole spacing are as important as the L/d ratio of the cooling holes in the heat conduction process. An average wall temperature drop of ~ 4.0 % of the mainstream temperature with respect to the isothermal level caused 5 to 8 % uncertainty on h, only for the two gauges located at $s/\bar{c}= \pm 0.01$. The wall temperature variations near the ejection holes were negligible when the coolant was ejected at the wall temperature .

The effect of coolant mass weight ratio is shown in fig.110. This parameter was varied from 0.48 % to 1.01 % for a fixed value of coolant to free stream temperature ratio ,(0.51) . Film cooling applied with a higher mass weight ratio provided a reduced heat transfer pattern along the pressure side. The row LP was ejecting along a concave surface at a quite high blowing rate,($m=2.56$).The measured heat transfer distribution showed that the coolant remains attached to this concave surface,providing a correct wall protection. This behaviour confirms the trends already observed in a low speed environment by GOLDSTEIN et al., [114].For a high coolant mass weight ratio (1.01 %),the blowing rate amounts to 8.79 across row LM whereas a value of 1.66 is observed across row LS. As might be expected,due to the high momentum flux of these jets,the disturbed region is enlarged on the suction side and the reattachment point is moved more downstream.Behind row LS,the first three gauges experience wall heat flux levels comparable to zero injection situation.From fig.110,there is experimental evidence that the jets ejected from row LS separate from this convex surface.Coolant jet separation from convex surfaces at high blowing rates is however a well known effect [114].After reattachment,measured wall heat flux values far downstream ($s/\bar{c} > 0.25$) are lower than when moderate mass weight ratios (0.50 %) are applied .In order to find the upper mass weight ratio limit before jet separation,heat transfer distributions were obtained for $\dot{m}_c/\dot{m}_{\infty}=0.60 \%$ and $T_c/T_{\infty}=0.52$ and 0.59 , (fig.111).For the lowest coolant temperature ratio,the coolant ejected through row LS is at the onset of separation : a slight

heat transfer augmentation is observed only at $s/\bar{c} = + 0.08$; the local blowing rates through rows LM and LS are respectively 5.22 and 0.93. Increasing the coolant temperature ratio, at an almost constant blowing rate, leads to a partially separated coolant flow situation. As a matter of fact, an increase of T_c/T_{∞} results in a decrease of ρ_c/ρ_∞ and hence, at constant m , in an increase of U_c/U_∞ and moreover of the momentum flux ratio, leading to a more severe jet separation. On the pressure side, no coolant jet separation has been observed.

Although strong variations exist near the leading edge, an attempt was done to define an average leading edge heat transfer coefficient as a function of coolant mass weight ratio and coolant to free stream temperature ratio, (fig.112), using only 4 gauges located on both sides of the stagnation point; \bar{h} and \bar{h}_e (heat transfer coefficient without ejection) were obtained as arithmetical averages both on suction and pressure side. On an average basis, the cooling looks more effective along the pressure side than along the suction side. As the mass weight ratio increases, the suction side appears to be less protected because of jet separation and upstream disturbances created by row LM. The strong influence of T_c/T_{∞} is also demonstrated.

4.2.1.2 RESULTS AT OTHER INCIDENCES, ($i=-10, +10$) -

The effect of incidence variation upon leading edge heat transfer in the presence of film cooling was investigated for constant values of mass weight ratio, temperature ratio and outlet Reynolds number. Results as well as estimated flow paths are given in fig.113 whereas aerodynamic predictions were given in fig.103. For $i=10$, the stagnation point is very close to row P. The ejection in such a low velocity area provides a much higher local blowing rate (4.17) than at zero incidence (2.0). On the pressure side the laminar region, observed between point A and $s/\bar{c} = -0.10$ without ejection, obviously disappears because of the disturbing nature of the coolant jets in the boundary

layer. However, the cooling along this surface is not as efficient as for the zero incidence configuration. The local blowing ratios across rows LM and LS are 1.61 and 0.96 . The coolant layers provide a very efficient wall protection as a result of a very smooth coolant introduction into the suction surface boundary layer.

For $i = -10$, the position of the stagnation point (C) suggests that the suction surface boundary layer is only affected by the jets issued from row LS ($m=2.05$). The cooling efficiency is rather poor, most probably because of a very small portion of fluid ejected through this row. Cooling of the pressure side through rows LM and LP provides heat transfer coefficient reductions to values equal to at least half of those obtained for the noncooled configuration in between C and $s/\bar{C} = -0.30$.

The main experimental parameters of the tests discussed in section 4.2.1 are summarized in Table 4.

4.2.2 SUCTION SIDE HEAT TRANSFER WITH FILM COOLING

Qualitative ("low speed") oil flow visualizations were performed in a low speed environment in order to assess the spanwise uniformity of the coolant flow as well as the film coverage downstream of the ejection rows,(fig.114).Visual investigation downstream of the ejection site showed a quite uniform coolant field in the spanwise direction. It was also observed that the secondary flow region did not significantly affect the coolant field.

The influence of the blowing rate m on the suction side convective heat transfer is shown in fig.115.The blowing rate was varied from 0.37 to 0.99 for a constant value of coolant to free stream temperature ratio ($T_c / T_{\infty} = 0.51$).In all cases,a significant protection of the wall was achieved,especially close to the ejection holes, ($x/d < 40$) .Typical velocity profiles,near and far downstream of the ejection rows,have been extracted from the literature [94,124] , (fig.116).For low blowing rates ($m=0.40$) ,low mean velocity gradients near the wall and important momentum deficits above $y/\delta = 0.2$ are typically encountered.If m is raised up to 1.0,a velocity excess region is observed near the wall.Above this zone,the overall mean velocity gradient is very low compared to the low blowing rate case.Since the turbulent kinetic energy production is related to the mean velocity gradient [124],higher heat flux levels are expected for low blowing rates whereas,except in the near wall region,a reduction in overall heat flux will be observed for $m=1.0$. In the near wall region,the heat transfer augmentation observed for $x/d < 40$ may be related to the velocity excesses shown in fig.116 .Very steep mean velocity gradients near the wall as well as an eventual jet penetration into the mainstream yields large shear stress and turbulent kinetic energy levels in this region. A schematic figure of jet penetration into the mainstream and the interaction of the hot gases with the wall are shown in figure 117. For most of the above mentioned studies,[94,124] ,the approaching mainstream boundary layer thickness δ has the same order of magnitude as

the injection hole diameter. Although the mean velocity profiles provided by BERGELES ,YAVUZKURT [94,124] provide a good aid in the interpretation of the data presented in fig.115, the d/d ratio predicted for the present experiments is about 1/5, closer to the situation on an actual blade .A strong dominance of the new cold injected layers is therefore expected to take place.

Significant coolant temperature effects on convective heat transfer have also been observed.Fig.118 presents the results obtained for $m=0.40$.Important h/h_0 reductions were achieved when the coolant temperature was changed from wall temperature, down to half of the mainstream level,especially near the injection site ($x/d < 40$).The downstream values of h/h_0 smoothly increase and far downstream ($x/d =100$), the heat flux level differences due to coolant temperature variations are not as large as the differences occurring close to the ejection rows.Increasing m up to 0.96 provided the results presented in fig.120, with considerably lower heat transfer levels.Just downstream of the ejection site ($x/d < 40$), a local heat transfer augmentation,occurring almost independently of the coolant temperature level,is observed,($m=0.96$).This augmentation has been related to very high overall turbulent shear stress and turbulent kinetic energy levels near the wall, existing for such a blowing rate value . Another expected reason was "hot mainstream gas/wall" interaction due to severe coolant jet penetration into the mainstream.The penetrating coolant jets were expected to reduce the overall film cooling coverage just downstream of the ejection site,because of reduced lateral jet spread.In this zone,the wall has more chances to be influenced by the hot mainstream gas.After a certain distance,when the abrupt changes in the hydrodynamics structure start to decay,an almost linear h/h_0 rise take place, ($x/d = 30$).As opposed to the $m=0.4$ case,the far downstream influence of the coolant temperature on h/h_0 was very much pronounced.At $m=0.96$,mainly because of the considerably high momentum flux of the discrete coolant jets ,the coolant layers tend to dominate even at far downstream locations of the ejection site,as far as convective heat transfer is concerned.

4.2.3 PRESSURE SIDE HEAT TRANSFER WITH FILM COOLING

The pressure side discrete hole film cooling configuration ($s/\bar{c}=-0.315$) is shown in fig.88. The plenum chamber flow and the spanwise uniformity of the coolant jets have been checked by means of a qualitative ("low speed") surface oil flow visualization technique. A typical flow visualization picture shows the satisfactory spanwise uniformity of the discrete jets and the near hole film coverage behaviour, (fig.121). The jet separation and reattachment zone is clearly marked within the first 10 hole diameters distance from the row.

The heat transfer coefficient h_a , (in the absence of any coolant ejection), distribution used to non dimensionalize the film cooling data along the pressure side is presented in fig.122. Four tests at identical free stream conditions were performed at different times and using different measurement channels, in order to assess the repeatability of the measurements.

The blowing rate of the coolant jets ejecting along a concave surface is particularly important because of coolant penetration effects. A simple mathematical model concerning the coolant flow and inviscid mainstream flow on curved surfaces shows that when $I \cdot \cos^2\alpha$ is less than unity, the coolant layers on a concave wall tend to penetrate into the mainstream as shown in fig.42, [114]. DANIELS also pointed out that when the blowing rate is small ($m < 1$), the coolant jets act only as boundary layer trips ($T_c = T_{\infty}$) and almost no reduction in heat transfer is obtained, [34]. The present experiments were mainly performed at quite high blowing rates ($m = 1.74 \dots 4.23$), whereas the local coolant mass weight ratio (only for the pressure side) was ranging from $\dot{m}_c / \dot{m}_{\infty} = 0.3 \%$ to 0.7% .

The heat transfer data shown in fig.123 reveal that, at high blowing rates, the coolant jets strongly penetrate into the mainstream and reattach at about 10 hole diameters downstream of the ejection holes. The strong jet penetration and reattachment

enhances the turbulent mixing levels near the ejection site. The heat transfer maximum observed at $x/d \sim 10$ is closely related to such enhancements. An almost 20 % increase of h/h_e near the ejection site seems to occur when the coolant is at the same temperature as the wall. This enhancement dies out with decreasing blowing rates indicating the importance of reduced turbulence mixing (or less severe penetration) on film cooling heat transfer near the ejection site. Far downstream ($x/d > 40$), the effect of blowing rate on h/h_e is very weak.

As a result of the data shown in fig.123, one might conclude that film cooling does not provide a reduced h/h_e pattern near the ejection site, when $m > 1.74$ and $T_c = T_w = 0.7 \times T_{\infty}$. However, in real engines the coolant fluid is much colder than the above mentioned value. The h/h_e data measured at $T_c = 0.49 \times T_{\infty}$ shows a better situation as a result of film cooling along the pressure side, evaluated at constant blowing rate ($m = 2.16$), (fig.124). Although slight h/h_e augmentations appear, the overall h/h_e reduction is about 30 % when $m = 2.16$ and $T_c/T_{\infty} = 0.49$.

The minimum h/h_e value occurs about 40 hole diameters downstream of the ejection site. The influence of an increasing blowing rate is also shown in fig.124, at a low coolant temperature level, ($T_c/T_{\infty} \sim 0.5$). The h/h_e distribution is influenced over a length equal to 20 hole diameters downstream of the ejection holes, when m is raised from 2.16 to 3.70. But, even for $m = 3.70$, the overall cooling efficiency is improved a lot compared to the data, shown in fig.123 for $T_c/T_{\infty} \sim 0.7$. The wall heating pattern at lower blowing rates are also discussed in chapter 4.2.4.2.

4.2.4 SIMULTANEOUS COOLANT EJECTION THROUGH THE LEADING EDGE,SUCTION SIDE AND PRESSURE SIDE

The part of the research reported in this section is devoted to the investigation of multilocational,discrete hole film cooling on a high pressure turbine rotor blade under well simulated mainstream and coolant flow conditions. Film cooling was provided simultaneously around the leading edge,along the suction side ($s/\bar{c} \approx 1/5$) and the pressure side, ($s/\bar{c} \approx 1/3$) as it has been described in figs.89,90 and 91 in section 3.2.The coolant air was fed through a single coolant channel at the root of the blade ,but independent plenum chambers were used for each of the injection sites,providing an independent monitoring of coolant pressure and temperature in each plenum.Local coolant hydrodynamic behaviour,heat transfer without and with film cooling were successively investigated in a wide range of coolant to free stream mass weight ratios and temperature ratios.The influence of free stream turbulence intensity was also studied.

4.2.4.1 COOLANT HYDRODYNAMICS -

4.2.4.1.1 Total Coolant Mass Flow Versus Local Plenum Chamber Pressure -

Multi-location film cooling on the turbine blade was performed using a single coolant entry channel through the blade root. The total coolant mass flow rate \dot{m}_c accurately measured by means of a sonic orifice , was shared in between the ejection sites P,S and L.The amount of coolant mass flow rate passing through each ejection site was however needed in order to obtain local coolant to free stream mass weight ratios and blowing rates.Fig.125 shows the strong functional dependency between the normalized mass weight ratio $\frac{\dot{m}_c}{\dot{m}_\infty} \sqrt{\frac{T_c}{T_{cf}}}$ and P_{oc}/P_∞ for each independent ejection site.The measurements were taken at 3

different coolant temperature levels ($T_c/T_{cm} = 0.7, 0.6, 0.5$) simultaneously with the heat transfer measurements. Since the total coolant mass flow rate passing through the root of the blade is inversely proportional to the square root of the coolant temperature, a normalized mass weight ratio was defined in order to establish a single functional dependency between the local plenum chamber pressure and the total coolant flow.

4.2.4.1.2 Local Discharge Coefficients -

A mean value of the local discharge coefficient was evaluated experimentally for each ejection site from the independent measurements of S,L and P. \bar{C}_d was evaluated experimentally using eqs.(59.a) and (59.b). Independent monitoring of local coolant mass flow rate,plenum chamber pressure and temperature were very useful in determining the deviation from isentropic coolant mass flow rate as the discharge coefficient of the local ejection site,as shown in fig.126. Significant isentropic losses in the leading edge cooling flow were observed relative to other ejection sites.The leading edge \bar{C}_d data showed some qualitative agreement with TILLMAN et al.'s data,[153],taken on a film cooled cylinder in cross flow.However,their tests were carried out in a water tunnel compared to well simulated mainstream of the present tests. Relatively lower \bar{C}_d values of the leading edge injection compared to ejection sites P and S were expected to occur because of highly complicated nature of the plenum chamber flow,with compound angled injection holes discharging into the stagnation zone through 3 rows.The \bar{C}_d was varying between 0.4 and 0.5 for most of the tests,in the ejection sites P and S.

4.2.4.1.3 Coolant Split Between Plenum Chambers -

The determination of the coolant mass flow rate passing through each ejection site was only possible after combining local P_{oc}/P_∞ data obtained from $\frac{\dot{m}_c}{\dot{m}_\infty} \frac{\sqrt{T_c}}{\sqrt{T_{ref}}}$ (fig.125), T_c and \bar{C}_d (fig.126) for the case of multilocation simultaneous film cooling study with a single coolant entry passage at the root of the blade. The quantity \dot{m}_{ei}/\dot{m}_c characterizing the coolant split is shown in fig.127. At low P_{oc}/P_∞ values due to flow conditions which are not very well defined in ejection site L, very low \bar{C}_d values resulted in . The cooling rows S and P then perform the largest percentage of the ejection. However for a typical $\dot{m}_c/\dot{m}_\infty = 3.0 \%$; the coolant split was 40 % , 35 % and 25 % corresponding to the ejection sites L,S and P.

4.2.4.1.4 Local Blowing Rates -

The most important outcome of determining the actual local coolant mass flow rates from measured \bar{C}_d , P_{oc} and T_c was the evaluation of local blowing rates as presented in fig.128. As it was already shown in figs.108,110 and 111, within a nominal \dot{m}_c/\dot{m}_∞ range , the mid row of holes located very near the stagnation line ejects coolant at a very high local blowing rate. This effect is because of very small free stream mass flux rates near the stagnation point.

4.2.4.1.5 Verification Of The Estimated Hydrodynamic Data -

Although a precise procedure was incorporated in determining the local blowing rates and the local coolant mass flow rates , a further check of the hydrodynamic data was performed. Film cooling heat transfer tests had been performed and reported on the same leading edge as discussed in chapter 4.2.1.1. Direct measurements of the leading edge coolant mass

flow rate were available, for the data with a better heat flux measurement resolution, as they were given in chapter 4.2.1.1. In order to asses the validity of the estimated local coolant mass flow rates for the multilocation study reported here, the simultaneous injection heat transfer data near the leading edge were compared with the only leading edge injection data presented previously. Very good agreement of the two types of film cooling heat transfer data sets shown in fig. 129 a-b-c-d provides a further quantitative check on the hydrodynamic data evaluated using the measured local discharge coefficients.

4.2.4.2 FILM COOLING HEAT TRANSFER, LOCAL INVESTIGATIONS -

The heat transfer data were obtained for a $\frac{\dot{m}_c}{\dot{m}_\infty}$ parameter ranging between 0.5 and 3.3 % whereas the coolant to free stream temperature ratio was varied between 0.51 and 0.70. The tests were performed at constant downstream Reynolds (23.2×10^5) and Mach (0.925) numbers. The free stream total temperature was equal to 415 K.

4.2.4.2.1 Stagnation Region Film Cooling Behaviour downstream of Row (LS)

The effect of overall mass weight ratio on the leading edge heat transfer distribution is shown in figures 130, 131.a. It should however be noted that the uncertainty associated with the measurements obtained from the two gauges located in between rows LM, LP and LS is quite high as they are affected by undesirable conduction phenomena as well as strong deviations from the assumed one dimensional heat transfer. For low overall mass weight ratio values (0.5 % 0.93 %), the heat transfer behaviour is quite smooth downstream of row LS whereas, for higher values (1.47 % ... 3.09 %) a continuously increasing heat transfer augmentation is measured around $s/\bar{C}=0.08$. The latter is due to a high blowing rate ejection effect across a highly convex surface.

4.2.4.2.2 Stagnation Region Film Cooling Behaviour downstream of Row (LP)

Pressure side ejection near downstream of the leading edge provided coolant layers on a highly convex leading edge where $s/\bar{C} < -0.08$. Under the influence of the strong convex curvature, the coolant layers originating from row (LP) at $s/\bar{C} = -0.026$ were expected to lift-off before $s/\bar{C} = -0.08$, resulting in some heat

transfer augmentations measured near $s/\bar{C}=-0.08$, as shown in fig.130.b and fig.131. After the change of sign of curvature at $s/\bar{C}=-0.08$, even at high blowing rates, the concave curvature was expected to induce the reattachment of the cold layers. The merging data points at $s/\bar{C}=-0.16$, corresponding to the tests run at $\dot{m}_c/\dot{m}_\infty = 1.47 \%, 1.66 \%, 2.07 \%$ and 3.09% confirmed this expectation.

4.2.4.2.3 Heat Transfer-downstream Of Row (P)

The ejection geometry of location P as shown in fig.88 was designed to supply high blowing rate coolant, originated from induced reattachment considerations on a concave surface over a certain momentum flux level,[114]. At a very low \dot{m}_c/\dot{m}_∞ of 0.5 %, the jets issued from P were surely moved away from the surface at a local blowing rate of $m_p=1.42$, fig.130.a. A further increase up to $m_p=1.94$, improved the overall cooling efficiency by forcing the coolant layers through the concave wall. Although the coolant layers were pressed on the concave surface at far downstream of (P), the near ejection site turbulence augmentation was very much pronounced, above $m_p=2.70$, (fig.130.b). Moreover, the far downstream cooling efficiency was improved dramatically because of completely attached or even pressed coolant layers between the mainstream and the concave wall, above $m_p=2.70$. However the data taken at $\dot{m}_c/\dot{m}_\infty = 2.07 \%$ and 3.09% showed important local wall heating patterns very near the ejection site (P).

4.2.4.2.4 Heat Transfer-downstream Of Row (S)

Heat transfer downstream of the ejection site (S) was found to be sensitive to changes in local blowing rate m , only at near downstream locations, where turbulent mixing is enhanced by increased blowing rate values, for $\dot{m}_c/\dot{m}_\infty = 1.66 \%$. As shown in fig.130.b and fig.131.(a and b) a local wall heating

augmentation occurred along the first 30 hole diameters downstream of ejection was related to very high overall turbulent shear stress and turbulent kinetic energy levels near the wall". Another expected reason was "hot mainstream gas/wall" interaction due to some coolant jet penetration into the mainstream. Such a penetration is mainly the result of coolant ejection at increased blowing rates on a convex surface,[114]. The penetrating discrete jets were expected to reduce the overall film cooling coverage at just downstream of the ejection site,because of reduced lateral jet spread.In this zone,the wall has more chance to be influenced by the hot mainstream gas.After a certain distance when the abrupt changes in the hydrodynamics structure start to decay,an almost linear h/h_0 rise take place.

4.2.4.2.5 Influence Of Coolant Temperature -

In order to investigate the changes in the hydrodynamics structure of film cooling heat transfer,a number of tests were performed at a coolant temperature ratio of $T_c/T_{\infty}=0.7$,as shown in fig.130 and fig.131.a.However in an aero engine a typical coolant temperature level is in the order of half of the mainstream temperature level.Three data sets sampled at $\dot{m}_c/\dot{m}_{\infty}=3.2 \% \pm 0.1 \ %$,at 3 different coolant temperature levels are presented in fig.131.b.Significant reductions in overall wall heating pattern all around the blade were achieved when $T_c/T_{\infty}=0.51$,compared to $T_c/T_{\infty}=0.70$.Near downstream of the ejection site LS,the reductions were not very much pronounced because of over ejection behaviour of LM.Although the local blowing rates were kept constant,some local and qualitative heat transfer coefficient differences,originating from different coolant temperature levels were observed,fig.131.b. Near ejection site wall heating augmentations(S,LP and P),wall heating augmentations became less pronounced when the coolant temperature was reduced to $T_c/T_{\infty}=0.51$.This phenomenon was attributed to the fact that,the (momentum flux X density ratio) product is constant at different coolant temperatures,provided

that the blowing rate remains constant.

4.2.4.2.6 Heat Transfer In The Absence Of Stagnation Region Ejection -

Experiments were carried out by blocking only the leading edge site,(LM,LS and LP),artificially. At downstream of ejection site (S),almost no significant influence of the leading edge ejection through rows LM and LS was found.However,under nominal testing conditions,shown in fig.132,the over-ejecting row (LM) and its downstream row LS was only tripping the suction side boundary layer near the leading edge as mentioned in the previous paragraphs .Almost non-cooled h/h_{∞} values had been observed,between $s/\bar{C}=0.$ and $s/\bar{C}=0.2,$ even in the presence of coolant ejection.Film cooling heat transfer at downstream of (S) was not influenced from leading edge ejection through LM and LS.Film cooling heat transfer at downstream of row (P) showed strong dependency to leading edge ejection through row (LP) as shown in fig.132. h/h_{∞} values from the experiment without leading edge ejection were considerably higher than the case with leading edge ejection,showing the importance of coolant film superposition on the pressure side.

4.2.4.2.7 Influence Of Free Stream Turbulence Intensity On Film Cooling Heat Transfer -

The free stream turbulence intensity was varied from 0.8 to 5.2 % to see the influence of mainstream fluctuations on coolant film behaviour ,for $\dot{m}_c/\dot{m}_{\infty}=2.4+0.1$ %.No significant changes in the wall heating pattern were observed regardless of the location on the blade,at $T_c/T_{\infty}=0.40 +0.02$ in this TU_{∞} range,fig.133.Because of high injection hole diameter Re number of the present experiments,fully turbulent coolant jets were guarantied at all three of the injection sites.Observed

unchanged wall heating pattern at different T_{U_∞} levels is expected to be result of relatively large thickness of the newly originating, highly turbulent and dense film cooling layers, compared to the boundary layer without ejection. As a matter of fact, the boundary layer had not been significantly influenced from T_{U_∞} even without film cooling as it was shown in section 4.1.2, fig.101, due to its highly turbulent nature.

4.2.4.2.8 Influence Of Incidence On Film Cooling Heat Transfer, ($|s/\bar{c}| > 1/3$) -

Effect of incidence angle on film cooling heat transfer on the suction side and on the pressure side has been studied at 3 incidences (+10, 0, -10), for $T_c/T_{\infty} = 0.40$. paragraph, (fig.113). The h variations at $i=+10, 0$ and -10 are shown in fig.135,134 and 136. The free stream static pressure variations on the suction side and pressure side ejection sites were not significant as shown from finite area calculations of local Ma numbers. Therefore, changes in the local blowing rates of the sites S and P were not expected to be large enough to cause coolant layer modifications from the heat transfer point of view. The comparison of the film cooling data at various incidences is given in fig.137. The heat transfer deviations from $i=0$ case on the suction side ($|s/\bar{c}| > 1/5$) and on the pressure side ($|s/\bar{c}| > 1/3$) were found to be markedly influenced from the near downstream h behaviour of the showerhead region ejection on the leading edge.

4.2.5 CONCLUSIONS

In this chapter, experimental results of a test program on a film cooled gas turbine blade were discussed in detail. Wall heat transfer coefficients were evaluated under well simulated mainstream conditions in addition to a realistic coolant hole diameter to momentum thickness ratio.

When there is no coolant ejection; stagnation region wall heating rates were found to be comparable with cylinder in cross flow heat transfer correlations, even in the presence of leading edge coolant holes. Inlet Reynolds number (based on chord length) significantly influenced the overall level of heat transfer coefficient distribution. Boundary layer transition was a strict function of the incidence on both sides of the blade, especially at low free stream turbulence intensity level. The increases in free stream turbulence level only influenced the laminar and transitional boundary layers covering only a very small portion of the total surface area on this specific blade.

In the presence of coolant ejection; at a typical coolant to free stream temperature ratio of 0.5, very significant heat transfer coefficient reductions were observed. The importance of the local blowing rate were shown especially on the showerhead region of the blade. It has been shown that , a cooling row located near the stagnation point ejects at a very high blowing rate. This overerejection phenomenon definetely influences the downstream development of the boundary layer wall heating rates.

On the suction side ejection site, near hole heat transfer coefficient reductions were quite substantial. Even negative wall heat fluxes (from the wall to the mainstream) were observed in the first few hole diameters distance. Increasing blowing rates improved the overall protection of the wall. However, above $m=0.6$, a near ejection site augmentation in h occurred because of enhanced turbulent mixing.

On the pressure side;overall effectiveness of cooling was improved when m was increased from 1.42 to 1.94. This improvement has been attributed to the concave curvature of the pressure side. However, above $m=2.51$, the initial momentum of the jets created some penetration into the mainstream, resulting in h augmentation. This augmentation was significant only in the first 30 hole diameters region.

The conclusions about the simultaneous ejection;influence of incidence angle and free stream turbulence intensity on film cooling heat transfer are given in chapter-6.

CHAPTER 5

HEAT TRANSFER PREDICTIONS

In this chapter numerical predictions of heat transfer on the film cooled blade by convection and conduction are discussed. Forced convection heat transfer in the boundary layers of the turbine blade was computed using a two-dimensional, differential boundary layer code. Specific curvature models were implemented into the code in order to take into account strong wall curvature effects on outer layer mixing length. Numerical simulations in the presence of film cooling were also performed. A new approach to obtain mixing length augmentations just downstream of the ejection site was presented. The computations were compared with the measured data.

Heat conduction calculations were carried out by means of a method based on a finite element solution. The external boundary conditions were obtained from the measured data. A pipe flow and a channel flow heat transfer correlation were also employed in the determination of internal boundary conditions.

5.1 HEAT TRANSFER PREDICTIONS IN THE ABSENCE OF COOLANT EJECTION

5.1.1 DESCRIPTION OF THE NUMERICAL METHOD

In order to numerically predict the heat transfer rate evolution along the blade surface, the "STAN5" computer program, developed by CRAWFORD et al. [133] at Stanford University was selected. This program is based on the well known Spalding-Patankar approach [134] to compute boundary layer flows; it uses a finite difference technique to solve, through a streamwise space marching procedure, the simplified two dimensional boundary layer equations as applied to the flow developing along a flat wall, in a tube or in a jet. The mass, momentum and energy conservation equations solved for the boundary layer flows over a flat wall are as follows:

$$\frac{\partial(\rho U)}{\partial x} + \frac{\partial(\rho V)}{\partial y} = 0 \quad (60)$$

$$\rho U \frac{\partial U}{\partial x} + \rho V \frac{\partial U}{\partial y} = 0 \quad (61)$$

$$\rho U \frac{\partial I^*}{\partial x} + \rho V \frac{\partial I^*}{\partial y} = \frac{\partial}{\partial y} \left\{ \mu_{eff} \frac{\partial I^*}{\partial y} + \mu_{eff} (1 - \frac{1}{Pr_{eff}}) \frac{\partial}{\partial y} \left(\frac{U^2}{2} \right) \right\} \quad (62)$$

I^* , the total enthalpy, is defined by the following relation:

$$I^* = I + \frac{U^2}{2} \quad (63)$$

The effective viscosity μ_{eff} is defined as the sum of a molecular and a turbulent viscosity.

$$\mu_{\text{eff}} = \mu + \mu_t = \rho(\gamma + \epsilon_m) \quad (64)$$

where turbulent viscosity is given as follows

$$\mu_t = \rho \cdot \epsilon_m = \rho \cdot \frac{-\overline{u'v'}}{\frac{\partial U}{\partial y}} \quad (65)$$

The effective Prandtl number Pr_{eff} is defined as a function of the eddy viscosity ϵ_m , the molecular and the turbulent Prandtl numbers :

$$\text{Pr}_{\text{eff}} = \frac{1 + \frac{\epsilon_m}{\nu}}{\frac{1}{\text{Pr}} + \frac{\epsilon_m}{\nu} \cdot \frac{1}{\text{Pr}_t}} = \frac{\mu_{\text{eff}}}{\frac{k}{c} + \frac{(k)}{c_t}} \quad (66)$$

and

$$\text{Pr}_t = \frac{\epsilon_m}{\epsilon_H} \quad (67)$$

Using Prandtl's mixing length theory, the eddy diffusivity of momentum can be related to the mean velocity gradient through the following relation:

$$\epsilon_m = l^2 \cdot \left| \frac{\partial U}{\partial y} \right| \quad (68)$$

The specific mixing length and turbulent Prandtl number distributions across the boundary layer will be described in section 5.1.2.2. The basic concepts used to model the turbulent shear stresses and heat fluxes have been summarized in appendix-4. The system of partial differential equations has to satisfy the following boundary conditions:

$$U(x,0) = 0 \quad (69)$$

$$V(x,0) = 0 \quad (70)$$

$$\lim_{y \rightarrow \infty} U(x,y) = U_\infty \quad (71)$$

$$I^*(x,0) = I_W^* \quad (72)$$

$$\lim_{y \rightarrow \infty} I^*(x,y) = I_\infty^* \quad (73)$$

5.1.2 DETAILS OF THE REQUIRED PHYSICAL INPUTS

5.1.2.1 MIXING LENGTH VARIATION ACROSS THE BOUNDARY LAYER -

In the region immediately adjacent to the wall ($y^+ < 10$), the mixing length distribution is computed from the following equations:

$$\begin{aligned} y^+ &= y \cdot \frac{U_\tau}{v_0} \\ U_\tau &= \left(\frac{\tau_0}{\rho_0} \right)^{1/2} \\ D &= 1.0 - \exp(-\frac{y^+}{A^+}) \end{aligned} \quad (74)$$

$$l = k \cdot y \cdot D$$

where y^+ is the normal distance to the wall, k (0.41) the von Karman constant, D the van Driest damping factor and A^+ the effective viscous sublayer thickness. A^+ carries information about the influence of pressure gradient, surface roughness and transpiration:

$$A^+ = \frac{A_{fp}^+ (=25)}{a \cdot \left[v_0^+ + b \left(\frac{p^+}{1+cV_0^+} \right) \right] + 1.0} \quad (75)$$

$$V_0^+ = \frac{V_0}{U_\tau} \quad (76)$$

$$P^+ = \frac{v_0}{\rho_0 U_\tau^3} \cdot \frac{dp}{dx} \quad (77)$$

Eq. (75) was shown to be successful in predicting accelerating and decelerating flat, smooth wall flows by KAYS and MOFFAT,[138]. Since there is no transpiration in the present study, $V_G^+ = 0$. $a=7.10, b=4.25$ and $c=10.0$ are the suggested values,[133]. The variation of A with p is shown in appendix-5.

In the near wall region (outside the viscous region but inside the outer wake region) the mixing length is computed from the following equation:

$$l = k \cdot y \quad (y^+ > 10) \quad (78)$$

In the outer (wake) region, one uses the following relationship

$$l = \lambda \cdot \delta_{99} \quad (79)$$

$$\lambda = 0.085 \quad \left(\frac{y}{\delta} \geq \frac{\delta}{k} \right) \quad (80)$$

λ is generally described as an outer layer constant ($\lambda = 0.085$). However, there is evidence that λ is larger than 0.085 in boundary layers in which the momentum thickness Reynolds number is less than 5500. At low Reynolds numbers, the sublayer is expected to occupy a larger fraction of the boundary layer and the approximation of a constant mixing length over the remainder of the boundary layer is less valid. The following relation is proposed to model λ in the low $Re_{\bar{\theta}}$ region,KAYS,[142]. This relation represents an increased outer region activity in low $Re_{\bar{\theta}}$ flows:

$$\lambda = 0.250 \cdot Re_{\bar{\theta}}^{1/8} (1.0 - 67.5 \cdot F) \quad (81)$$

$$\lambda = 0.085 \quad \text{if} \quad \lambda < 0.085 \quad (82)$$

where F is the entrainment fraction which controls the boundary layer entrainment,

$$F = \frac{\bar{\rho}_0 \bar{V}_0}{\rho_\infty U_\infty} \quad (83)$$

where $\bar{\rho}_0 \bar{V}_0$ is entrained mass flux rate. A typical value of $F=0.005$ is suggested by ,CRAWFORD [133].

5.1.2.2 VARIABLE TURBULENT PRANDTL NUMBER -

Although the order of magnitude of the turbulent Prandtl number is about 1 for air,experimental data [133] suggest lower values in the wake region and higher values near the wall.The behaviour of this quantity in the ($y^+ < 10$)region is quite uncertain.However,because of the predominant molecular conduction mechanism governing this region,the computation is not affected significantly by this uncertainty.Because of smaller heat flux levels measured in the wake region,the effect of Pr_t uncertainties on the calculation is also limited.The present calculation method models the turbulent Prandtl number variation throughout the boundary layer by using a turbulent Peclet number:

$$Pr_t = \left[\frac{\alpha^2}{2} + \alpha \cdot c \cdot Pe_t - (c \cdot Pe_t)^2 \cdot \left[1.0 - \exp\left(-\frac{\alpha}{c \cdot Pe_t}\right) \right] \right]^{-1} \quad (84)$$

where $c=0.2$ and $\alpha = \left(\frac{1}{PRT} \right)^{1/2}$. PRT is the asymptotic value of Pr_t for large y^+ ,($PRT=0.86$).The turbulent Peclet number is the ratio of turbulent heat convection to molecular heat

diffusion, ($P_{t,t} = \frac{\epsilon_m}{v} Pr$). The variation of turbulent Prandtl number with molecular Prandtl number is shown in appendix-6, as a function of y^+ .

5.1.2.3 LAMINAR TO TURBULENT TRANSITION -

The onset of boundary layer transition is defined by imposing a certain value on the momentum thickness Reynolds number. A gradual transition process is enforced by modifying the effective thickness of the viscous sublayer (A^+). through the following empirical intermittency relationship :

$$A^+ = A^+ + (300 - A^+) \cdot \left[1.0 - \sin \frac{1.57}{Re_{tr}} \frac{(Re_{\theta} - Re_{tr})}{\theta} \right] \quad (85)$$

This equation provides a gradual increase of the turbulent viscosity in the near wall region between the location where the transition is triggered ($Re_{\theta} = Re_{tr}$) and a position where Re_{θ} is equal to two times the Re_{tr} value.

5.1.2.4 FLUID PROPERTIES (AIR) -

All the fluid properties e.g. density, absolute viscosity are treated as temperature dependent quantities and are described by the "KEENEN and KAYE Gas Tables", [135]. A maximum temperature of 2564 K ensures the covering of the whole range of gas turbine oriented calculations.

5.1.3 CALCULATIONS AND COMPARISON WITH THE MEASURED DATA ALONG THE SUCTION SIDE

The boundary layer developing along the suction side of the blade is affected by a strong favourable pressure gradient as well as by longitudinal convex curvature. These effects are discussed in appendix-1. In addition to them, the surface roughness created by the existence of the cooling holes located in the leading edge area is responsible for an early boundary layer transition (even without coolant ejection), as discussed in section 4.1.2. Due to cooling hole induced tripping activity, the total length at which the boundary layer stays laminar is very short, ($0 < s/\bar{C} < 0.10$) on the strongly curved near leading edge zone. Within the laminar part of a boundary layer, curvature effect on heat transfer are of second order compared to a turbulent boundary layer, VAN DYKE, [50]. For this reason, the curvature modifications in the present calculations were invoked only when the boundary layer was turbulent.

The prediction method described in section 5.1.1 has been modified to take the strong convex curvature effects into account, using the mixing length model developed by ADAMS and JOHNSTON, [52]. The outer layer mixing length model equation taking streamwise curvature effects into account is written as follows:

$$\frac{\lambda}{R} = 0.0025 \tanh(34.5 \frac{\delta}{R}) \quad (86)$$

This equation reduces the outer layer mixing length with decreasing radius of curvature and assumes a constant λ/R equal to 0.0025, for large δ/R . The model was evaluated on the basis of recent experimental data from a number of studies [147], [51] by ADAMS and JOHNSTON, [52]. The examination of their data revealed that significant $-p u' v'$ reductions exist in the outer region of a turbulent boundary layer growing on a highly convex wall. In the layers farthest from the wall, the reductions are largest. Even laminar shear stress levels may exist. Eq.(86) has the nature of simulating this significant phenomenon as a function of the

radius of curvature.

In the log region, the Adams and Johnston's model is based on the concepts developed by BRADSHAW [49]. The mixing length is related to a Richardson number defined as the ratio of Coriolis to viscous forces:

$$Ri = S_c(1+S_c) \quad (87)$$

$$S_c = \frac{2 \frac{U}{R}}{\frac{\partial U}{\partial y} - \frac{U}{R}} \quad (88)$$

Under the influence of curvature, the mixing length becomes equal to:

$$\frac{\lambda}{\lambda_0} = \frac{1}{1+\beta Ri} \quad (89)$$

where λ_0 is the flat wall mixing length and β is equal to 6.

The initial velocity and enthalpy boundary layer profiles, necessary to start the calculation were obtained from a cylinder in cross flow analytical solution and have been given in appendix-7. The format of the data is the same as the input data format described in STAN5,[133]. This solution also provides an evaluation of the stagnation region heat transfer. The nominal test conditions have been summarized in fig.94. The Mach number

evolution along the suction side has been presented in section 4.1 and shown in fig.92. The curvature distribution used in the computation of the mixing length is presented in fig.138.

The suction side predictions taking the longitudinal convex curvature effects into account provided the boundary layer thickness and outer layer mixing length distributions plotted in fig.138. Momentum thickness Reynolds numbers computed with curvature correction were always smaller than these obtained from the flat wall predictions, (fig.139). This might be explained by the smaller outer layer mixing length values used under the influence of curvature. A second source of modification in the outer layer mixing length was the adjustment of the outer layer constant taking into account low momentum thickness Reynolds number flow along the suction side, through eq.(81). Along the convex surface, reductions in outer layer constant depending upon the radius of curvature were shown in fig.138. Measured and computed Stanton number distributions are compared in fig.140. These results clearly demonstrate the overprediction observed without any curvature modification and assess the improvement obtained through a rather simple approach as the one presented herein. Variations of transitional Re_g from 20 .. 175 up to 200 did not affect significantly the downstream convective wall heating rate level. The data scatter observed between $s/\bar{C}=0.25$ and 0.35 has been attributed to the disturbing influence of the large cooling holes, (rows LM and LS, fig.115), although the coolant plenum chamber was filled with an insert. As a matter of fact, the boundary layer thickness near the suction side ejection site, was computed to be only about 0.2 mm, i.e. almost 5 times smaller than a cooling hole diameter.

5.1.4 CALCULATIONS AND COMPARISON WITH THE MEASURED DATA ALONG THE PRESSURE SIDE

A numerical prediction of the wall heating rates along the pressure side was attempted using the same method described in section 5.1.1, but with a mixing length model taking the concave curvature of this surface into account. The influence of streamwise curvature on convective heat transfer was described using the turbulent mixing length variation, suggested by BRADSHAW [49], and SO [54] . The mixing length variation is described by the following equation:

$$\frac{\lambda}{\lambda_0} = \left(1 - \frac{1}{2} \cdot \beta \cdot Ri\right)^{3/4} \quad (90)$$

$$\text{where } Ri = S_C(1+S_C) \quad \text{and,} \quad (91)$$

$$S_C = \frac{2 \frac{U}{R}}{\frac{\partial U}{\partial y}} \quad (92)$$

$$\text{and } \beta=6$$

The curvature distribution along the pressure surface is plotted in fig.141 and the free stream velocity distribution corresponding to the nominal flow conditions is given in fig.142 ,with the dashed line. The velocity peak downstream of the stagnation area ($s/\bar{C}=-0.08$) was found as the prime cause of the appearance of a zone with flow reversal in the viscous layers. The velocity profile was therefore artificially flattened in this region in order to avoid any trouble during the calculation process. As a matter of fact ,the present boundary layer method is not able to treat back flow regions.

The initial velocity and enthalpy profiles were evaluated downstream of stagnation line from a cylinder in crossflow analytical solution. These profiles have been described in appendix-8.

On the pressure side, the influence of the concave curvature on heat transfer is possibly enhanced by the existence of a leading edge flow. The vortices with streamwise vorticity vectors parallel to the mainflow direction are closely spaced near the stagnation point and the amount of heat transfer is proportional with the spacing of these vortices. This complicated flow structure is expected to breakdown when the curvature inversion occurs near downstream of the leading edge, $s/\bar{C} = -0.08$. After the breakdown, the boundary layer continues to develop on a highly concave surface. In the past it was a well documented fact that, the turbulent length scale was increased on concave surfaces, resulting in enhanced wall heating rates when compared to flat walls. The simultaneous influence of the leading edge flow and the strong concave curvature makes the prediction of heat transfer relatively difficult in comparison to the flow on a concave wall with no leading edge of the type of a turbine blade. Furthermore the influence of cooling row (non-ejecting) LP is expected to exist. The row was located just downstream of the stagnation point, ($s/\bar{C} = -0.026$) in a region where the flow strongly accelerates around the leading edge radius, (fig.108).

Because of the highly accelerating nature of the mainstream flow after $s/\bar{C} = -0.2$, (fig.142), a laminarization process depending upon the pressure gradient parameter $K = \frac{V}{U^2} \frac{dU_w}{dx}$ is expected. This process reduces wall heating rates in contrary to the enhancements resulting from the interaction of the leading edge flow and the concave curvature of the pressure side.

Stanton number predictions taking the concave curvature into account are shown in fig.143. Since a precise determination of the onset of transition was difficult, a set of predictions in a range of transitional Re_{θ} from 10 to 200 were evaluated and compared with the measured data. The computed momentum thickness Reynold number distributions shown in fig.144 reveal a low Re_{θ} distribution on the pressure side when compared to the suction side variation. Re_{θ} has a value around 100 at the curvature inversion point. The best agreement with the measured data was

found when the transition was triggered in a range from $Re_{\bar{G}} = 10$ to $Re_{\bar{G}} = 100$. The predictions performed at $Re_{\bar{G}} = 150, 175$ and 200 resulted in greater discrepancies in comparison to the measured data; due to enlarged laminar zones in the computations. Heat transfer predictions, far downstream of the leading edge, (when $|s/\bar{c}| > 0.7$) showed good quantitative agreement with the measured data, regardless of the onset of transition point, (or $Re_{\bar{G}}$). The predictions with and without curvature correction were compared in fig. 145. The correction generates some heat transfer augmentation compared to the flat wall prediction. However, even with the curvature correction, the discrepancy between the data and the computation is quite large especially in the first half of the pressure surface. Probably a more complex flow structure is existing in this zone than the flow numerically simulated by the differential equations described in section 5.1.1.

5.2 NUMERICAL SIMULATION OF FILM COOLING HEAT TRANSFER

5.2.1 SIMULATIONS ON THE SUCTION SIDE AND COMPARISONS WITH THE MEASURED DATA

In this section, a numerical simulation of discrete hole film cooling process on the suction side of the turbine blade will be attempted. After the description of a semi-empirical modelling approach, dealing with the determination of the mixing length and coolant distributions throughout the boundary layer; the results of the numerical simulations will be compared with the measured data generated under well simulated mainstream and coolant flow conditions. A special emphasis is given to develop a predictive capability when the coolant layer thickness is much larger than the approaching mainstream boundary layer. This is the actual case in an high temperature aeroengine.

A discrete hole coolant ejection process is typically characterized by a three dimensional however spanwise periodical behaviour just downstream of the ejection holes. Due to this periodicity, two dimensional boundary layer codes were most of the time selected to compute film cooling heat transfer coefficients and validated within a given range of assumptions and modifications. Although, a number of three dimensional Navier-Stokes solvers applied to film cooling applications, BERGELES et al. [137, 139] are available, the computer core requirements and very long running times limit their extensive use. Up to now, most computer codes dealing with film cooling were based on the development of empirical constants evaluated from low speed film cooling experiments, CRAWFORD, CHOE, [133, 140].

The boundary layers are subject to strong free stream acceleration rates and streamwise curvature effects along a turbine blade. Additionally, the existence of coolant layers which are easily a few times thicker than the approaching boundary layer increases the complexity of the problem. The momentum and energy equations without any ejection were solved up to the ejection site using the numerical method explained in section 5.1.1. When a film cooling ejection site is encountered, the velocity and total energy profiles should be modified in such a way that momentum and energy conservation laws are satisfied even with coolant ejection. A typical control volume chosen in a region where a circular coolant jet interacts with the approaching boundary layer is shown in fig.146. The upper and lower limits of the control volume are described by the streamlines Ψ and $\Psi + \Delta\Psi$. The incoming mass flow rate per unit depth to this control volume is \dot{m}_{old} , the mean incoming stream tube velocity is \bar{U}_{old} and the mean incoming total enthalpy is \bar{T}_{old} , before any coolant/mainstream interaction. These are known values from the upstream computations with the method described in section 5.1.1. A certain amount of coolant mass $\delta\dot{m}$ is shed into this control volume, (fig.146), before the jet enters to the upper stream tube (above $\Psi + \Delta\Psi$). During the coolant mass shedding, the momentum and energy conservation laws in the control volume, (fig.146) describe the new values of the mean stream tube velocity and the total energy after coolant/mainstream interaction.

$$\dot{m}_{new} = \dot{m}_{old} + \delta\dot{m}$$

$$(\dot{m}_{old} + \delta\dot{m}) \cdot \bar{U}_{new} = \dot{m}_{old} \cdot \bar{U}_{old} + \delta\dot{m} \cdot \bar{U}_J \cdot \cos\alpha$$

$$\delta\dot{m}(\bar{U}_{new} - \bar{U}_J \cos\alpha) = C_D \cdot \frac{1}{2} \cdot \rho \cdot A_J (\bar{U}_{old}^2) \quad (92a)$$

where,

$$A_j = d \cdot \delta y$$

$$\dot{m}_{old} = \bar{U}_{old} \cdot \rho \cdot \delta y \cdot P \quad (92b)$$

δy is the distance between the two stream tubes and P is the spanwise distance between the axis of two adjacent cooling holes. After elimination of the drag coefficient term C_d , the final forms of momentum and energy equations are as follows,

$$\frac{\bar{U}_{new}}{\bar{U}_{old}} = \frac{1}{(1 + \frac{\delta \dot{m}}{\dot{m}_{old}})} \left(1 + \frac{\delta \dot{m}}{\dot{m}_{old}} \cdot \frac{\bar{U}_j \cos \alpha}{\bar{U}_{old}} \right) \quad (93)$$

$$\frac{T_{new}}{T_{old}} = \frac{1 + \frac{\delta \dot{m}}{\dot{m}_{old}} \cdot \frac{T_j}{\bar{U}_{old}}}{1 + \frac{\delta \dot{m}}{\dot{m}_{old}}} \quad (94)$$

where U_j and T_j are the mean velocity and total enthalpy of the coolant jet at the exit of a coolant hole. Using eq.(93) and (94), the change in the boundary layer structure (\bar{U}_{new} and T_{new}) can be computed in terms of the mass shed ratio $\bar{U}_j \cos \alpha$, \bar{U}_{old} and T_{old} . However the eqs.(93 and 94) describe only the changes in the mean velocity and total enthalpy field. Since film cooling process disturbs the flow near downstream of the ejection site, the Reynolds stresses in this region are significantly altered. The state of the Reynolds stresses in the presence of film cooling was taken into account by means of a mixing length augmentation over a classical Prandtl's mixing length. The specific approach developed for the determination of the augmented mixing lengths with film cooling is described in

the following paragraphs.

In a film cooling configuration the spanwise averaged mixing length ,near downstream of the ejection holes is mainly controlled by the blowing rate, the boundary layer thickness to hole diameter ratio and the ejection angle. These three parameters also control the distribution of coolant in the approaching boundary layer and the penetration depth of the ejected fluid. When the coolant fluid remains in the wall region along a flat wall,a mixing length distribution was suggested by CHOE,CRAWFORD,[140,133], as it is shown in fig.151.a.However,when the penetration depth is of the same order of magnitude as the approaching boundary layer thickness, the film cooling effects on the mixing length are expected to extend to the outer region of the boundary layer,(fig.151.b).

The ejection hole diameter \bar{d} to momentum thickness $\bar{\theta}$ ratio has been one of the basic simulation parameters in the area of discrete hole film cooling.In the present situation, the $\bar{d}/\bar{\theta}$ ratio was computed to be 43 whereas the \bar{d}/δ ratio was calculated to be 4.75,(Fig.149), these values are quite similar to those observed in actual engines.Looking at the geometry used in [133], $\bar{d}/\bar{\theta}$ and \bar{d}/δ values respectively equal to 10 and 1 were observed, fig.149. The coolant layers along an actual blade are expected either to occupy a major portion of the boundary layer or to penetrate into the mainstream and reattach farther downstream to the wall,depending upon the blowing rate level. Therefore the blowing rate dependency of the augmented mixing length \bar{x}_{max} and mass shed ratio $\delta m/m_{id}$ the two most important parameters modelling the ejected flow are strongly needed.

In order to establish the relationship between mass shed ratio and blowing rate, the coolant distribution was assumed in such a way that the total penetration depth did not exceed the approaching boundary layer thickness just downstream of the coolant row. The coolant mass shed ratio was altered from a

reasonably low value to a value which gives a penetration depth of $\overline{PD}/\delta = 0.8$, for a fixed blowing rate. The resulting $\delta m/m_{\text{add}}$ values are shown in fig.148 . Although this approach did not simulate the most accurate coolant distribution across the boundary layer, it was expected to simulate the overall hydrodynamic nature of the coolant layers downstream of the ejection site, where the boundary layer thickness suddenly increases due to the added coolant flow. This approach adds at least the correct amount of coolant mass and momentum to the viscous flow field. The numerically simulated boundary layer thickness variation downstream of the suction side ejection site is given in fig.149, for $m=0.0, 0.37$ and 0.61 , ($T_c/T_{\text{ext}} = 0.5$). An example of a mesh evolution in the streamwise direction is shown in fig.150. The influence of the cooling provided by a double row of holes on the mesh growth is also shown in the figure.

The augmented mixing length $\bar{\lambda}_{\text{max}}$ representing the maximum disturbance to the boundary layer because of ejection, has been considered in the present study, as an averaged quantity, responsible for the gross mixing length modifications in the viscous layers. Moreover, the wall heat flux augmentation due to the "mainstream gas/wall" interaction was expected to be simulated using this same $\bar{\lambda}_{\text{max}}$ parameter. Especially, for high blowing rates above 0.7, the hot mainstream gases were expected to move around the discrete coolant jets because of their higher coolant jet momentum flux levels resulting in jet penetration. This phenomenon was especially significant just downstream of an ejection site where three dimensional effects were still dominant. The interaction of the hot gases with the wall within this highly disturbed three dimensional flow field locally increases the wall heating rates. Such increases were also related to the spanwise averaged (near wall) mean velocity gradient ($\frac{\partial U}{\partial y}$) behaviour in the boundary layer at high blowing rates. The experimental data showing the low and high m behaviour were discussed in section 4.2.2 and in fig.115 . As shown in the figures, while the low blowing rate data were indicating a very smooth downstream increase of h/h_0 ; the high blowing rate data showed first a sudden enhancement in h/h_0 and a continuous

downstream increase followed. The exponentially decaying ℓ_{\max} variation used by CRAWFORD et al., [133] was found to be satisfactory to simulate a mixing length augmentation which was spread over the entire boundary layer, with a penetration depth located at 80 % of the approaching boundary layer thickness, fig. 151.b. F is the exponential mixing length decaying function. The mixing length augmentation variation due to coolant ejection is modelled as follows:

$$\ell_{\max} = \bar{\ell}_{\max} \cdot F \quad (95)$$

$$F = 2.718 \left(\frac{y}{\overline{PD}} \right)^2 \left[\exp - \left(\frac{y}{\overline{PD}} \right)^2 \right] \quad (96)$$

$$\overline{PD} = 0.8\delta \quad (97)$$

The effective augmented mixing length distribution downstream of an ejection location is computed using the following equation developed by YAVUZKURT,[141],

$$\ell_{\text{eff}} = \bar{\ell}_{\max} \cdot \exp \left[- \left(\frac{x}{2\delta} \right) \right] \quad (98)$$

where x is the streamwise distance measured from the ejection site. Since ℓ_{eff} was decayed exponentially in the streamwise direction with a decaying constant of two boundary layer thicknesses, the influence of coolant ejection on the mixing length disappears farther away from the ejection site. Finally, the mixing length including the curvature effects and film ejection can be written as,

$$\ell = \begin{pmatrix} ky \\ \lambda\delta \end{pmatrix} + \ell_{\text{eff}} \cdot F \quad (99)$$

The mixing length is also damped in the near wall region ($y^+ < 10$), using eq.(74). A quantitative determination of the augmented mixing length $\bar{\ell}_{\max}$ has to be performed through direct measurements of $u'v'$ in film cooled boundary layers. However, this kind of measurements in a short duration facility is extremely difficult to perform across a very thin boundary layer of the thickness of about 1/4 mm.

In this study, a semi-empirical determination of $\bar{\ell}_{\max}$ was attempted from measured wall heat flux, downstream of the suction side ejection site.

For this purpose, two sets of measured non-dimensional heat transfer coefficient (h/h_0) distributions in downstream direction were taken as modelling data sets. The data measured at $m=0.44$ and at 0.69 with a coolant at the wall temperature level were simulated using the computational model described above. At this stage, the aim was to develop the unknown $\bar{\ell}_{\max}$ values for a given range of m . For each of the two blowing rates, $\bar{\ell}_{\max}$ has been varied until a satisfactory h/h_0 versus s/\bar{C} simulation was obtained. The two $\bar{\ell}_{\max}$ values (at both limits of the blowing rate range) providing the best simulation of the h/h_0 data sets were accepted as the modelling values as they are indicated in fig.152. The straight line "A" drawn between the two modelling $\bar{\ell}_{\max}$ was used for further predictions.

Nine simulations of h/h_0 in a blowing rate range from 0.40 to 0.73 were obtained at three different coolant temperature levels ($T_c/T_{\infty}=0.72 \dots 0.64 \dots 0.55$), as shown in figs.153 and 154. The $l..$ values used in simulations were shown in fig.152. Even at different coolant temperature levels, the best predicting $\bar{\ell}_{\max}$ values were found to be very close to the modelling line "A". The comparison of the present measured h/h_0 data with the numerical simulations using the modelling line "A" showed good agreement. A successful simulation of the essential features of discrete hole film cooling process both near and far downstream of the ejection site was obtained, in the blowing rate range from 0.40 to 0.73 .

For the blowing rates greater than 0.76, the numerical simulations of h/h_0 were found to underpredict the measured data, when the augmented mixing lengths were evaluated on line "A". The discrepancies were especially significant in the first 30 hole diameters downstream of the ejection site, where the flow has a definite three dimensional pattern. It was concluded from this fact that, the numerically simulated near hole hydrodynamic flow disturbances represented by the augmented mixing length line "A" were not substantial enough when $m > 0.76$. Hence, a second modelling line "B" was established using the same approach as described for the low blowing rate range, (line "A").

The six simulations of h/h_0 were compared with the measured film cooling data in the high blowing rate range, as they are shown in fig.155 and 156. The simulated h/h_0 values were typically exhibiting a heat transfer excess region in the first ~ 10 hole diameters downstream of the ejection site. However, farther downstream of this region, the simulations agreed very well with the measured data. The simulations of the near ejection site heat transfer with film cooling were observed to be controlled by the augmented mixing length. The influence of varying \bar{t}_{\max} on near hole h/h_0 simulations is given in fig.155.a and c with dashed lines. However far downstream influence is not quite significant. A comparison of the augmented mixing lengths developed in this study with CRAWFORD et al.'s,[133] values obtained for slant-angled ejection on a flat wall is shown in fig.152.b. The experimentally evaluated line "A" and "B" of the present study show quite higher values than CRAWFORD et al.'s , [133]. model. The high turbulence augmentation levels of the present study were attributed to the hole diameter to momentum thickness ratio which, in the present model is about 5 times higher compared to [133]'s flat wall model.

5.3 FINITE ELEMENT ANALYSIS OF THERMAL CONDUCTION IN THE FILM COOLED TURBINE BLADE

An experimental and analytical investigation of convection heat transfer in film cooled boundary layers of a gas turbine blade were presented in chapter 4 and chapter 5. The investigations were only limited to convection heat transfer on the external sides of the blade. However, an accurate thermal analysis of a film cooled blade is only possible by finding the local internal conduction heat flow patterns using the external convection information in addition to the internal convection data for the specific blade geometry. The geometry of film cooled blades are most of the time very complex. In order to solve the heat conduction equation for such geometrical shapes, a numerical method based on a finite element analysis were implemented. The basic principles of this numerical approach are given by ZIENKIEWCZ, in [144].

5.3.1 DISCRETIZATION OF THE BLADE AND BOUNDARY CONDITIONS

The finite element discretization of the blade is shown in fig.161. Since this is a two dimensional calculation method, the three dimensionality of the circular coolant hole was represented by a "slot" type geometry. The "near film cooling hole" discretization is also shown in the figure. A typical finite element size was about two percent of the blade chord length ,when an almost square element was used,in the regions where a high computational resolution was required. The elements chosen were second order, curved and isoparametric finite elements. Near the sharp corners of the coolant passages and near the trailing edge, triangular elements were employed in addition to the regular rectangular elements. The specific discretization for the film cooled case is also shown in fig.161.

The external convective heat transfer coefficients in the absence of film cooling were evaluated from the experiments as discussed in section 4.1.2. Fig. 162 shows the external heat transfer coefficients used in the analysis both in the absence and presence of film cooling. For the case of film cooling, the coolant to free stream temperature ratio was 0.50 at a blowing rate of unity.

The convective boundary conditions around the film cooling holes were determined from "fully developed turbulent pipe flow" correlation given by DITTUS and BOELTER,[146].

$$h = \frac{\bar{k}}{d} \cdot 0.023 \cdot Re^{0.8} \cdot Pr^{0.4} \quad (99a)$$

However, the actual cooling geometry used in the computations is somewhat different than a flow in a pipe having a uniform circular cross section in longitudinal direction of the pipe. There is a conically shaped section near the exit of the cooling hole, as shown in fig. 161. This conical shape was taken into account by introducing an average cooling hole diameter of $d=0.95$ mm. The heat transfer coefficients in the internal cooling passages were evaluated from a correlation as discussed by AINSWORTH and JONES,[145]. Reynolds numbers in internal coolant passages were calculated using the hydraulic diameter of each of the passages. The heat transfer correlation is as follows,

$$h = (\rho_c U_c) \cdot C_p \cdot \exp \left[-3.796 - 0.205 \cdot \ln Re - 0.505 \cdot \ln Pr - 0.0225 \cdot (\ln Pr)^2 \right] \quad (99b)$$

5.3.2 THE METHOD OF ANALYSIS

The steady two dimensional temperature distribution in a film cooled gas turbine blade may be calculated solving the partial differential equation given in equation (100).

$$\nabla^2 T(x,y) = 0 \quad (100)$$

The associated boundary condition of the heat conduction problem is as follows,

$$-k \left[\frac{\partial T}{\partial x} n_x + \frac{\partial T}{\partial y} n_y \right] = h \left[T_{0\infty} - T(x,y) \right] \quad (101)$$

where k is the thermal conductivity of the solid material and h is the convective heat transfer coefficient along the boundaries. Fig. 158 shows a solution domain and the boundaries for the formulation. Equation (100) is solved using a finite element technique which is based on Euler theorem of variational calculus. The solution of equation (100) satisfying the boundary condition given in equation (101) is identical to minimizing an integral statement given in equation (102) over the whole domain.

$$I_F = \iint_S \frac{1}{2} k \left[\left(\frac{\partial T}{\partial x} \right)^2 + \left(\frac{\partial T}{\partial y} \right)^2 \right] \cdot dx \cdot dy + \int_L \frac{1}{2} h(T - T_{0\infty})^2 dL \quad (102)$$

where $dS=dx \cdot dy$ is an infinitesimal area in the domain and dL is an infinitesimal length over the curved boundary of the domain. The two dimensional domain is discretized using isoparametric finite elements on which the integral statement

I_F is minimized. The final result of this minimization procedure is a set of linear algebraic equations and its solution leads to the temperature distribution in the domain of interest. The further details of the analysis are given in the following paragraphs.

Each of the elements shown in fig.159 is transformed into a standard square and then the integral statement given in equation (150) is minimized over this standard square. A typical finite element used in the analysis has eight nodal points and the shape functions at each nodal point of the element are shown in fig.160. The transformation from global coordinates to local coordinates is as follows.

$$\begin{aligned} x &= x(\epsilon, n) \\ y &= y(\epsilon, n) \end{aligned} \quad (103)$$

and the determinant of the jacobian matrix is given as,

$$\det [J] = \begin{vmatrix} \frac{dx}{d\epsilon} & \frac{dy}{d\epsilon} \\ \frac{dx}{dn} & \frac{dy}{dn} \end{vmatrix} \quad (104)$$

For a one to one transformation, this determinant is always greater than zero. The temperature field in the body may be written down in terms of the second order shape functions given in fig.160.

$$T = T_1 N_1 + T_2 N_2 + \dots + T_8 N_8 = \sum_{i=1}^{\infty} T_i N_i \quad (105)$$

Also, the coordinate transformation given in equation (103) may be expressed in terms of the shape functions,

$$x = x(\epsilon, \eta) = x_1 N_1 + x_2 N_2 + \dots + x_8 N_8 = \sum_{i=1}^{\infty} x_i N_i \quad (106)$$

$$y = y(\epsilon, \eta) = y_1 N_1 + y_2 N_2 + \dots + y_8 N_8 = \sum_{i=1}^{\infty} y_i N_i$$

Since the temperature field given in equation (105) and the geometry in equation (106) are approximated using the same kind of second order shape functions which are given in fig.160, the finite elements used are called isoparametric finite elements. For a given element, the form of the temperature field in global coordinates is as follows,

$$T = Ax^2 + By^2 + Cxy + Dx + Ey + F \quad (107)$$

The integral statement given in equation (102) is minimized over the whole domain, element by element. The minimization is done with respect to the theory given in [144] and the result is as follows.

$$\iint_S k [B] [B^T] \cdot dx dy + \int_L h [n] [n^T] \cdot dL = \int_L h \cdot T_{0\infty} [n] \cdot dL \quad (108)$$

$$[n] = \begin{bmatrix} N_1 \\ N_2 \\ \vdots \\ \vdots \\ N_8 \end{bmatrix} \quad (109a)$$

$$[\tilde{t}] = \begin{bmatrix} T_1 \\ T_2 \\ \vdots \\ \vdots \\ T_8 \end{bmatrix} \quad (109b)$$

$$\tilde{T} = [\tilde{n}^T] [\tilde{t}] \quad (110)$$

The temperature gradient in global coordinates may be written as,

$$\begin{bmatrix} \frac{\partial T}{\partial x} \\ \frac{\partial T}{\partial y} \end{bmatrix} = \begin{bmatrix} \frac{\partial N_1}{\partial x} & \frac{\partial N_2}{\partial x} & \dots & \frac{\partial N_8}{\partial x} \\ \frac{\partial N_1}{\partial y} & \frac{\partial N_2}{\partial y} & \dots & \frac{\partial N_8}{\partial y} \end{bmatrix} \cdot \begin{bmatrix} T_1 \\ T_2 \\ \vdots \\ \vdots \\ T_8 \end{bmatrix} \quad (111)$$

defining a new matrix for shape function derivatives,

$$[\tilde{B}^T] = \begin{bmatrix} \frac{\partial N_1}{\partial x} & \frac{\partial N_2}{\partial x} & \dots & \frac{\partial N_8}{\partial x} \\ \frac{\partial N_1}{\partial y} & \frac{\partial N_2}{\partial y} & \dots & \frac{\partial N_8}{\partial y} \end{bmatrix} \quad (112)$$

substituting equation (112) into (111),

$$\begin{bmatrix} \frac{\partial T}{\partial x} \\ \frac{\partial T}{\partial y} \end{bmatrix} = [B^T] \cdot \begin{bmatrix} t \\ \sim \end{bmatrix} \quad (113)$$

The surface integrals and line integrals given in equation (156) have to be calculated in local coordinates. Using the chain rule of differentiation, the derivatives in local coordinates,

$$\begin{aligned} \frac{\partial N_i}{\partial \epsilon} &= \frac{\partial N_i}{\partial x} \cdot \frac{\partial x}{\partial \epsilon} + \frac{\partial N_i}{\partial y} \cdot \frac{\partial y}{\partial \epsilon} \\ \frac{\partial N_i}{\partial \eta} &= \frac{\partial N_i}{\partial x} \cdot \frac{\partial x}{\partial \eta} + \frac{\partial N_i}{\partial y} \cdot \frac{\partial y}{\partial \eta} \end{aligned} \quad (114)$$

in matrix form,

$$\begin{bmatrix} \frac{\partial N_i}{\partial \epsilon} \\ \frac{\partial N_i}{\partial \eta} \end{bmatrix} = \begin{bmatrix} \frac{\partial x}{\partial \epsilon} & \frac{\partial y}{\partial \epsilon} \\ \frac{\partial x}{\partial \eta} & \frac{\partial y}{\partial \eta} \end{bmatrix} \cdot \begin{bmatrix} \frac{\partial N_i}{\partial x} \\ \frac{\partial N_i}{\partial y} \end{bmatrix} \approx [J] \cdot \begin{bmatrix} \frac{\partial N_i}{\partial x} \\ \frac{\partial N_i}{\partial y} \end{bmatrix} \quad (115)$$

Inverting equation (115),

$$\begin{pmatrix} \frac{\partial N_i}{\partial x} \\ \frac{\partial N_i}{\partial y} \end{pmatrix} = [J]^{-1} \cdot \begin{pmatrix} \frac{\partial N_i}{\partial \epsilon} \\ \frac{\partial N_i}{\partial n} \end{pmatrix} \quad (116)$$

The infinitesimal surface element dS in global coordinates may also be expressed in terms of the local coordinates and the determinant of the jacobian matrix of the transformation.

$$dS = dx \cdot dy = \det [J] \cdot d\epsilon \cdot dn \quad (117)$$

The surface integral in equation (108) may be numerically evaluated using the equations from (109.a) to (117) for a given element. If the element has a convective boundary condition, the line integrals may be calculated along the convective nodal points using Lagrange interpolation functions. Evaluating the surface integral, the line integral and superposing them onto a global matrix, results in an equation,

$$\begin{matrix} [A] \cdot [t] & [R] \\ \approx & \sim & \sim \\ N \times N & N & N \end{matrix} \quad (118)$$

where N is the total number of nodal points in the domain. $[R]$ carries information about the convective boundaries. $[A]$ is the global matrix and includes both nodal point conductive contributions and convective boundary contributions. For this specific problem, the global matrix is symmetric and banded. Equation (118) is a system of linear algebraic equations and there is no specific difficulty in solving this system for $[t]$, using Gauss elimination method.

5.3.3 COMPUTATIONAL RESULTS

5.3.3.1 ONLY INTERNAL CONVECTION COOLING -

The first computation shown in fig.163 was simulating an "only internal convection cooling" case. No film cooling was applied on the gas side of the blade. Coolant to free stream mass weight ratio was about 3.5 %. The total coolant mass flow rate was distributed in internal coolant passages as follows:

channel	coolant distribution
L	25 %
S	25 %
P	20 %
T	30 %

The coolant in each passage was assumed to be entering through the blade root and discharged into the mainstream from the tip. The heat conduction analysis described in section 5.3.1 resulted in the local temperature map shown in fig.163 . Although this configuration is not the closest case to an actual film cooled blade, it was considered to be a baseline case to compare the temperature field in the presence and absence of film cooling. The internal heat transfer coefficients from the highest to the lowest level were in the order of passage "L", "T", "S" and "P". The magnitude of the internal heat transfer coefficient in each passage, the interaction of the two neighbouring passages, gas side heat transfer coefficient without film cooling, the specific blade geometry, gas total temperature and the thermal conductivity of the blade material were the determining factors in evaluating the temperature field given in fig.163.

Although the highest external heat loads were observed near the leading edge zone,(fig.162),the internal cooling activity of channel "L" and to a less extend the cooling from the neighbouring channel "S" provided an average wall to free stream temperature ratio of (1150/1650=0.69).

The trailing edge of the blade was observed to be the hottest part.In spite of the fact that,a trailing edge cooling passage (T) was located; the slender geometry and high gas side heat loads resulted in quite high wall temperatures compared to the leading edge area.In practice,more specific trailing edge cooling schemes are used to cool down this region.

The flow of thermal energy by molecular conduction process can be simulated by computing local heat flux vectors.Once the temperature field is known,the temperature gradients and eventually the heat fluxes may be evaluated through equation (111).The resulting heat flux vectors from this analysis are given in fig.164.Although quite reduced wall temperatures were found,the highest wall heat flux levels were observed near the leading edge channel.Due to the effective heat removal through channel "L",the flow of heat is quite induced in the direction from the mainstream to the coolant channel.

We define the solid walls in between the coolant passages as "bridges". The bridges play a significant role in the conduction process as shown in fig.164.A part of the heat flow from the gas side was transferred into the internal channels from both ends of the bridge.The heat flux vectors on bridge-1 was found to meet at the mid section.Quite reduced heat flux patterns and almost minimal bridge temperatures were observed at this area.

The external heat loads evaluated qualitatively from the computed local heat flux pattern were shown as dashed arrows. The heat flux vectors were almost normal to the inner and outer skin of the blade except the bridges,when the heat removal by means of the coolant channel was quite effective (L,S,T).When

the internal cooling effort was not significant (channel P), the heat flux vectors became more tangential to the inner skin of the blade. Therefore with the help of the heat flux components, almost parallel to the external skin of the blade shell, a part of the heat is transferred to the neighbouring coolant channels, (vectors X,Y,Z,T,U,W,R,S), fig.164. The curved corners close to the bridges were observed to be highly thermally loaded. Very large temperature gradients and magnitudes of heat flux were found.

5.3.3.2 FILM COOLING RESULTS -

When film cooling is applied on the suction side, the computed temperature profiles are shown in fig.165. The film cooling through a double row of discrete holes was assumed to start at $s/\bar{C}=0.235$. In this phase of the analysis, the influence of the convective boundaries surrounding the discrete cooling holes was ignored on the conduction field. The analysis was performed with external film cooling boundary conditions downstream of the ejection site on the suction side. The remarkable influence of film cooling on the downstream temperature evaluation was observed, fig.165. The temperature field in bridge-1 was very similar to the case without film cooling. However, bridge-2 was influenced from film cooling because of the close distance to the film ejection site. The near leading edge temperature pattern was not significantly altered because of the film cooled boundary conditions.

Because of the very low (even negative, fig.162) heat transfer coefficients just downstream of the ejection site ($s/\bar{C}=0.235$), the heat flux vectors showed a very specific variation compared to the only internal cooling case, CASE-1. Heat was transferred from the wall to the free stream (zone YY), in the first 6-7 hole diameters region. The heat transfer coefficient h in this study was defined as follows:

$$h = \frac{\dot{q}_s}{(T_{0\infty} - T_w)} \quad (119)$$

Since $(T_{0\infty} - T_w)$ is always positive, a negative heat flux can only be represented using a negative heat transfer coefficient as it was indicated in fig.162. In the vicinity of the wall, the heat may be transferred from the wall to the adjacent coolant layer because of very low coolant temperatures where the film temperature is still very close to the coolant temperature in the plenum chamber. If one follows the wall heat flux component normal to the wall from point 1 to 4 in fig.166, non-negligible heat flux levels from the wall to the film(between 1 and 2) are encountered. At about point 2 almost an adiabatic zone is observed. After point 2, the heat flow is from the film to the wall.

5.3.3.3 THE INFLUENCE OF THE COOLING HOLE -

In figs.165 and 166, the conduction pattern as a result of film cooling was indicated. However, the influence of the cooling hole induced heat transfer by convection was not included. The result of the computation taking this influence into account is shown in figs.167 and 168. A very strong deviation from the case without cooling hole influence, but with film cooling,(CASE-2,figs.C and D) were observed at near upstream and downstream of the cooling hole. A very steep temperature gradient occurring in the first 10 hole diameters upstream of the hole was found only as a result of the existence of the cooling hole. Downstream of the cooling hole, the wall temperatures were considerably lower than the temperature given for CASE-2. The surface temperature variation on the suction side for only internal cooling,CASE-1,film cooling without cooling hole

influence and film cooling with the cooling hole effects included,CASE-3 are compared in fig.169.A significant contribution of the cooling hole both upstream and downstream of the hole is apparent.This contribution almost disappears at $s/c=0.70$ (~ bridge-3) in downstream direction.The cooling hole induced conduction does not affect the temperature field near the leading edge,up to $s/c=0.1$ on the suction side.Further downstream ,the significance of the hole continuously increases up to the hole location.

Looking at fig.168,a very strong heat sink effect of the hole is observed.Most of the heat flux vectors tend to direct themselves through the cooling hole . Very high levels of heat flux exist upstream of the hole.Near downstream of the hole,in accordance with CASE-2,fig.166;first a wall to coolant film heat transfer zone,an almost adiabatic zone and a film to wall heat transfer region was observed.Downstream of the film cooling location,especially in between the outer and inner skin of the blade,the main heat conduction tendency was the flow of heat from downstream to upstream in a direction almost parallel to the external contour of the blade.The bridges also slightly modified the heat flux field.

CHAPTER 6

CONCLUSIONS

An experimental and theoretical study of film cooling on a HP turbine blade has been carried out under realistic gas turbine conditions. A heat transfer instrumented blade has been manufactured and used in the generation of data sets with and without film cooling. The theoretical study consists of the prediction of film cooling heat transfer in the boundary layers of the blade and the computation of the heat conduction field in the solid walls of the blade. The main conclusions of the study are given in the following paragraphs.

6.1 HEAT TRANSFER IN THE ABSENCE OF COOLANT EJECTION

Measured stagnation region heat transfer data sets on the rotor blade were compared with various cylinder in cross flow correlations. Enhancement in h_o due to increases in TU_∞ , was found to be compatible with the correlations, provided that inlet Re_∞ number remains constant. However, the present leading edge consists of 3 rows of cooling holes as roughness elements even

without ejection compared to the smooth cylinder case of the correlations.

At zero incidence, the stagnation point was at $s/\bar{C} = -0.019$, just downstream of the mid row of holes on the leading edge. Hence, the suction side boundary layer was tripped by rows LM and LS. The tripping action promoted a quite earlier and abrupt transition on the suction side compared to the case with no tripping action. The pressure side boundary layer was found to be almost uninfluenced from row LP. This behaviour was attributed to the fact that the initial strong convex curvature, the curvature inversion and the associated near leading edge mainstream pressure gradient are more dominant parameters compared to the size of the hole disturbance created by row LP. The initial development and growth of three dimensional streamwise vortical structures and their breakdown near the leading edge (pressure side) were also expected to be interacting phenomenon on the near leading edge, (pressure side) heat transfer behaviour.

Influence of changing inlet Re_{∞} number on h_e appeared as the change in local Re numbers, when exit Mach number was kept constant. An increased inlet Re_{∞} number caused a relatively earlier apparent transition point on the suction side of the blade. The Nu number versus local Re number variation on the suction side established a straight line in between turbulent and laminar flat wall correlations. At a given local Re number, smaller Nu numbers than the flat wall were attributed to the turbulence cancelling property of the strong convex curvature.

The increases in TU_{α} result in quite negligible heat transfer enhancements on the blade surfaces except the region between $s/\bar{C} = -0.01$ and 0.20. On the present model, due to tripping action on the leading edge, laminar or transitional boundary layers cover only a very small portion of the total surface area in contrary to a smooth blade with no cooling holes.

Incidence angle variations strongly influenced the boundary layer momentum and heat exchange on both sides of the stagnation point. There are two major mechanisms influencing the heat transfer related with the incidence angle changes. The change of the position of the stagnation point and the definite change in local Re numbers near the leading edge are strongly determining factors on a smooth blade with no cooling holes. On a blade with leading edge cooling rows of holes, the position of the stagnation point relative to the coolant rows is important because of its major role in how the downstream boundary layers are tripped.

6.2 FILM COOLING HEAT TRANSFER ON THE LEADING EDGE

Film cooling from 3 rows of spanwise angled cooling holes resulted in significant wall protection at both downstream of the showerhead region, provided that the coolant temperature is about half of that of the mainstream.

The local blowing rates of the rows (LP, LM and LS) were evaluated from measured(averaged) \bar{C}_d for the showerhead configuration. Relatively high blowing rate ($m=3.9$ to 8.8) of the mid row of holes (LM), located very close to the stagnation point was attributed to very low free stream mass flux rates occurring in the near stagnation zone.

Stagnation point prediction and qualitative oil flow visualizations showed that the suction side wall heating is affected by the coolant jets from rows LM and LS whereas the pressure side heat flux is only affected by row LP, at zero incidence.

On the suction side, highly penetrating jets from row LM disturb the approaching mainstream boundary layer just downstream of this row. The local poor cooling efficiency at

$s/\bar{c}=0.01$ was attributed to this disturbance.

It has been shown that,a cooling row located near the stagnation point ejects at a quite high blowing rate,in a showerhead cooling configuration. The deflection direction of the jets from this row,mainly depends upon the incidence angle.Important disturbances(enhanced turbulent mixing)may create poor cooling efficiencies at near downstream of the deflected over ejecting jets.

The convective heat transfer coefficient h was evaluated under an "isothermal wall" assumption.on the present model.In the absence of coolant ejection,this assumption holds,as far as the experimental technique is concerned.However coolant ejection at $T_c/T_{\infty}=0.5$ caused some conduction patterns in the showerhead region,even with a model having a very low thermal conductivity and diffusivity.Such conduction effects were negligible after 3 hole diameters downstream of the showerhead region.In actual case,due to highly conducting behaviour of superalloys compared to the present model's low conductivity material;the showerhead region conduction pattern was expected to occur in a stronger way. The actual local wall temperature near the ejection site resulted in more realistic heat transfer coefficients compared to an isothermal approach.

Increasing coolant to free stream mass weight ratio (0.48 % to 1.01 %) improved the cooling action on the pressure side,near the leading edge. On the suction side,some local h enhancements near downstream of LS was attributed to the disturbance of the overrejecting mid row of holes and increased local blowing rate of ejection from LS.

The coolant blanket effect because of leading edge ejection appeared to exist all over the surfaces of the blade.Even at far downstream locations(trailing edge),the h reductions due to ejection was observed to be proportional with the amount of coolant added to the boundary layer at a prescribed coolant temperature.

Although, the showerhead region heat transfer shows strong local variations, an attempt was made to define an averaged leading edge heat transfer coefficient as a function of coolant mass weight ratio and temperature ratio on both suction side and pressure side downstream of the showerhead region. As the mass weight ratio increased, the suction side appeared to be less protected because of jet penetration and upstream disturbances from row LM. The cooling looked more effective on the pressure side than on the suction side. The influence of coolant temperature or ρ_c/ρ_∞ on heat transfer is very strong at a given coolant mass weight ratio.

Variation of incidence angle affects the film cooling heat transfer through the changes in the number of cooling rows, ejecting on a given surface, because of changing stagnation point position. At positive incidence angles, when a laminar or transitional heat transfer evolution existed on the pressure side ($s/\bar{C} > -0.2$); film cooling from row LP destroyed the laminar or transitional heat transfer evolution resulting in a turbulent boundary layer variation, ($TU_{\infty} = .8 \%$).

Local wall heating rates downstream of the showerhead region were also observed to be directly related to the local blowing rate distribution in between the three rows. This distribution is definitely a result of the static pressure distribution around the leading edge, at various incidence angles.

6.3 FILM COOLING HEAT TRANSFER ON THE SUCTION SIDE

Application of film cooling heat transfer on the suction side ($s/\bar{C} = 1/5$), significantly reduced the wall heat flux with a discrete hole configuration having double rows of staggered and shaped holes. Near hole effectiveness downstream of the rows was high. This resulted in negative heat fluxes (from the wall to the mainstream) in the first few diameters distance. Increasing

blowing rates improved the overall protection of the wall. However, above $m=0.61$, a near ejection site augmentation in h occurred because of enhanced turbulent mixing.

Reducing the coolant temperature from wall temperature to half of that of the mainstream lowered the heat transfer coefficient at constant m . At high blowing rates, ($m \approx 0.96$), this effect was more pronounced than the case for $m \approx 0.40$.

6.4 FILM COOLING HEAT TRANSFER ON THE PRESSURE SIDE

Film cooling heat transfer on the pressure side of the rotor blade was performed at ($s/\bar{C} = 1/3$), from a single row of shaped holes, in a blowing rate range from $m=1.42$ to 4.23 . The corresponding mass weight ratio was ranging from $\dot{m}_c/\dot{m}_{\infty} = 0.25\%$ to 0.73% .

Overall effectiveness of cooling increased, when m was increased from 1.42 to 1.94 . This improvement has been attributed to the concave curvature of the pressure side; in contrary to film cooling behaviour on a convex surface. However, above $m=2.51$, the initial momentum of the jets created some penetration into the mainstream, resulting in h augmentation. This augmentation was significant only in the first 30 hole diameters region. At far downstream, high blowing rates caused a more effective protection of the wall.

6.5 FILM COOLING HEAT TRANSFER FROM SIMULTANEOUS EJECTION

At low blowing rates (or mass weight ratios), when the mid row of holes is blocked (due to coolant plenum chamber pressures which are not enough to eject coolant near the stagnation point), relatively smoother h/h_{∞} variations on the pressure side and suction side downstream of the showerhead region were

found, compared to nominal conditions. Especially, the smooth and effective h/h_{∞} rise on the suction side ($.03 < s/\bar{C} < 0.20$) was explained by the disappearance of the disturbing (overrejecting) jets from mid row of holes.

On the suction side and on the pressure side, the qualitative heat transfer behaviour from simultaneous ejection was unchanged when compared to independent ejection studies on the same locations. However, superposition of the leading edge ejection with the pressure side ejection resulted in as much as 15 % reduction in h/h_{∞} on the pressure side. The contribution of the leading edge ejection to suction side heat transfer was quite negligible under nominal operating conditions, ($\dot{m}_e/\dot{m}_{\infty} = 3.1 \%$).

The free stream turbulence intensity did not influence the heat transfer coefficient with coolant ejection in a TU_{∞} range from 0.8 % to 5.2 %, ($\dot{m}_e/\dot{m}_{\infty} = 2.45 \%$, $T_e/T_{\infty} = 0.40$), within the experimental accuracy of h measurements. This behaviour was explained with the fully turbulent nature of the coolant boundary layers covering the surfaces of the blade.

The influence of changing incidence angle(at far downstream of the showerhead region) on both sides ($|s/\bar{C}| > 1/3$) has been found to be related to the changes in local blowing rates of the showerhead region ejection rows. Furthermore, the trajectories of coolant jets, stagnation point movements, local Re number changes and pressure gradient evolution near the leading edge played important roles in the downstream heat transfer behaviour of coolant layers, at various incidences.

6.6 CONVECTIVE HEAT TRANSFER PREDICTIONS IN BOUNDARY LAYERS IN THE ABSENCE AND PRESENCE OF COOLANT EJECTION

When there is no coolant ejection, convective heat transfer predictions on the suction side were performed using a two dimensional boundary layer code. A convex curvature model was implemented into the program in order to account for the strong curvature influence on turbulent shear stresses. A better agreement between the predictions (with the curvature model) and the measured data was found compared to the boundary layer code using a flat wall mixing length model. A second mixing length model taking the concave curvature effects into account on the pressure side was also implemented into the boundary layer code. Some discrepancy was found between the numerical computation and the measured pressure side data. Although the concave curvature effects were simulated, the near leading edge flow with acceleration and deceleration near the curvature inversion point (leading to a possible vortex stretching), very favourable pressure gradient and the turbulence augmenting nature of the concave surface make the heat transfer predictions very difficult to perform on this surface.

A numerical simulation of convective heat transfer with coolant ejection on the suction side was attempted. Near ejection hole mixing length augmentations were determined as a function of the blowing rate, using an experimental procedure. The coolant was assumed to be distributed in a fixed distance measured from the wall just downstream of the ejection row. The specific approach was found to be very successful in simulating film cooling heat transfer especially when the cooling hole diameter is much larger than the thickness of the approaching boundary layer, ($d/\delta \approx 4.75$).

6.7 FINITE ELEMENT ANALYSIS OF THERMAL CONDUCTION IN THE FILM COOLED TURBINE BLADE

A predictive capability based on a finite element method has been developed to investigate the thermal conduction heat transfer behaviour of a film cooled gas turbine blade. The blade wall temperatures and local wall heat fluxes were obtained with a fine resolution.

When only internal convection cooling was applied without external film cooling, the leading edge was found to be the most critical area as far as local wall heat fluxes were concerned. However, wall temperatures in this region were quite reduced ($T_w/T_{cof} \sim 0.7$) due to the effective cooling from internal channel "L".

The results with external film cooling on the suction side revealed that downstream of a coolant ejection site is far from being neither an adiabatic surface nor an isothermal wall. The addition of the convective heat transfer contribution of coolant ejection holes to heat conduction analysis indicated that, the direction and magnitude of near ejection hole local wall heat fluxes are strongly controlled by the coolant hole convection behaviour. Near the ejection site, very significant flow of heat through the film cooling hole both from upstream and downstream direction showed the heat sink influence of the hole. Just downstream of the hole the wall temperatures were very close to the coolant temperature in the plenum chamber, indicating the effectiveness of film cooling in this region. The solid walls between the coolant passages were also found to be transmitting significant levels of heat to the internal coolant stream. Large temperature gradients were shown to be accumulated near the corners of internal coolant passages.

REFERENCE LIST

1. HOLLAND,M.J.,THAKE,T.F., "Rotor Blade Cooling in High Pressure Turbines," AIAA Journ.of Aircraft, Vol:17, No:6, June 80, pp.412-418.
2. KERREBROCK,J.L., "Aircraft Engines and Gas Turbines," The MIT Press, London, 1977, pp.174.
3. OLSSON,U., "Advanced Engine Technology and its Influence on Aircraft Performance," AIAA Journal of Aircraft, Vol:19, No:5, May 82, pp.380-384.
4. LIEBERT,C.H.,STEPKA,F.S., "Ceramic Thermal Barrier Coatings for Cooled Turbines," AIAA Journal of Aircraft, Vol:14, No:5, May 77, pp.487-493.
5. HALLS,G.A., "Air Cooling of Turbine Blades and Vanes," Supersonic Turbojet Propulsion Systems and Components, AGARDograph 120, 1967, pp.241-285.
6. ESGAR,J.B., "Turbine Cooling," Transactions of the ASME, July 59, pp.226.
7. ALPERT S.,GREY R.E.,DRAKE D., "Application of Internal Cooling to Gas Turbine Rotors," Transactions of the ASME, Aug.56, pp.1257.
8. RICE,I.G., "The Reheat Gas Turbine Combined Cycle," ASME Mechanical Engineering, Apr.82, pp.46-57.
9. METZGER,D.E., "Gas Turbine Engines," ASME Mechanical Engineering, June 83, pp.44-52.
10. FLOURSCHUETZ, L.W.,METZGER, D.E. and SU,C.C., "Heat Transfer Characteristics for Jet Array Impingement with Initial Cross-flow" ASME paper No. 83-GT-28, 1983.
11. MOSKOWITZ,S.L.,LOMBARDO,S., "2750 F Engine Test of a Transpiration Air Cooled Turbine," Trans. of the ASME, Apr.71, pp.238.
12. KRUSE,H., "Investigation on Temperature Distribution Near Film Cooled Airfoils," AGARD conference proceedings No:229, High Temperature Problems in Gas Turbine Engines, Ankara, Sep.77.

13. TAKAHARA K., MINODA M., YOSHIDA T., SASAKI M., YAMAMATO A., SAKATA K., "High Temperature Turbine Researches at National Aerospace Lab in Japan", ASME paper ASME 74-GT-16, April 74.

14. HENNECKE, D.K., "Turbine Blade Cooling in Aero Engines" Von Karman Institute Lecture Series- Film cooling and turbine blade heat transfer, February 22-26, 1982.

15. ABRAMOWICH, G.N., "The Theory of Turbulent Jets", MIT Press, Cambridge, Mass., 1963, pp.3-25, 195-201, 541-556.

16. KEFFER J.F., BAINES W.D., "The Round Turbulent Jet in a Cross Wind", Journal of Fluid Mechanics, Vol.15, No.4, 1963, pp.481-495.

17. MEINER P.L., "Fortran Program for Calculating Coolant Flow and Metal Temperatures of a Full Coverage Film Cooled Vane or Blade", NASA technical paper 1259, 1978.

18. BARRY B., "The Aerodynamic Penalties Associated with Turbine Blade Cooling", Von Karman Institute for Fluid Dynamics, Lecture Series:83, Jan.76.

19. MUKHERJEE D.K., FREI O., "Temperature Measurements on Cooled Gas Turbine Stator blades," ASME paper 74-GT-31, April 74.

20. GRAHAM R.W., "Fundamental Mechanisms that Influence the Estimate of Heat Transfer to Gas Turbine Blades", Heat Transfer Engineering, Vol:2, Sep.80.

21. BOLDMAN D.R., BRINICH P.F., "Mean Velocity, Turbulence Intensity and Scale in a Subsonic Turbulent Jet Impinging Normal to a Large Flat Plate", NASA TP1037, 1977.

22. KESTIN J., WOOD R.T., "The Mechanism which Causes Free Stream Turbulence to Enhance Stagnation Line Heat and Mass Transfer," Heat Transfer 1970, vol.2, Paper fc2..7, Elsevier, Amsterdam, 1970.

23. SADEH W.Z., BRAVER H.J., GARRISON J.A., "Visualization Study of Vorticity Amplification in Stagnation Flow", SQUID-CSU-1-PU, Colorado State University, Fort Collins, Col., Oct.77.

24. COLLADAY R.S., "Turbine Cooling- Turbine Design and Application," NASA sP 290, 1975.

25. KESTIN J., MAEDER P., SOGIN H., "The Influence of Turbulence on the Transfer of Heat to Cylinders Near the Stagnation Point", Z. Angew. Math. Physics, 12, 1961, pp.115-132.

26. LOWERY G.W. and VACHON R.I., " The Effect of Turbulence on Heat Transfer From Heated Cylinders", International Journal of Heat and Mass transfer, 18, 1975, pp.1229-1242.
27. TRACI R.M. and WILCOX D.C., " Free Stream Turbulence Effects on Stagnation Heat Transfer", AIAA Journal, 3, July 75.
28. SMITH M., and KUETHE A., " Effects of Turbulence on Laminar Skin Friction and Heat Transfer", Physics of fluids, 9, 1966, pp.2337-2344.
29. HARTSEL J.E., " Prediction of effects of mass transfer cooling on the blade-row efficiency of turbine airfoils", ASME paper 72-11, 1972.
30. GORLA R.S.R., " Influence of turbulence intensity and free stream velocity oscillations on stagnation point heat transfer", International Journal of Heat and Fluid Flow, Vol.3, No.4, Dec.82, pp.195-200.
31. BASE T.E., PATEL J.M., VALAITIS G.C., " Heat transfer from cylinders in unsteady flow," Canadian J. Chemical Engineering, 59, 1981, pp.247-250.
32. MARZIALE M.L., MAYLE R.E., " Effect of an oscillating flow direction on leading edge heat transfer," 1983 Tokyo International gas turbine Congress, 83-TOKYO-IGTC-5, Oct.83, pp.37-44.
33. RICHARDS B.E., " Heat transfer to cooled turbine blades", Von Karman Institute for fluid dynamics, Lecture Series 83, Jan.76.
34. DANIELS L.C., " Film cooling of gas turbine blades", Ph.D. Thesis , Dept. of Engineering Science, University of Oxford, England, 1978.
35. CEBECI,T.,BRADSHAW,P., "Momentum Transfer in Boundary Layers," Hemisphere Publishing Corporation,London,1977.
36. FERNHOLZ H.H., " External flows", Topics in Applied Physics, V.12, "Turbulence", (edited by P. Bradshaw), Springer-Verlag, Berlin, 1976.
37. KEMP A., " Boundary layer development on turbine blades in the presence of Goertler vorticity", Cambridge University , Engineering Department, Ph.D. Thesis, (1976).
38. HAN L.S., COX W.R., "A visual study of turbine blade pressure side boundary layers," ASME, Journal of Engineering for power, vol.105, Jan. 83, pp.47-52.

39. MARTIN B.W., BROWN A., "Factors influencing heat transfer to the pressure surfaces of gas turbine blades," International journal of heat and fluid flow, Vol.1, No.3, 1979, pp.107-114.
40. BRADSHAW, P., "Prediction of turbulent shear layers in turbomachines," NASA SP-304, Fluid Mechanics, Acoustic and Design of Turbomachinery, 1974.
41. HORLOCK, J.H., "Boundary layers in axial turbomachines," Flow research and blading, (ed. by L.Z. Dzung), Elsevier Press, 1969.
42. JOHNSTON, J.P., "Internal flow," Topics in Applied Physics, V.12, "Turbulence," (ed. by P.Bradshaw), Springer Verlag, Berlin, 1976.
43. MARCIAL, Ph., SIEVERDING, C.H., "Secondary flows within turbomachinery bladings," In Secondary Flows in Turbomachines, AGARD CP 214, 1977, paper 11, Also VKI preprint 1977-11.
44. MORETTI, P.M., "Heat transfer through an incompressible turbulent boundary layer with varying free stream velocity and varying surface temperature," Ph.D. Thesis, 1964, Stanford University.
45. JONES, W.P., LAUNDER, B.E., "Some properties of sink flow boundary layers," Journal of fluid mechanics, 46, 1972.
46. LAUNDER, B.E., JONES, W.P., "Sink flow turbulent boundary layers," Journal of fluid mechanics, 38, 1969.
47. BACKWELDER, R.F., KOVASNAY, L.S.G., "Large scale motion of a turbulent boundary layer during relaminarization, J. Fluid Mechanics, 53, 1972.
48. KRESKOVSKY, J.P., SHAMROTH, S.J., McDONALD, H., "Application of a general boundary layer analysis to turbulent boundary layers subjected to a strong favorable pressure gradient," ASME, Journal of Fluids Engineering, June 75, pp.217-224.
49. BRADSHAW, P., "Effects of streamline curvature on turbulent flow," AGARDograph No:169, 1973.
50. VAN DYKE, M., "Higher order boundary layer theory," Annual review of fluid mechanics, Vol.1, 1969.
51. SIMON, T.W., MOFFAT, R.J., KAYS, W.M., "Turbulent boundary layer heat transfer experiments: Convex curvature effects, including introduction and recovery," Report HMT-32, Thermosciences Division, Mechanical Engineering Dept., Stanford Univ., Nov. 80.

52. ADAMS, E.W., JOHNSTON, J.P., "A mixing length model for the prediction of convex curvature effects on turbulent boundary layers," ASME paper, 83-GT-80.

53. SO, R.M.C., MELLOR, G.L., "Experiment on convex curvature effects in turbulent boundary layers", Journal of Fluid Mechanics, V.60, Part 1, 1973.

54. SO, R.M.C., "On the curvature/buoyancy analogy for turbulent shear flows," ZAMP, V.31, Fasc.5, 1980, pp.628-633.

55. GIBSON, M.M., "An algebraic stress and heat flux model for turbulent shear flow with streamline curvature," International Journal of Heat and Mass Transfer, V.21, pp.1609-1617.

56. SO, R.M.C., EDELFELT, I.H., ELOVIC, E., KERCHER, D.M., "A 2-D boundary layer program for turbine airfoil heat transfer calculation," ASME paper 82-GT-93.

57. GILLIS, J.C., JOHNSTON, J.P., "Turbulent boundary layer flow and structure on a convex wall and its redevelopment on a flat wall," Journal of Fluid Mechanics, V.135, pp.123-153, 1983.

58. BRADSHAW, P., "Effect of free stream turbulence shear layers," Imperial College AERO. report 74-10, Oct.74.

59. LAUNDER, B.E., YORK, J., "Discrete hole cooling in the presence of free stream turbulence and strong favourable pressure gradient," Imperial College rep. HTS/7/37, 1971.

60. TURNER, A.B., "Local heat transfer measurements on a gas turbine blade," Journal of Mechanical Engineering Science, V.13, No.1, 1971, pp.1-12.

61. SCHULTZ, D.L., OLDFIELD, M.L.G., JONES T.V., "Heat transfer rate and film cooling effectiveness measurements in a transient cascade," AGARD Conference Proceedings No.281, Testing and measurement techniques in heat transfer and combustion, Brussels, May 80.

62. CONSIGNY, H., RICHARDS, B.E., "Short duration measurements of heat transfer rate to a gas turbine rotor blade," ASME Journal of Engineering for Power, V.104, No.3, July 82, pp.542-551.

63. DYBAN, I., EPIK, H., "Calculation of convective heat transfer from statistical characteristics of turbulence," Heat transfer-Soviet Research, V.9, No.4, 1977.

64. ISHIGAKI, H., "The effect of oscillation on flat plate heat transfer," Journal of Fluid Mechanics, V.47, 1971, pp.437.
65. BAYLEY, F.J., PRIDDY, W.J., "Studies of turbulence characteristics and their effects upon the distribution of heat transfer to turbine blading," AGARD conference proceedings No.281, Testing and measurement techniques in heat transfer and combustion, Brussels, May 80.
66. BUSHNELL, D.M., CAREY, A.M., HOLLEY, B.B., "Mixing length in low Re number compressible turbulent boundary layers," AIAA Journal, V.13, Aug. 75.
67. CONSIGNY, H., "Etude experimentale et theorique des echanges thermiques convectifs a la surface des aubes de turbines," Ph.D. Thesis, VKI-Brussels University, 1980.
68. GRIEPENTROG, H., "Shock wave boundary layer interaction in cascades," AGARDograph 164, "Boundary Layer effects in turbomachines," ed. by J. Surugue, 1972.
69. GADD, G.E., "Interactions between normal shock waves and turbulent boundary layers," A.R.C. R and M 3262, 1962.
70. GREEN, J.E., "Interactions between shock waves and turbulent boundary layers," Progress in Aerospace Sciences, edited by D. KUCHEMAN, V.11, Pergamon Press, 1970.
71. PEARCEY, H.H., "Some Effects of Shock Induced Separation of Turbulent Boundary Layers on Transonic Flow past Airfoils," A.R.C., R and M 3108, 1967.
72. SEDDON, J., "The Flow Produced by the Interaction of Turbulent Boundary Layer with a Normal Shock Wave Strength to Cause Separation," A.R.C. R and M 3502, 1967.
73. MC. DEWITT, J.B., LEVY, L.L. JR., DEIWERT, J.S., "Transonic flow about a thick circular-arc airfoil," AIAA Journal, V.14, May 76.
74. BALDWIN, B.S., Mac CORMACK, R.W., DEIWERT, G.S., "Numerical Techniques for the Solution of the Compressible Navier-Stokes equations and Implementations of Turbulence Models," AGARD L.S.73, Editor E. KRAUSE, 1975.
75. PANARAS, A.G., "Calculation of a Boundary Layer Interacting with a Normal Shock by a Discontinuity Analysis," V.K.I., TN-121, Oct. 76.

76. BACK,L.H.,CUFFEL,R.F., "Shock Wave/Turbulent Boundary Layer Interaction with and without Surface Cooling," AIAA Journal,V.14,Apr.76.
77. OATES,G.C., "Shock Boundary Layer Interaction," V.K.I. Lecture Series 86,Compressible Turbulent Boundary Layers,1976.
78. HANKEY,W.L.,HOLDEN,M.S., "Two Dimensional Shock Wave Boundary Layer Interactions in High Speed Flow," AGARDograph 203,1975.
79. SASAKI,M., TAKAHARA, K., KUMAGAI, T., HAMANO,M., " Film Cooling Effectiveness for Injection from Multi-row holes," ASME Jour. of eng. for power, V.101, Jan.79, pp.101-108.
80. WILSON, D.G. ,POPE, J.A. , "Convective Heat Transfer to Gas Turbine Blade Surfaces," Proceedings of the institute of Mechanical Engineers, V.168,1954.
81. AINLEY,D.G., "Internal Air Cooling for Turbine Blades," A.R.C. R and M 3013,1957.
82. WALKER,L.A. and MARKLAND,E., "Heat Transfer to Turbine Blading in the Presence of Secondary Flow," Int.Journal of Heat and Mass Transfer, V.8,1965, pp.729-748.
83. RICHARDS,B.E., "Heat Transfer Measurements Related to Hot Turbine Components in the Von Karman Institute Hot Cascade Tunnel," AGARD Conference Proceedings,No.281,Testing and Measurement Techniques in Heat Transfer and Combustion,Brussels,May 80.
84. SPALDING, D.B., PATANKAR, S.V., "Heat and Mass Transfer in Boundary Layers," Morgan - Grampian, London, 1967.
85. BOGOLOMOV,E.N.,PIOTUKH,S.M., "Efficiency of Film Cooling of Fixed Gas Turbines," Thermal engineering-Teploenergetica,1978,V.25,pp.6-9 .
86. BAYLEY,F.J.,MILLIGAN,R.W., "The Effect of Free Stream Turbulence upon Heat Transfer to Turbine Blading," AGARD conference proceedings No.229,Ankara,Sep.77.
87. DUNN,M.G., "Measurement of Heat Flux and Pressure in a Turbine Stage," AFWAL-TR-81-2055,CALSPAN advanced technology center, Buffalo,N.Y. 14225,July 81.
88. DANIELS, L.D., BROWNE, W.B., "Calculation of Heat Transfer Rates to Gas Turbine Blades," Int. J. Heat and Mass Transfer, V.24, N.5, 1981, pp.871-879.

89. KERCHER, D.M., SHEER, R.E., SO, R.M.C., "Short Duration Heat Transfer Studies at High Free Stream Temperatures," ASME Journal of Engineering for Power, V.105, Jan.83, pp.156-166.

90. Bammert, K., Sandsteede, H., "Measurements of the Boundary Layer Development Along a Turbine Blade with Rough Surfaces," ASME Journal of Engineering for Power, Oct.80, V.102, pp.978-983.

91. Goldstein, R.J., Eckert, E.R.G., Ramsey, J.W., "Film Cooling with Injection through holes: Adiabatic Wall Temperatures Downstream of a Circular Hole," ASME Journal of Eng. for Power, V.90, 1968, pp.384.

92. Launder, B.E., York J., "Discrete Hole Cooling in the Presence of Free Stream Turbulence and Strong Favourable Pressure Gradient," Int. J. of Heat and Mass Transfer, V.17, pp.1403-1409.

93. Louis, J.F., Goulios, G.N., Demirjian, A.M., Wiedhope, J.M., "Short Duration Studies of Turbine Heat Transfer and Film Cooling Effectiveness," ASME Paper, No.74-GT-131, March 74.

94. Bergeles, G., Gosman, A.D., Launder, B.E., "Nearfield Character of a Jet Discharged through a Wall at 30 degree to a Mainstream," AIAA Journal, V.15, No.4, Apr.77, pp.499-504.

95. Bergeles, G., Gosman, A.D., Launder, B.E., "Double Row Discrete Hole Cooling. An Experimental and Numerical Study," ASME Journal of Engineering for Power, V.102, Apr.80, pp.498-503.

96. Pedersen, D.R., Eckert, E.R.G., Goldstein, R.J., "Film Cooling with Large Density Differences Between the Mainstream and the Secondary Fluid Measured by the Heat-Mass Transfer Analogy," ASME Journal of Engineering for Power, V.99, Nov.77, pp.620-627.

97. Jabbari, M.Y., Goldstein, R.J., "Adiabatic Wall Temperature and Heat Transfer Downstream of Injection through two Rows of Holes," ASME Journal of Engineering for Power, V.100, Apr.78, pp.303-307.

98. Goldstein, R.J., Eckert, E.R.G., Burggraf, F., "Effect of Hole Geometry and Density on three Dimensional Film Cooling," Int. Journal of Heat and Mass Transfer, V.17, 1974, pp.595.

99. Afekuku, W.O., Hay, N., Lampard, D., "The Film Cooling Effectiveness of Double Rows of Holes," ASME Jour. of Engineering for Power, V.102, No.3, July 80, pp.601-606.

100. SELLERS, J.P., JR., "Gaseous Film Cooling with Multiple Injection Stations," AIAA Journal, V.1, 1963, pp.2154-2156.
101. LIESS, C., "Experimental Investigation of Film Cooling with Ejection from a Row of Holes for Application to Gas Turbine Blades," ASME paper No.74-GT-5, March 74.
102. GOLDSTEIN, R.J., YOSHIDA, T., "The Influence of a Laminar Boundary Layer and Laminar Injection on Film Cooling Performance," ASME paper No.81-HT-38, Apr.1981.
103. LOFTUS, P.J., JONES, T.V., "The Effect of Temperature Ratios on the Film Cooling Process," ASME Journal of Eng. for Power, V.105, July 83, pp.615-620.
104. RICHARDS, B.E., APPELS, C., VILLE, J.P., SALEMI, C., "Film Cooling of Heated Turbine Surfaces at Simulated Conditions," AIAA/SAE 13.th Propulsion Conference, Florida, paper 77-947, July 77.
105. CAMCI,C., LIGRANI, P.M.L., HAY,N., "Investigation of Heat Transfer Rates on a Film Cooled Plate with and without a Pressure Gradient," Von Karman Ins., Internal Note-68, July 81.
106. LANDER, R.D., FISH, R.W., SUO, M., "External Heat Transfer Distribution on Film Cooled Turbine Vanes," AIAA Journal of Aircraft, V.9, No.10, Oct. 72, pp.707-714.
107. MIRHOSSEINI, A., BARROW, H., "Experimental Determination of Heat Transfer Near the Leading Edge of a Film Cooled Gas Turbine Blade," Intern. Journal of Heat and Fluid Flow, V.1, No.4, Dec. 79, pp.155-159.
108. LUCKEY, D.W., WINSTANLEY, D.K., HANUS, G.J., L'ECUYER, M.R., "Stagnation Region Gas Film Cooling for Turbine Blade Leading Edge Applications," AIAA Journal of Aircraft, V.14, N.5, May 77, pp.494-501.
109. HARTSEL, J.E., "Prediction of Effects of Mass Transfer Cooling on the Blade Row Efficiency of Turbine Airfoils," ASME paper 72-11, 1972.
110. FOSTER, N.W., LAMPARD, D., "The Flow and Film Cooling Effectiveness Following Injection through a Row of Holes," ASME Journal of Eng. for Power, V.102, July 80, pp.584-588.
111. HANUS, G.J., L'ECUYER, M.R., "Leading Edge Injection for Film Cooling of Turbine Vanes," AIAA Journal of Energy, V.1, No.1, Jan. 77, pp.44-49.

112. NEALLY, D.A., MIHELC, M.S., HYLTON, L.D., GLADDEN, H.J., "Measurements of Heat Transfer Distribution over the Surfaces of Highly Loaded Turbine Nozzle Guide Vanes," ASME Journal of Gas Turbines and Power, V.106, No.1, Jan. 84, pp.149-158.
113. MUSKA, J.F., FISH, R.W., SUO, M., "The Additive Nature of Film Cooling from Rows of Holes," ASME Journal of Eng. for Power, Oct. 76, pp.457-463.
114. ITO, S., GOLDSTEIN, R.J., ECKERT, E.R.G., "Film Cooling of a Gas Turbine Blade," ASME Journal of Eng. for Power, V.100, NO.3, July 78, pp.476-481.
115. DRING, R.P., BLAIR, M.F., JOSLYN, H.D., "An Experimental Investigation of Film Cooling on a Turbine Rotor Blade," ASME Journal of Eng. for Power, V.102, Jan. 80, pp.81-87.
116. GLADDEN,H.J.,GAUNTNER,J.W., "An Adverse Effect of Film Cooling on the Suction Side of a Turbine Vane," NASA TN-D-7618, 1974.
117. GAUNTNER,J.W., "Effects of Film Injection Angle on Turbine Vane Cooling," NASA TP-1095 ,1977.
118. GOLDSTEIN, R.J., ECKERT, E.R.G., CHIANG, H.D., ELOVIC, E., "Effect of Surface Roughness on Film Cooling Performance," ASME paper 84-GT-41.
119. SCHMIDT,E., "Einfuhrung in die technische Thermodynamik und in die Grundlagen der Chemischen Thermodynamik, 10 th ed., Berlin, 1963.
120. SCHLICHTING, H., "Boundary Layer Theory," Seventh Ed., McGraw Hill Co., 1979, pp.271-275.
121. TABAKOFF,W.,HAMED,A., "Theoretical and Experimental Study of Flow through Turbine Cascade with Coolant Flow Injection," AIAA paper no.75-843, 1975.
122. HESS,W.G., "Advanced Cooled Turbine Airfoil Aerodynamic Investigation," AIAA Jour. of Aircraft V.15, No.9, Sep.78, pp.582-588.
123. MCDONEL J.D.,EISWERTH,J.E., "Effects of Film Injection on Performance of a Cooled Turbine," AGARD CP-229,High Temperature Problems in Gas Turbine Engines, Ankara, Sep.77.
124. YAVUZKURT, D.L., MOFFAT, R.J. and KAYS, W.M., "Full-coverage Film cooling.Part 1.Three Dimensional Measurements of Turbulence Structure," Journal of Fluid Mechanics, V.101, pp. 120-158, 1980.
125. SCHULTZ,D.L.,JONES,T.V., "Heat Transfer Measurements in Short Duration Hypersonic Facilities," AGARDograph no.165, Feb.73.

126. JONES,T.V.,SCHULTZ,D.L.,HENDLEY,A.D., "On the Flow in an Isentropic Free Piston Tunnel," A.R.C. R and M 3731, Jan.73.

127. ARPACI,V.S., "Conduction Heat Transfer," Addison-Wesley, June 66, pp.343-345.

128. LIGRANI,P.M.,CAMCI,C.,GRADY,M.S., "Thin Film Heat Transfer Gauge Construction and Measurement Details," Von Karman Institute Technical Memorandum No.33, Nov.82.

129. BAINES, W.D. and PETERSON, E.G., "An Investigation of Flow Through Screens," Transactions of the ASME 73, 1951, pp.467.

130. TSUI,H.,HAMA,F.R., "Experiment on the Decay of Turbulence Behind Two Grids," Jour. of Aero.Sci.20, 1953, pp:848.

131. OLIVARI,D., "Data Acquisition Systems for Wind Tunnel Testing," In : Designing with the Wind Symposium, Nantes, France, June 81. Also, VKI preprint 1981-20.

132. KLINE,S.J.,Mc CLINTOCK,F.A., "Describing Uncertainties in Single Sample Experiments," ASME Mechanical Engineering, V.75, No.1, 1953, pp.3-8.

133. CRAWFORD,M.E.,KAYS,W.M., "STAN5 ,A Program for Numerical Computation of Two Dimensional Internal / External Boundary Layer Flows," Stanford University, Dept.of Mech.eng., Thermosciences Division, Report HMT-23, December 1975.

134. PATANKAR,S.V. and SPALDING,D.B., "Heat and Mass Transfer in Boundary Layers," 2nd. Ed., International Textbook company Ltd., London, 1970.

135. KEENEN,J.H.,and KAYE,J., "Gas Tables", John Wiley and Sons Inc., New York, 1948.

136. CRAWFORD,M.E.,KAYS,W.M.,MOFFAT,R.J., "Full Coverage Film Cooling.Part II :Heat Transfer Data and Numerical Simulation," Trans. of the ASME, Jour.of Eng.for Power, V.102, Oct.80, pp.1006-1012.

137. BERGELES,G. ,GOSMAN,A.D, LAUNDER, B.E., "The Prediction of 3D Discrete Hole Cooling Processes.Part-1 Laminar flow," ASME Jour. of Heat Transfer, Vol.98, 1976, pp.379.

138. KAYS,W.M. and MOFFAT,R.J., "Studies in convection", V.1, Academic Press, pp.213-219.

139. BERGELES, G. ,GOSMAN, A.D. and LAUNDER, B.E., "The Turbulent Jet in a Cross Stream at Low Blowing Rates:A Three dimensional Numerical

Treatment,"Numerical Heat Transfer ,V.1, 1978, pp.217.

140. CHOE,H., KAYS, W.M. and MOFFAT, R.J., "Turbulent Boundary Layer on a Full Coverage Film Cooled Surface-An Experimental Heat Transfer Study with Normal Injection," NASA Rep. CR-2642, 1976 (Also Stanford Univ. ,dept.of mech. eng., Report HMT-22).

141. YAVUZKURT, S., MOFFAT, R.J. and KAYS, W.M., "Full-Coverage Film Cooling: 3-Dimensional Measurements of Turbulence Structure and Prediction of Recovery Region Hydrodynamics," NASA Rep. CR-3104, 1979.

142. MOFFAT,R.J., "Curvature Effects and Turbulent Boundary Layers,"in Lecture Series 1982-02,Film Cooling and Turbine Blade Heat Transfer,Von Karman Institute for Fluid Dynamics, Feb.82,BELGIUM.

143. SHAPIRO, A.H., "The Dynamics and Thermodynamics of Compressible flow, Vols.I and II" Ronald Press, New York, 1953.

144. ZIENKIEWICZ,O.C., "The Finite Element Method in Engineering Science," Mc Graw Hill,London,1971.

145. AINSWORTH,R.W.,JONES,T.V., "Measurements of Heat Transfer in Circular,Rectangular and Triangular Ducts,Representing Typical Turbine Blade Internal Cooling Passages,Using Transient Techniques," ASME paper 79-GT-40, 1979.

146. DITTUS,F.W. and BOELTER, L.M.K., Univ.Calif. (Berkeley) Pub.Eng. ,V.2,1930,pp:443.

147. GILLIS, J.C., JOHNSTON, J.P., KAYS,W.M. ,MOFFAT,R.J., "Turbulent Boundary Layer on a Convex Curved Surface," Report HMT-31, thermosciences div.,mech. eng. dept.,Stanford University,1980.

148. ARTS,A.; "Cascade Flow Calculations Using a Finite Volume Method",in "Numerical Methods for Flow in Turbomachinery", VKI LS 1982-05, April 1982.

149. VAN DEN BRAEMBUSSCHE,R.; "Calculation of Compresssible Subsonic Flow in Cascades with Varying Blade Height,"ASME Trans., Series A-J.Engineering for Power,Vol.95,No.4,October 1973,pp 345-351.

150. KAYS,W.M. ,CRAWFORD,M.E.; "Convective Heat and Mass Transfer".Second edition,McGraw-Hill,1980.

151. BUYUKTUR,A.R.,KESTIN,J.,MAEDER,P.F., "Influence of Combined Pressure Gradient and Turbulence on the Transfer of Heat from a Plate," Int. J.Heat and Mass Transfer,Vol.7,1964,p 1175.

152. JUNKHAN, G.H., SEROVY, G.K., "Effects of Free Stream Turbulence and Pressure Gradient on Flat Plate Boundary Layer Velocity Profiles and Heat Transfer," ASME Trans., Series C-J. Heat Transfer, Vol. 69, No. 2, May 1967, pp 169-176.

153. TILLMAN, E.S., HARTEL, E.O., JEN, H.F., "The Prediction of Flow through Leading Edge Holes in a Film Cooled Airfoil with and without Inserts," ASME paper No:84-GT-4, June 84.

APPENDIX-1

BOUNDARY LAYERS AND HEAT TRANSFER ON A TURBINE AIRFOIL A LITERATURE REVIEW

A-1.1 HEAT TRANSFER NEAR THE STAGNATION POINT REGION

On the leading edge of a turbine blade on both sides of the stagnation line, very thin and laminar boundary layers start to grow up. GRAHAM, [20], suggests that, impingement of a jet on a flat plate or a cylinder in cross flow may be representative cases for the leading edge of a turbine blade. For the real case, free stream carries important amount of turbulence intensity and unsteadiness up to ~ 10 KHz because of blade to blade interaction. BOLDMAN and BRINICH , [21] reports turbulence intensities of an impinging jet on a flat plate . Their data shows very high turbulence intensity values near the stagnation line. According to [20] , stagnation on a flat plate and stagnation on a cylinder appear to be similar mechanisms. For both of the cases, amplification of turbulence augments the local heat transfer between the fluid and the wall. KESTIN and WOOD , [22] suggests a 3D boundary layer structure in the laminar boundary layer near the stagnation line as responsible from high heating rates occurring in this zone. They suggest vortical structures parallel to the flow vector around the nose. The

spacing of the vortices are proportional with Re and the level of upstream turbulence. Increasing the turbulence reduces this spacing and enhances the stagnation heat transfer. SADEH , [23] performed a visual study of these vortices with stagnation flow across a cylinder. For the heat transfer coefficient distribution around the stagnation line of a cylinder in cross flow TURNER and COLLADAY, [24] used an empirical relation as follows,

$$h = a \cdot \left[1.14 \frac{k}{D} Re_D^{1/2} Pr^{0.4} \left(1 - \left| \frac{\phi}{90} \right|^3 \right) \right] \quad -80^\circ < \phi < +80^\circ \quad (A.1)$$

where Re_D is free stream Reynolds number based on nose diameter, k is thermal conductivity, D is nose diameter. ϕ is angular distance from the stagnation line, a is an augmentation factor dealing with free stream turbulence intensity.

KESTIN and WOOD have presented an empirical expression taking into account free stream turbulence intensity,

$$\frac{Nu}{Re_D^{1/2}} = 0.945 + 3.48 \frac{Tu_\infty Re_D^{1/2}}{100} - 3.99 \cdot \left(\frac{Tu_\infty Re_D^{1/2}}{100} \right)^2 \quad (A.2)$$

$$\text{where } Tu_\infty = \frac{\sqrt{U'^2}}{U_\infty}$$

[25], [26] and [27] also suggests empirical relations of the same type as [22] and [24].

SMITH and KUETHE , [27] suggests

$$\frac{Nu}{Re_D^{1/2}} = \left[1 + 0.0277 \left(1 - \exp(-2.91 \times 10^5 \times Re_D) \right) \cdot Tu_\infty Re_D^{1/2} \right] \quad (A.3)$$

As a result of their experimental programme LOWERY and VACHON [26] presents the following empirical relationship,

$$\frac{Nu}{Re_D^{1/2}} = 1.01 + 2.624 \cdot \left(\frac{Tu_\infty \cdot Re_D^{1/2}}{100} \right) - 3.07 \cdot \left(\frac{Tu_\infty \cdot Re_D^{1/2}}{100} \right)^2 \quad (A.4)$$

TRACI and WILCOX , [28] have studied the problem analytically and obtained a model taking into account the following parameters,

$Tu_\infty Re_D^{1/2}$ turbulence intensity

$L / (D \cdot Re_D^{1/2})$ scale of the turbulence

Re_D Reynolds number

- - -

HIIKATA, YOSHIDA and MORI , [29] studied turbulence effects on heat transfer around a cylinder in cross flow through the solution of a k- ϵ model. They introduced an anisotropy equation to explain the production of turbulence energy due to anisotropy between the longitudinal and lateral Reynolds stress components in the free stream. They found good agreement between the calculated stagnation point heat transfer rates and their measurements.

Influence of turbulence intensity and free stream velocity oscillations on stagnation point heat transfer has been investigated by GORLA , [30] . A model is proposed for the momentum eddy diffusivity induced by free stream turbulence intensity and integral length scale. A good agreement between the experimental data and the heat transfer calculations based on the solution of steady momentum and energy equations with the proposed model is reported. A new normalized turbulence parameter taking into account the frequency of the free stream velocity is suggested as,

$$\hat{f} \cdot Tu_\infty^2 \cdot Re_D \quad (A.5)$$

where Strouhal number is $\hat{f}D/U_\infty$, D is the diameter of the cylinder , \hat{f} is the frequency of the velocity oscillations.

In a study by MARZIALE and MAYLE [32], an experimental investigation was conducted to examine the effect of a periodic variation in incidence angle on heat transfer at the leading edge of a gas turbine blade. A comparison of the unsteady and steady results indicate that the effect is dependent on the Strouhal number, turbulence level and the turbulence length scale, but the largest observed effect was only a 10 % augmentation at the nominal stagnation position.

A.1.2 LAMINAR BOUNDARY LAYER DEVELOPMENT, INSTABILITIES AND TRANSITION

State of laminar boundary layers developing on a gas turbine blade is reviewed in a detailed way by RICHARDS , [33] and DANIELS,[34] . On the suction side of the turbine blade,[33] states that the existence of high free stream turbulence and a

favourable pressure gradient are the major parameters determining the augmented heat transfer levels in the laminar boundary layers. In such a strong acceleration medium, when acceleration parameter K is greater than 0.15×10^{-5} a normal transition based on a certain momentum thickness Re number will not occur even with external turbulence levels as high as $\sim 5\%$, [33]. A normal transition is prevented by the strong acceleration of the mainstream fluid. A survey of the transition process on the suction side and the pressure side is given by [34]. A number of transition criterions are also discussed in CEBECI and BRADSHAW , [35]. Laminar to turbulent transition induced by the separation and the reattachment of a laminar boundary layer is reviewed by FERNHOLTZ , [36].

An argument about the unstable behaviour of boundary layers developing on concave surfaces was first introduced by von KARMAN, in 1934. Later on, Goertler examined the stability of a laminar boundary layer and showed the existence of a row of parallel vortices with the vorticity vector aligned with the streamwise direction. KEMP,[37] carried out an experimental investigation on a large scale turbine blade. Using surface flow visualization and pitot traverses, he showed the existence of counter rotating Taylor-Goertler vortex system on the pressure side. From a study of his pitot profiles, one may conclude that the transport processes on the pressure side of a turbine blade are much higher than in the laminar boundary layer developing on a flat plate. A visual study of pressure side boundary layer has been performed by HAN and COX,[38]. The investigation revealed the existence of the Goertler's vortices in smoke visualization tests in the range from $Re = 7.9 \times 10^5$ to 10.3×10^5 . The authors mention about the difficulties to describe the origin of the vortices. HAN and COX 's discussion on the origin of Goertler's vortices leads to the conclusions that the observed vortices were not those originating in the stagnation region as suggested by KESTIN and WOOD ,[21] and SADEH ,[22] . Transition of the laminar boundary layer on the concave side of the airfoil is strongly influenced by the curvature induced Goertler's vortices. Transition seems to occur right after the

initiation of the concave curvature, very close to the leading edge. MARTIN and BROWN , [39] studied factors influencing heat transfer to the pressure surfaces of gas turbine blades. They conclude that , boundary layer transition on the pressure side appears to be primarily controlled by the interaction between Taylor Goertler vorticity and mainstream turbulence in terms of a transition Goertler number which diminishes with increasing mainstream turbulence.

A-1.3 TURBULENT BOUNDARY LAYERS ON A TURBINE BLADE

Turbulent boundary layer behaviour in turbomachinery is discussed in a paper by BRADSHAW , [40]. He points out a number of important factors as far as turbomachinery flows are concerned. Almost the same tabulation of such effects are given by DANIELS , [34]. Turbulent flow on a turbine blade may be investigated from the viewpoint of the factors as follows.

THREE DIMENSIONAL EFFECTS : For the blade sections sufficiently far away from the root or tip of the blade, the three dimensional effects have shown to be negligible, by HORLOCK , [41]. Later on, JOHNSTON , [42] supported this conclusion. Secondary flows within turbomachinery blading have been investigated by MARCHAL and SIEVERDING , [43]. Under the influence of a variation of the inlet boundary layer thickness and the blade loading, a very detailed study of three dimensional structures are presented, both for a compressor and a turbine cascade. Results of laser illumination, oil flow visualisation and 5 hole probe measurements indicate that due to the existence of the blade leading edge, the approaching boundary layer separates from the endwall resulting in a vortical structure wrapping along the suction side. Suction side leg of the leading edge vortex, then interacts with the secondary flow, generated by the cross channel pressure gradient. The two vortical structures rotates in opposite direction with respect to each other. The

pressure side leg of the leading edge vortex form a passage vortex. Very complicated 3 D flows originates and interacts in a turbine cascade as shown by MARCHAL and SIEVERDING ,[43];the influence of all those structures are quite negligible on the development of the boundary layers at the mid span of a turbine blade. However,such effects may become pronounced when the aspect ratio of the blading is reduced.

STRONG FAVOURABLE PRESSURE GRADIENT : MORETTI and KAYS ,[44] reports substantial reductions in local Stanton number as a consequence of acceleration of the main stream. Significant drop of the St is achieved.LAUNDER and JONES,[45], [46] and BACKWELDER and KOVASNAY ,[47] also showed that strongly favourable pressure gradients may change the structure of a turbulent boundary layer.LAUNDER and JONES have suggested that when the acceleration parameter $K = \frac{v}{U^2} \frac{dU_\infty}{dx}$ exceeds 2×10^{-6} ,relaminarization effects become significant.In a typical high pressure turbine stage,approximate values for K varies from 4×10^{-6} to 30×10^{-6} on the pressure surface of a turbine blade ,DANIELS ,[34].On the pressure side,relaminarization trends and an augmentation in transport properties due to its concave curvature are superposed on each other and makes this side very difficult to predict.Theoretical predictions of a turbulent boundary layer development under the influence of strong favourable pressure gradient made using a finite difference calculation procedure are compared to experimental data ,in KRESKOWSKY,SHAMROTH,Mc DONALD, [48].The turbulence model used is governed by an integral form of the TKE equation.

CURVATURE EFFECTS ON THE DEVELOPMENT OF TURBULENT BOUNDARY LAYERS : In recent years,numerous investigators showed that,streamline curvature in the plane of mean shear,produces important changes in the turbulence structure of shear layers.These changes are usually an order of magnitude more important than normal pressure gradients and other explicit terms appearing in the mean motion equations for curved flows, BRADSHAW,[49].The momentum and heat transfer effects are very important on highly cambered turbomachinery blades where

turbulence may be nearly eliminated on highly convex surfaces, while on highly concave surfaces, momentum transfer by quasi-steady longitudinal vortices dominates the ordinary turbulence process.[49]. distribution for a gas turbine rotor blade is presented in fig.18,[99] .Suction side is dominated by a convex curvature, while on the pressure side a concavely curved surface is followed after a convex leading edge part.Especially,for the turbine blades which are film cooled on the leading edge,a very early transition of the suction side and pressure side boundary layers near the leading edge is expected due to artificial roughening of the leading edge because of film injection.As a result of such an early transition,the already turbulent boundary layers developing near the leading edge,following the highly curved streamlines of this region are under the strong influence of the strong curvature.In laminar boundary layers, the effects of streamwise curvature are second order in terms of δ/R ,the strength of curvature parameter. Van DYKE ,[50].BRADSHAW,[49] showed that,for turbulent boundary layers ,significant effects on skin friction and heat transfer are seen even when δ/R is as small as 0.01 and the curvature effect is even greater as δ/R grows,GILLIS et al. ,[50],SIMON et al.,[51].ADAMS and JOHNSTON ,[52] presents an improved curvature model for the computation of turbulent boundary layers with convex longitudinal curvature. For strong curvature,GILLIS et al.,[50] and SO and MELLOR ,[53] have shown that,turbulent shear stress is rapidly destroyed by negative turbulent stress production. Such a stabilization also causes the turbulent kinetic energy to drop in the curved region .The turbulent kinetic energy drop is especially strong in the outer part of the layer.GILLIS ,[50] evaluated mixing length profiles from measured turbulent shear stress data using,

$$l^2 = - \frac{\overline{u'v'}}{\frac{\partial U}{\partial y}} \quad : \quad (A.6)$$

The mixing length profiles obtained from eq.(A.6) are presented in [52] for different regions having different radius of curvatures.A typical model for mixing length profiles for inner and outer layers of a boundary layer growing on a highly curved surface is given by ADAMS and JOHNSTON ,[52] .Nearer the wall,in the log region the same investigators followed the idea of BRADSHAW [49] who proposed that the dissipation length scale is related to the Richardson number which is the ratio of Coriolis forces to viscous forces.The work of BRADSHAW,[49] and SO ,[54] suggest that,in flows with streamline curvature,the turbulent mixing length λ should be modified to read,

$$\lambda = \lambda_0 \left(1 - \frac{1}{2} \beta \text{Ri}\right)^{3/4} \quad (\text{A.7})$$

where λ_0 is the mixing length on a flat wall.Ri is the gradient Richardson number defined as,

$$\text{Ri} = S_c (1 + S_c) \quad (\text{A.8})$$

$$S_c = \frac{2 \frac{U}{R}}{\frac{\partial U}{\partial y}} \quad (\text{A.9})$$

assuming that ,there is no rotation.Mixing lengths are generally augmented through negative (concave) curvature and stabilized through positive (convex) curvature values as it appears in S_c ,eq.(A.9) . β is a constant whose value is generally set between 1.0 and 10.0 ,EIDE and JOHNSTON,[58].SO ,[54] suggests a value of $\beta = 6.0$.Recent studies by GIBSON,[55] and SO,[54] indicate that the assumption of constant turbulent Prandtl number may not be valid under the influence of streamline curvature.This is specially true in the outerpart of the boundary layer where the influence of the

streamline curvature on the turbulence field is most pronounced. Comparisons of calculated and measured effect of streamline curvature on St number is given by SO,EDELFELT,ELOVIC,[56].A detailed investigation of turbulent boundary layer flow and structure on a convex wall and its redevelopment on a flat wall is reported by GILLIS and JOHNSTON,[59].

EFFECT OF FREE STREAM TURBULENCE : At present, very limited amount of information about the intensity or scale of the real engine turbulence is available. LAUNDER and YORK ,[59] suggested that turbulence levels as high as 30 % may be possible. According to TURNER ,[60] free stream turbulence intensity has a significant effect on the mean heat transfer rate and he reports that as TU_∞ increases from 0.6 to 5.9 %, a 40 % increase in the heat transfer coefficient may occur. Up to now, as a result of the basic research on flat plates, disturbances in the free stream velocity are known to accelerate transition ,increase the growth rate of the boundary layer and increase the skin friction,DANIELS,[34].Bradshaw ,[58] reports at least 10 % C_f increase due to a 3 % TU_∞ change in the free stream. He also quotes that heat transfer is dependent upon the complete statistical description of the free stream disturbances and not just on the longitudinal velocity component fluctuation.

Combustion system creates very large turbulence intensities and R.M.S. velocity fluctuations of up to 20 % as far as the nozzle guide vane leading edges are concerned. These extreme variations are partially suppressed by expansion through nozzle guide vanes. But the rotor blades experience not only the remaining mainstream velocity fluctuations but also the variations between those average values and the lower values in the wakes behind the nozzle trailing edges. Those latter may occur at the blade passing frequency typically at ~ 10 KHz.

,RICHARDS, [33].

Free stream turbulence and its scale is very difficult to simulate in a cascade facility as far as actual engine conditions are considered. According to SCHULTZ,OLDFIELD and JONES,[61] ,turbulence in an aero engine is extremely inhomogeneous and U'/U levels vary from 12 to 14 %. U'/U may be as much as 18 % at blade root and tip due to 3 D behaviour and secondary flows in these regions. First of all,turbulence has spatial nonuniformities in an engine. On the other hand,even a free stream intensity level close to 10 % has not so far been possible in most of the experimental facilities,SCHULTZ et al.[61]. In the Oxford university free piston tunnel,turbulence levels of up to 4 % could be achieved,[34].In the VKI CT-2 compression tube facility, TU_{α} levels up to 5 - 6 % has so far been used,CONSIGNY and RICHARDS ,[62]. According to CONSIGNY [62] and DANIELS [34]'s observations,using conventional upstream bar grids is an effective way of promoting transition early on the suction surface of a turbine blade.On the suction side,laminar to turbulent transition advances upstream as the turbulence level increased.After the transition region, wall heat fluxes increase by factor of two compared to the values before transition, CONSIGNY [62].Near the trailing edge,flow becomes increasingly turbulent with increase in free stream turbulence. The time required to settle the turbulence in a transient facility is an important parameter.This has been investigated by SCHULTZ ,[61], from the wiewpoint of grid generated turbulence.The turbulence structure behind the grids of a transient facility was established in the time scale of the experiments.It takes 5 msec. for the wakes behind the turbulence grid bars to extend to 100 bar diameters when the inlet Ma number is around 0.3,typically.

Up to now,turbulence intensity has traditionally been regarded as the principal turbulence parameter ,but DYBAN and EPIK [63] suggest that each of the threee components of velocity fluctuation,the energy spectrum and the correlation coefficient and the so called intermittency factor need to be known to

define precisely a turbulent flow. Ishigaki,[64] showed that mainstream velocity fluctuations associated with artificially induced mainstream turbulence influences the local heat transfer rates. He also showed that under such conditions the frequency of the perturbations as well as their intensity is important in determining the convection process. Such effects may be important for the case of turbine rotor blades where rotor blade speed may change. The change in the rotor blade speed may induce the frequency of the perturbations in flow velocity.

LOW MOMENTUM THICKNESS REYNOLDS NUMBER BEHAVIOUR : At present, the physics of the turbulent processes in a low Re number boundary layer is not well understood. According to DANIELS [34], viscous effects in the outer region of the boundary layer and at the interface between the boundary layer and the free stream seem to be the most likely the cause. BUSHNELL et al. , [66] indicates a possibility that the low Re effects are caused by disturbances generated in the transition region. At low Re numbers the transport processes are higher than one would expect from simple theories and extrapolation from normal turbulent boundary layers, BRADSHAW , [40].

SHOCK BOUNDARY LAYER INTERACTIONS : Under transonic operating conditions shock boundary layer interaction can have a very profound influence on the aerodynamic performance of the turbine blading. separation as a result of the shock boundary layer interaction effects the aerodynamic performance and the local heat transfer rates to the blade. The general aspects of the shock boundary layer interaction in turbomachinery cascades have been studied by GRIEPENTROG, [68]; GADD, [69]; PEARCEY , [71]; SEDDON, [72]; MC DEVITT, [73]; BALDWIN, [74]; PANARAS, [75]. BACK and CUFFEL,[76] states that the temperature of the wall may have an important effect on shock boundary layer interaction, especially in cooled turbulent boundary layers. Detailed reviews of various aspects of the phenomena is presented by OATES,[77]; GREEN,[70]; HANKEY and HOLDEN,[78] .

ROUGHNESS EFFECTS : A very important factor influencing the heat transfer on a turbine blade is surface roughness resulting from corrosion, erosion and deposits in the very harsh operating medium of the aeroengine. The prime influence of the surface roughness, is on the losses on a turbine blade. BÄMMERT and SANDSTEDE [90] studied the boundary layer behaviour along a turbine blade with rough surfaces. They found momentum thicknesses up to 3 times as great as that on smooth surfaces. They also observed a rise in the friction factor and a shift of the transition location on the suction side due to roughness. This study indicates that, rough wall turbulent boundary layers may show higher wall heating rates through an analogy between skin friction and heat transfer, compared to the ones developing on smooth ones.

APPENDIX-2

FILM COOLING HYDRODYNAMICS AND HEAT TRANSFER ON FLAT WALLS

GOLDSTEIN, ECKERT and RAMSEY [91], studied the variation of adiabatic wall temperature downstream of a film cooling injection hole. The boundary layer along the wall from which the heated jet issues at an angle of 35 degrees is turbulent. The flow field associated with an inclined jet interacting with a mainstream is shown in fig. 12 as given by GOLDSTEIN et al. in [91]. A qualitative description of coolant jet free stream interaction is given by ABRAMOWICH,[15]; KEFFER et al [16]. As shown in fig. 12, as the secondary coolant jet leaves the injection hole, it slows down the main flow along the upstream side of the jet, causing a pressure rise on this side of the jet. The pressure difference between the upstream and downstream side of the jet deforms the jet. Circulatory motions are caused by the intensive intermixing of the two flows. The deformation of the jet is affected by the coolant to free stream mass flux rate ratio which is also defined as the blowing rate . GOLDSTEIN et al [91] found considerably different film cooling effectiveness than the slot cooling situation. Discrete hole film cooling in the presence of free stream turbulence and strong favourable pressure gradient have been investigated by LAUNDER and YORK , [92]. The main finding of their study is that, steep streamwise accelerations delays the transition of the jet from laminar to turbulent, improving the streamwise effectiveness of discrete

hole film cooling. A secondary influence of acceleration has been found to be reduced lateral spread of the coolant jet, LAUNDER [92]. LOUIS et al., [93] made short suration studies of turbine heat transfer and film cooling effectiveness in a shock tunnel. Isothermal wall effectiveness downstream of a single hole blowing at $m=0.4$ and 0.6 are shown in fig.31. During the tests, their Re and T_w/T_{∞} range were simulated adequately for gas turbine applications. Effects of density and velocity ratio on discrete hole film cooling is a paper published by FOSTER and LAMPARD , [110]. Their results presented that film cooling effectiveness is dependent upon the coolant to free stream density ratio, in addition to velocity ratio. Measurements are reported of the flow created by the injection of a circular jet at 30 deg. through a plane wall into an external stream, by BERGELES, GOSMAN, LAUNDER, [94]. Upstream influence of the injected jet has been found to be small at 30 deg angled injection compared to 90 deg. normal injection case. Fig.32 shows the distrubutions of static pressure in the vicinity of the hole for various values of blowing rate $m = \rho_c U_c / \rho_{\infty} U_{\infty}$. The plotted value is the pressure coefficient C_p which is defined as,

$$C_p = \frac{P - P_{ref}}{\frac{1}{2} \rho_c U_c^2} \quad (A.10)$$

where P_{ref} is the undisturbed static pressure at the upstream of the hole. A positive C_p value representing an excess in the local static pressure because of film cooling is due to the free stream deceleration or deflection because of the coolant jet which is almost acting like a solid wall disturbance. Acceleration appears as negative pressure coefficients downstream of the hole. At a low blowing rate of $m=0.2$ wall static pressure changes because of injection. The isobar lines becomes narrower both in spanwise and streamwise directions with increasing blowing rate on the wall surface. This is due to the fact that more coolant fluid is sent to the outer layer of the boundary layer and wall effects becomes less appreciable with increasing blowing rates. Typical velocity

profiles just after double rows of film cooling holes are given in fig.33 by BERGELES et al.,[95].These are centerline profiles at different streamwise stations for a boundary layer having a thickness of almost one hole diameter at just downstream of the injection rows.At all measurement stations downstream of second row of holes,velocity profiles show important deficits.The maximum deficit occurs in the profile closest to the hole.Very close to the wall at all the locations,velocity gradients are lower than no cooling profiles.This may cause lower friction factors at the wall.The profiles tend to recover to no injection profiles with increasing downstream distance.For $m=0.5$ the height of the velocity defect region is almost constant at a value of $y/d=.8$.A very slight increase in the penetration distance of the jet is also observed from these profiles.PEDERSEN,ECKERT and GOLDSTEIN,[96] investigated film cooling with large density differences between the mainstream and the secondary fluid measured by an heat and mass transfer analogy.A porous slot and single row of 15 holes spaced 3 hole diameters apart has been studied.The injection angle was 35 deg. toward the plate surface in main flow direction.They found a strong effect of density ratio on the film effectiveness for injection through holes.They also noted that the centerline effectiveness increases with a decreasing ratio of boundary layer thickness to hole diameter ratio.A study of adiabatic wall temperature and heat transfer downstream of injection through two rows of holes is given by JABBARI and GOLDSTEIN ,[97].A review of the literature on discrete hole film cooling with single row of holes is also presented in this reference.Maximum effectiveness occurs along the centerline of the downstream holes and the minimum effectiveness at 1 hole diameter away from the centerline.The film cooling effectiveness from staggered double row of holes increases with increasing blowing rate and unlike the effectiveness from single row of holes,it does not decrease as the blowing rate increases over 0.5,[97].Thickening of the approaching boundary layer reduces the centerline effectiveness. Increasing blowing rate m ,improves adiabatic wall effectiveness till an optimum value is reached for a single row injection situation;further increase in blowing rate decreases

effectiveness particularly at locations very close to the injection location,[97].The cooling effectiveness of double row of staggered holes increases with increasing blowing rate.Effectiveness does not decrease with further increases in m over an optimum blowing rate.A comparison of effectiveness for single row of holes and double rows of holes in a blowing rate range from 0.1 to 2.2 is shown in fig.34 Effects of hole geometry and coolant density on three dimensional film cooling is presented by GOLDSTEIN,ECKERT and BURGRAFF,[98].They quote significant gains in adiabatic wall effectiveness by shaping the cylindrical film cooling holes at the exit of the hole.They report appreciably higher film cooling effectivenesses with a higher density coolant than when air is injected. CO fog visualization shows that, the jet from the shaped hole lies much closer to the surface while the jet from the cylindrical hole penetrates into the mainstream.At large distances downstream of a jet, the lateral adiabatic wall effectiveness distributions are smoothed out.The effect of shaped hole is more pronounced at high blowing rates when $m > 0.40$.Film cooling effectiveness with double row of holes has been reported by AFEJUKU,HAY and LAMPARD ,[99].They compare a staggered configuration with an in line configuration.They also report that,normal injection gives lower effectivenesses compared to a 35 deg. injection angle with the wall,in the mainstream direction.

Sellers hypothesized that individual data sets from single row film cooling situations can be used in order to evaluate the adiabatic film cooling effectiveness at downstream of multi row injection sites, [100]. For the case of multi row injection, at downstream of an injection location ,one may hypothesize the resulting adiabatic wall temperature of the upstream injection row , as the mainstream total recovery temperature assigned to the downstream injection location .Adiabatic wall effectiveness for individual injection locations ,

$$\eta_1 = \frac{T_{0\infty} - T_{aw1}}{T_{0\infty} - T_{C1}} \quad (A.11)$$

$$\eta_2 = \frac{T_{0\infty} - T_{aw2}}{T_{0\infty} - T_{C2}} \quad (A.12)$$

For the case of double row injection,

$$\eta = \frac{T_{0\infty} - T_{aw}}{T_{0\infty} - T_c} \quad (A.13)$$

, by definition and where $T_{c_2} = T_{c_1} = T_c$

Using Seller's hypothesis,[100], the effectiveness at downstream of the second injection location,

$$\eta_2 = \frac{T_{aw_1} - T_{aw}}{T_{aw_1} - T_c} \quad (A.14)$$

$$T_{aw} = \eta_2 \cdot T_c + (1-\eta_2) \cdot T_{aw_1} \quad (A.15)$$

$$T_{aw_1} = T_{0\infty} - \eta_1 (T_{0\infty} - T_c) \quad (A.16)$$

Inserting eq.(A.14) into eq.(A.15)

$$T_{aw} = \eta_2 \cdot T_c - (1-\eta_2) \cdot \left[T_{0\infty} - \eta_1 (T_{0\infty} - T_c) \right] \quad (A.17)$$

$$T_{aw} = \eta_2 \cdot T_c + (1-\eta_2) \left[\eta_1 T_c + T_{0\infty} (1-\eta_1) \right] \quad (A.18)$$

Eq.(A.13) defines η as follows,

$$\eta = \frac{T_{0\infty} - T_{aw}}{T_{0\infty} - T_c} = \frac{T_{0\infty} - \eta_2 T_c - (1-\eta_2) \left[\eta_1 T_c + T_{0\infty} (1-\eta_1) \right]}{(T_{0\infty} - T_c)} \quad (A.19)$$

$$\eta = \frac{T_{0\infty} (\eta_2 - 1 - \eta_1 \eta_2 + \eta_1) + T_c (\eta_1 \eta_2 - \eta_1 - \eta_2)}{(T_{0\infty} - T_c)} \quad (A.20)$$

$$\eta = 1 - (1-\eta_1)(1-\eta_2) \quad (A.21)$$

When there are n rows of film cooling holes, at a location downstream of the n th row of holes, the total adiabatic wall effectiveness may be predicted, as follows,

$$\eta = \sum_{i=1}^n \eta_i \cdot \prod_{j=0}^{i-1} (1-\eta_j) \quad (A.22)$$

A comparison of the measured adiabatic wall effectiveness data from double row of staggered holes with the predictions made using single row of holes measurements through Seller's superposition hypothesis is presented by AFEJUKU et al., [99]. Their data is under-predicted at high blowing rates. SASAKI et al., [102] presented film cooling effectiveness for injection from multirow of staggered holes using an infrared imaging system, on an adiabatic flat plate. They demonstrated the

additive nature of film cooling in the presence of mainstream pressure gradient, experimentaly. They found slightly higher centerline adiabatic wall effectiveness with a moderate mainstream acceleration in a blowing rate range from $m=0.1$ to $m=1.1$, than zero pressure gradient case.

LIESS , [101] performed an experimental study of film cooling from a row of inclined circular holes, on a flat plate. As a result of his investigations on adiabatic walls, he found that Ma number and Re number have no measurable effect on the film cooling parameters. He suggests to apply the results of low speed tests to turbine blades with local Ma numbers up to $Ma=0.9$. He found that, increasing displacement thickness to hole diameter ratio decreases the adiabatic wall effectiveness, considerably for $\delta/d > 0.20$. The presence of a favourable pressure gradient in the main flow can cause a considerable reduction of the adiabatic wall effectiveness, especially at low blowing rates. GOLDSTEIN and YOSHIDA , [102] investigated the influence of a laminar boundary layer and laminar injection on film cooling performance, using single row of cooling holes. They use a very low speed mainstream flow, in order to simulate the low momentum thickness Re behaviour of a gas turbine blade leading edge on an adiabatic flat plate. They also suggest that, coolant film may be laminar in the film injection holes at low blowing rates. Laterally averaged adiabatic film cooling effectivenesses are shown in fig.35 for $m=0.5$ and $m=0.99$. They concluded that when a turbulent coolant jet enters a laminar boundary layer, somewhat higher heat transfer coefficients are observed than with the laminar jet and the laminar boundary layer. They reported no significant difference in heat transfer for both a laminar coolant and a turbulent coolant jet, in a fully turbulent mainstream boundary layer. They found that, when the approaching boundary layer is laminar, higher effectivenesses with turbulent cooling jets occur compared to a turbulent approaching boundary layer.

Effect of wall to free stream temperature ratio and coolant to free stream temperature ratio on the film cooling process has been studied by LOFTUS and JONES,[103].They also investigated the effect of a prescribed wall temperature on turbulent boundary layer behaviour.They found that, when the wall temperature is smaller than the free stream temperature, the effect of gas to wall temperature ratio on flat plate heat transfer is small.

The effect of surface curvature,Re number,Ma number and pressure gradient has been investigated by RICHARDS,VILLE and APPELS,[104].Heat transfer investigation of a film cooled flat plate with and without a strong pressure gradient has been studied by CAMCI,LIGRANI and HAY,[105]. Measurements of wall heat flux,adiabatic wall effectiveness and isothermal wall effectiveness are presented for three different coolant temperatures in a range of blowing rates, at downstream of the three sets of double row injection rows.Fig.36 shows adiabatic wall effectiveness distributions,downstream of injection locations.For the case of favourable pressure gradient,slightly higher effectiveness values may be due to thinning of the mainstream boundary layer or increasing thickness of the viscous sublayer.

Effect of surface roughness on film cooling performance on a flat plate was investigated by GOLDSTEIN,ECKERT,CHIANG and ELOVIC.[118].Adiabatic wall effectiveness measurements from a gas chromatography technique were reported for one and two rows of holes.Helium is used as the secondary fluid providing a density ratio of $\rho_c/\rho_\infty = 1.0$.They observed a reduction in η of the order of 10 to 20 % at low blowing rates,relative to a smooth surface.However at higher blowing rates,very significant η increases (as much as 40 - 50 %) were reported.Their explanation was " greater turbulence and mixing with the rough surface which tends to dissipate the injected flow and prevent it from penetrating as far into the mainstream" .A relatively uniform lateral distribution of η as compared to that of a smooth surface was found for injection through a single row of

holes on roughened surfaces.

APPENDIX-3

WALL HEAT FLUX MEASUREMENT DETAILS

A-3.1 TRANSIENT HEAT CONDUCTION IN A SEMI-INFINITE BODY

The one dimensional differential equations describing heat conduction across a metallic thin film and its substrate are written as follows, (fig.53):

$$\frac{\partial^2 \theta_1}{\partial x^2} = \frac{1}{\alpha_1} \cdot \frac{\partial \theta_1}{\partial t}$$

$$\theta = T(x,t) - T(\infty)$$

$$T(x,t) = T(\infty) \quad \text{at } x = \infty$$

and

$$\frac{\partial^2 \theta_2}{\partial x^2} = \frac{1}{\alpha_2} \cdot \frac{\partial \theta_2}{\partial t} \quad (\text{A.23})$$

$\alpha = \frac{k}{\rho c}$ is the thermal diffusivity of the considered material. These equations have to satisfy the following boundary conditions:

$$-k_1 \cdot \frac{\partial \theta_1}{\partial x} = \dot{q}_s \quad \text{at } x = 0 \quad (\text{a})$$

$$k_1 \cdot \frac{\partial \theta_1}{\partial x} = k_2 \frac{\partial \theta_2}{\partial x} \quad \text{at } x = \epsilon \quad (\text{b})$$

$$\theta_1 = \theta_2 \quad \text{at } x = \epsilon \quad (\text{c})$$

$$\theta_2 = 0 \quad \text{at } x = \infty \quad (\text{d}) \quad (\text{A.24})$$

Equation (A.24.c) expresses an important assumption,i.e. the substrate is semi-infinite.

Furthermore,one assumes that conduction effects across the film are negligible and hence,that the film is at a uniform temperature because of its small thickness ϵ If ϵ tends to zero,equations (A.24) and (A.25) become :

$$\frac{\partial^2 \theta}{\partial x^2} = \frac{1}{\alpha} \cdot \frac{\partial \theta}{\partial t} \quad (\text{A.25})$$

which has to verify the following boundary conditions:

$$\theta = 0 \quad \text{at } x = \infty \quad (\text{A.26a})$$

$$-k \cdot \frac{\partial \theta}{\partial x} = \dot{q}_s \quad \text{at } x = 0 \quad (\text{A.26b})$$

The initial condition for equation (A.25) is written as follows:

$$\theta = 0 \quad \text{at } t = 0 \quad \text{for all } x \quad (\text{A.26c})$$

The application of a Laplace transformation to the right hand side of equation (A.25) provides the following relation:

$$\mathcal{L}\left(\frac{\partial \theta}{\partial t}\right) = \left[\theta(t=\infty) - \theta(t=0) + S\bar{\theta}\right] \quad (\text{A.27})$$

whereas the left hand side becomes:

$$\mathcal{L}\left(\frac{\partial^2 \theta}{\partial x^2}\right) = \frac{1}{\alpha} \cdot \mathcal{L}\left(\frac{\partial \theta}{\partial t}\right) \quad (\text{A.28})$$

$$\frac{\partial^2 \bar{\theta}}{\partial x^2} = \frac{1}{\alpha} \cdot \left(\theta(t=\infty) - \theta(t=0) + S\bar{\theta} \right) \quad (A.29)$$

$$\frac{\partial^2 \bar{\theta}}{\partial x^2} - \frac{1}{\alpha} \cdot S \cdot \bar{\theta} = \frac{1}{\alpha} \cdot \left(\theta(t=\infty) - \theta(t=0) \right) \quad (A.30)$$

The solution of this ordinary differential equation is written under the following form:

$$\bar{\theta} = \frac{1}{\alpha} \left(\theta(t=\infty) - \theta(t=0) \right) + A \exp\left(\sqrt{\frac{\rho c}{k}} S \cdot x\right) + B \exp\left(-\sqrt{\frac{\rho c}{k}} S \cdot x\right) \quad (A.31)$$

Evaluating the Laplace transform of the boundary condition (A.26.a), provides the following relation:

$$\bar{\theta} = 0 \quad \text{at } x = \infty \quad (A.32)$$

Substituting equation (A.32) into (A.31) immediately results in,

$$A = 0 \quad (A.32a)$$

Whereas the condition (A.26.b) becomes

$$-k \cdot \frac{\partial \bar{\theta}}{\partial x} = \dot{q}_S \quad \text{at } x = 0 \quad (A.33)$$

The x derivative of equation (A.31) results in the following equation:

$$\frac{\partial \bar{\theta}}{\partial x} = \frac{1}{\alpha} \left[\theta(t=\infty) - \theta(t=0) \right] x - B \sqrt{\frac{\rho c}{k}} S \cdot \exp \left(\sqrt{\frac{\rho c}{k}} S \cdot x \right) \quad (\text{A.34})$$

which, combined with equation (A.33), provides:

$$\dot{q}_s = -\rho c \left[\theta(t=\infty) - \theta(t=0) \right] x + B \sqrt{k} \sqrt{\rho c S} \cdot \exp \left(-\sqrt{\frac{\rho c}{k}} S \cdot x \right) \quad (\text{A.35})$$

At $x=0$, equation (A.31) yields,

$$\bar{\theta}(x=0) = B \quad (\text{A.36})$$

Substituting equation (A.36) into equation (A.35), one gets the following relation to express the wall heat flux rate in the Laplace transform domain:

$$\dot{q}_s = \bar{\theta}(x=0) \cdot \sqrt{k} \cdot \sqrt{\rho c S} \quad (\text{A.37})$$

Replacing $\bar{\theta}(x=0)$ by $\bar{\theta}_s$, the surface temperature variation, yields:

$$\bar{\theta}_s = \frac{1}{\sqrt{\rho c k}} \cdot \frac{\dot{q}_s}{\sqrt{s}} \quad (\text{A.38})$$

The restitution of equation (A.38) in the real time domain is obtained through the following steps :

$$\text{Letting } \overline{f(s)} = \frac{1}{\sqrt{s}} \quad , \quad \overline{g(s)} = \overline{\dot{q}_s} \quad \text{and} \quad (\text{A.39})$$

writing the inverse Laplace transforms

$$\mathcal{L}^{-1}\left[\frac{1}{\sqrt{s}}\right] = f(t) = \frac{1}{\sqrt{\pi t}} \quad \mathcal{L}^{-1}\left[\frac{\dot{q}_s}{s}\right] = g(t) = \dot{q}_s \quad (\text{A.40})$$

According to the convolution theorem, ARPACI, [127], one gets:

$$\mathcal{L}\left[\int_{\tau=0}^t f(t-\tau) \cdot g(\tau) \cdot d\tau\right] = \overline{f(s)} \cdot \overline{g(s)} \quad (\text{A.41})$$

$$\overline{f(s)} \cdot \overline{g(s)} = \frac{\overline{\dot{q}_s}}{\sqrt{s}} = \mathcal{L}\left[\int_{\tau=0}^t \frac{1}{\sqrt{\pi(t-\tau)}} \cdot \dot{q}_s(\tau) \cdot d\tau\right] \quad (\text{A.42})$$

$$\overline{f(s)} \cdot \overline{g(s)} = \overline{\theta_s} \cdot \sqrt{\rho ck} \quad (\text{A.43})$$

taking the inverse Laplace transform of both sides, the surface temperature rise, due to a time dependent surface heat flux rate may be evaluated as,

$$\dot{\theta}_s = \frac{1}{\sqrt{\rho ck}} \cdot \int_{\tau=0}^t \frac{\dot{q}_s(\tau)}{\sqrt{\pi(t-\tau)}} d\tau \quad (A.44)$$

It is important to remember that equation (A.44) provides the variation of the surface temperature with time assuming that:

(1) the film has a negligible effect on heat conduction, ($\epsilon \rightarrow 0$)

(2) the substrate is semi-infinite

(3) the heat transfer into the substrate is one dimensional.

If a constant heat flux is applied ,then a parabolic temperature rise on the surface will be observed.The integration of equation (A.44) provides as a matter of fact the following result:

$$\dot{\theta}_s = \frac{1}{\sqrt{\rho ck}} \cdot \frac{2\dot{q}_s \sqrt{t}}{\sqrt{\pi}} \quad (A.45)$$

where $\dot{\theta}_s = 0$ at $t=0$.

Alternatively, for the wall heat flux, one gets:

$$\dot{q}_s = \frac{\sqrt{\pi}}{2} \cdot \sqrt{\rho c k} \cdot \dot{\theta}_s \quad (\text{A.46})$$

A-3.2 ELECTRICAL ANALOG OF HEAT TRANSFER INTO A SEMI-INFINITE BODY

Although an analytical solution of one dimensional transient heat conduction into a semi-infinite body is provided in equation (A.44), the wall heat flux measurements of the present study have been performed using an electrical analogy. This approach results in a much faster and more precise quantitative determination of the time dependent wall heat flux, compared to its purely numerical evaluation from measured wall temperature data.

An electrical analogy of the flow of heat into a semi-infinite solid can be obtained from a series of resistances and capacitances in which voltages and currents behave similarly to temperatures and heat fluxes, (fig. 54). The behaviour of the analogues becomes obvious by looking at the equations modelling both configurations SCHULTZ and JONES,[126]:

Rate of gain of energy in
an element Δx

$$= - \frac{\partial q}{\partial x} \cdot \Delta x$$

Rate of gain of charge in
an element Δx

$$= - \frac{\partial i}{\partial x} \cdot \Delta x \quad (\text{A.47})$$

which, by conservation of energy, is equal to:

$$= \rho c \cdot \Delta x \cdot \frac{\partial T}{\partial t}$$

which, by conservation of charge, is equal to

$$= c' \cdot \Delta x \cdot \frac{\partial V}{\partial t} \quad (A.48)$$

where r' and c' being the resistance and capacitance per unit length

Thus

$$\frac{\partial q^*}{\partial x} = -\rho c \frac{\partial T}{\partial t}$$

The heat conduction equation is :

$$q = -k \frac{\partial T}{\partial x}$$

Combining the above equations, the diffusion equation is written as follows:

$$\frac{\partial^2 T}{\partial x^2} = \frac{\rho c}{K} \cdot \frac{\partial T}{\partial t} \quad (a)$$

$$\frac{\partial i}{\partial x} = -c' \frac{\partial V}{\partial t} \quad (A.49)$$

Ohm's law is :

$$i = -\frac{1}{r' \Delta x} \frac{\partial V}{\partial x} = -\frac{1}{r'} \frac{\partial V}{\partial x} \quad (A.50)$$

Combining the above equations, the transmission line equation is written as follows:

$$\frac{\partial^2 V}{\partial x^2} = r' c' \frac{\partial V}{\partial t} \quad (b) \quad (A.51)$$

Comparing equations (A.51.a) and (A.51.b), it is obvious that the heat diffusion equation is analogous to the electrical transmission line equation. The Laplace transform of equation (A.51.b) yields:

$$\frac{\partial^2 V}{\partial x^2} = r' c' \left(sV + V(t=\infty) - V(t=0) \right) \quad (A.52)$$

where $V(t=\infty) = 0$

The initial and boundary conditions are as follows:

- (a) $\bar{V} = 0$ at $t = 0$
- (b) $\bar{V} = 0$ at $x = \infty$
- (c) $-\frac{1}{r'} \cdot \frac{\partial \bar{V}}{\partial x} = \bar{i}_{in}$ at $x = 0$ (A.53)

Applying condition (A.53.a) to equation (A.52) and solving this differential equation provides the following relation:

$$\bar{V} = A \cdot \exp\left(x \cdot \sqrt{r' c' s}\right) + B \cdot \exp\left(-x \cdot \sqrt{r' c' s}\right) \quad (A.54)$$

where A and B are constants. Condition (A.53.b) yields A=0. Condition (A.53.c) allows to obtain:

$$\frac{\partial \bar{V}}{\partial x} = -\sqrt{r'c's} \cdot B \cdot \exp\left(-x\sqrt{r'c's}\right) = -\bar{i}_{in} r' \quad (A.55)$$

or alternatively

$$B = \bar{i}_{in} \sqrt{\frac{r'}{c'}} \cdot \frac{1}{\sqrt{s}} \quad (A.56)$$

So, at $x=0$, using equations (A.54) and (A.55), the voltage $\Delta\bar{V}$ measured at the input of the analogue circuit shown in fig.54 is expressed as follows

$$\Delta\bar{V} = \bar{i}_{in} \sqrt{\frac{r'}{c'}} \cdot \frac{1}{\sqrt{s}} \quad (A.57)$$

The circuit input is the thin film output $\dot{\theta}_s$, the surface temperature rise expressed by equation (A.45). This temperature rise is determined from the thin film resistance modification according to the following well known equation:

$$R = R_0 \left(1 + \alpha_R (T - T_0)\right) \quad (A.58)$$

where R is the film resistance at surface temperature T, R_0 the film resistance at temperature T_0 and α_R is the film temperature coefficient. When the film is supplied with constant current, equation (A.58) may be written as :

$$V = V_0 \left(1 + \alpha_R (T - T_0)\right) \quad (A.59)$$

If the reference voltage V_0 is then measured at the initial temperature before a test then $T(x=0) = T_0$ and :

$$\Delta V = \alpha_R \cdot V_0 \cdot \dot{\theta}_S \quad (A.60)$$

ΔV is the film output voltage $V - V_0$. In a Laplace transformed form, one gets:

$$\Delta \bar{V} = \alpha_R \cdot V_0 \cdot \bar{\theta}_S \quad (A.61)$$

Substituting equation (A.61) into (A.57) yields the following relation:

$$\bar{i}_{in} = \sqrt{s \frac{c'}{r'}} \cdot \alpha_R \cdot V_0 \cdot \bar{\theta}_S \quad (A.62)$$

$$\bar{i}_{in} = \sqrt{\frac{c'}{r'}} \cdot \alpha_R \cdot V_0 \cdot \sqrt{s \cdot \bar{\theta}_S} \quad (A.63)$$

Now the heat conduction equation analogous to equation (A.63) is equation (49) :

$$\dot{q}_S = \sqrt{\rho c k} \cdot \sqrt{s} \cdot \bar{\theta}_S \quad (A.64)$$

Substituting for $\bar{\theta}_S$ in equation (A.62) gives the following relation :

$$\dot{q}_S = \sqrt{\rho c k} \cdot \sqrt{\frac{r'}{c'}} \cdot \frac{1}{\alpha_R V_0} \cdot \bar{i}_{in} \quad (A.65)$$

For the analogue termination shown in fig.54, equation (A.65) becomes:

$$\dot{q}_s = \sqrt{\rho c k} \cdot \sqrt{\frac{r'}{c'}} \cdot \frac{1}{\alpha_R V_0} \cdot \frac{V_{out}}{R_1} \quad (A.66)$$

A calibration of these electrical analogues can be obtained by applying a step in heat flux ($\dot{q}_s = \text{constant}$), their calibration coefficient A/β is defined by the following equations,

$$\dot{q}_s = \frac{\sqrt{\pi}}{2} \cdot \frac{\sqrt{\rho c k}}{\sqrt{t}} \cdot \frac{\Delta V}{\alpha_R V_0} = \sqrt{\rho c k} \cdot \sqrt{\frac{r'}{c'}} \cdot \frac{1}{\alpha_R V_0} \cdot \frac{V_{out}}{R_1} \quad (A.67)$$

$$\frac{A^*}{\beta} = \sqrt{\frac{r'}{c'}} \cdot \frac{1}{R_1} = \frac{\Delta V}{2V_{out}} \cdot \sqrt{\frac{\pi}{t}} \quad (A.68)$$

During the calibration process a parabolic voltage variation ΔV corresponding to the time rise of the surface temperature $\dot{\theta}_s$ is applied into the circuit, (fig.55). The response of the analogue circuit to this signal is a steplike output signal V_{out} which is proportional to the wall heat flux rate, (fig.56). The A/β representing the analogue circuit behaviour coefficient obtained from equation (A.68) does not vary with time because ΔV is proportional to $t^{1/2}$, by definition.

The heat flux measured by a gauge operating at $T_\infty = T_e$ is obtained by substituting A^*/β into equation (A.66) :

$$\dot{q}_s = \frac{V_{out}}{V_0} \cdot \frac{\sqrt{\rho c k}}{\alpha_R} \cdot \frac{A^*}{\beta} \quad (A.69)$$

The latter equation is then used for heat transfer data evaluation, applying an additional temperature correction on α_R :

$$\dot{q}_s = \frac{V_{out}}{V_0} \cdot \frac{\sqrt{\rho c k}}{\alpha_R} \cdot \frac{A^*}{\beta} \left[1 + \alpha_R (T_0 - T_\infty) \right] \quad (A.70)$$

where T_0 is the temperature at which α_R has been evaluated and T_∞ is the temperature of the model just before a test.

APPENDIX-4

TURBULENT SHEAR STRESSES

X directional time averaged momentum equation in two dimensions,

$$\rho U \frac{\partial U}{\partial x} + \rho V \frac{\partial U}{\partial y} = - \frac{dp}{dx} + \frac{\partial}{\partial y} \left(\mu \frac{\partial U}{\partial y} - \rho \bar{u'v'} \right) + x \quad (A.71)$$

Pressure gradient in terms of free stream velocity and body force

$$- \frac{dp}{dx} = \rho_{\infty} U_{\infty} \frac{dU_{\infty}}{dx} - x \quad (A.72)$$

Turbulent shear stress is modelled through an eddy diffusivity concept as,

$$-\bar{u'v'} = \epsilon_m \frac{\partial U}{\partial y} = \frac{\mu_t}{\rho} \cdot \frac{\partial U}{\partial y} \quad (A.73)$$

TURBULENT HEAT FLUXES

The stagnation enthalpy equation

$$\rho U \frac{\partial I^*}{\partial x} + \rho V \frac{\partial I^*}{\partial y} = \frac{\partial}{\partial y} \left[\frac{k}{c} \frac{\partial I^*}{\partial y} - \overline{i^*'v'} + \mu \frac{\partial}{\partial y} \frac{U^2}{2} \right] + S \quad (A.74)$$

$$I^* = I + \frac{U^2}{2} \quad (A.75)$$

where S is the energy source term.

$\overline{i^*'v'}$ is the term dealing with the fluctuations in the stagnation enthalpy and cross stream velocity

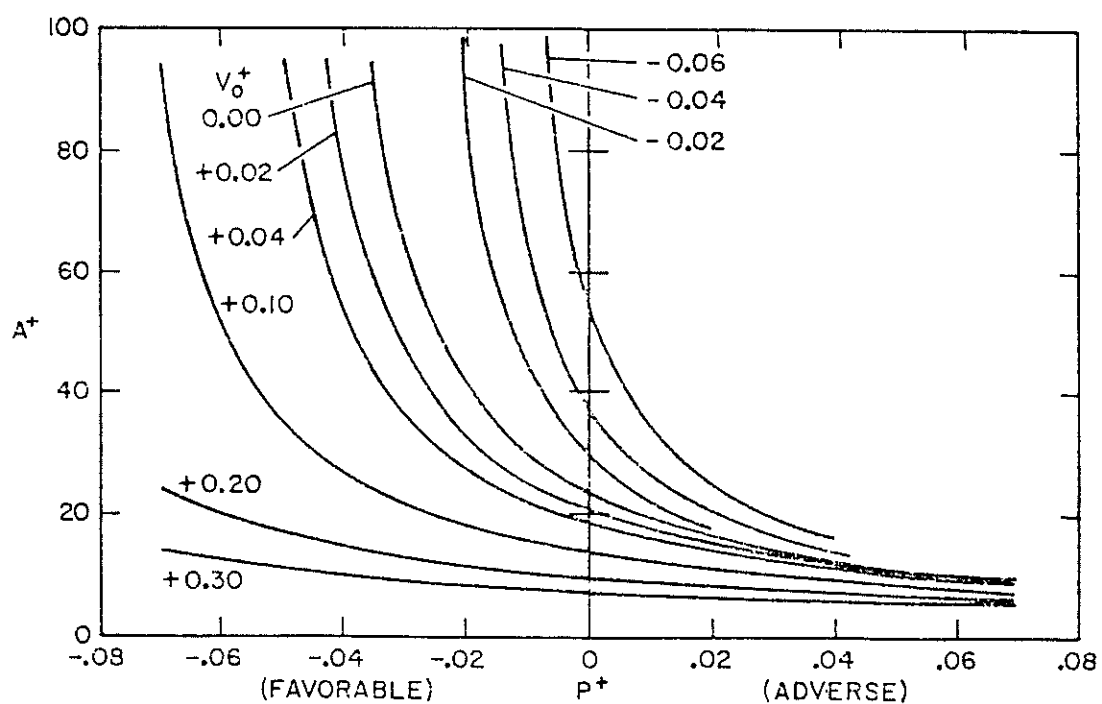
$$\overline{-i^*'v'} = -\overline{i^*v'} + U(-\overline{u'v'}) \quad (A.76)$$

where $\overline{i^*}$ is fluctuation in static enthalpy. The turbulent heat flux ($-i^*v'$) is modelled as,

$$-\overline{i^*v'} = \epsilon_H \frac{\partial I}{\partial y} = \left(\frac{k_t c}{\rho} \right) \frac{\partial I}{\partial y} \quad (A.77)$$

APPENDIX-5

VISCOUS SUBLAYER THICKNESS AS A FUNCTION OF PRESSURE GRADIENT, KAYS and MOFFAT, [138]

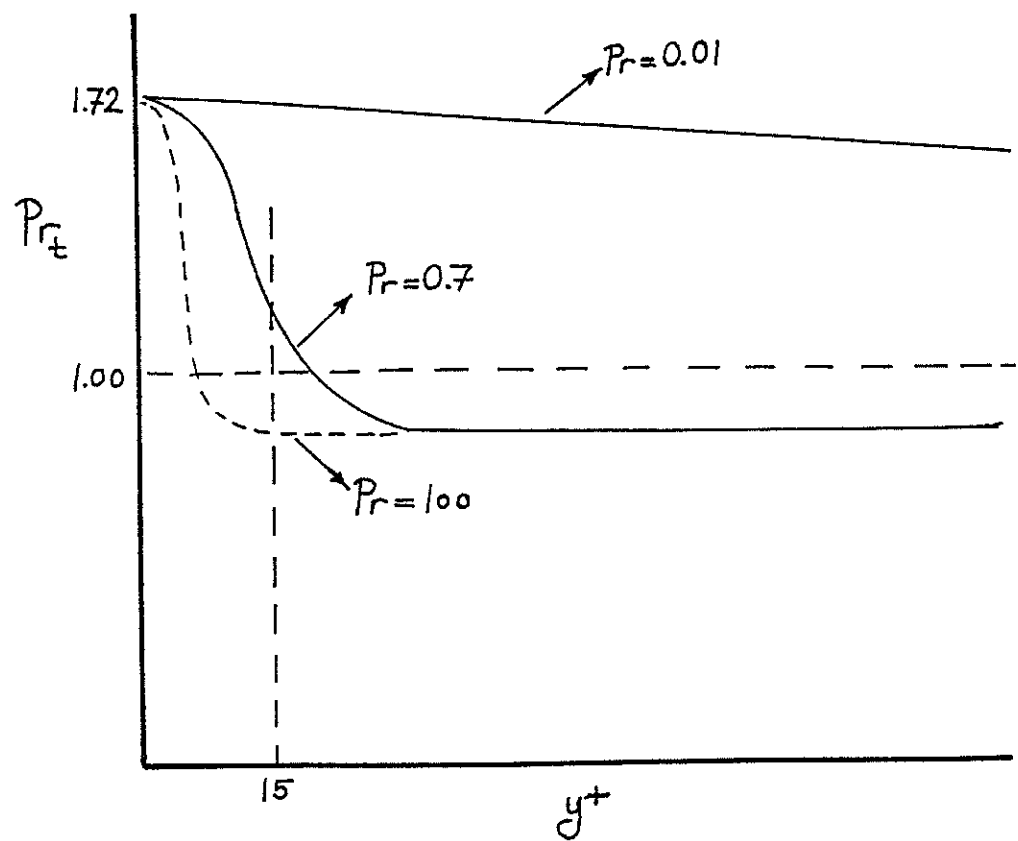


$$P^+ = \frac{v_0}{\rho_0 U_\tau^3} \frac{dp}{dx}$$

$$U_\tau = \sqrt{\frac{\tau_0}{\rho_0}}$$

APPENDIX-6

TURBULENT PRANDTL NUMBER VARIATION WITH MOLECULAR PRANDTL NUMBER



APPENDIX-7

INITIAL VELOCITY AND ENTHALPY PROFILES

DATA FORMAT IS THE SAME AS ref.[133]

HP GAS TURBINE ROTOR BLADE/BASELINE PREDICTIONS SUCTION SIDE	1	1	2	2	25	2	1	1	
.00131			.350		1.20		020.	.050	.005
0	0								
5764.43			.1494		.0000154		.699		
34	1								
.000787				1.					
.001312					1.				
.0026						1.			
.0066							1.		
.0131							1.		
.0210								1.	
.0315									1.
.0420									
.0551									1.
.0558					1.	0.00		0.00	
.0638						1.	0.00		0.00
.0709							1.		
.0814								1.	
.0919									1.
.0997									1.
.1076									1.
.1160									1.

.1234	1.
.1339	1.
.1430	1.
.1496	1.
.1588	1.
.1680	1.
.1864	1.
.2100	1.
.2283	1.
.2520	1.
.2756	1.
.2992	1.
.3118	1.
.3228	1.
.3360	1.
.3438	1.
.3517	1.
35.000	127.7
91.000	127.7
201.00	127.7
381.85	127.7
472.90	127.7
523.88	127.7
586.97	127.7
636.84	127.7
692.29	127.7
695.0	127.7
728.0	127.7
746.98	127.7
771.03	127.7
794.91	127.7
806.82	127.7
824.57	127.7
859.78	127.7
906.14	127.7
940.42	127.7
991.08	127.7
1051.71	127.7

*Int - fit
over by 100*

1089.50		127.7
1132.02		127.7
1152.95		127.7
1163.35		127.7
1163.35		127.7
1173.69		127.7
1178.84		127.7
1204.43		127.7
1219.65		127.7
1224.67		127.7
1194.26		127.7
1152.95		127.7
1131.99		127.7
.000000000	0.00	127.7
.00000070	0.68	128.6
.00000120	1.21	128.34
.00000150	1.50	128.50
.00000200	1.91	128.71
.00000240	2.35	128.95
.00000290	2.87	129.23
.00000400	3.91	129.79
.00000480	4.72	130.22
.00000560	5.46	130.61
.0000064	6.26	131.04
.00000770	7.50	131.70
.00001040	10.17	133.12
.00001370	13.38	134.83
.00001730	16.84	136.68
.0000216	20.98	138.89
.0000272	26.28	141.71
.0000336	32.26	144.90
.0000433	40.96	149.54
.0000561	51.45	155.13
.0000706	63.17	161.38
.0000899	75.76	168.09
.0001068	84.08	172.53
.0001201	88.45	174.86
.0001326	90.64	176.03

.0001396	91.00	176.22				
0.41	0.085	.01	0.22	0.377	1.0	
25.	0.0	0.				
4000.	0.86					1.00
32.2	778.	100.0				
	1 21 2 55 00 55					
1.050	1.500	22.				
2.	0.008202	0.003117	40.			

APPENDIX-8

INITIAL VELOCITY AND ENTHALPY PROFILES

DATA FORMAT IS THE SAME AS ref.[133]

HP GAS TURBINE ROTOR BLADE/BASELINE PREDICTIONS PRESSURE SIDE	1	1	2	2	25	2	1	1
.00020			.280		01.0	020.	.051	.005
0	0							
5781.61			.1502	.0000154		.6982		
29	1							
.0013			1.					
.0026			1.					
.0066			1.					
.0098			1.					
.0131			1.					
.0197			1.					
.0262			1.					
.0328			1.					
.0390			1.					
.0459			1.					
.0525			1.					
.0656			1.					
.0787			1.					
.0919			1.					
.1050			1.					
.1181			1.					
.13123			1.					

.14436	1.
.15748	1.
.17060	1.
.18373	1.
.19685	1.
.20997	1.
.22310	1.
.23622	1.
.24934	1.
.26247	1.
.27559	1.
.28871	1.
31.81	125.8
54.77	125.8
110.0	125.8
132.0	125.8
147.0	125.8
161.0	125.8
167.0	125.8
165.0	125.8
161.	125.8
160.0	125.8
160.1	125.8
169.0	125.8
187.0	125.8
212.0	125.8
245.0	125.8
286.0	125.8
322.70	125.8
368.23	125.8
413.44	125.8
477.38	125.8
540.78	125.8
603.32	125.8
677.37	125.8
751.32	125.8
838.94	125.8
936.82	125.8

1031.4		125.8				
1138.07		125.8				
1259.7		125.8				
.00000000	0.00	125.80				
.00000034	0.239	126.54				
.00000061	.423	127.13				
.00000075	.525	127.44				
.00000096	.668	127.89				
.00000118	0.821	128.37				
.00000144	1.002	128.94				
.00000197	1.368	130.08				
.00000237	1.651	130.96				
.00000274	1.909	131.76				
.00000315	2.189	132.63				
.00000377	2.621	133.98				
.00000512	3.556	136.87				
.00000673	4.676	143.94				
.00000851	5.885	148.20				
.00001063	07.33	153.17				
.00001338	9.187	159.0				
.00001653	11.277	166. 16				
.00002127	14.318	172.78				
.00002758	17.98	175.57				
.00003471	22.08	175.57				
.00004418	26.48	175.57				
.00005248	29.39	175.57				
.00005900	30.92	175.57				
.00006517	31.68	175.57				
.00006860	31.81	175.57				
0.41	0.085	.01	0.22	0.377	1.0	
25.	0.0	0.				
4000.	0.86					
32.2	778.					3.0
1	11	2	55	00	55	
0.085	0.05	14.				
1.	0.00984	0.02928		30.		

TABLE - 1

A REVIEW OF FILM COOLING HOLE SIZES ON THE LEADING EDGE
OF GAS TURBINE BLADES

SOURCE	REF.	CHORD LENGTH	HOLE DIAM.	d/c	HOLE SPAC.	ROW SPAC.
HANUS,L'ECUYER	[111]	...	1.17	...	4d	
MUSKA,FISH,SUO	[113]	90.2	1.20	.014	..	3d
HENNECKE	[14]	50.0	0.80	.018	5d	3d
BOGOLOMOV,PIOTUKH	[85]	88.4	0.50	.006	3d	4d
TAKAHARA et. al.	[13]			.013	3.5d	3d

TABLE - 2

A REVIEW OF INJECTION HOLE DIAMETERS ON
GAS TURBINE BLADES

SOURCE	REF.	CHORD LENGTH	HOLE	<i>d/c</i>
			mm	mm
KERREBROCK	[2]	...	0.5 .. 1.0	
LANDER et. al.	[106]	60.4	1.14	.019
		65.0	1.14	.017
DRING et. al.	[115]	166.5	3.20	.019
MUSKA et. al.	[113]	90.2	1.20	.013
BOGOLOMOV et.al.	[85]	88.4	0.50	.006
A GE BLADE		30.0	0.60	.020
A GE BLADE		55.0	0.80	.014
ITO et.al.	[114]	169.1	2.38	.014
DANIELS	[34]	50.8	1.00	.020

Table 3.

UNCERTAINTIES ON THE BASIC EXPERIMENTAL PARAMETERS

EXPERIMENTAL PARAMETER		UNCERTAINTY	NOMINAL MEASURED VALUE	RELATIVE UNCERTAINTY
		δA	A	$\delta A/A$
HEAT FLUX	\dot{q}_s	± 1.01	13.44	∓ 7.5 %
HEAT TRANSFER COEFFICIENT	h	∓ 82.4	1084	∓ 7.6 %
TEMPERATURE DIFFERENCE	$(T_{\infty} - T_w)$	∓ 2.48	124	∓ 2.0 %
PRESSURE	P	∓ 0.012	3.0	$\mp 0.4 \sim 0.6$ %
TEMPERATURE	T	∓ 2	417	∓ 0.5 %
BLOWING RATE	m	∓ 0.08	2.0	∓ 4.0 %

Table 4.

Main experimental parameters of the leading edge film cooling study

RUN	P _∞ b.	T _∞ K	T _w /T _∞	T _c /T _∞	P _{oc} b.	m̄/m _∞ %	M _{inlet}	M _{exit}	Re _{inlet}	T _w %	i deg.	
126	2.915	410.0	0.736			.240	.901	8.40 E5	5.2	0		
112	2.901	409.2	0.724			.251	.905	8.42 E5	5.2	0		
113	2.905	409.4	0.727			.251	.908	8.42 E5	5.2	0		
187	3.330	409.2	0.719			.251	.923	9.65 E5	5.2	0		
196	3.045	417.6	0.716			.316	.951	10.66 E5	0.8	+15		
198	3.040	417.8	0.713			.310	.948	10.25 E5	0.8	+10		
201	3.050	417.2	0.700			.271	.952	9.27 E5	0.8	0		
206	3.050	417.9	0.706			.263	.945	8.99 E5	0.8	-10		
202	2.885	417.3	0.705	.39	3.72	.87	.271	.952	9.27 E5	0.8	0	
199	2.902	418.3	0.710	.39	3.65	.84	.310	.948	10.25 E5	0.8	+10	
204	2.892	417.8	0.707	.38	3.69	.89	.263	.945	8.99 E5	0.8	-10	
154	2.883	408.9	0.722	.52	3.28	.50	.251	.905	8.42 E5	5.2	0	
155	2.895	409.5	0.727	.52	3.40	.62	.251	.905	8.42 E5	5.2	0	
157	2.891	409.3	0.731	.49	3.92	1.01	.251	.905	8.42 E5	5.2	0	
120	2.926	410.3	0.727	.59	4.02	.57	.251	.905	8.42 E5	5.2	0	
125	2.892	409.9	0.735	.59	3.73	.46	.251	.905	8.42 E5	5.2	0	
130	2.862	406.5	0.722	.70	3.69	.50	.251	.905	8.42 E5	5.2	0	

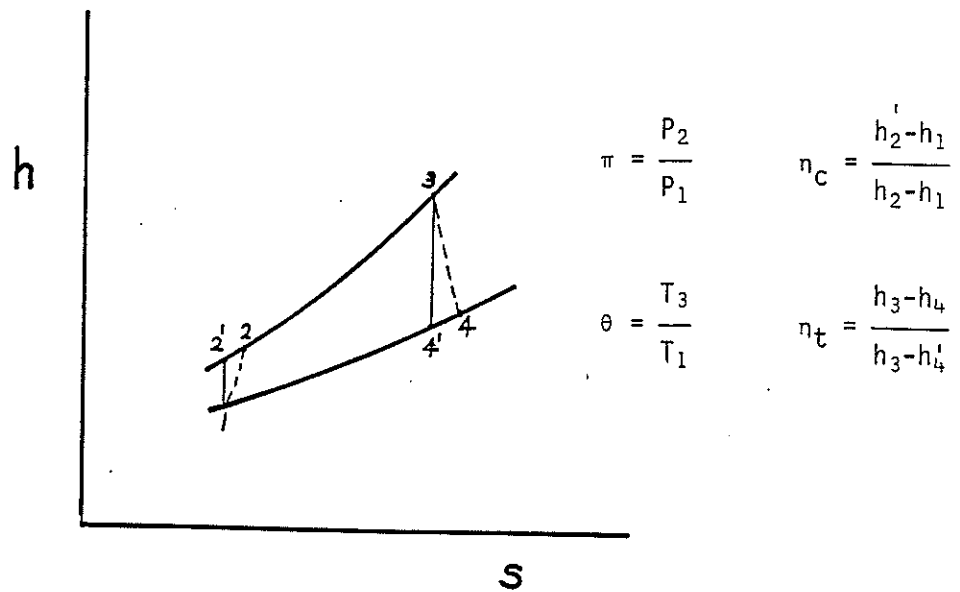


Fig.1 Enthalpy-entropy diagram of a simple gas turbine cycle

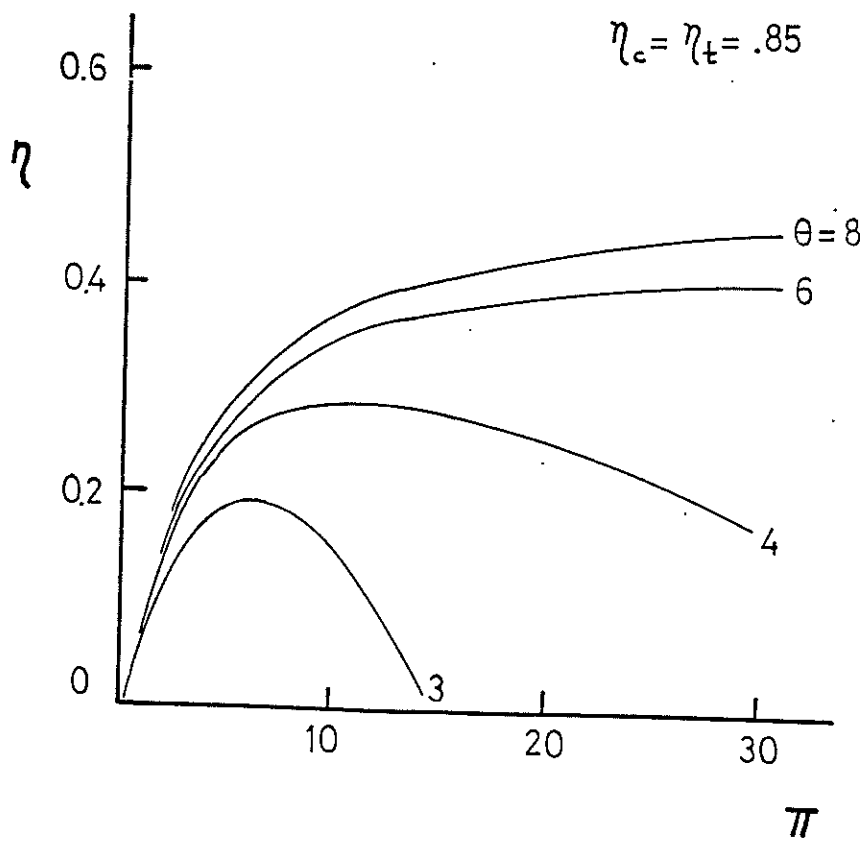


Fig.2 Variation of thermal efficiency with respect to pressure ratio and temperature ratio

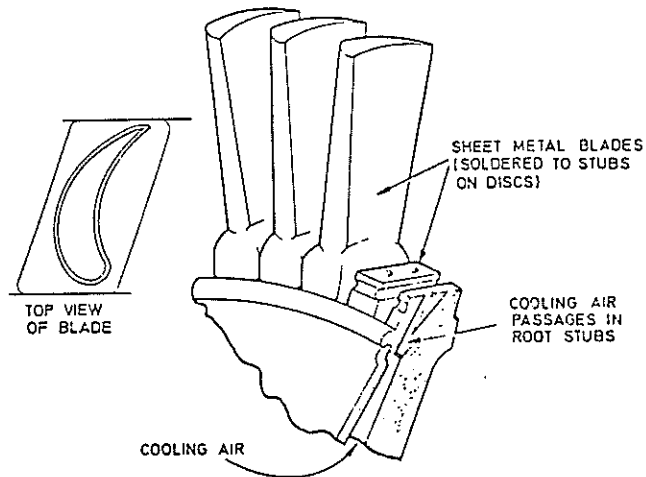


Fig.3 Internal convection cooling through a hollow blade,HALLS,[5]

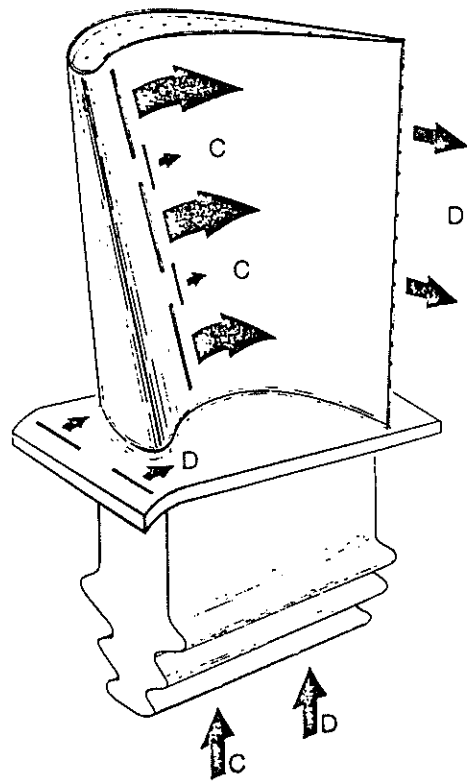


Fig.4 Steam cooling on the leading edge of a rotor blade,RICE,[8]

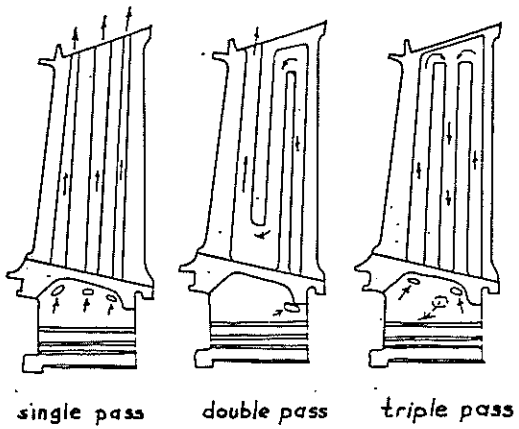


Fig.5 Internal convection cooling

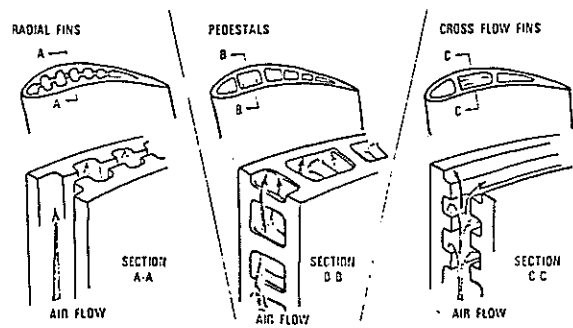


Fig.6 Extended surfaces used in convection cooling

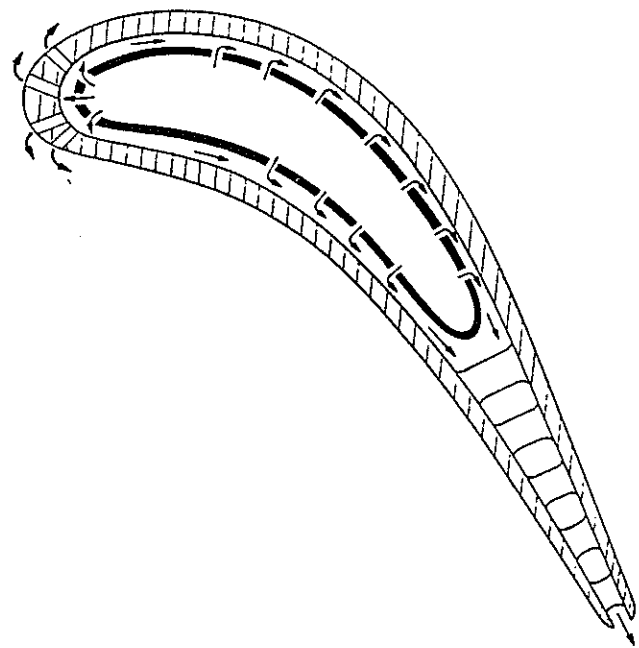


Fig.7 Impingement cooling+film cooling+trailing edge ejection,
METZGER,[9]

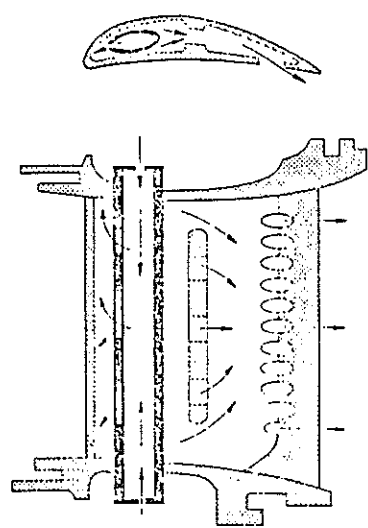


Fig.8 Impingement cooling+trailing edge ejection,HALLS,[5]

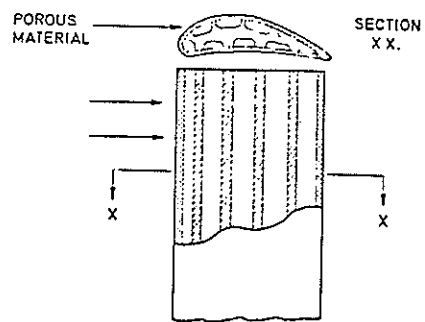


Fig.9 Transpiration cooling, HALLS, [5]

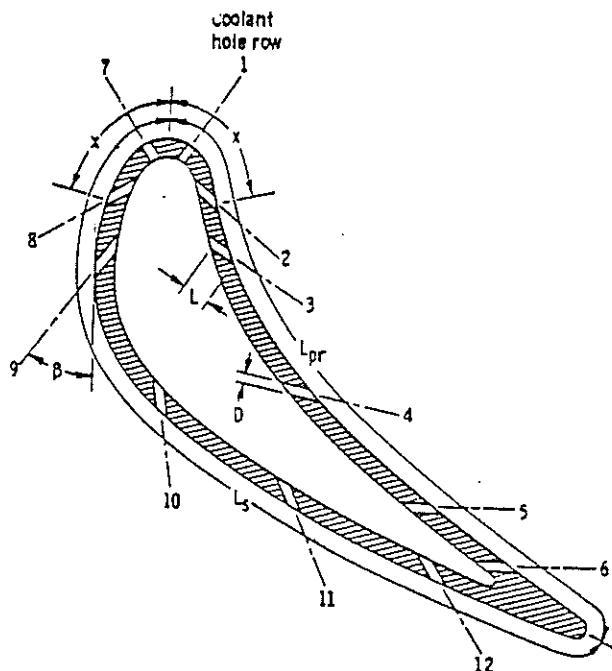


Fig.10 A film cooled turbine blade

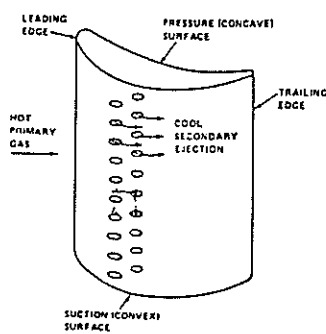


Fig.11 A film cooled turbine blade, double rows only

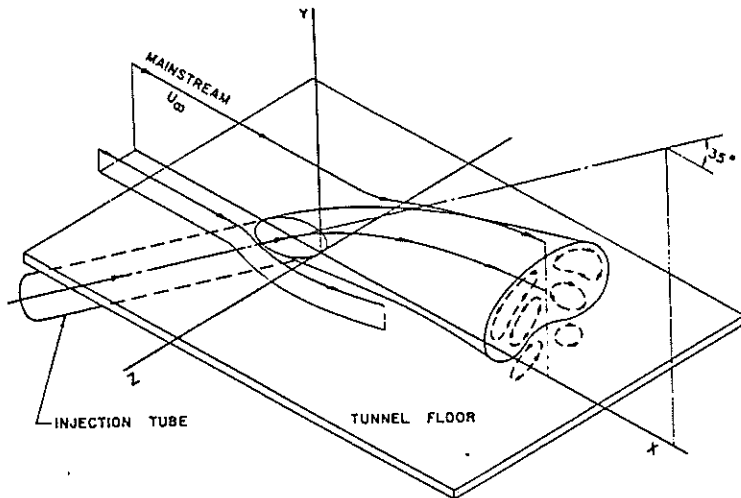


Fig.12 Coolant jet-mainstream interaction, GOLDSTEIN et al.,[91]

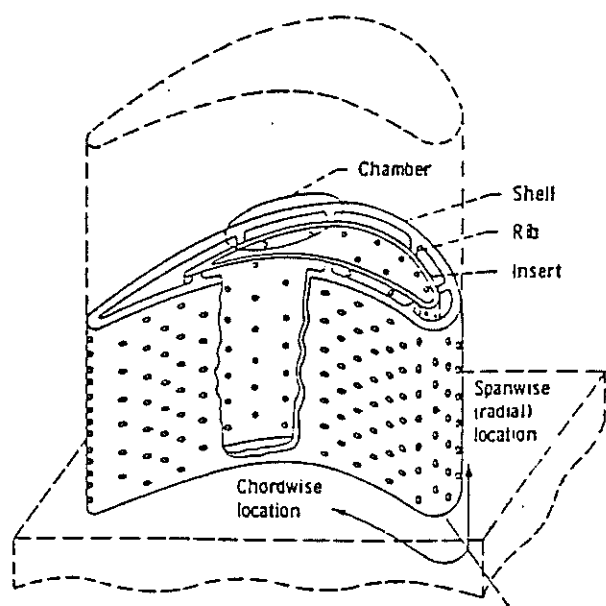


Fig.13 Full coverage film cooling, MEINER,[17]

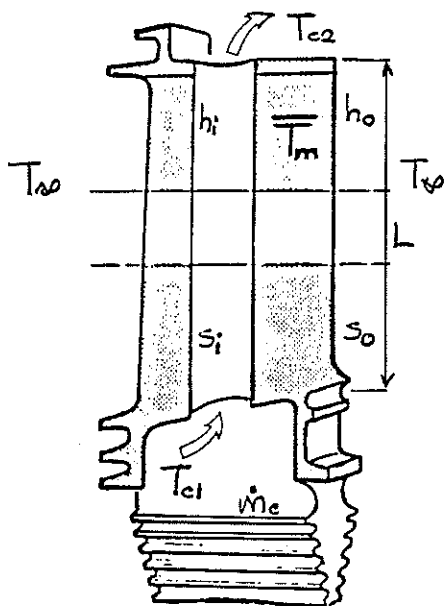


Fig.14 Thermal energy balance in a cooled turbine blade

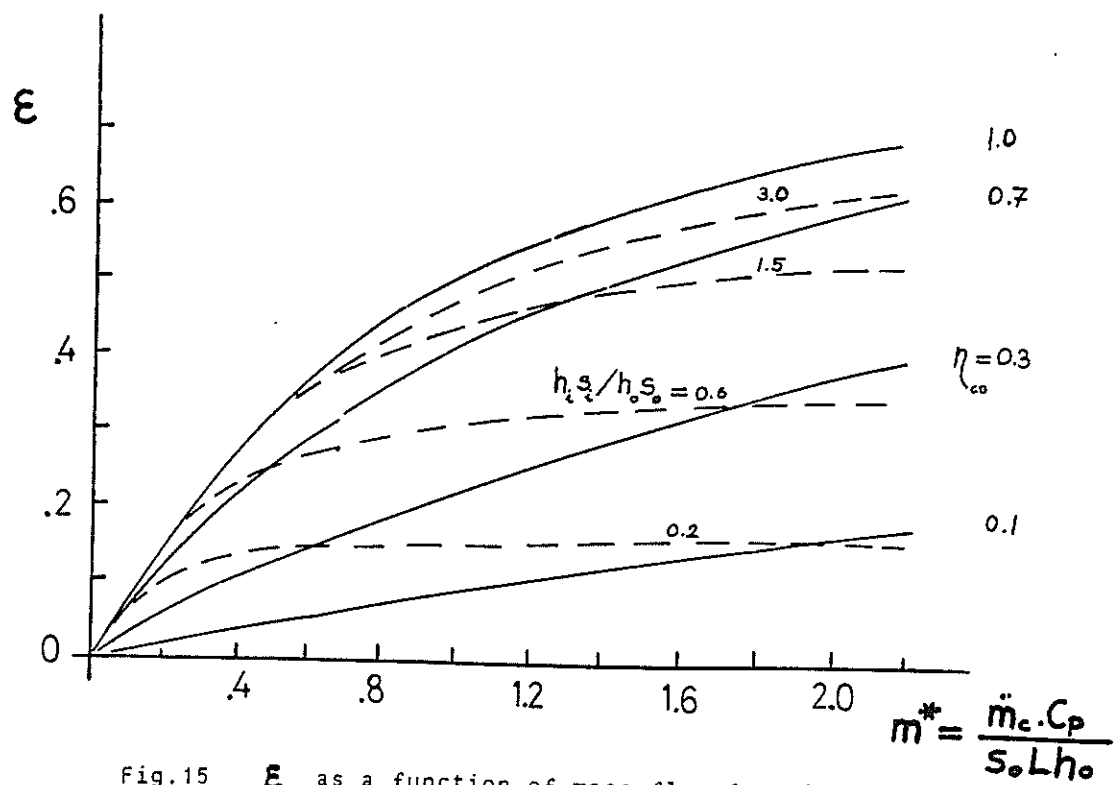


Fig.15 ϵ as a function of mass flow function

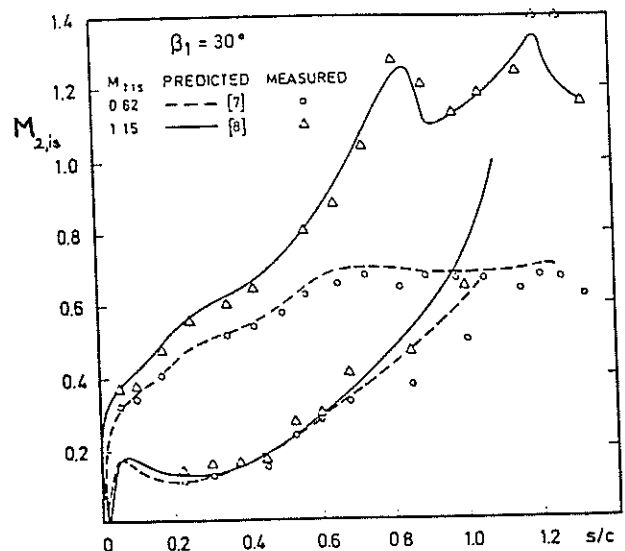
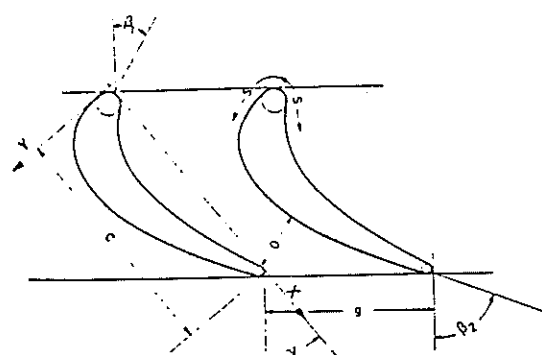


Fig.16 A turbine rotor blade and free stream Ma number distribution, CONSIGNY,[62]

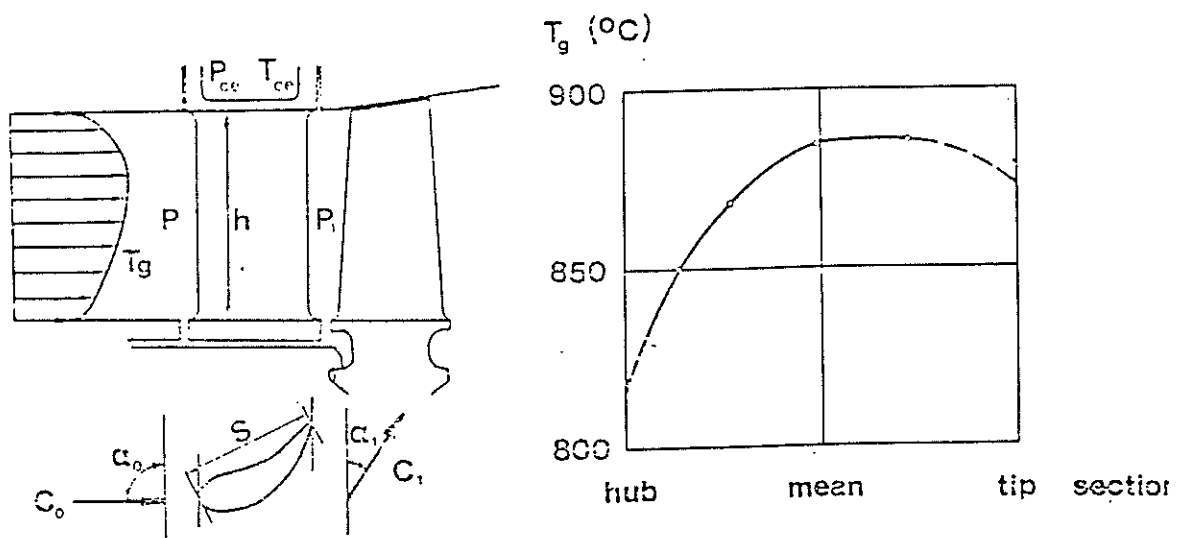


Fig.17.a Radial temperature variation in front of a nozzle guide vane,
MUKHERJEE,[19]

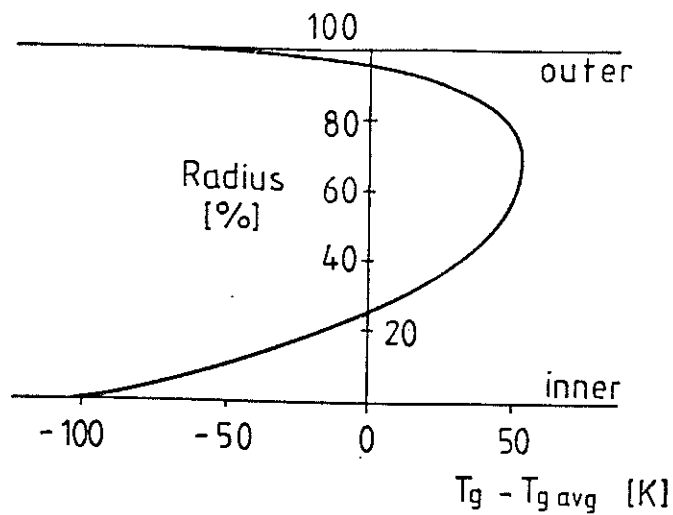


Fig.17.b Radial temperature variation in front of a nozzle guide vane
, HENNECKE, [14]

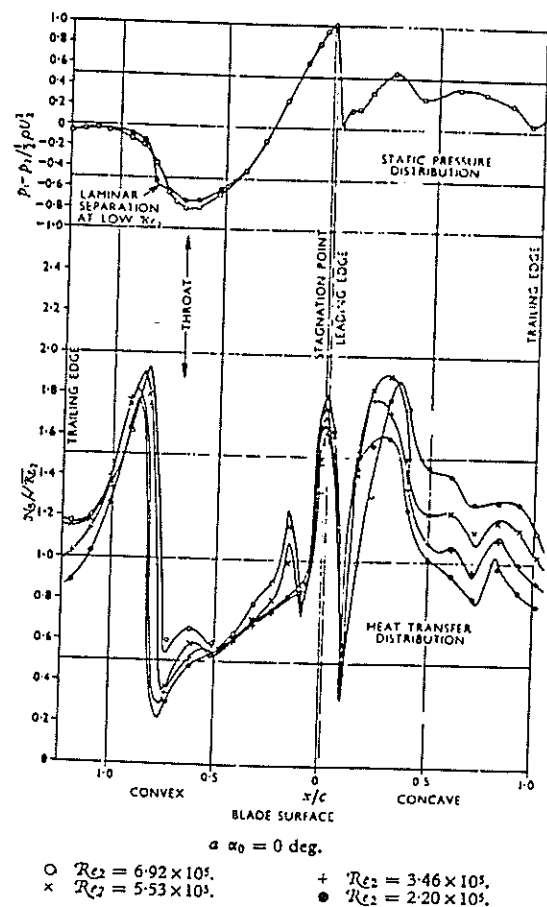


Fig.18 Heat transfer and free stream static pressure distribution around a turbine blade,WILSON and POPE,[80]

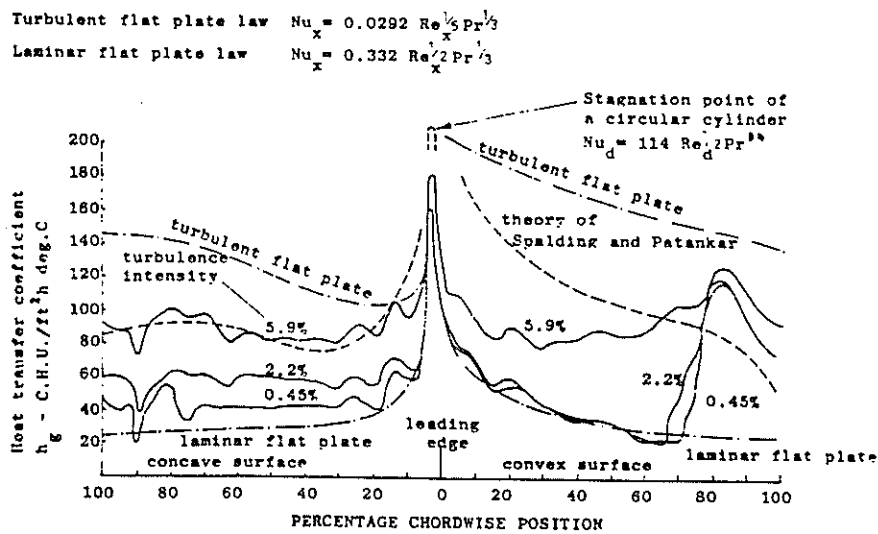


Fig.19 Heat transfer coefficients and comparisons with theory around a turbine blade, TURNER,[60].

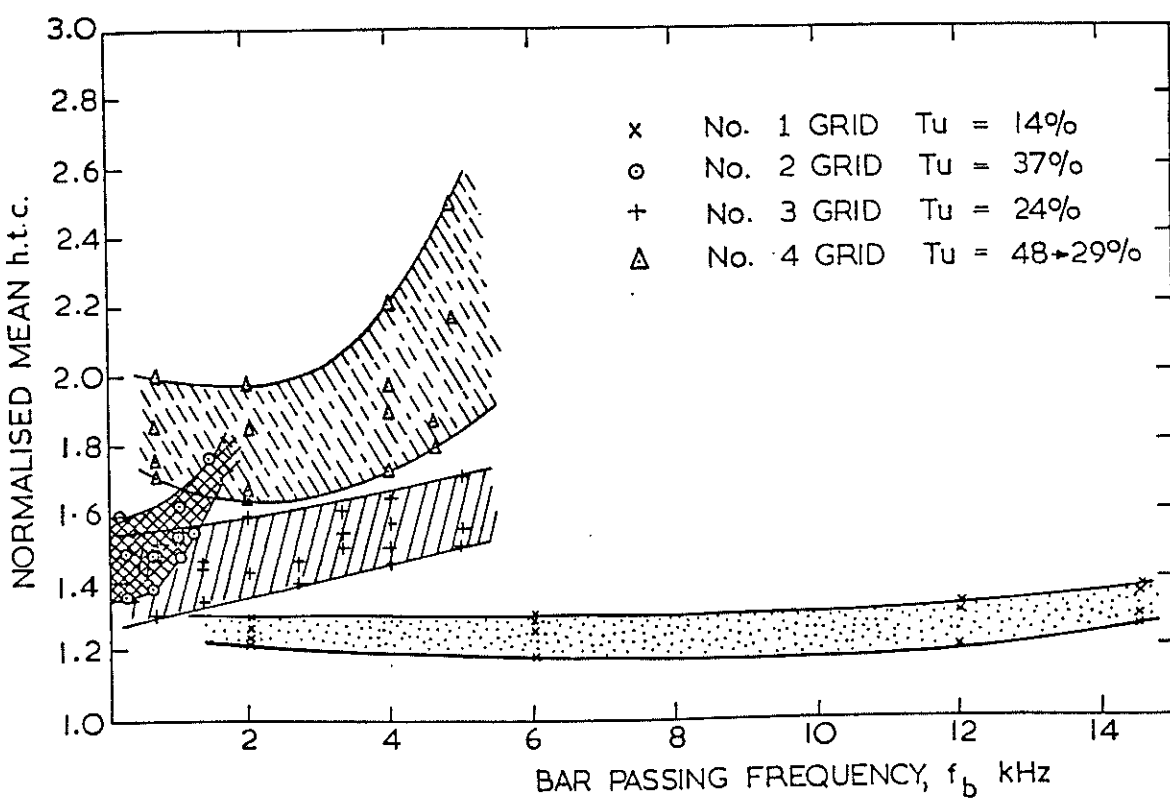


Fig.20 Effect of frequency of turbulence on heat transfer coefficient

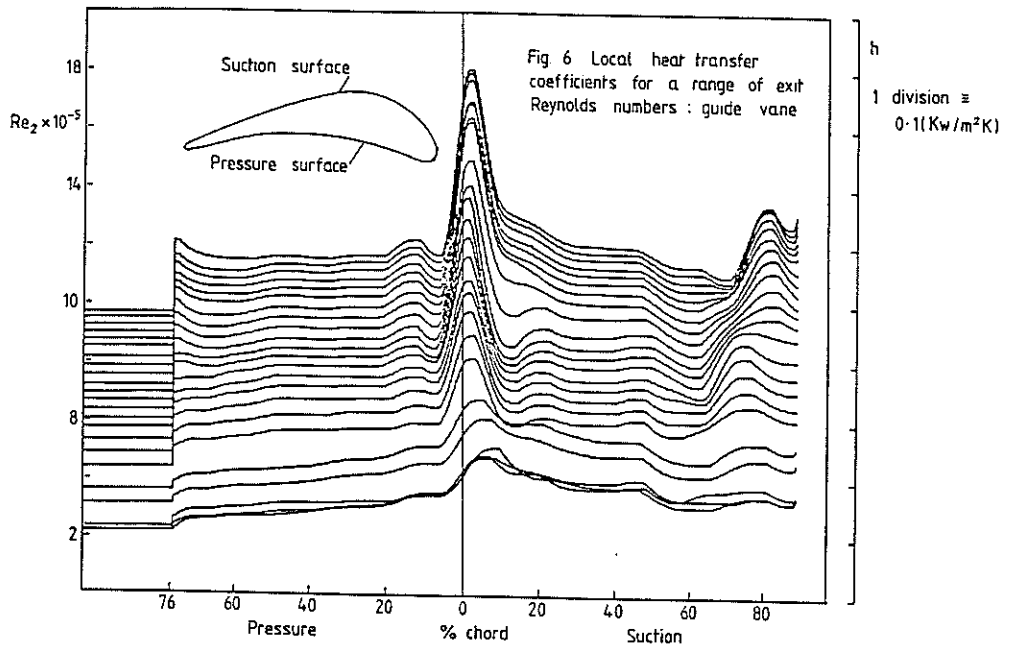


Fig.21.a Local heat transfer coefficients on a nozzle guide vane for a range of exit Re numbers.[65]

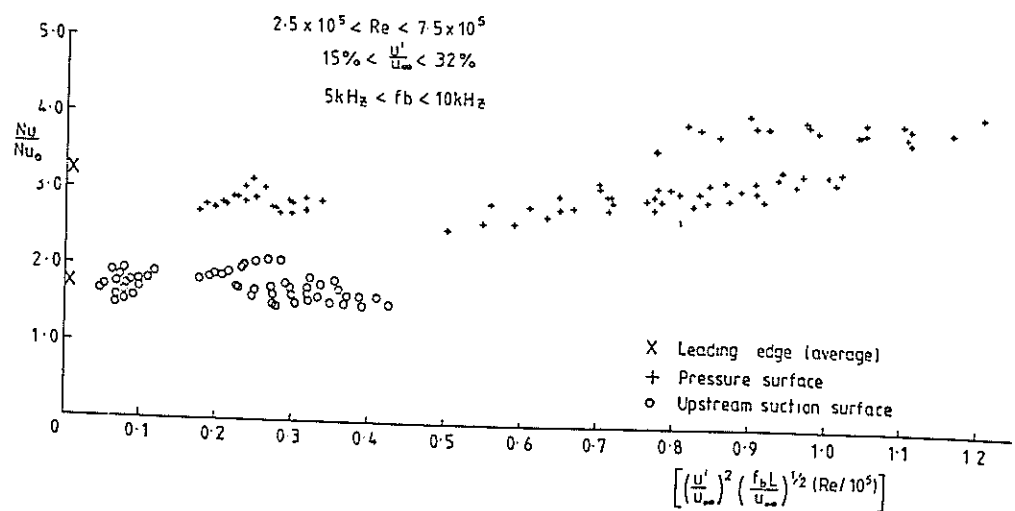


Fig.21.b Effect of intensity and frequency of turbulence on heat transfer at different locations on a turbine blade,[65]

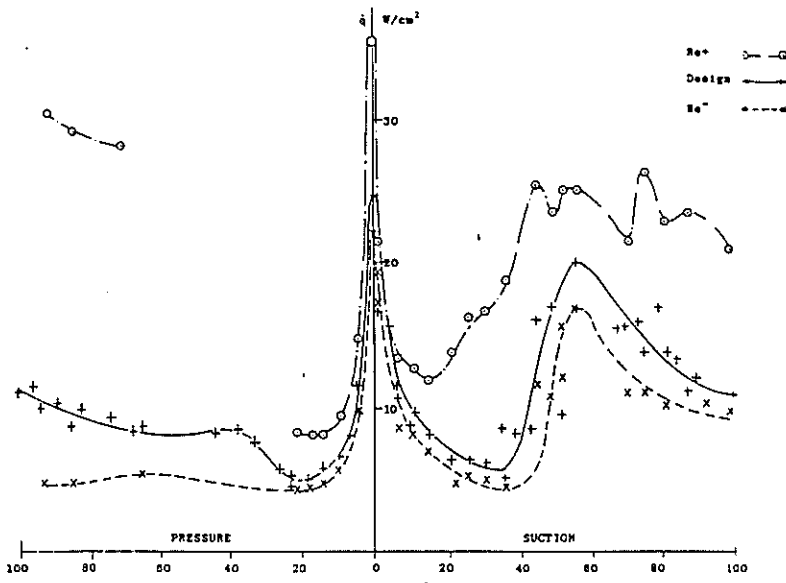


Fig.22 Effect of inlet Re number without turbulence grid,DANIELS,[34]

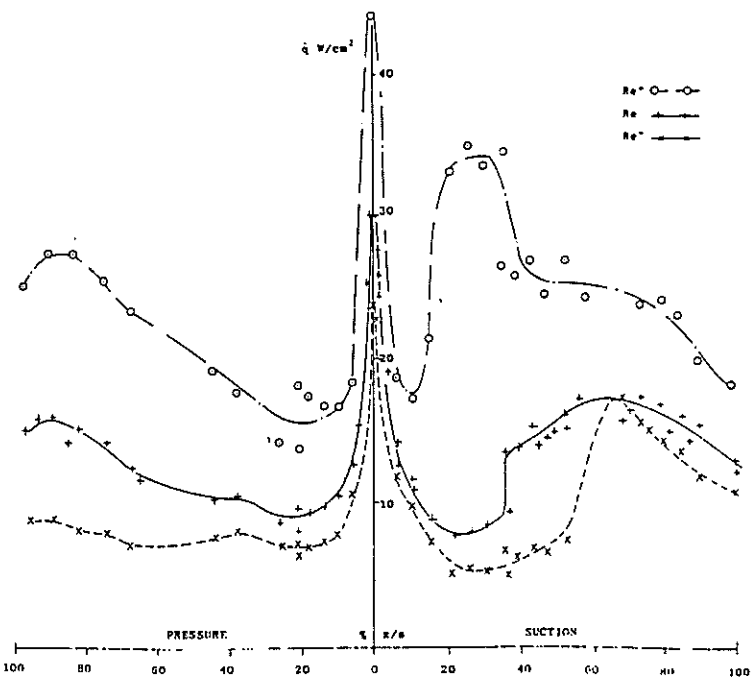


Fig.23 Effect of inlet Re number with turbulence grid,Daniels,[34]

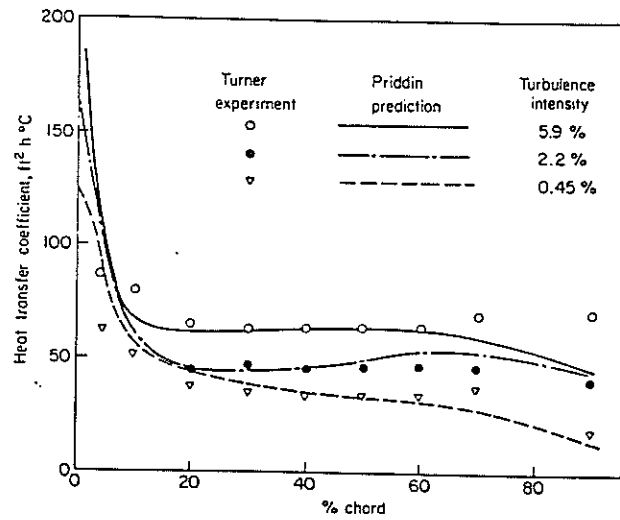


Fig.24 Comparison of TURNER's [83] heat transfer coefficients around a turbine blade with PRIDDIN's predictions.[84]

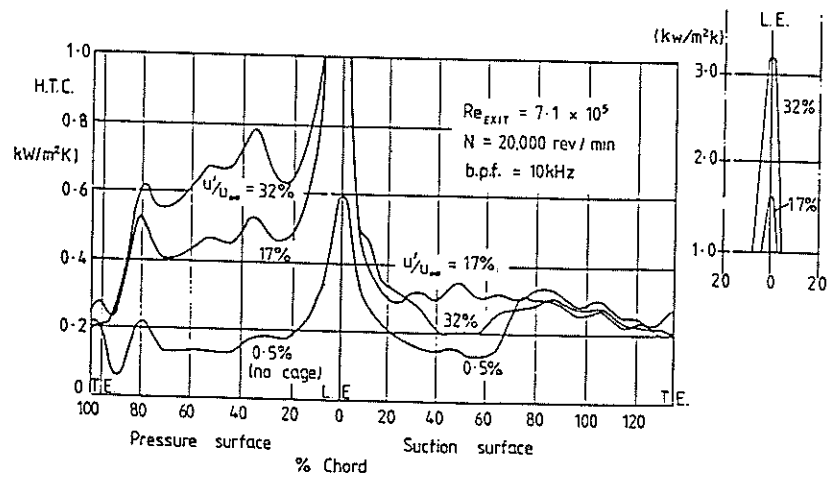


Fig.25 Effect of TU_∞ on heat transfer coefficients on a turbine blade,BAYLEY et al.,[65]

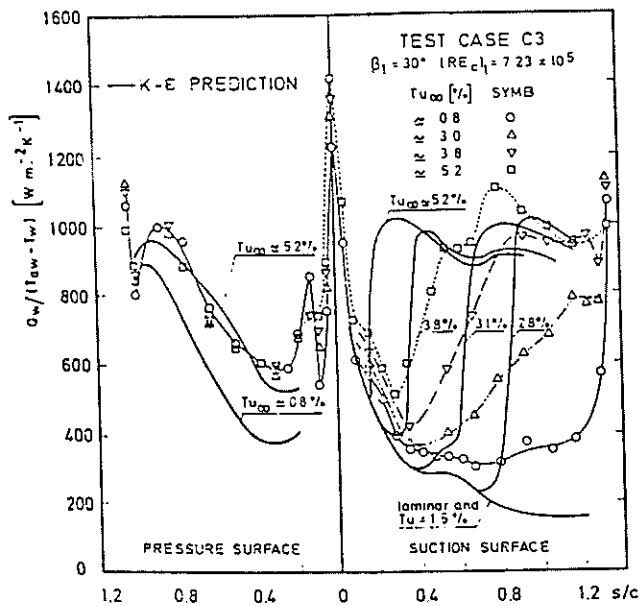


Fig.26 Comparison of k-ε predictions
 and heat transfer coefficients on a turbine
 blade, CONSIGNY, [62], $i=0$ deg

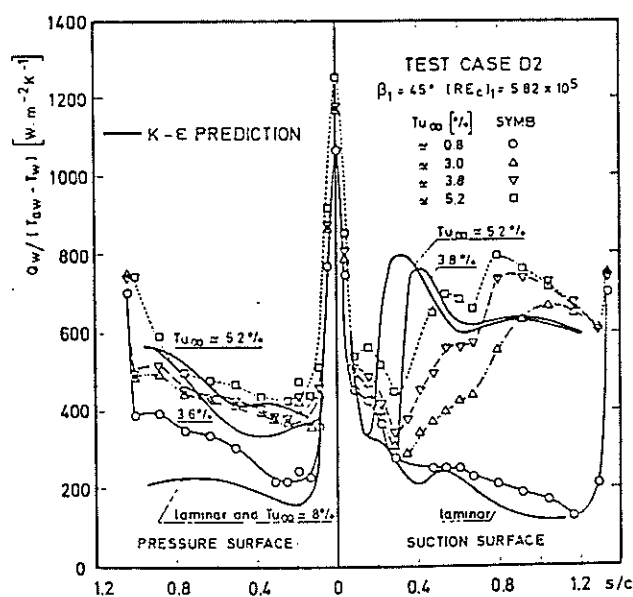


Fig.27 Comparison of k-ε predictions
 and heat transfer coefficients on a turbine
 blade, CONSIGNY, [62], $i=15$ deg

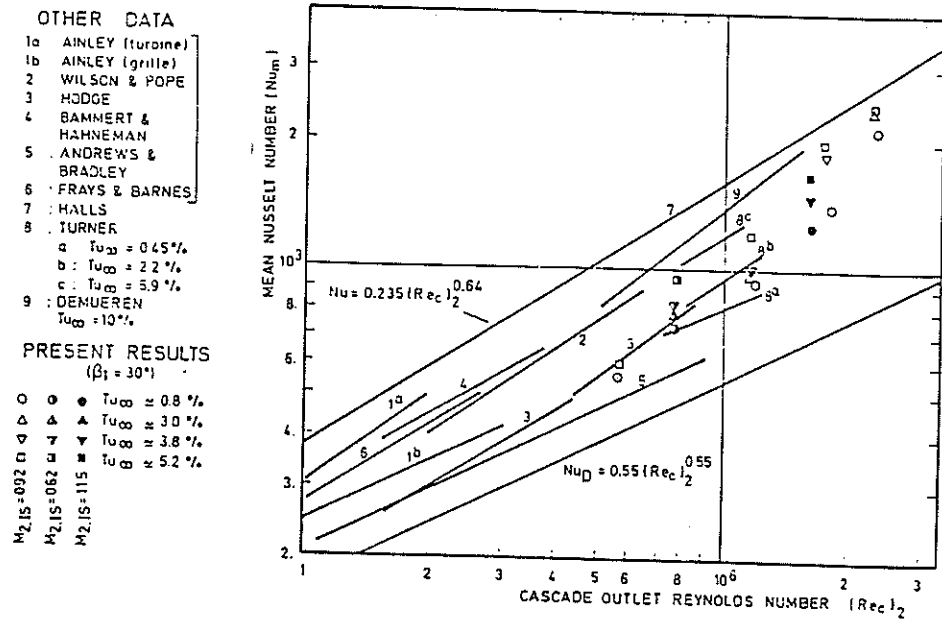


Fig.28 Influence of $T_{u\infty}$ on measured mean Nu number on a turbine blade and comparisons, CONSIGNY, [62]

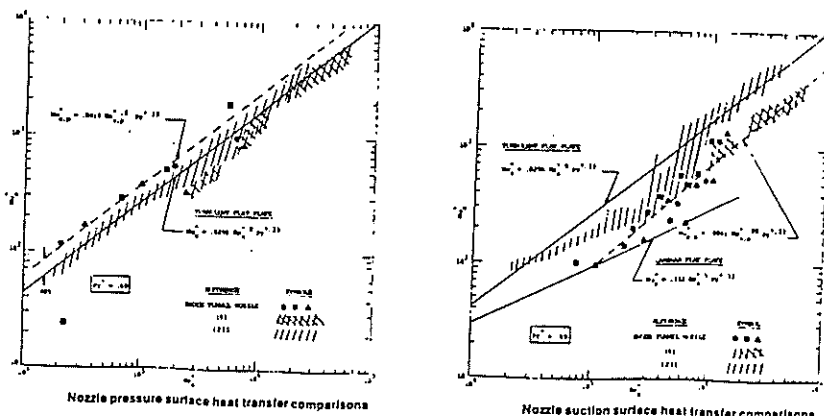


Fig.29
Heat transfer on the pressure side of a nozzle guide vane
KERCHER et al., [89]

Fig.30
Heat transfer on the suction side of a nozzle guide vane
KERCHER et al., [89]

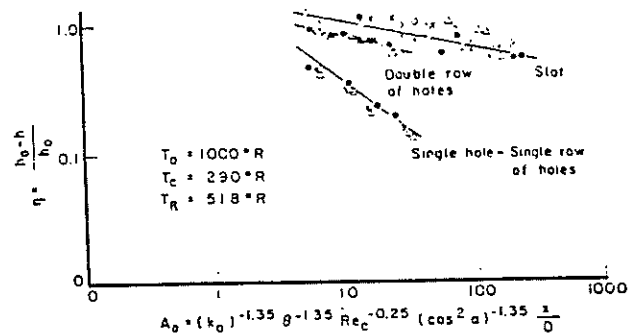


Fig.31 Discrete hole film cooling, isothermal wall effectiveness on a flat wall,[92]

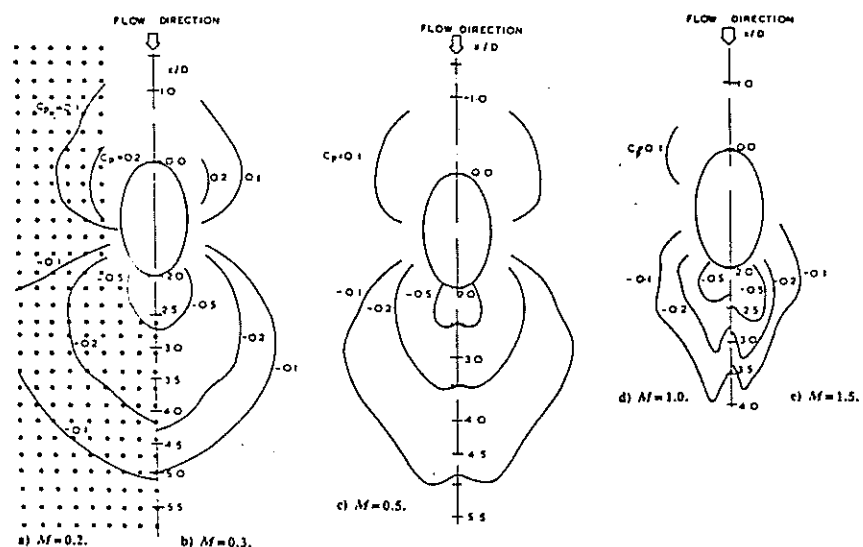


Fig.32 Static pressure variations around a film cooling hole,[94]

$$C_p = \frac{P - P_{ref}}{\frac{1}{2} \rho_e U_e U_\infty}$$

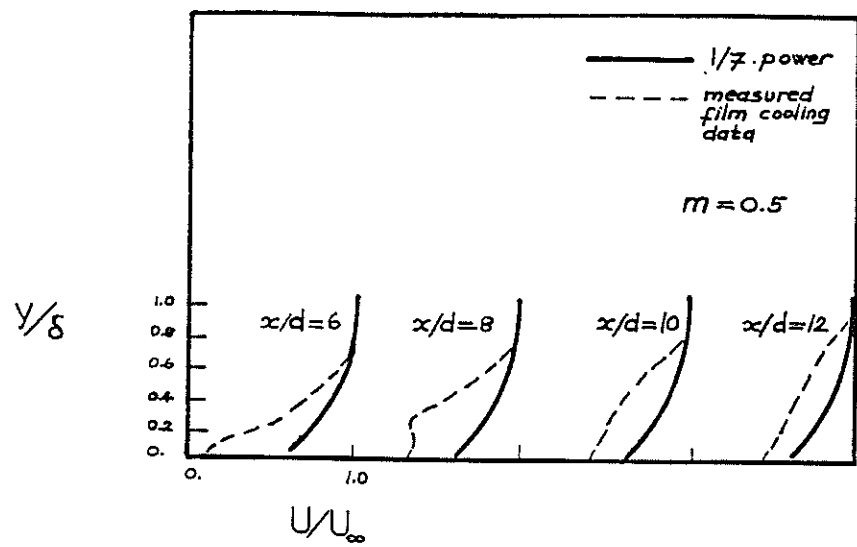


Fig.33 Velocity profiles just after double row of ejection holes,[95]

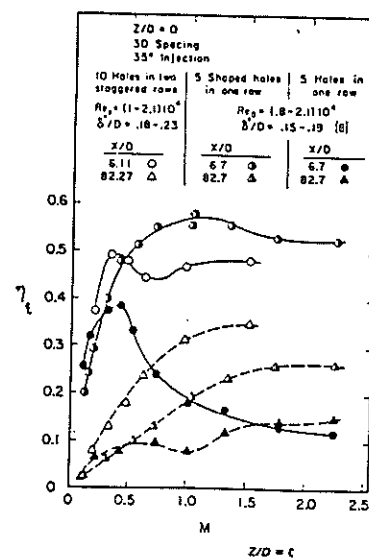


Fig.34 Comparison of adiabatic wall effectiveness from single row of holes and double row of holes,GOLDSTEIN et al.,[97]

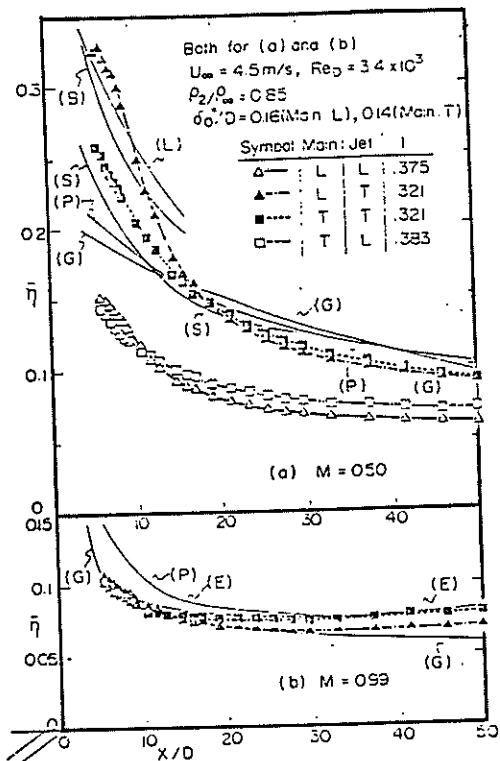


Fig.35 Influence of approaching boundary layer type, with a laminar and turbulent coolant jet on η , single row of holes.[102]

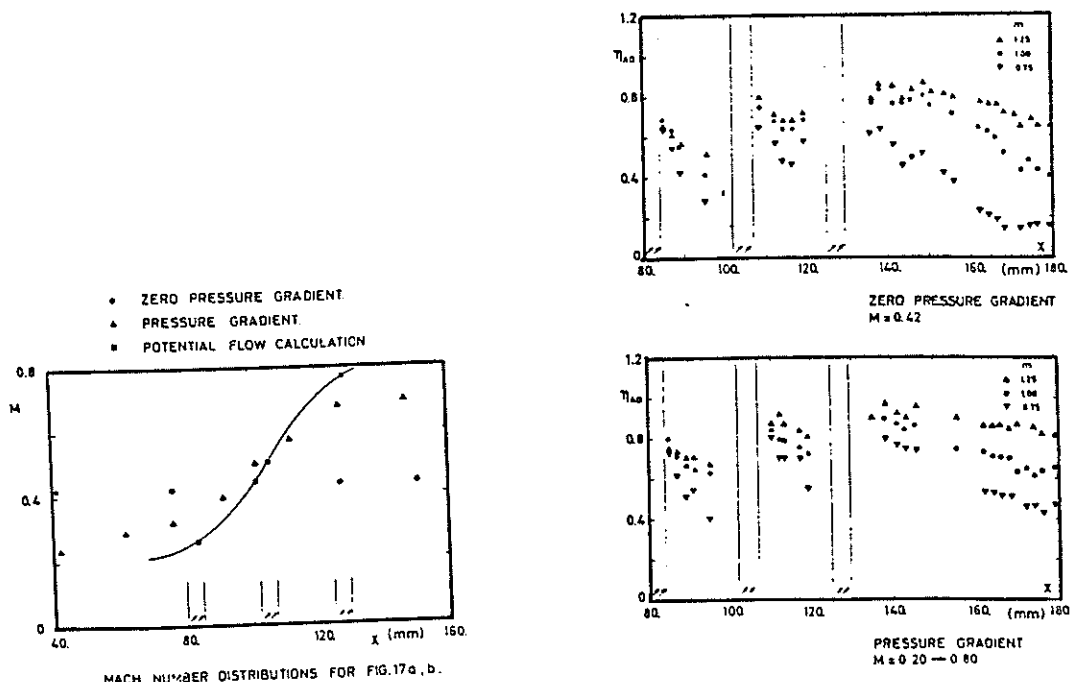


Fig.36 Adiabatic wall effectiveness distribution over a flat plate with three sets of injection rows, with and without a favourable pressure gradient [105]

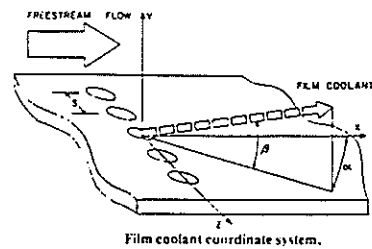


Fig.37 Film cooling geometry on the leading edge of a turbine blade compound angled ejection, LUCKEY et al., [108]

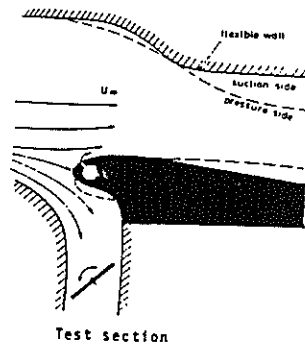


Fig.38 A turbine airfoil leading edge for film cooling studies, KRUSE, [12]

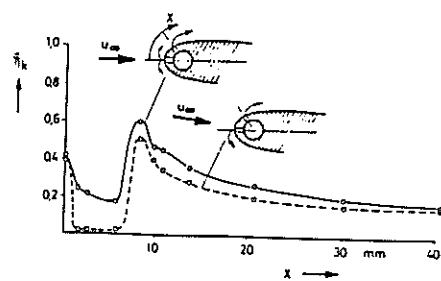


Fig.39 Variation of the stagnation line position with film cooling, KRUSE, [12]

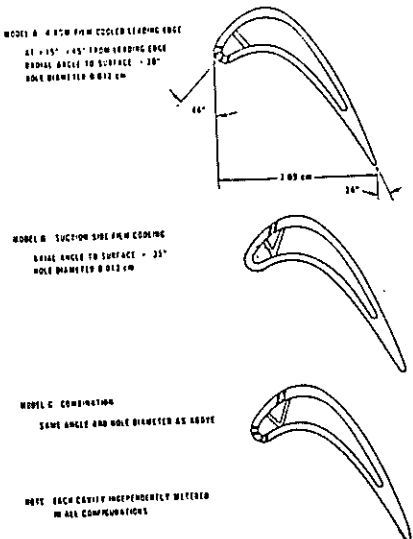


Fig.40 3 film cooling configurations on a turbine blade.[106]

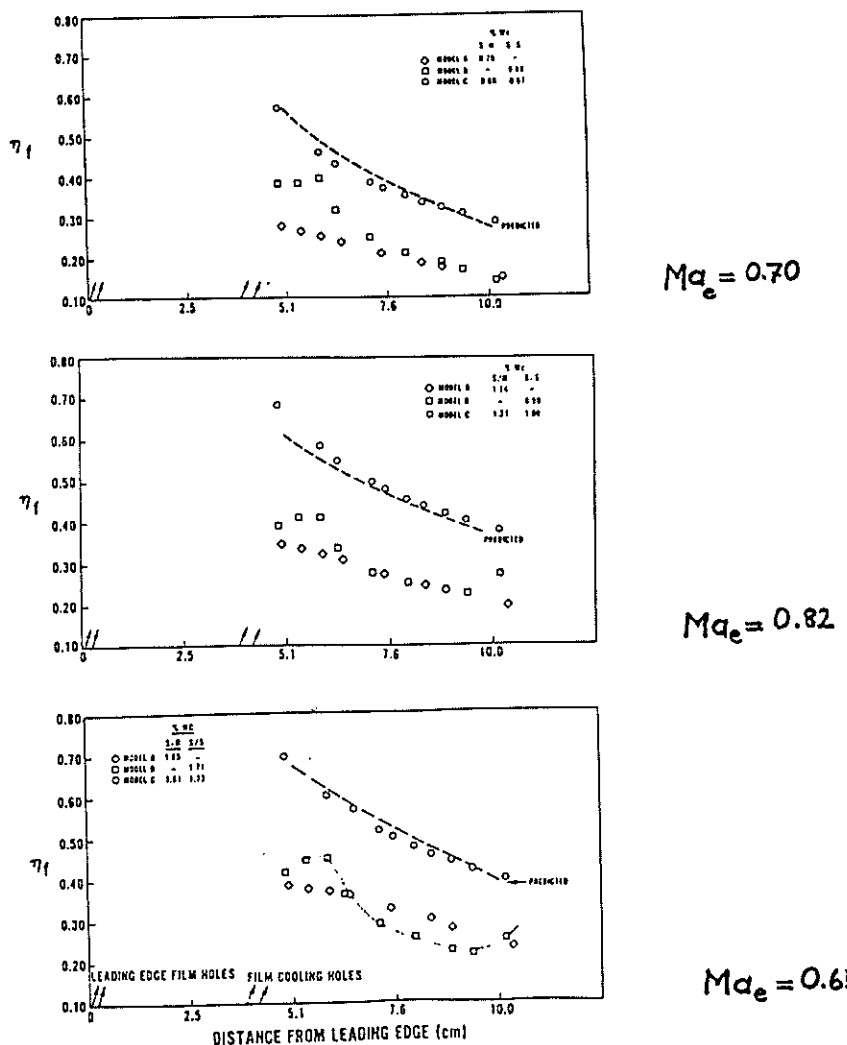


Fig.41 Superposition of cooling fields and effect of exit Re on adiabatic wall effectiveness.[106]

suction side
film injection

CURVATURE EFFECT
ON TURBINE BLADE
FILM
COOLING

r_{wall}

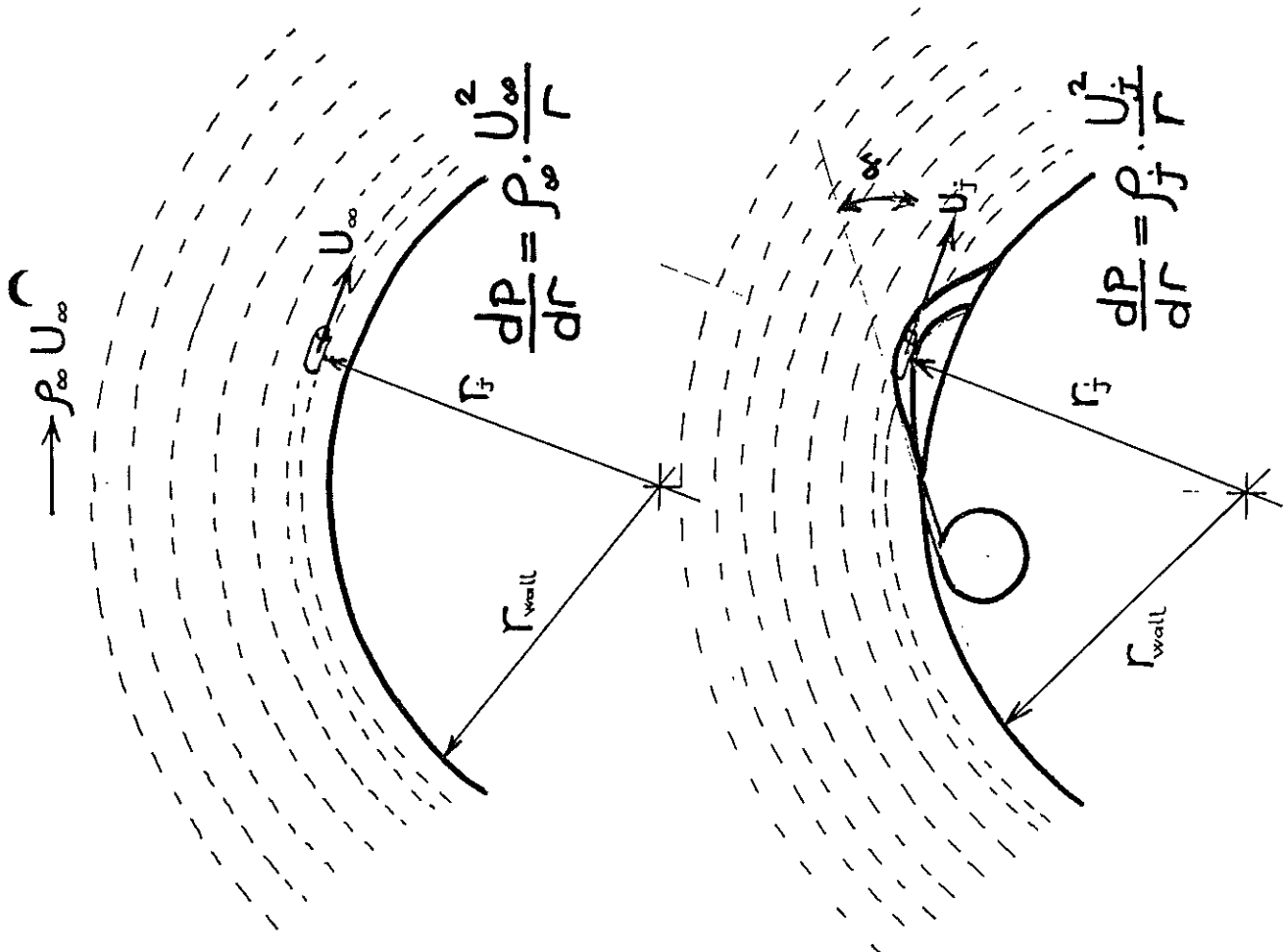
pressure side
film injection

r_{wall}

$$\frac{f_j}{r_w} = \frac{\rho_f U_j^2}{\rho_\infty U_\infty^2} = 1 + \phi \cdot (I \cos^2 \alpha - 1)$$

$$\text{where } \phi = \frac{\rho_f U_j^2 - \rho_\infty U_\infty^2}{\rho_2 U_2^2 \cos^2 \alpha - \rho_\infty U_\infty^2}$$

$$I = \frac{\rho_2 U_2^2}{\rho_\infty U_\infty^2}$$



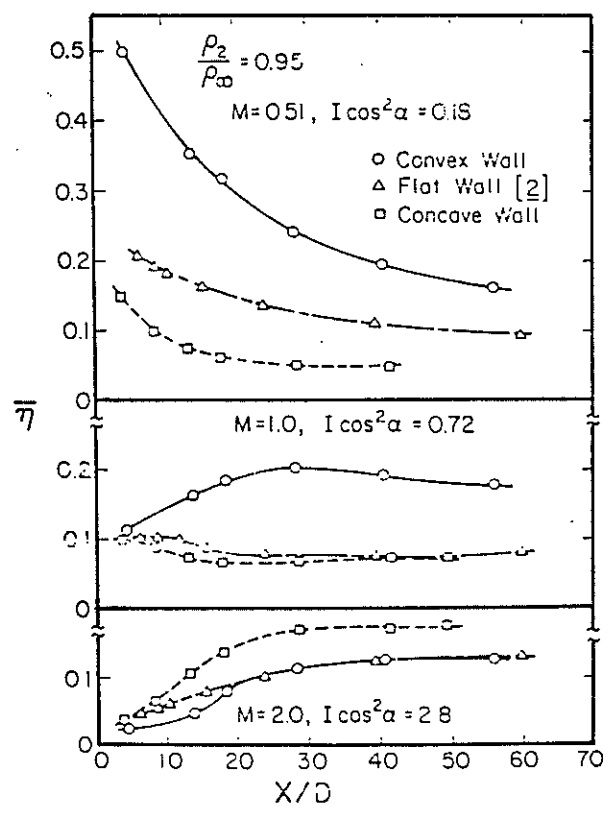


Fig.43.a Averaged adiabatic wall effectiveness on the surfaces of a gas turbine blade, [114] $\rho_e/\rho_\infty = 0.95$

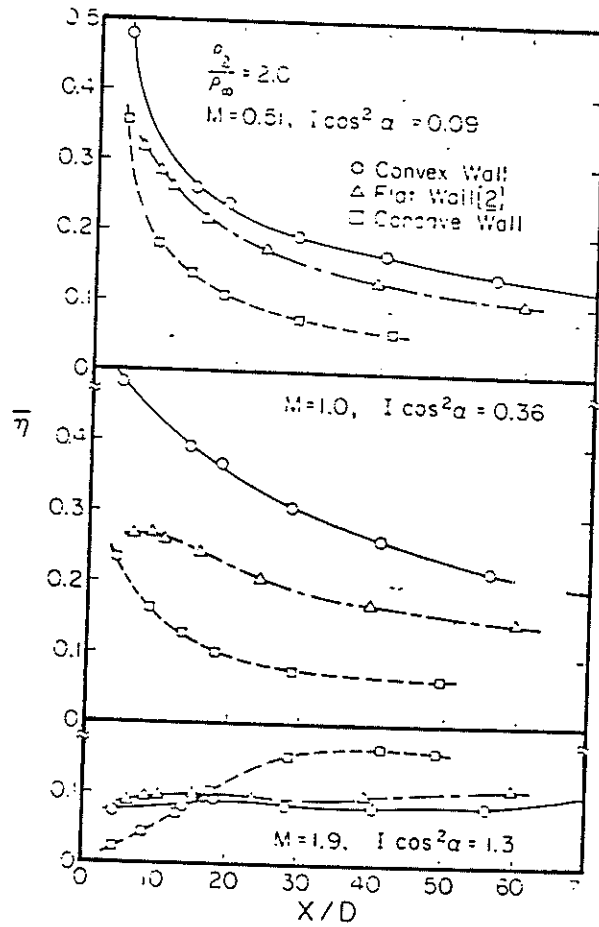
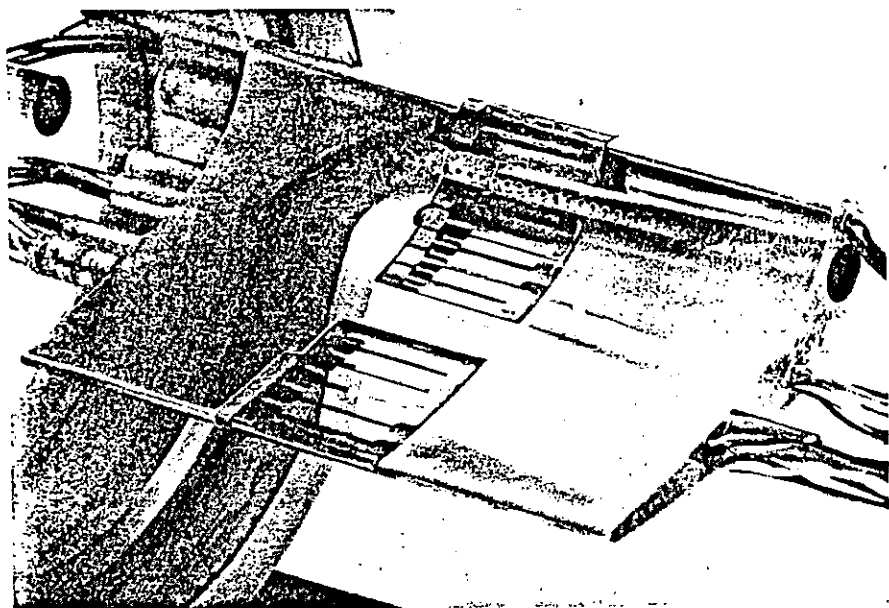
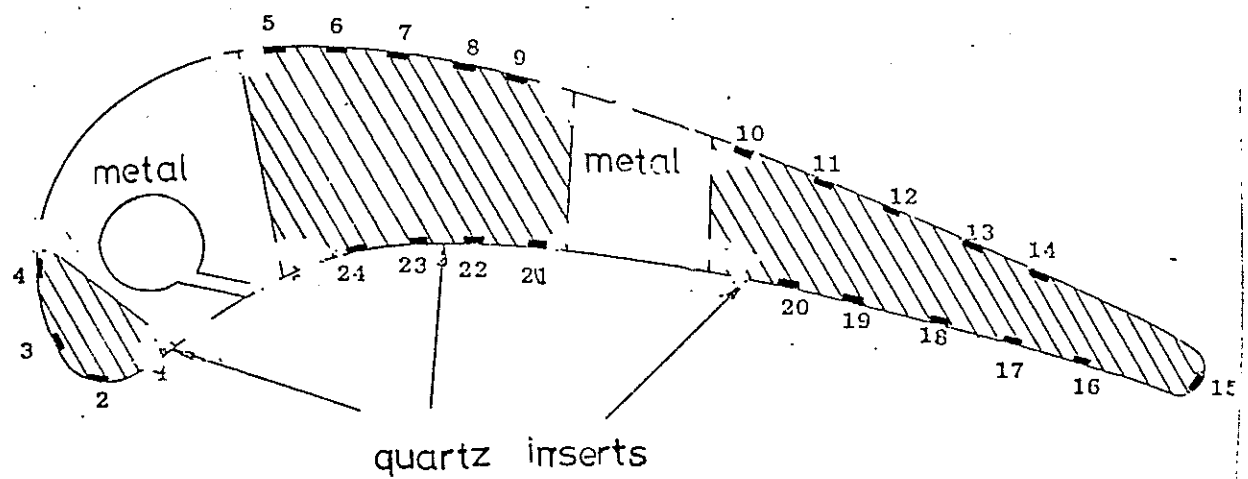


Fig.43.b Averaged adiabatic wall effectivenesses on the surfaces of a gas turbine blade,[114], $\rho_2/\rho_\infty = 2.0$



View of pressure surface of rotor blade with thin film gauge inserts (quartz) and film cooling holes.

Fig.44 Film cooling geometry of [34]

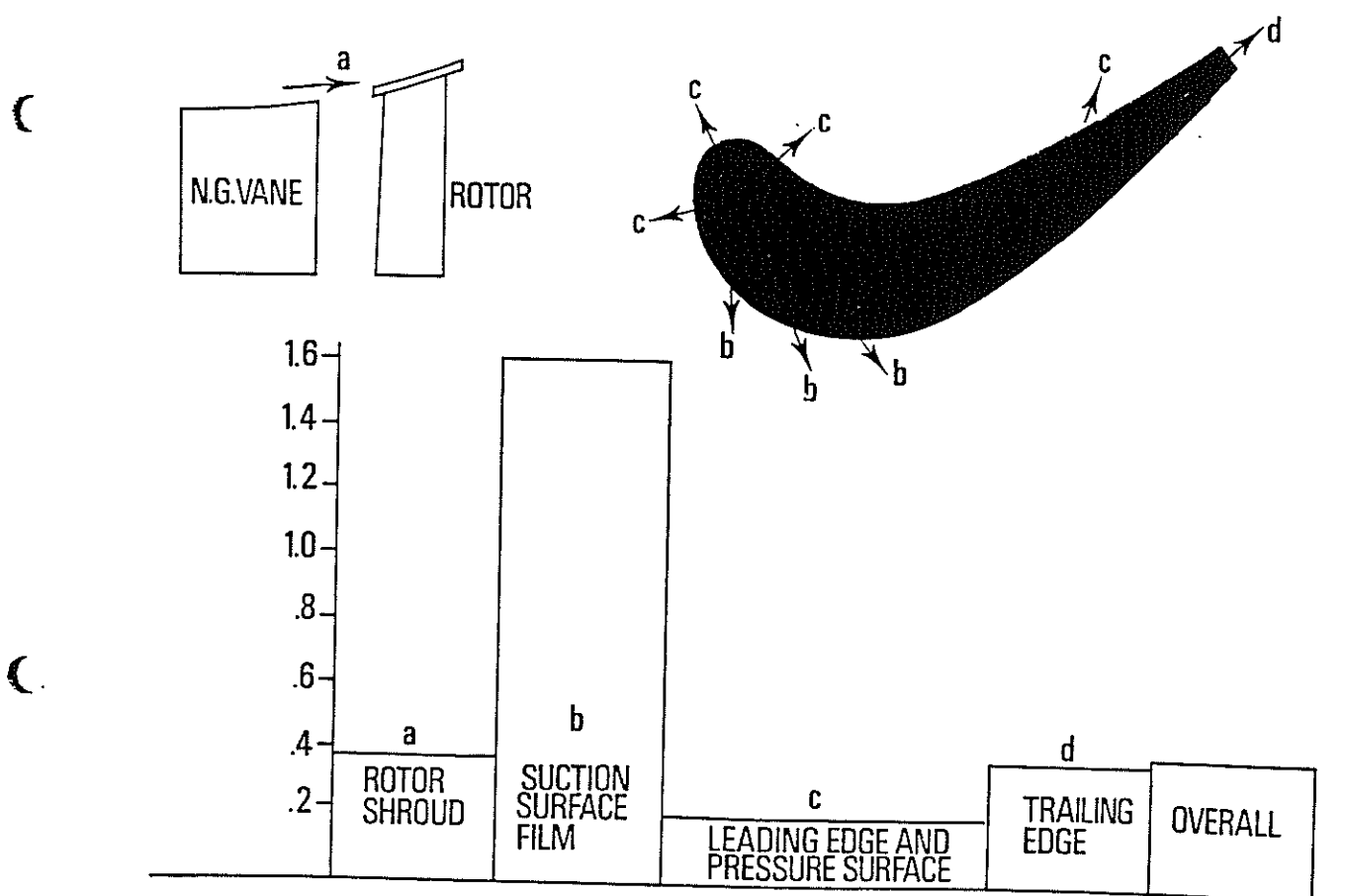


Fig.45 Breakdown of turbine efficiency loss associated with rotor cooling flows, BARRY, [18]

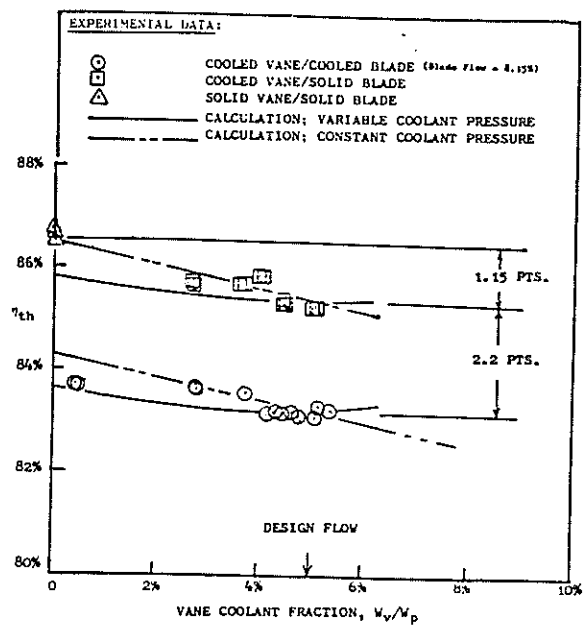


Fig.46 The thermal efficiency reductions due to coolant ejection
MC DONEL,[123]

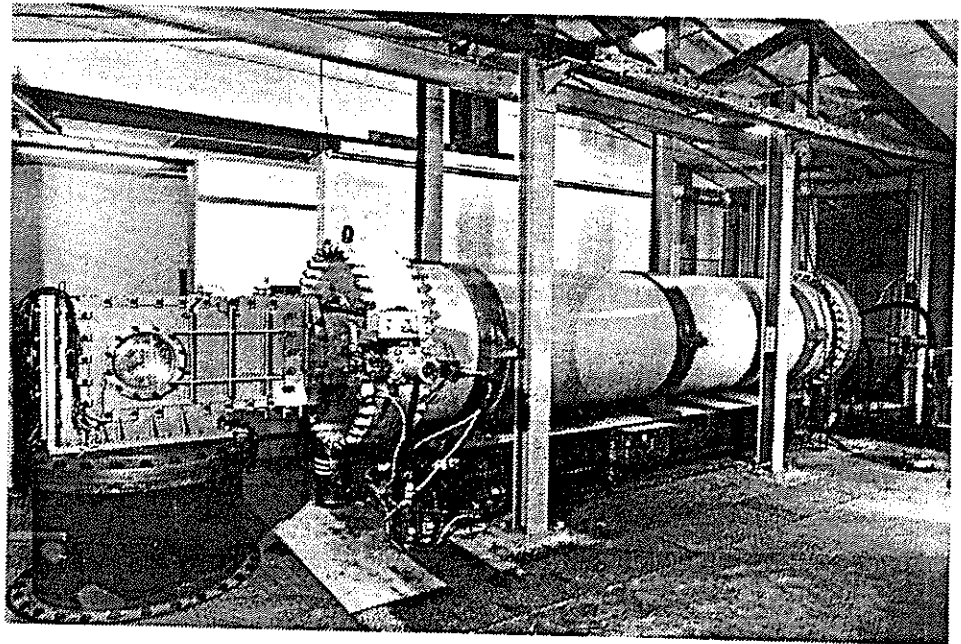


Fig.47 VKI/CT-2 compression tube facility

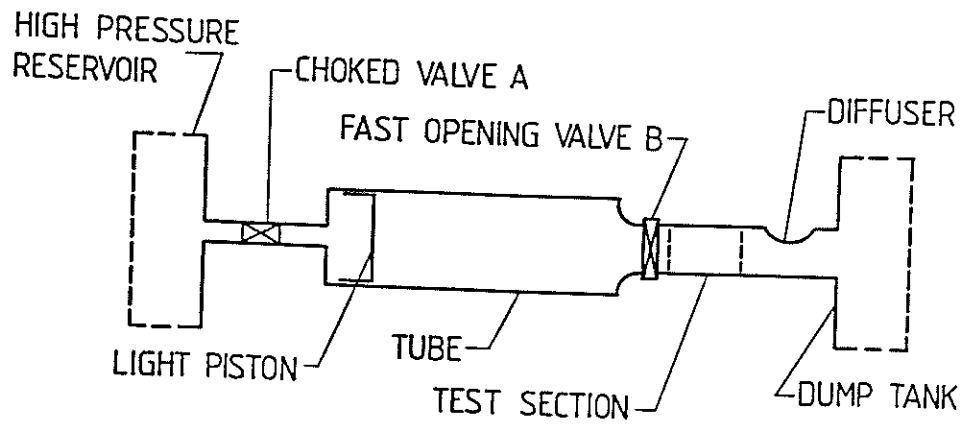


Fig.48 A schematic view of the compression tube

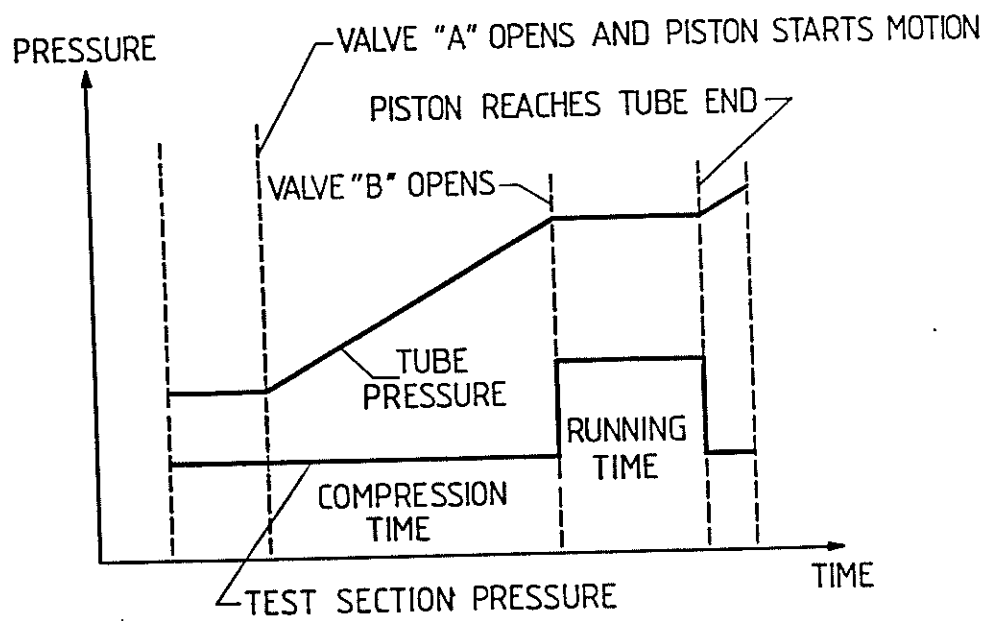


Fig.49 Timing of the events

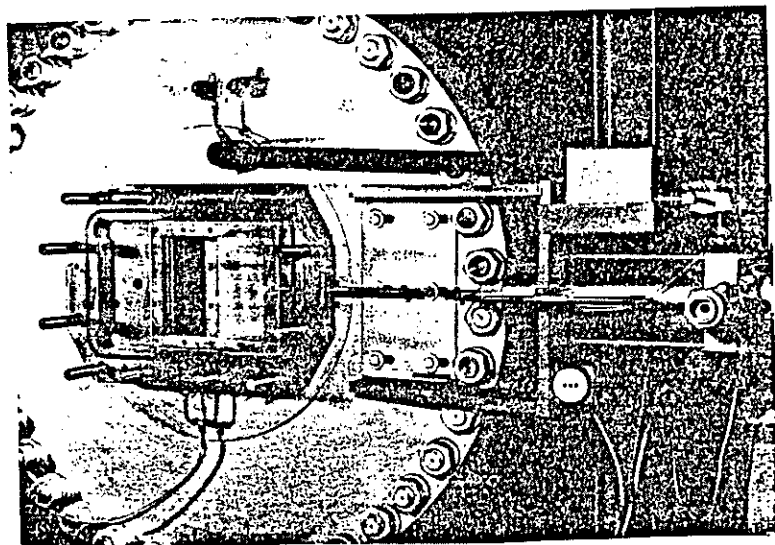


Fig.50 The fast opening valve

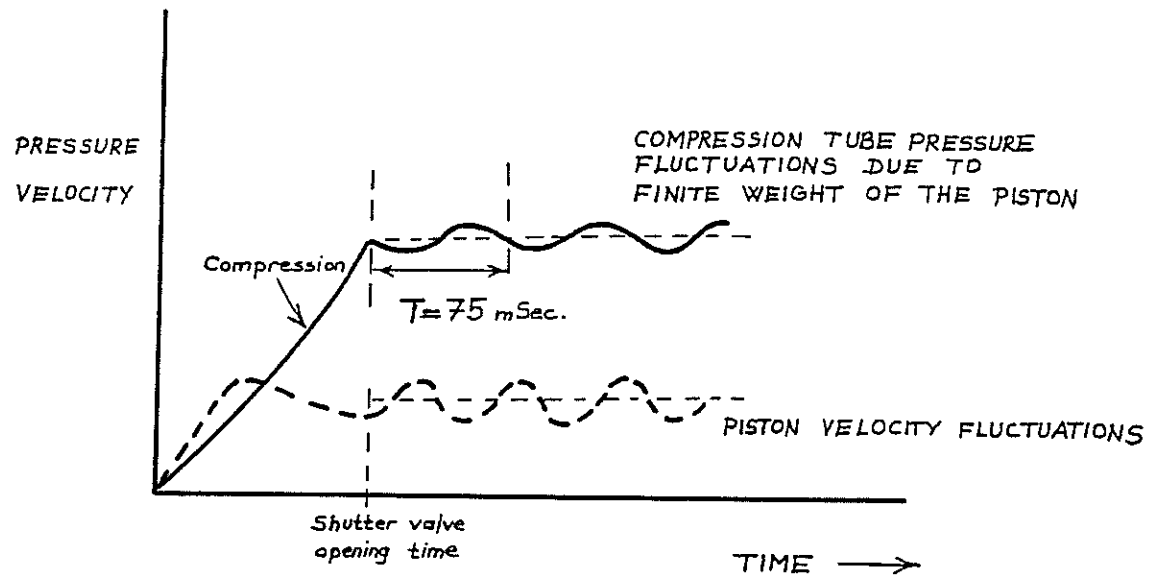


Fig. 51 Compression tube pressure and piston velocity, time history

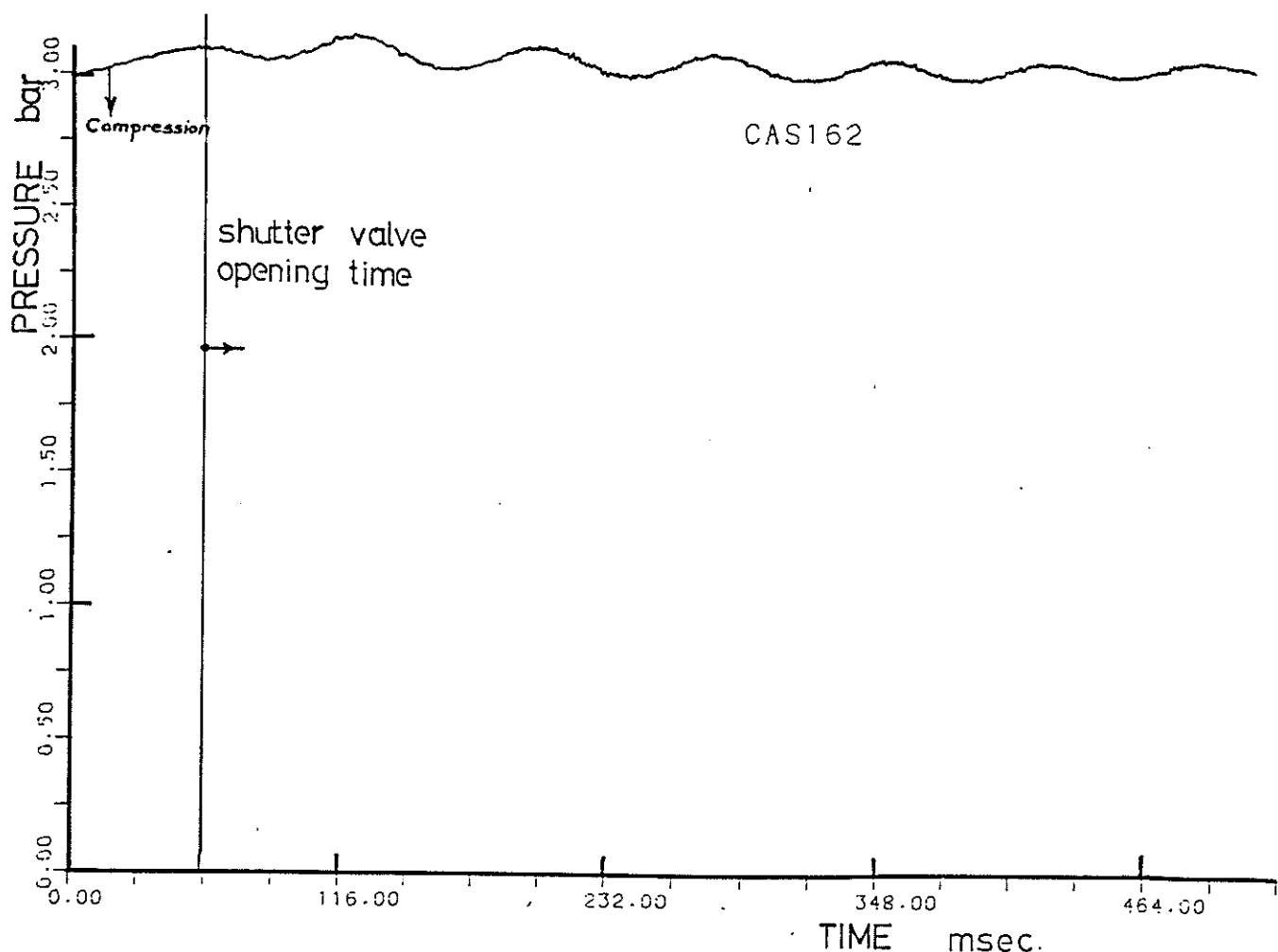


Fig. 52 Measured total pressure fluctuations in the test section of CT-2

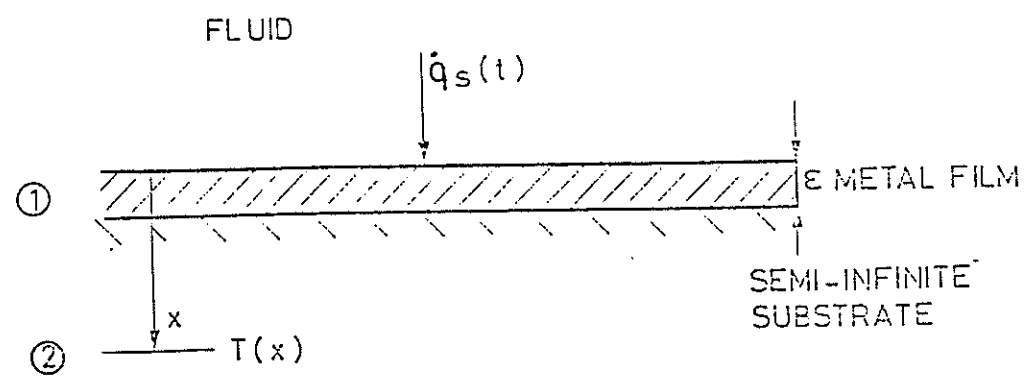


Fig.53 Heat conduction in a metallic film on semi-infinite insulating substrate

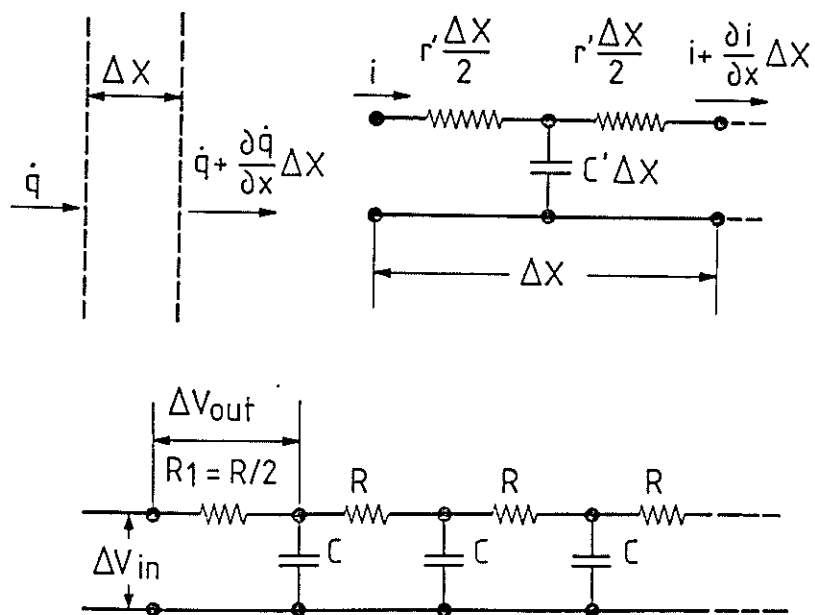


Fig.54 Electrical analogue using equal sections representing a homogeneous heat conductor

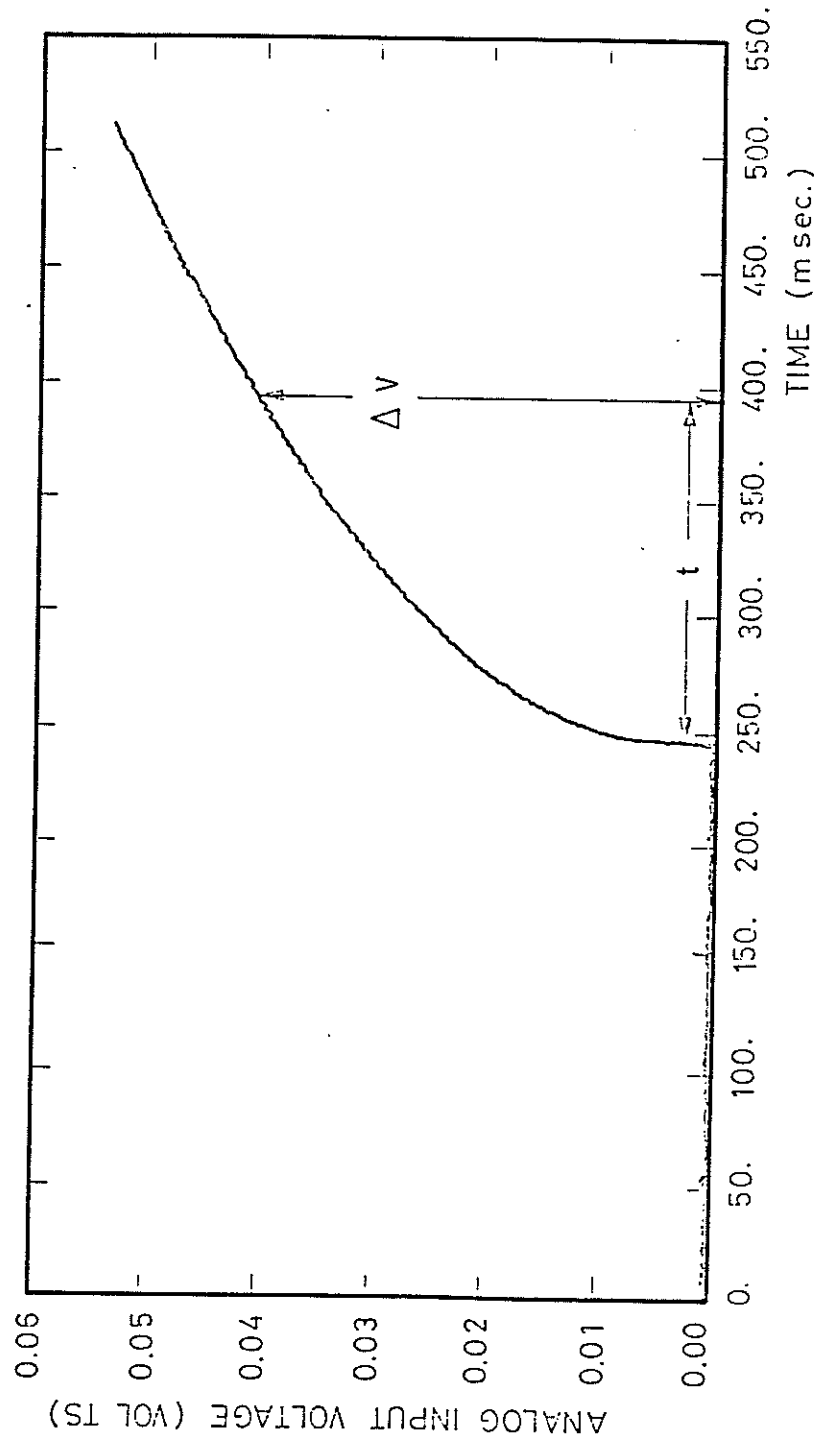


Fig. 55 Parabola input signal for calibration of analog circuits

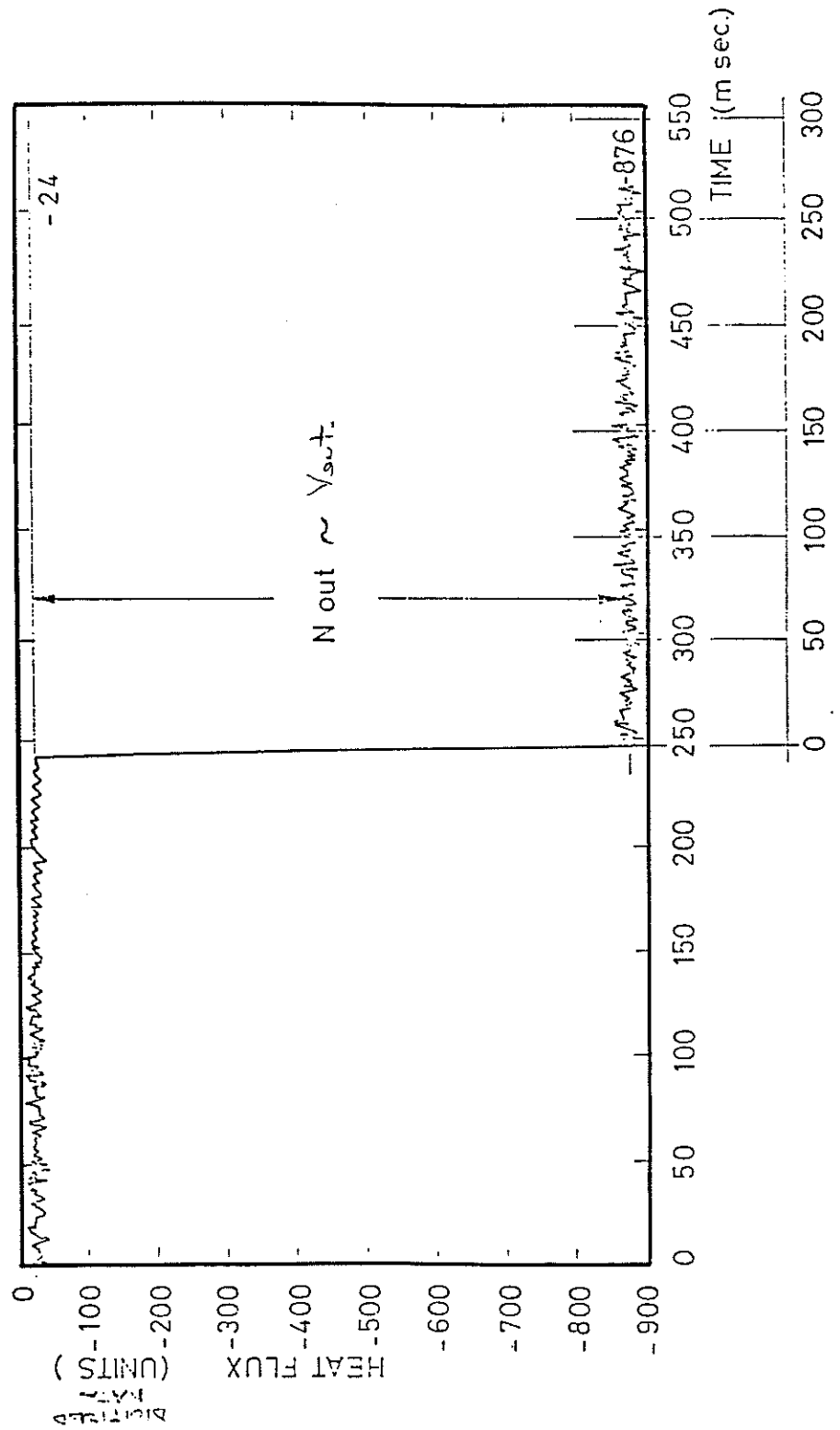


Fig. 56 Step output signal from a calibration of analogue circuit

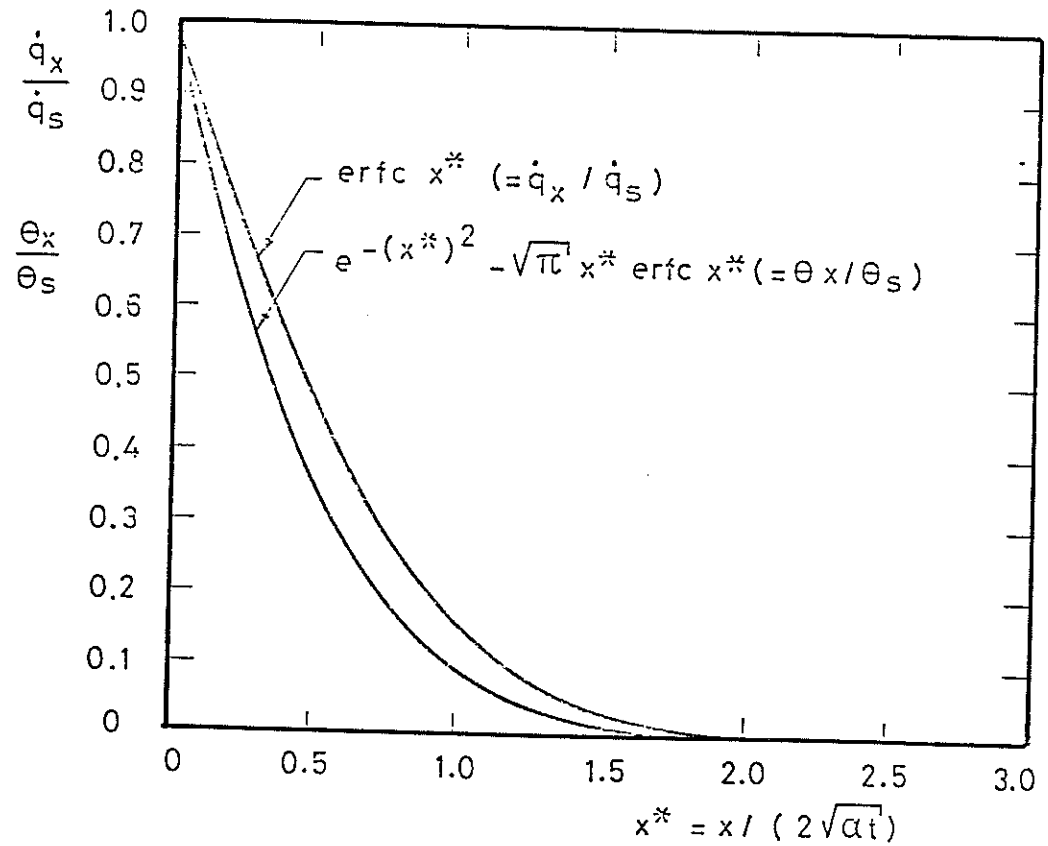


Fig. 57 Penetration of thermal pulse into substrate from step function in surface heat flux, from [125]

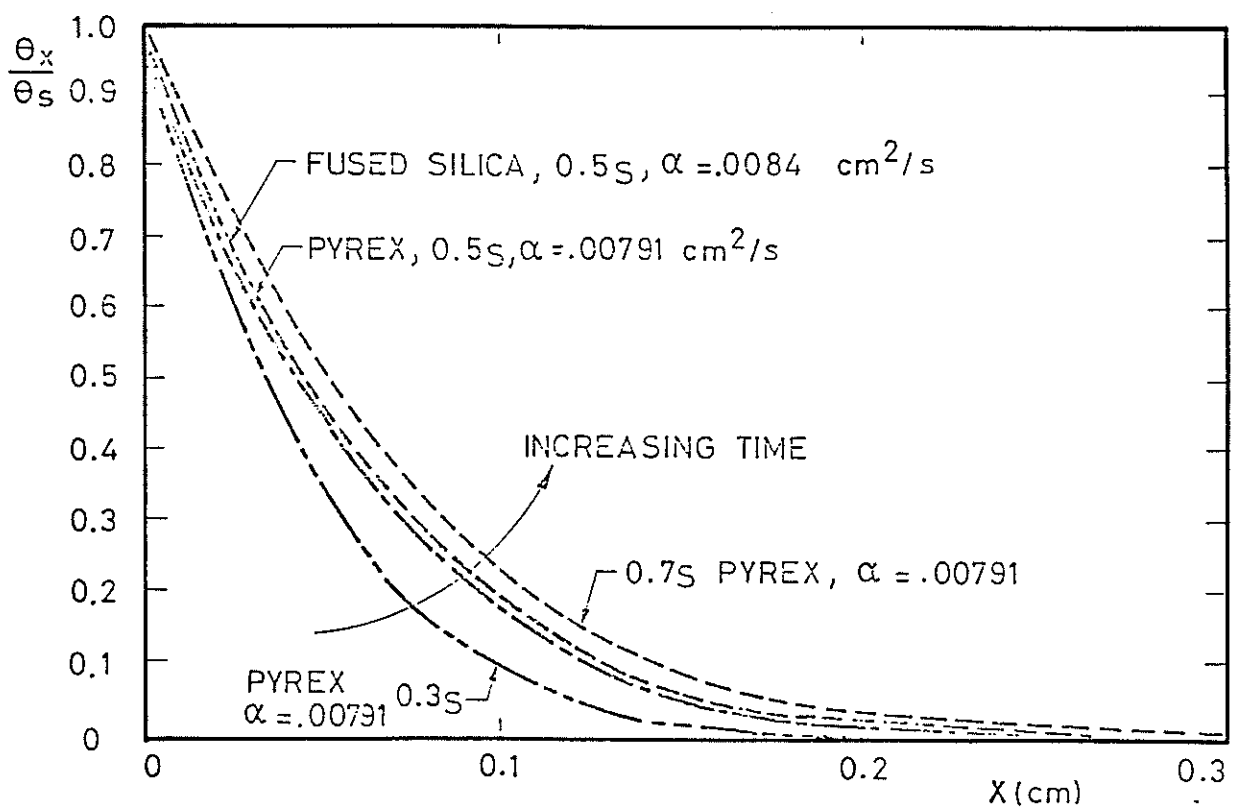


Fig.58 Penetration of thermal pulse into substrate due to step function in surface heat flux

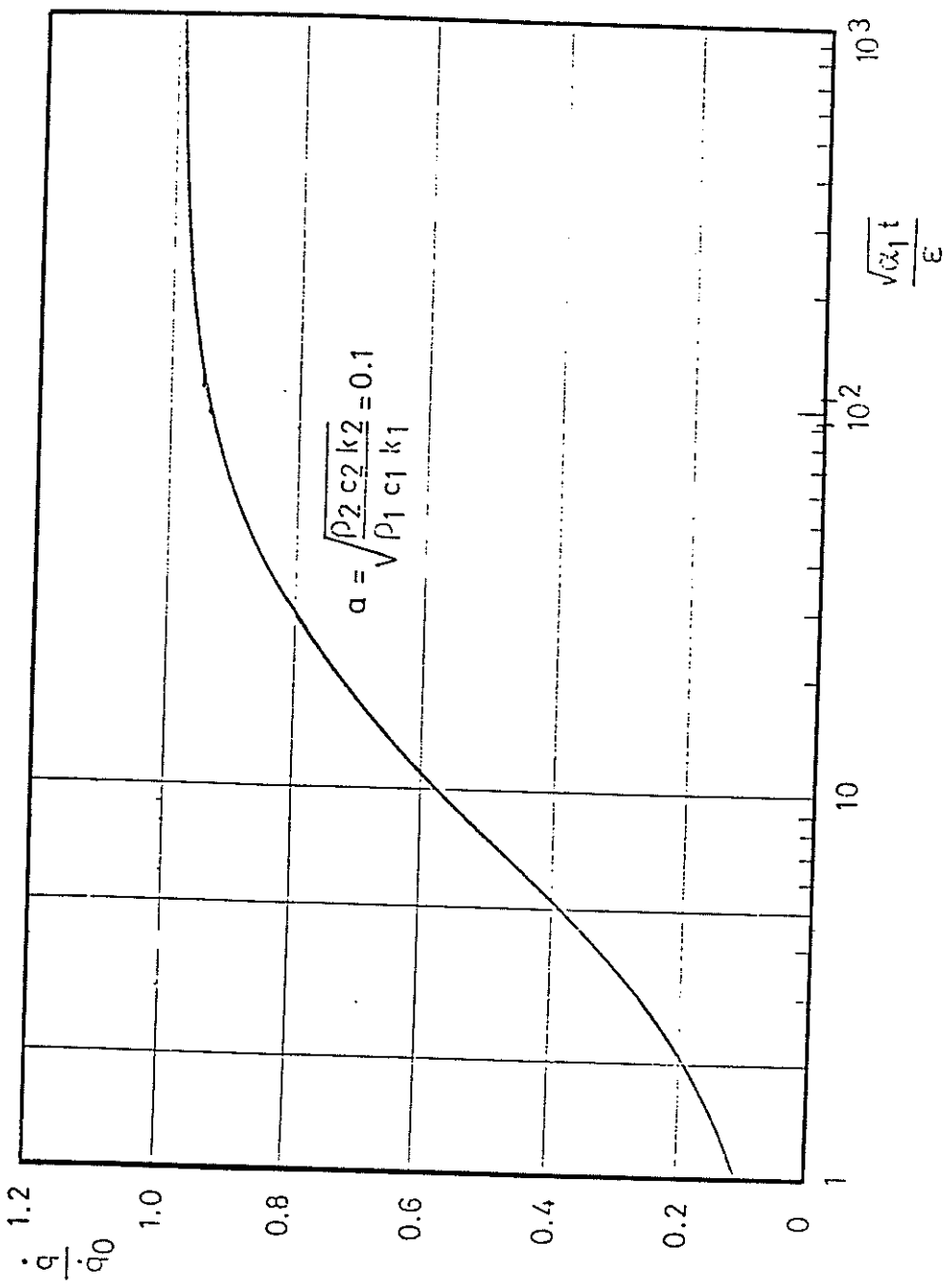


Fig. 59 Effect of surface metallic film on calculated heat transfer rate. q_0 = amplitude of actual step function in heat transfer rate from [ref]

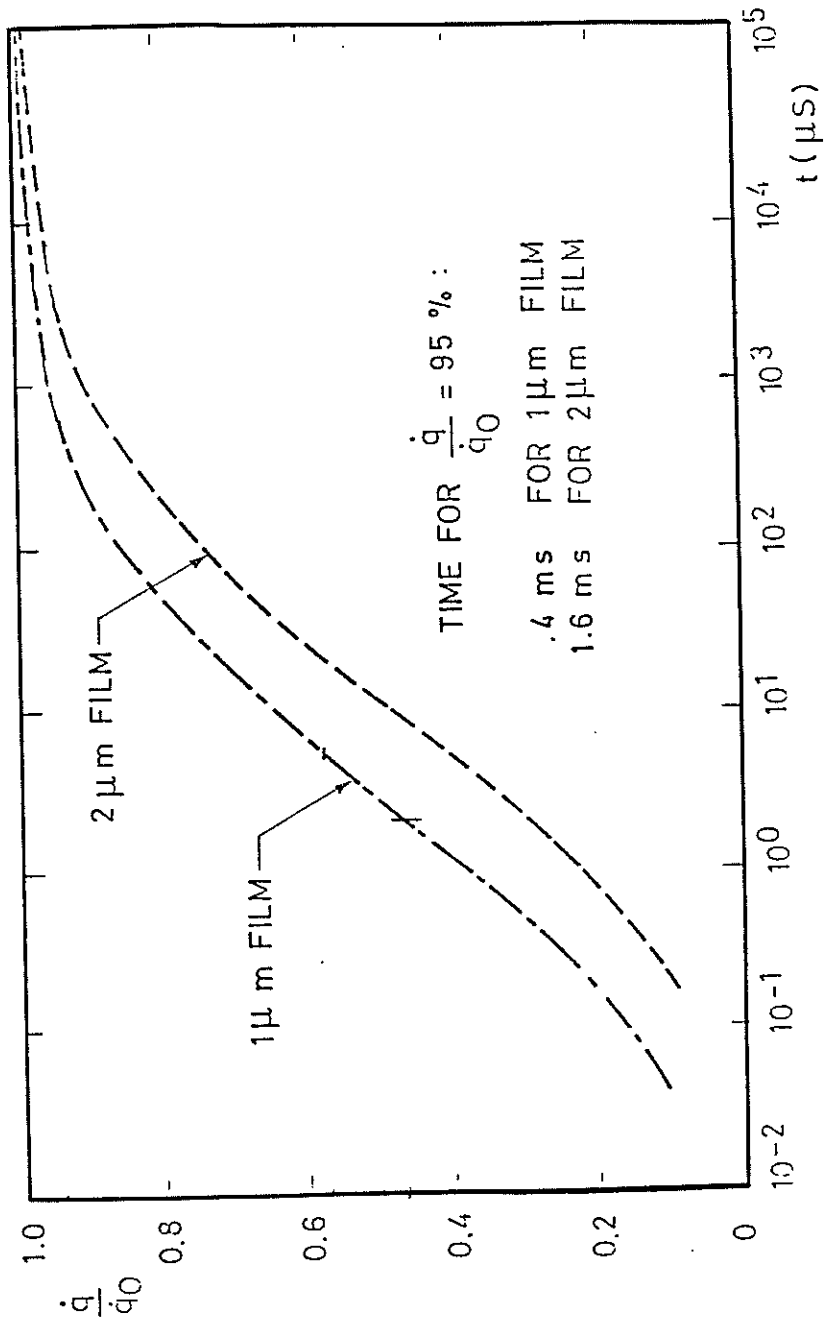


Fig. 6.0 Time response of a thin film platinum gauge with
 $\sqrt{\rho C_1 K_1 / \rho_2 C_2 K_2} = 0.10$ and $\alpha = 0.25 \text{ cm}^2/\text{s}$

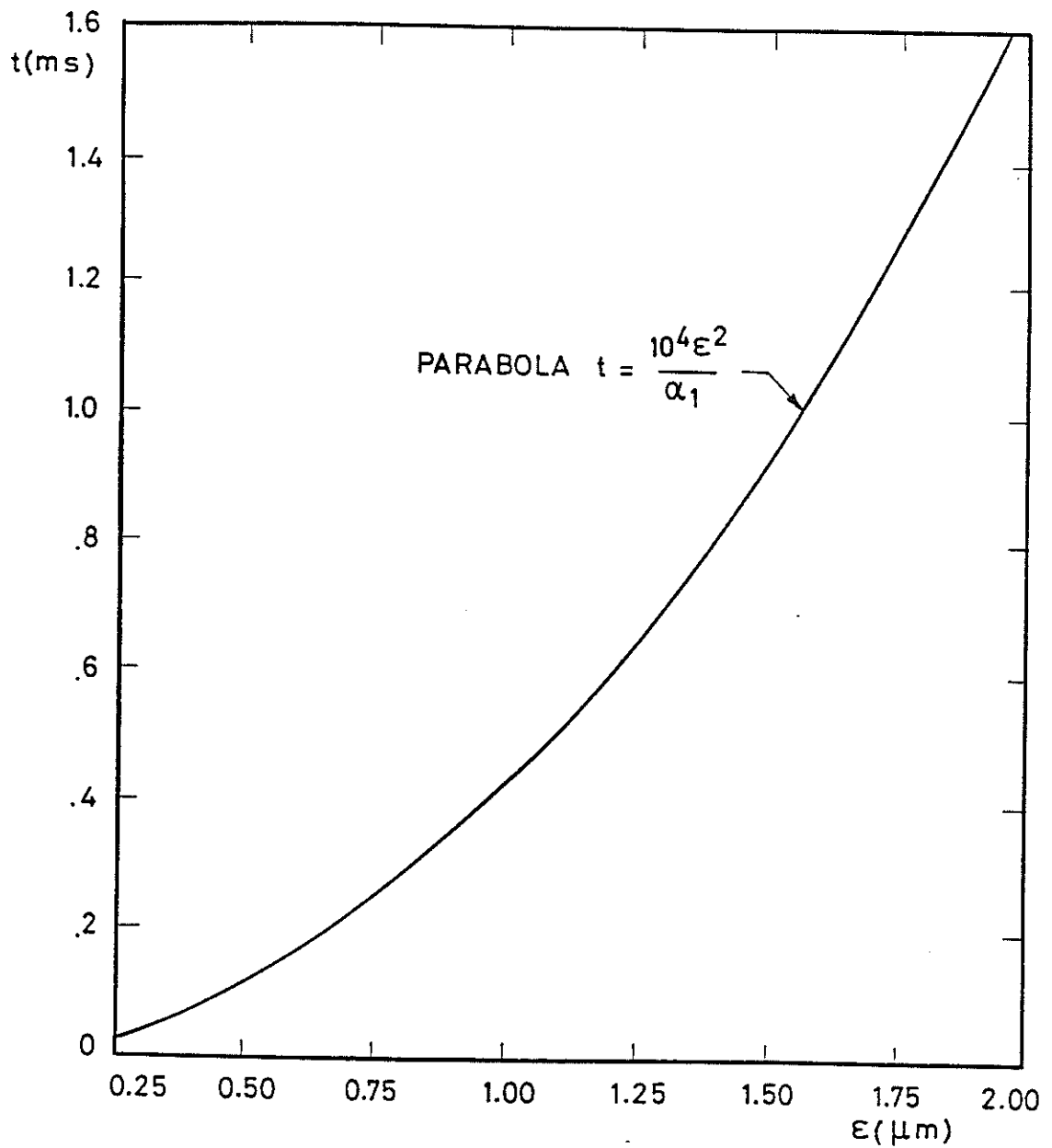


Fig.61 Response time from thin platinum film, time for the heat flow to reach 94 % of step input value with $\alpha=0.25 \text{ cm}^2/\text{s}$ and $\sqrt{\rho C_1 K_1 / \rho C_2 K_2} = 0.10$

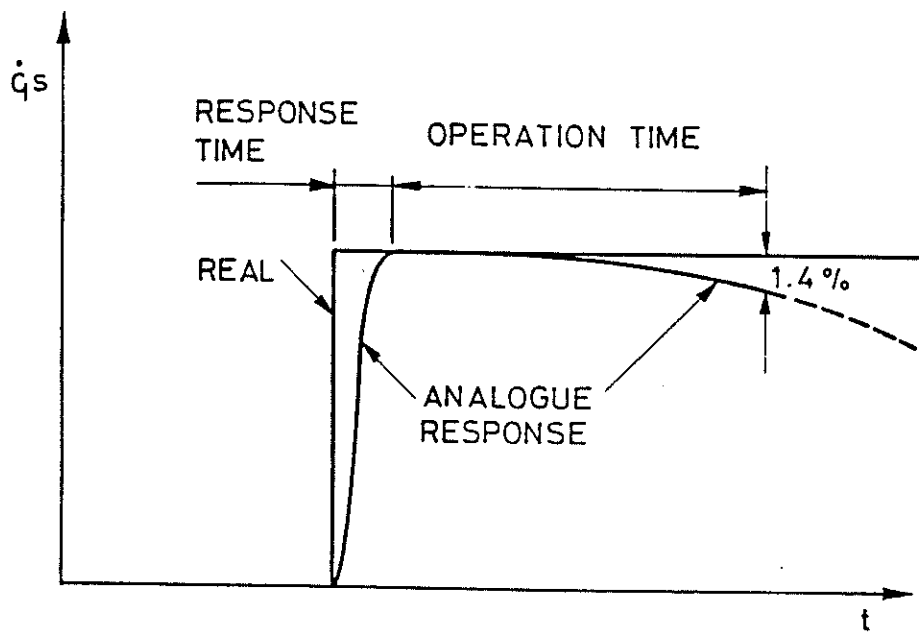


Fig.62 Sketch illustrating response criteria for electrical analogue circuits

Substrate	Pyrex	Pyrex	Pyrex	Pyrex	Pyrex	Ceramic	Ceramic	Ceramic	Ceramic
Film	1	2	3	4	5	6	2	3	8
$\alpha_R \times 10^2$ $^{\circ}K^{-1}$.2384	.2379	.2394	.2404	.2395	.2351	.2088	.2105	.2167
$R_0 (20^{\circ}C) \Omega$	25.44	61.52	58.98	35.89	49.75	86.30	85.01	45.68	91.90
$\Sigma (\text{error})^2$.0164	.1623	.1614	.0599	.1142	.3224	.0643	.0498	.2581

Fig. 64 Typical α_R calibration results

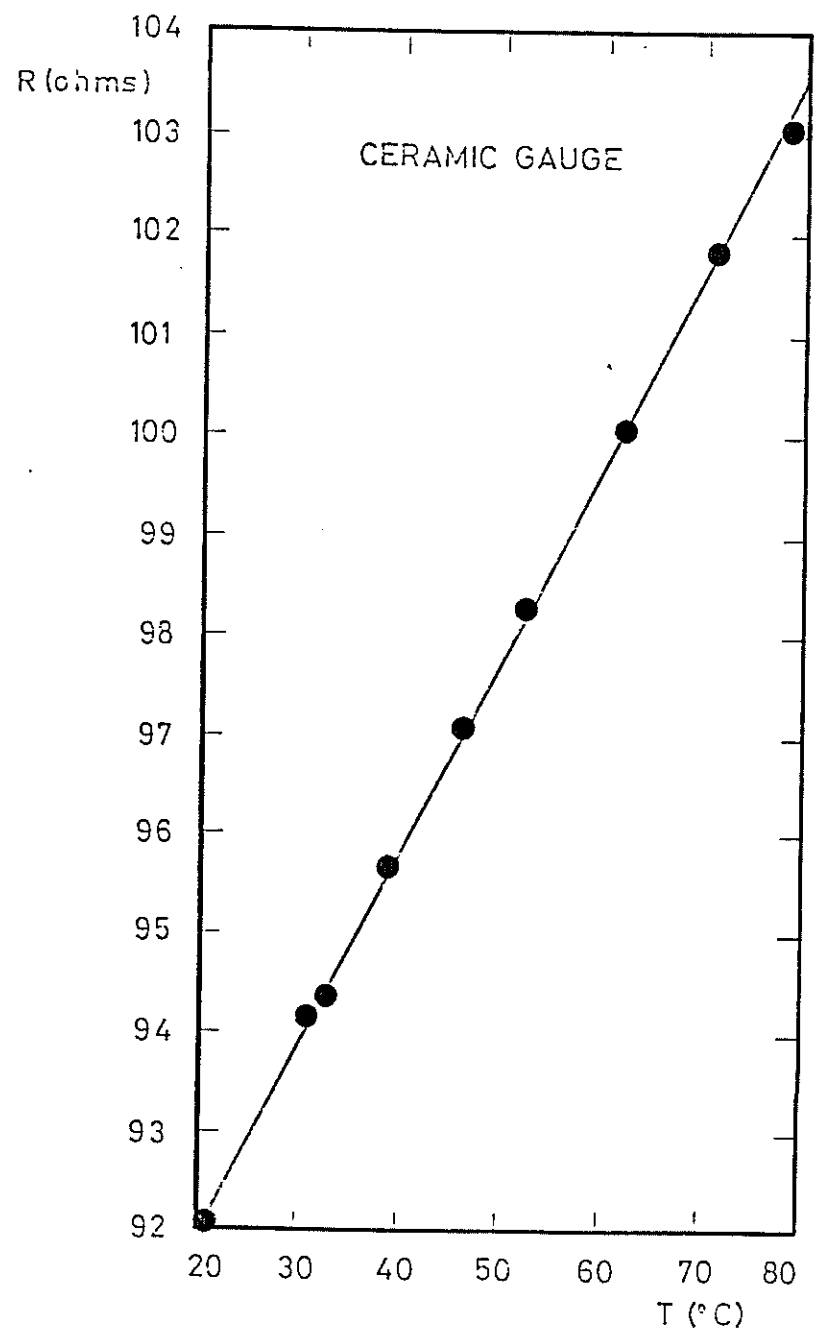


Fig.63 Typical calibration graph of a thin film gauge

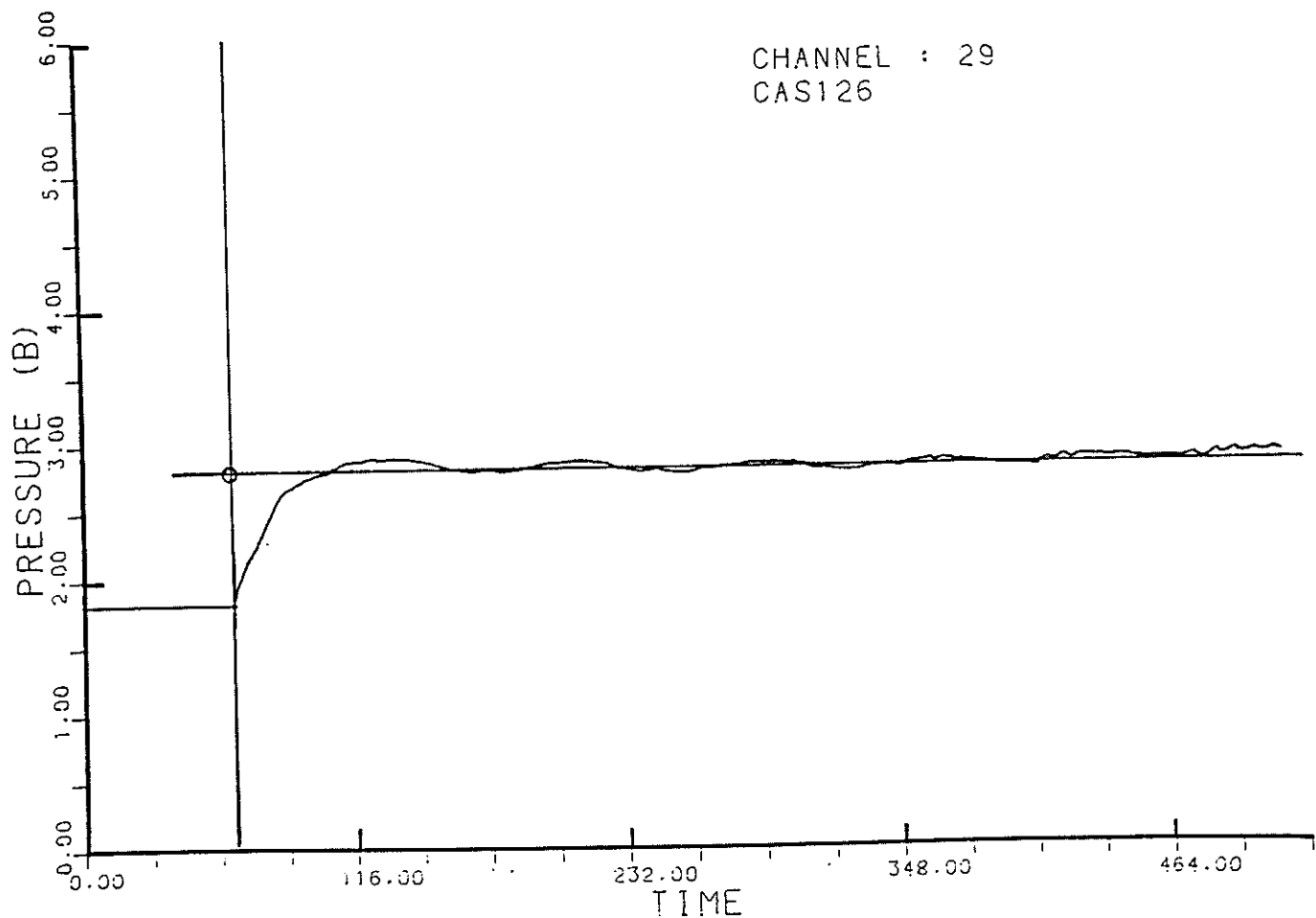
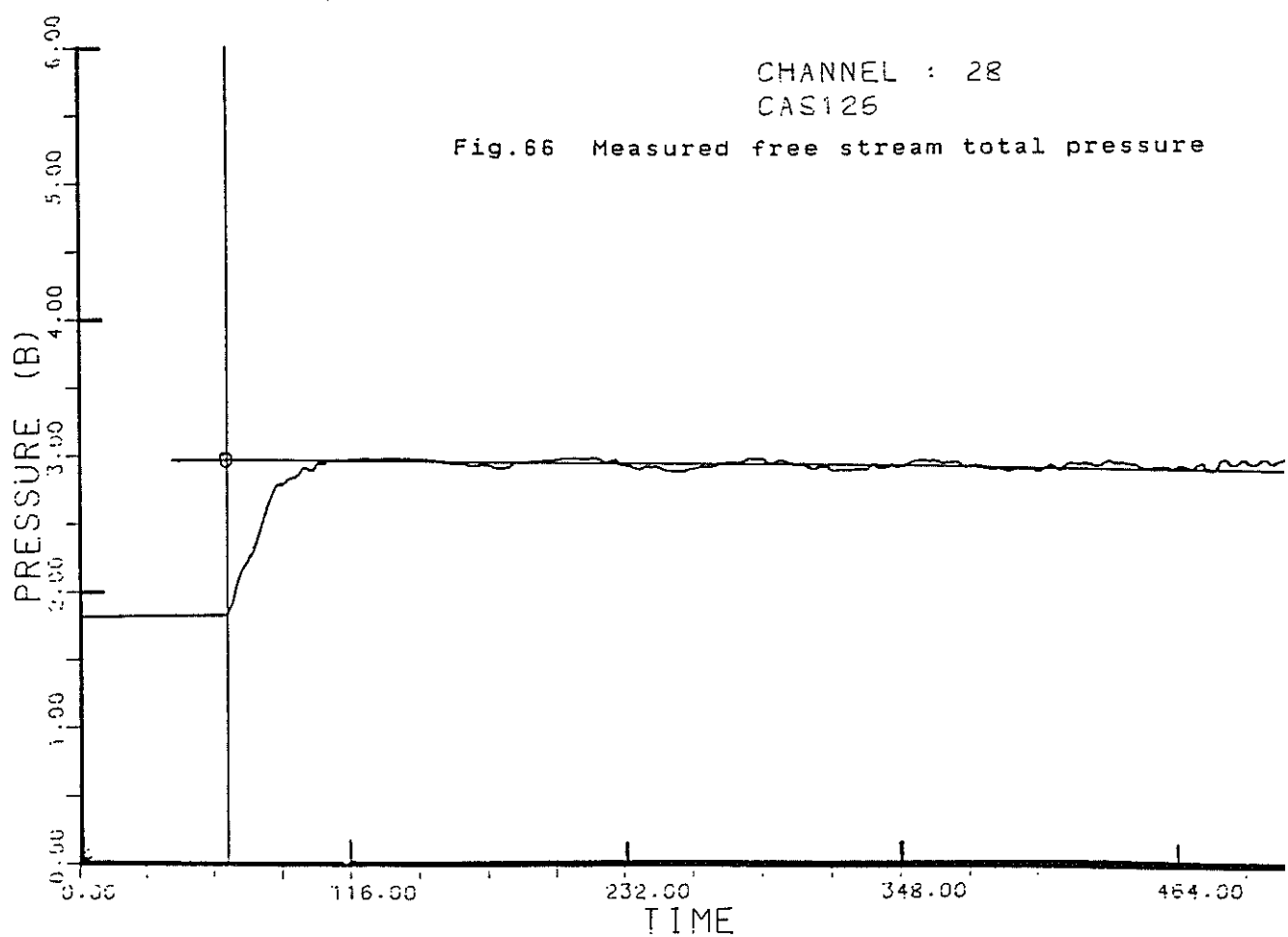
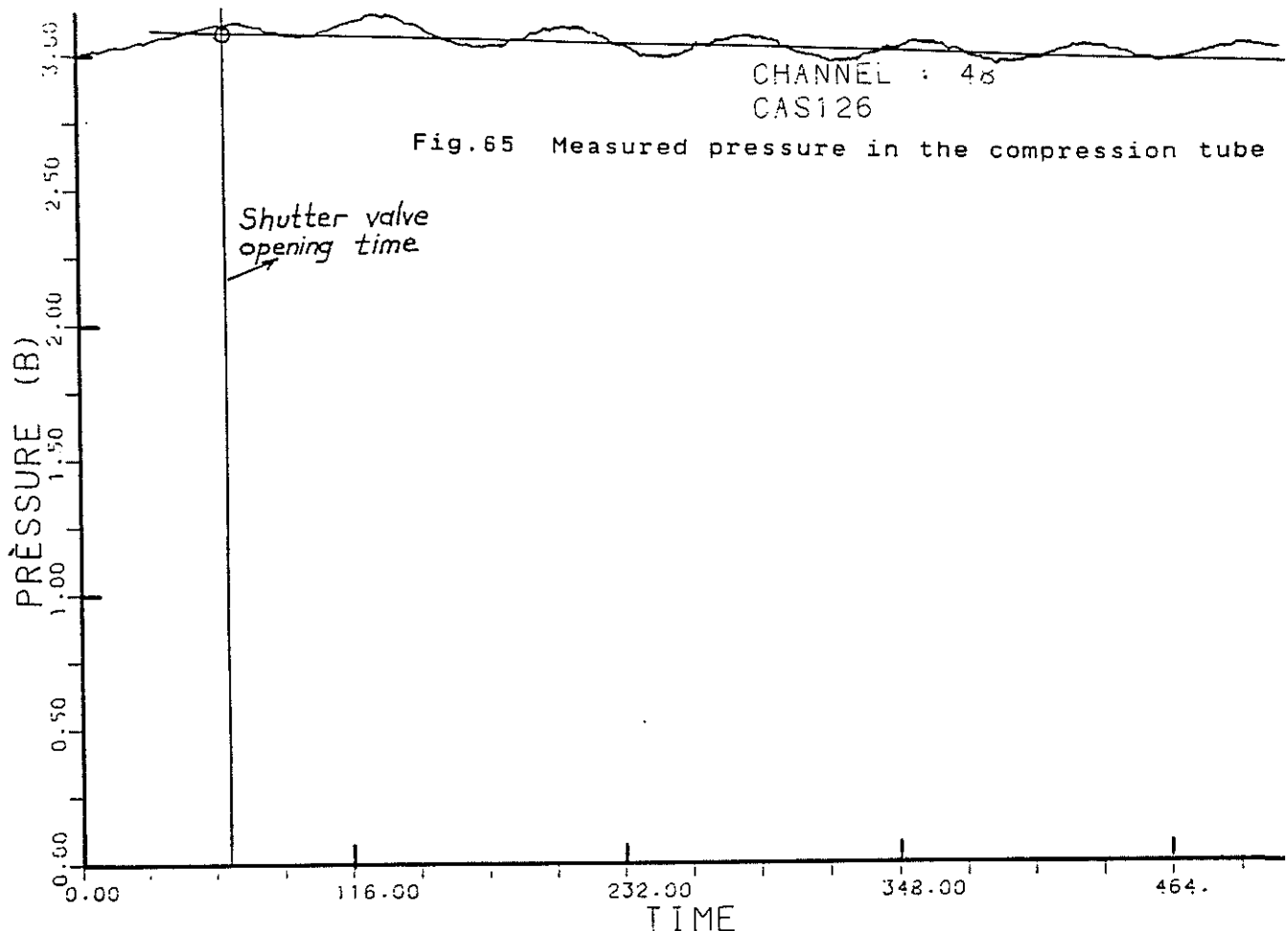


Fig.67 Inlet static pressure



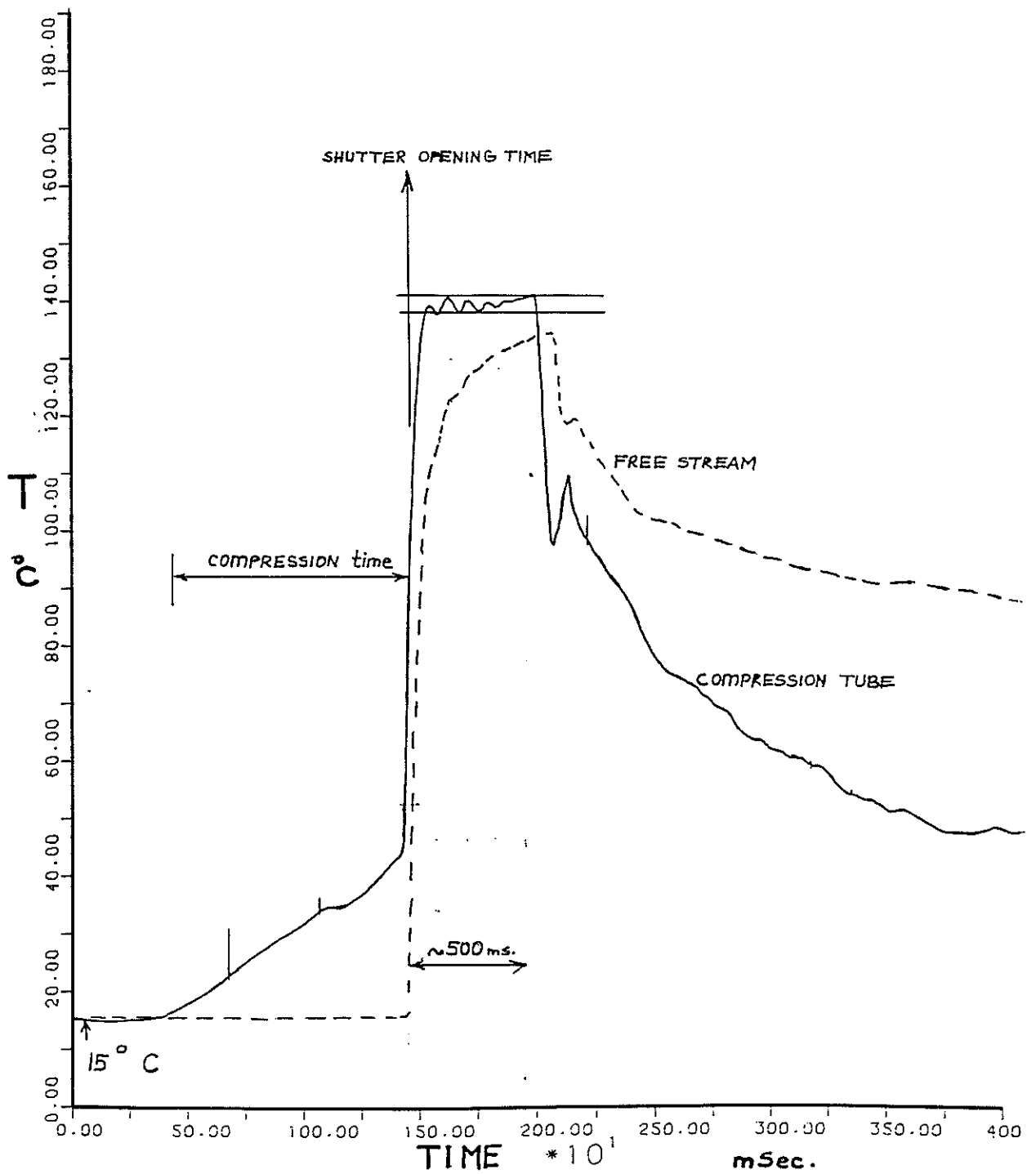
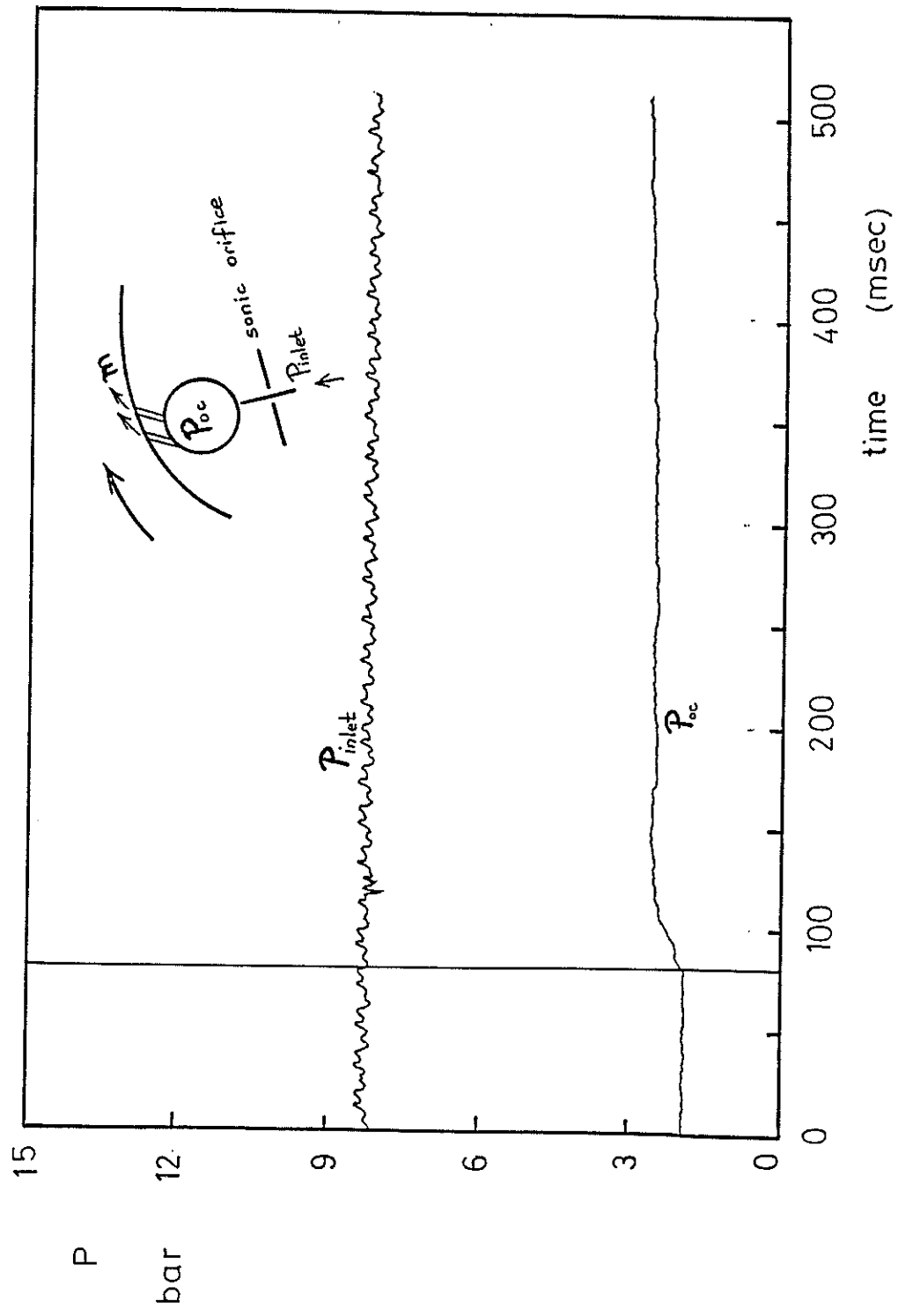


Fig. 69 Temperature measurement in the free stream and in the compression tube

EJECTION FROM THE
SUCTION SIDE
 $m = 0.44$
 $\dot{m}_e / \dot{m}_{\infty} = 0.49 \%$
EJECTION AT THE WALL
TEMPERATURE



P

bar

P

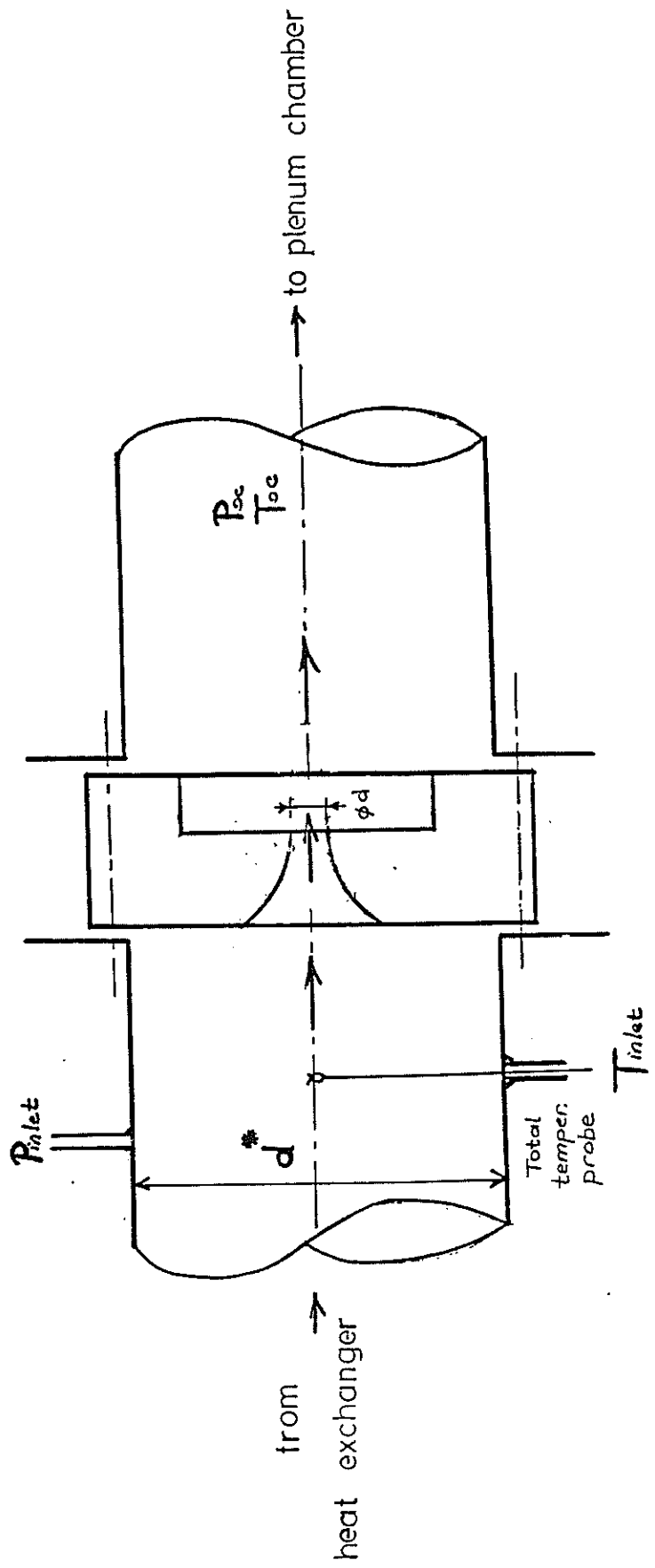
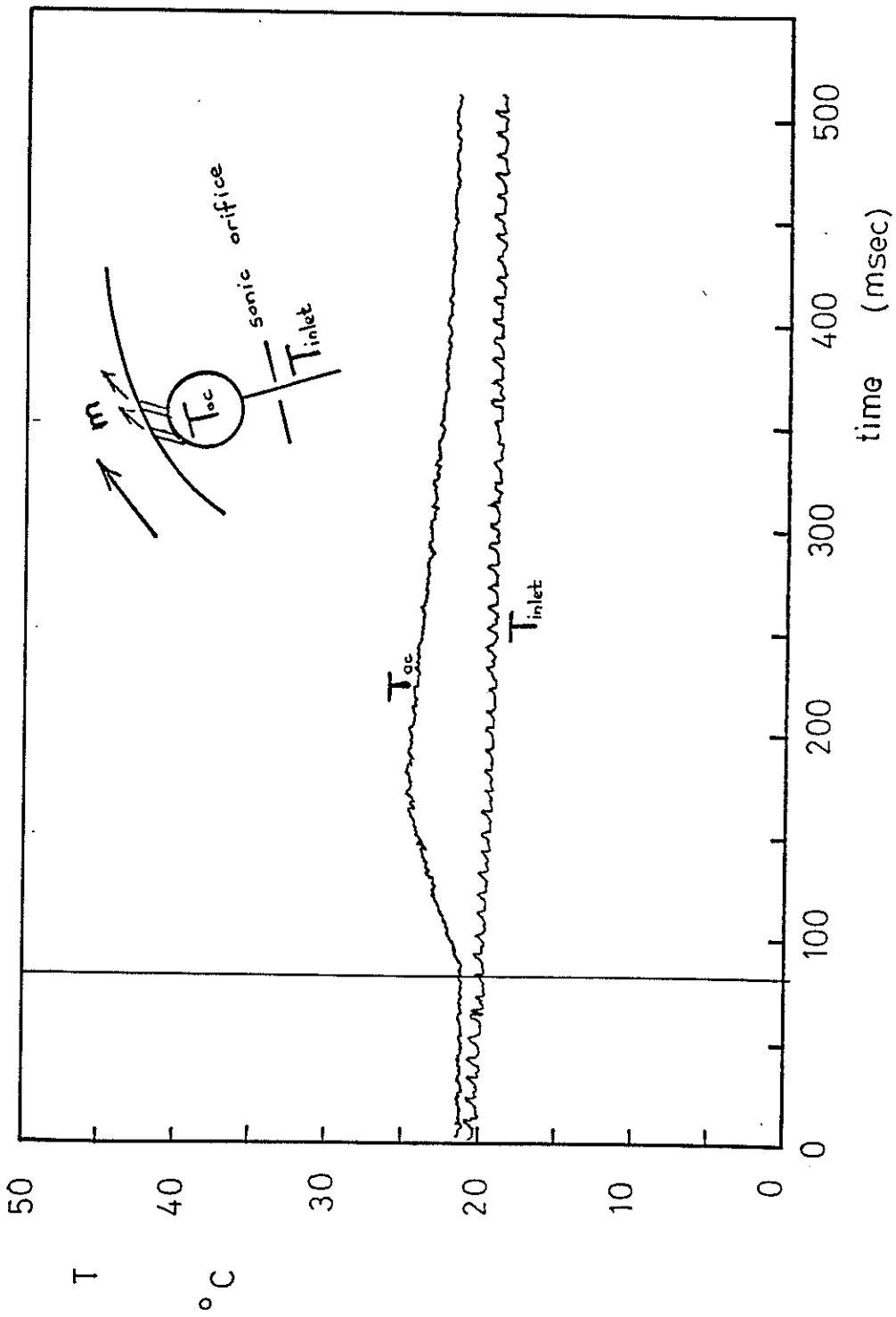


Fig. 71 A typical sonic orifice and measurement locations

EJECTION FROM THE
SUCTION SIDE
 $m=0.44$
 $\dot{m}_e/\dot{m}_{\infty}=0.49$ %
EJECTION AT THE WALL
TEMPERATURE



MEASUREMENT CHAIN

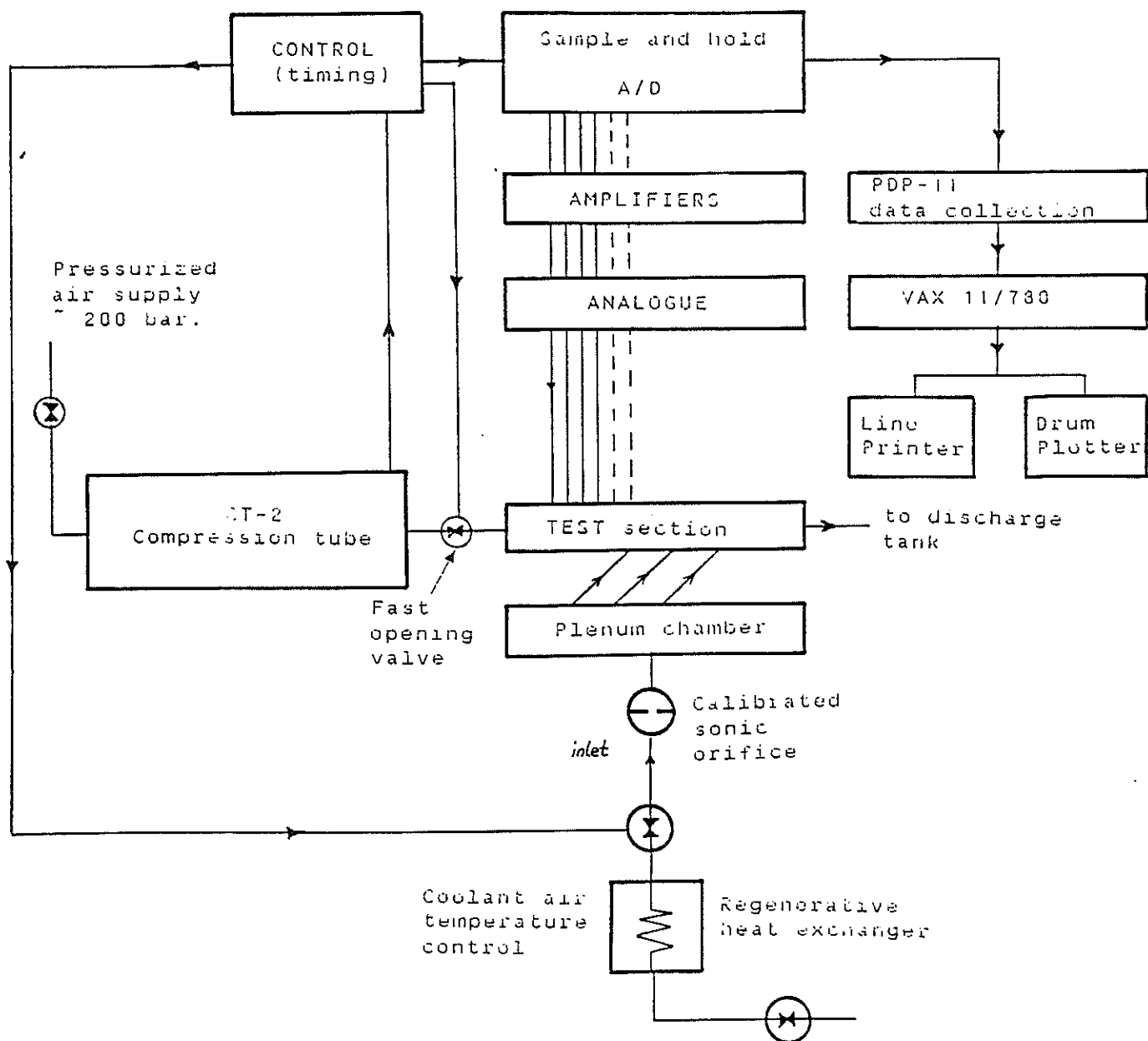


Fig. 70

Measurement chain

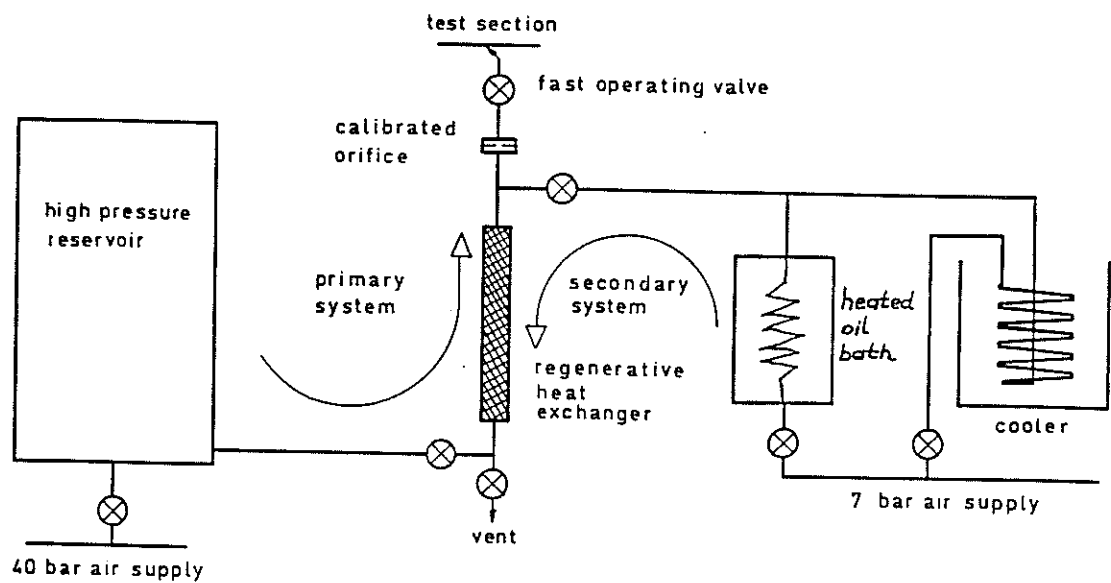


Fig.72 Coolant air supply

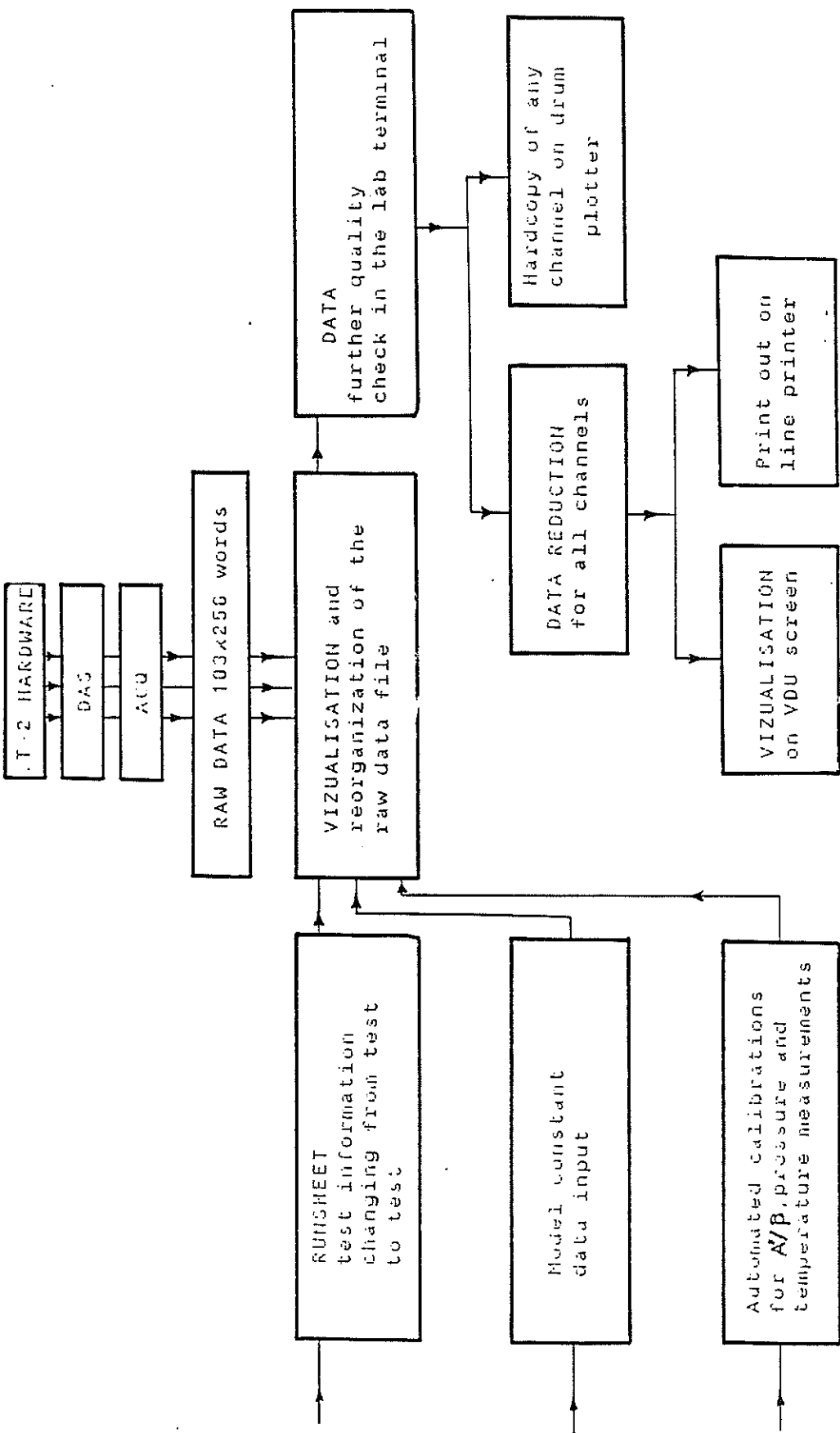


Fig.75 A flow chart for the software developed for CT-2

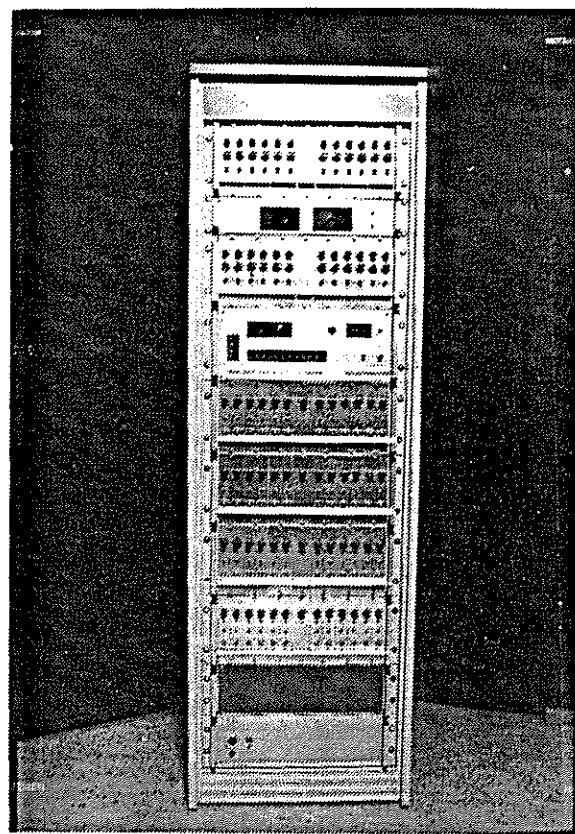


Fig.74 High speed data acquisition system and analogue circuits used for processing signals from thin-film gauges

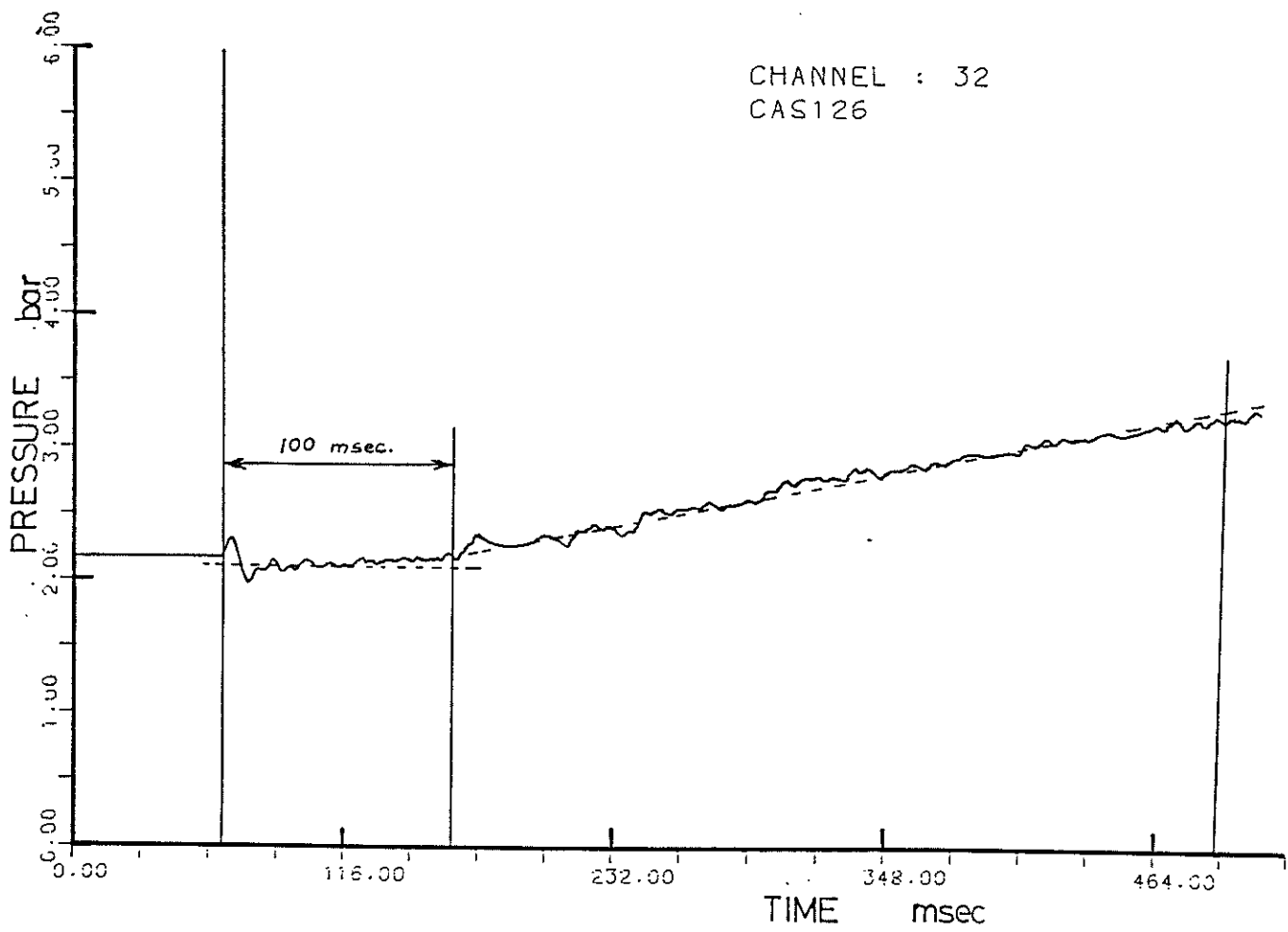


Fig. 76 A typical cascade exit static pressure trace

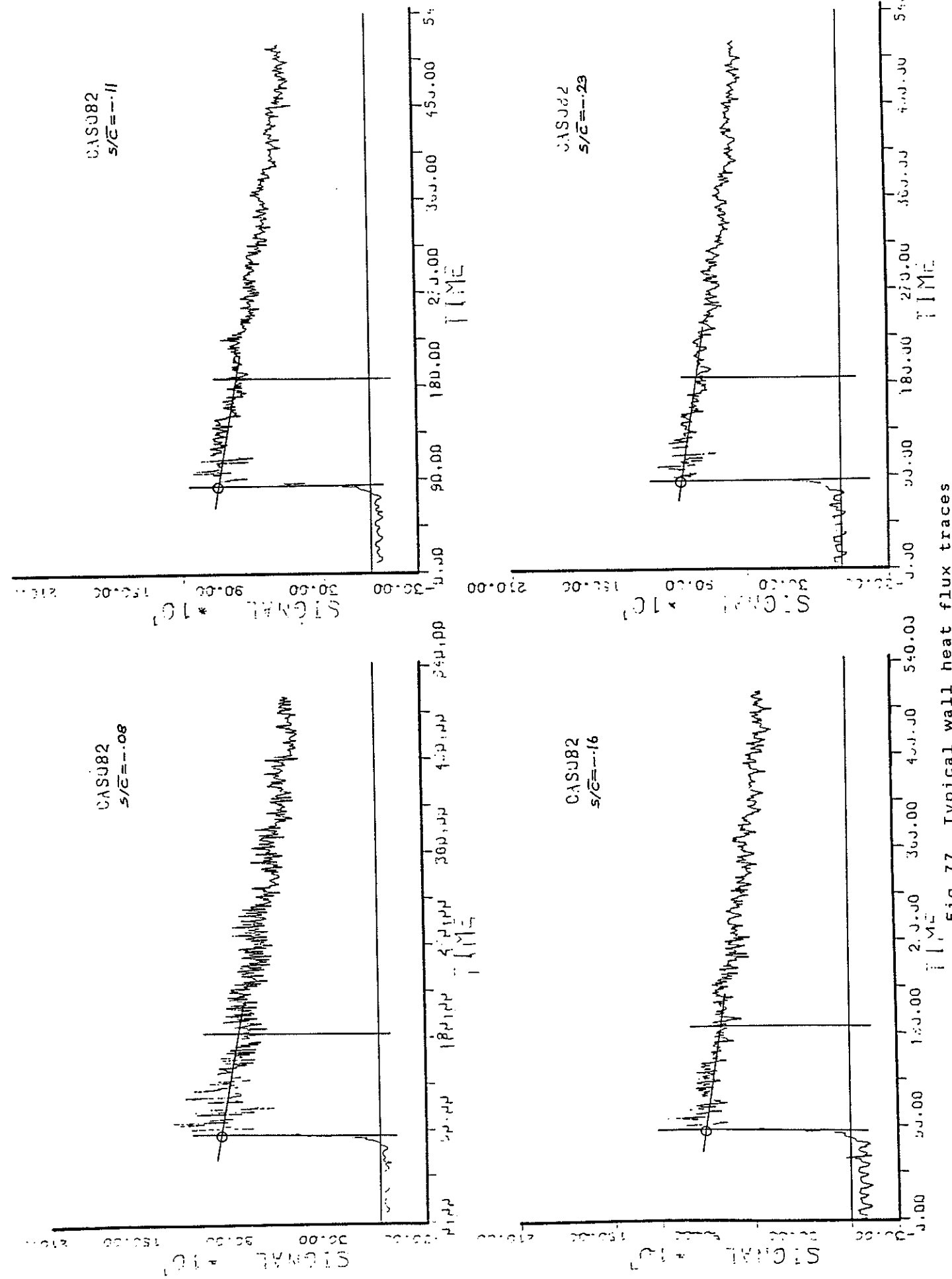


Fig.77 Typical wall heat flux traces

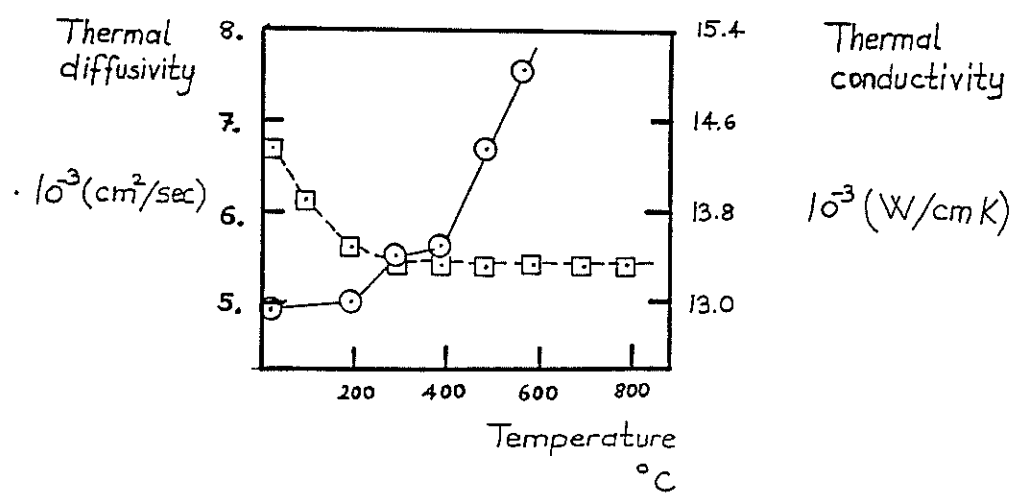


Fig.78 Temperature dependency of the thermal conductivity and the thermal diffusivity for machinable glass ceramic,[128]

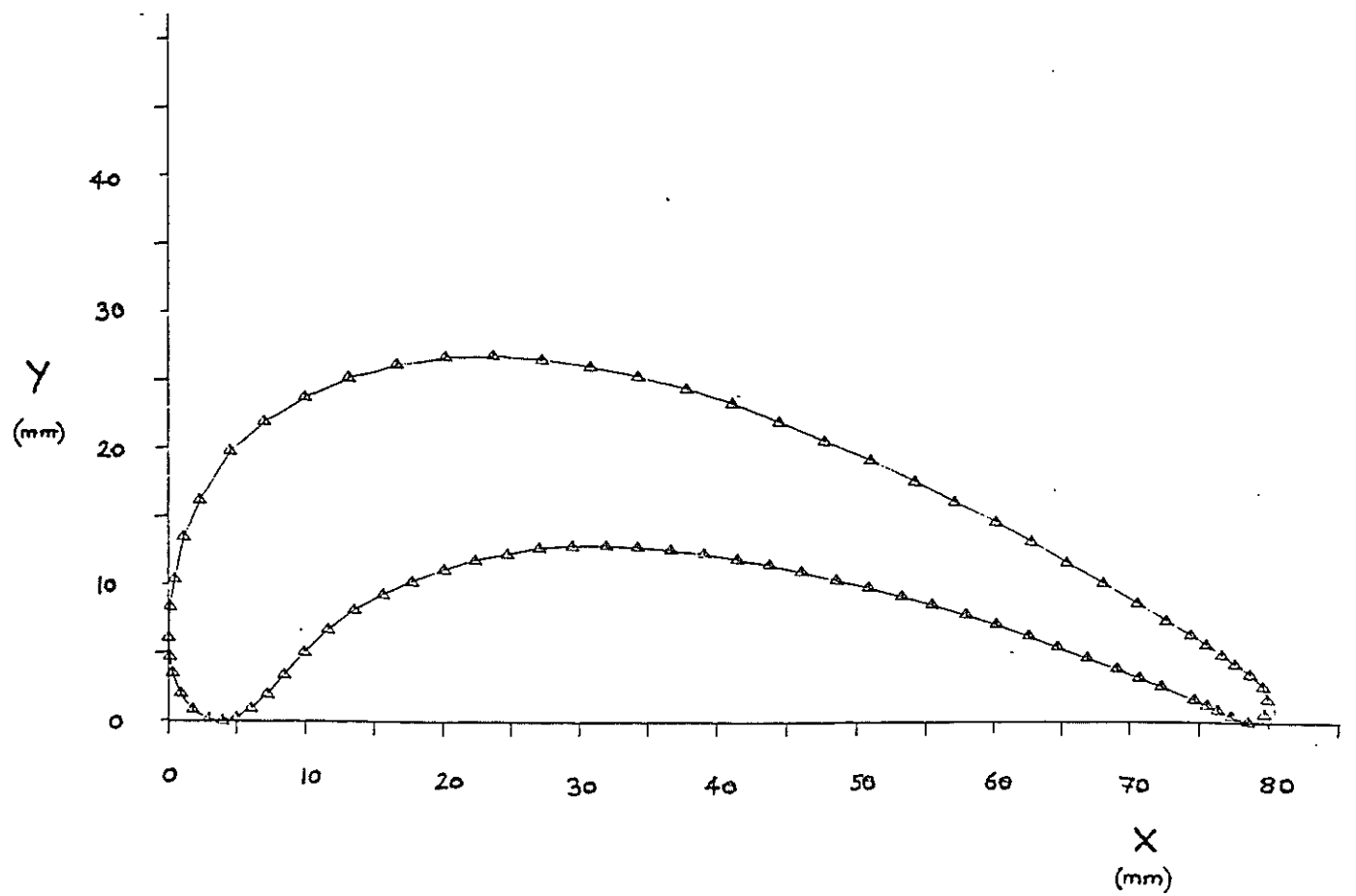


Fig.79 External profile of the blade

COORDINATES OF THE HP TURBINE ROTOR BLADE

[mm]			
X	Y	X	Y
4.05	0.00		
2.00	0.50		
1.13	1.65	1.13	1.65
0.50	3.00	0.50	3.00
0.00	6.87	4.05	0.00
0.12	8.75	5.50	0.50
0.28	10.64	7.53	2.15
0.75	13.00	8.75	3.50
1.51	14.87	10.35	5.50
2.75	17.50	12.24	7.18
4.71	20.03	14.12	8.40
6.50	21.50	16.47	9.63
8.47	22.99	18.75	10.56
11.00	24.25	20.71	11.30
14.12	25.46	23.25	11.94
16.75	26.20	26.35	12.52
19.29	26.62	29.50	12.75
22.25	26.75	32.00	12.81
24.94	26.77	34.75	12.75
27.75	26.56	37.65	12.45
30.59	26.12	40.50	12.00
33.50	22.50	43.29	11.56
36.24	24.80	46.00	11.00
39.00	23.86	48.93	10.35
41.88	22.92	52.00	9.50
45.50	21.50	54.59	8.88
48.94	20.08	57.50	7.94
53.25	18.00	60.24	7.13
57.41	16.02	63.25	6.00
61.50	13.75	65.88	5.13
65.88	11.45	68.75	4.00
69.75	9.25	71.53	2.86
74.35	6.37	73.50	2.00
77.18	4.52	75.29	1.21
79.06	3.25	76.75	0.65
80.00	1.69	78.35	0.00
79.81	0.85	79.81	0.85
78.35	0.00		

Fig. 80

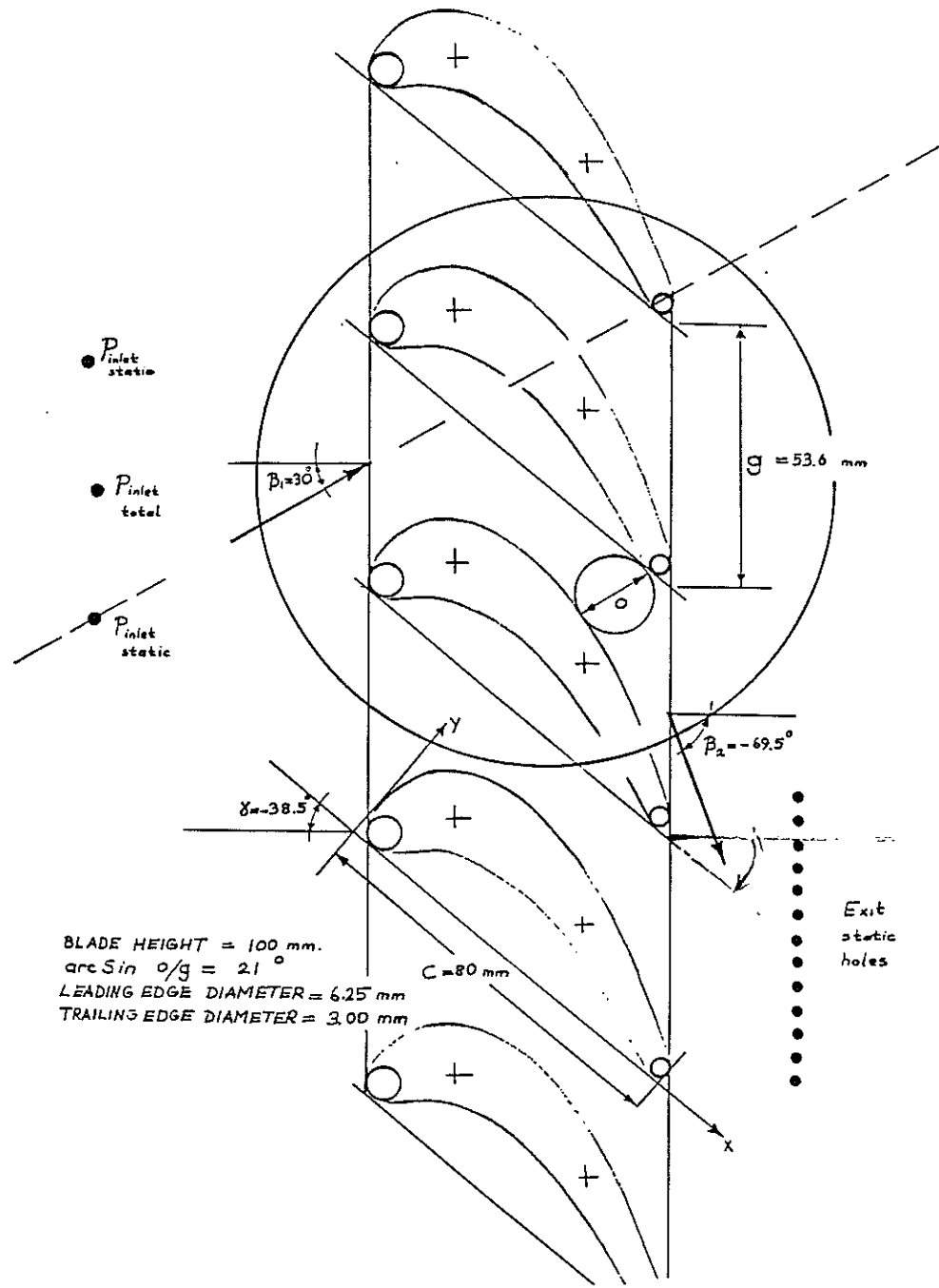
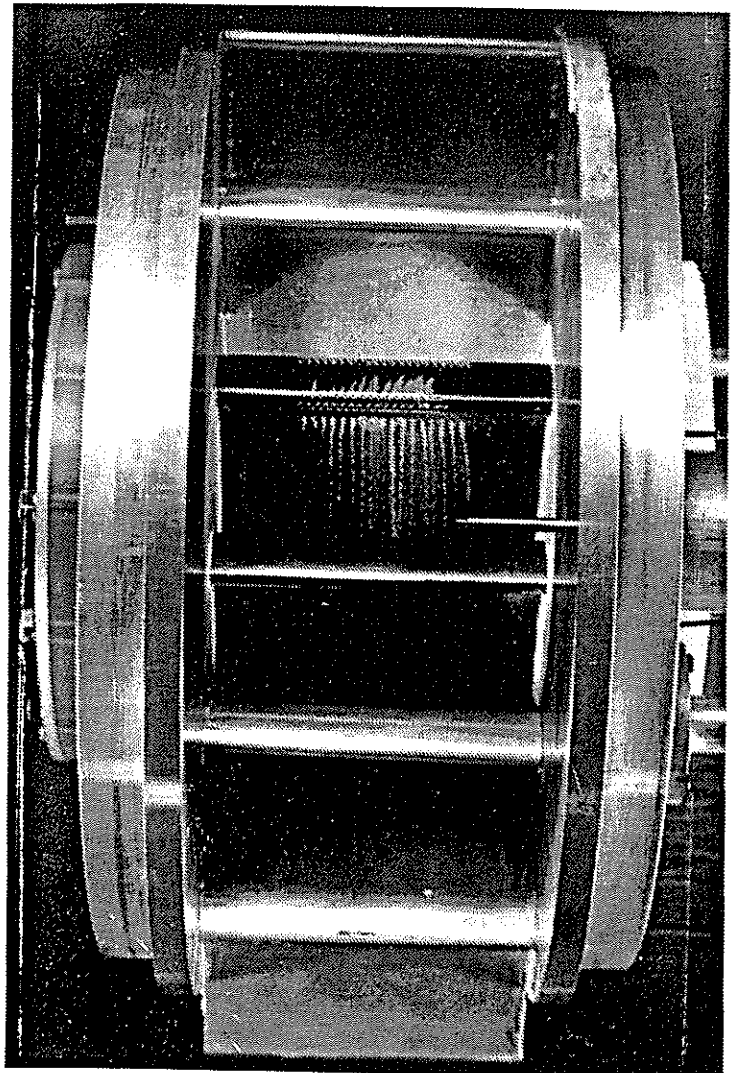
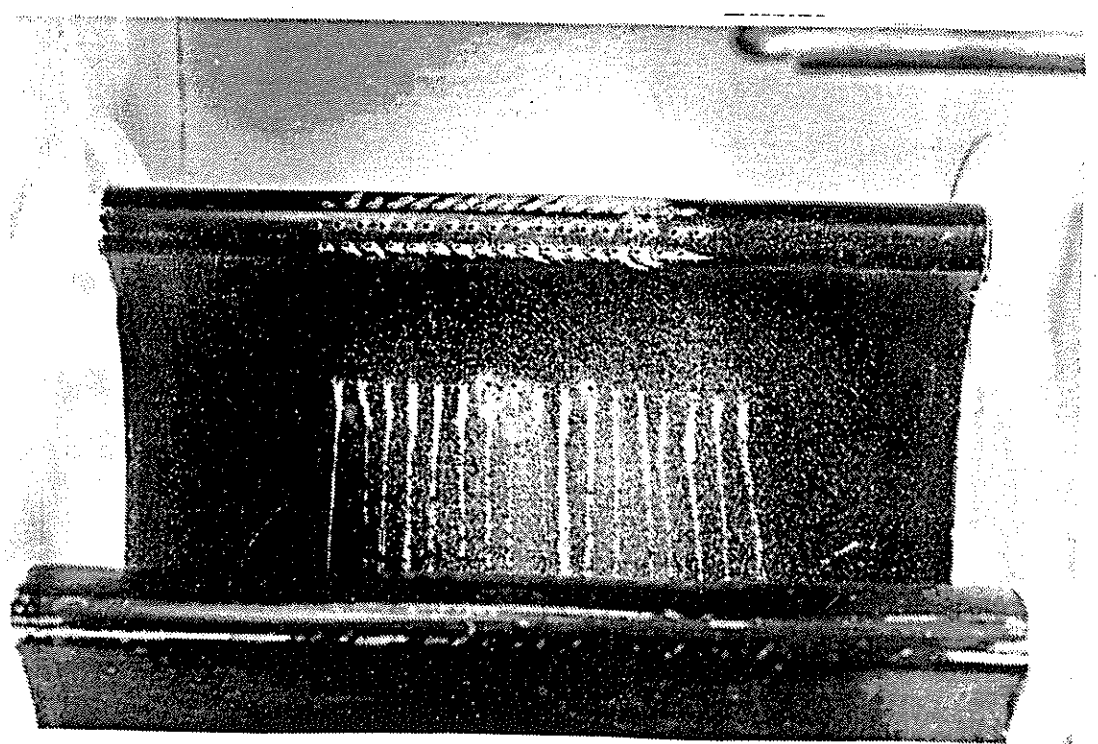


Fig.81 The cascade geometry

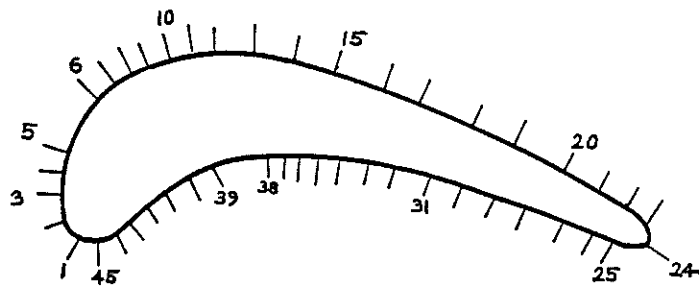


(a)



(b)

Fig. 82 The cascade



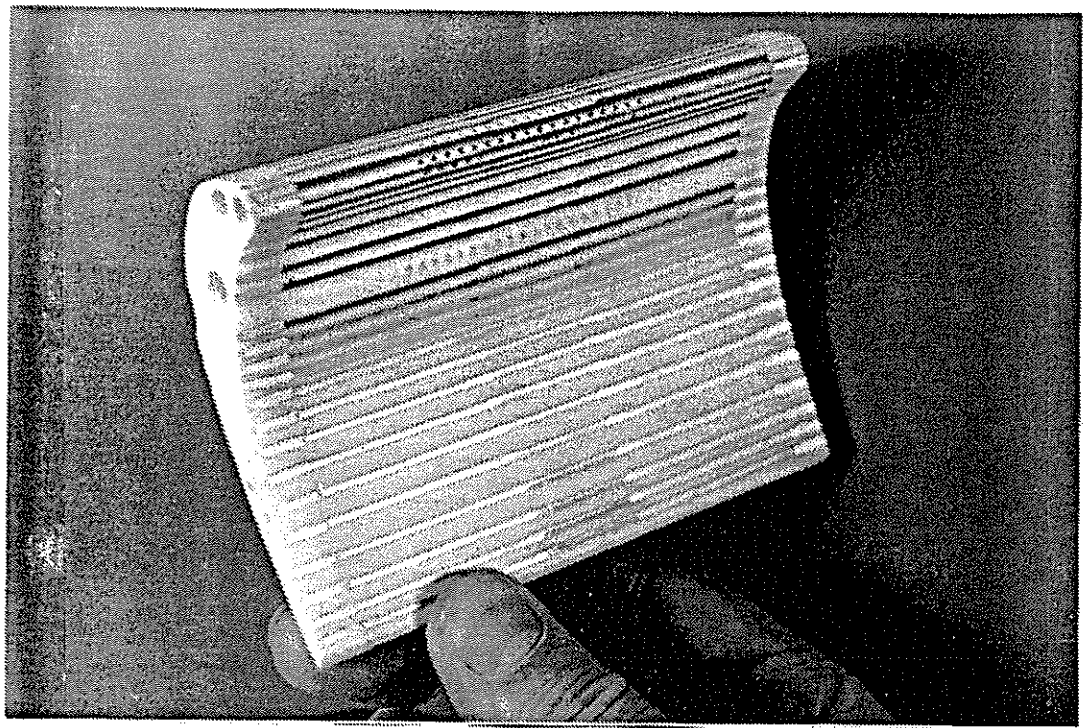
Gauge	s/C	Gauge	$-s/C$
1	0.010	25	0.000
2	0.050	26	0.050
3	0.000	27	0.000
4	0.120	28	0.000
5	0.100	29	0.770
6	0.270	30	0.710
7	0.310	31	0.050
8	0.350	32	0.500
9	0.000	33	0.540
10	0.410	34	0.400
11	0.470	35	0.400
12	0.510	36	0.420
13	0.570	37	0.300
14	0.640	38	0.350
15	0.710	39	0.270
16	0.000	40	0.230
17	0.870	41	0.100
18	0.000	42	0.110
19	1.050	43	0.000
20	1.140	44	0.050
21	1.200	45	0.010
22	1.200		
23	1.310		
24	1.34		

CHORD LENGTH 80 mm.

For the pressure side gauges (25 to 45) s/C are negative.

Fig.6C

Heat flux gauge locations



ACTIVE PORTION OF THE GAUGE

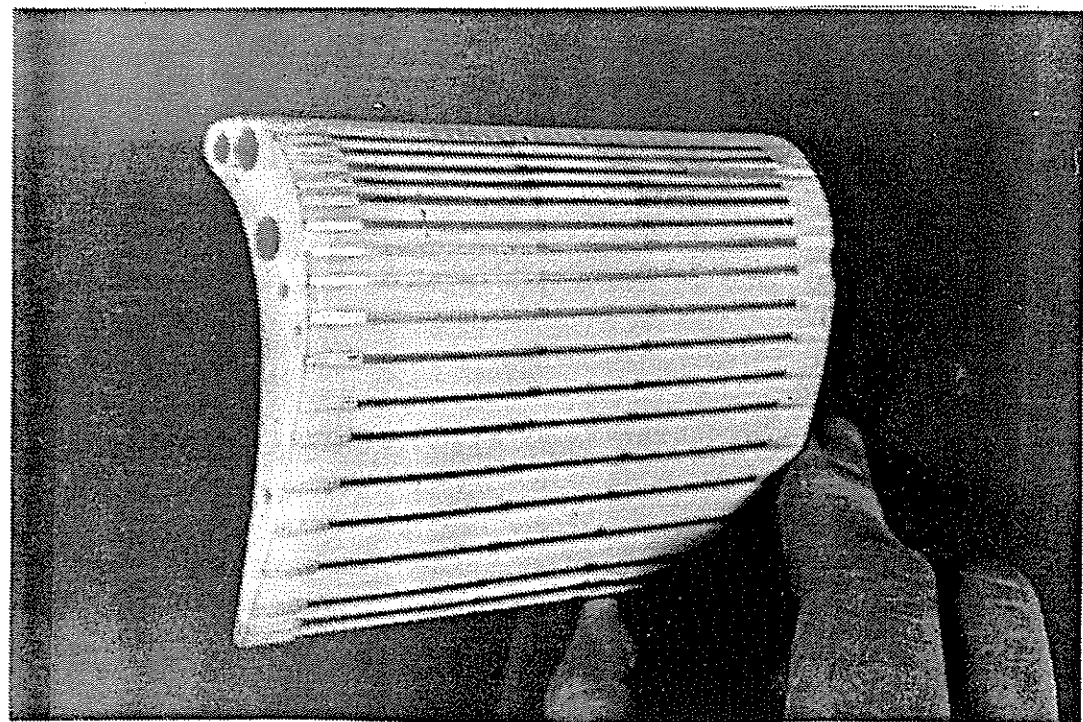
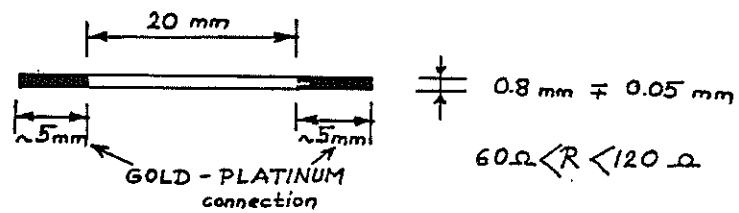


Fig.84 Thin film heat flux gauges mounted on the film cooled blade

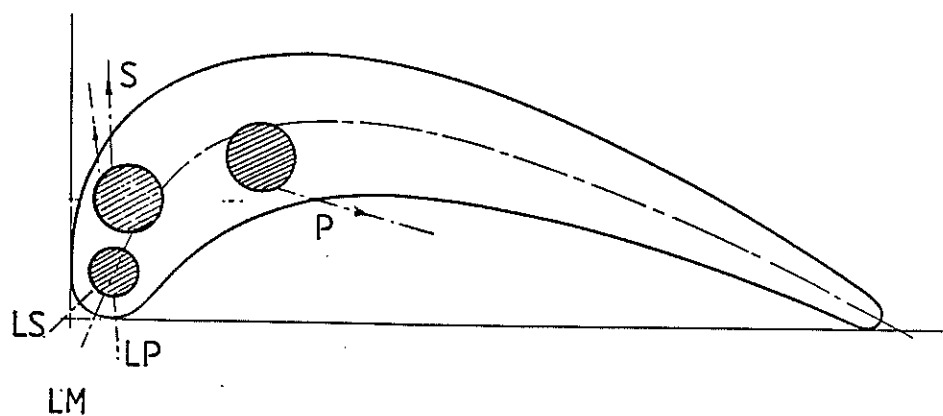


Fig.85 The three film cooling ejection sites

41 Conically shaped holes
in double rows
hole spacing = $2.8 \times d$
row spacing = $2.6 \times d$

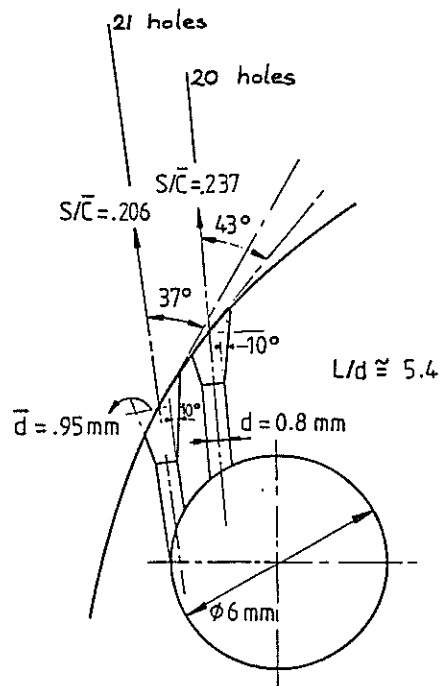


Fig. 87 The geometrical details of the SUCTION SIDE ejection site

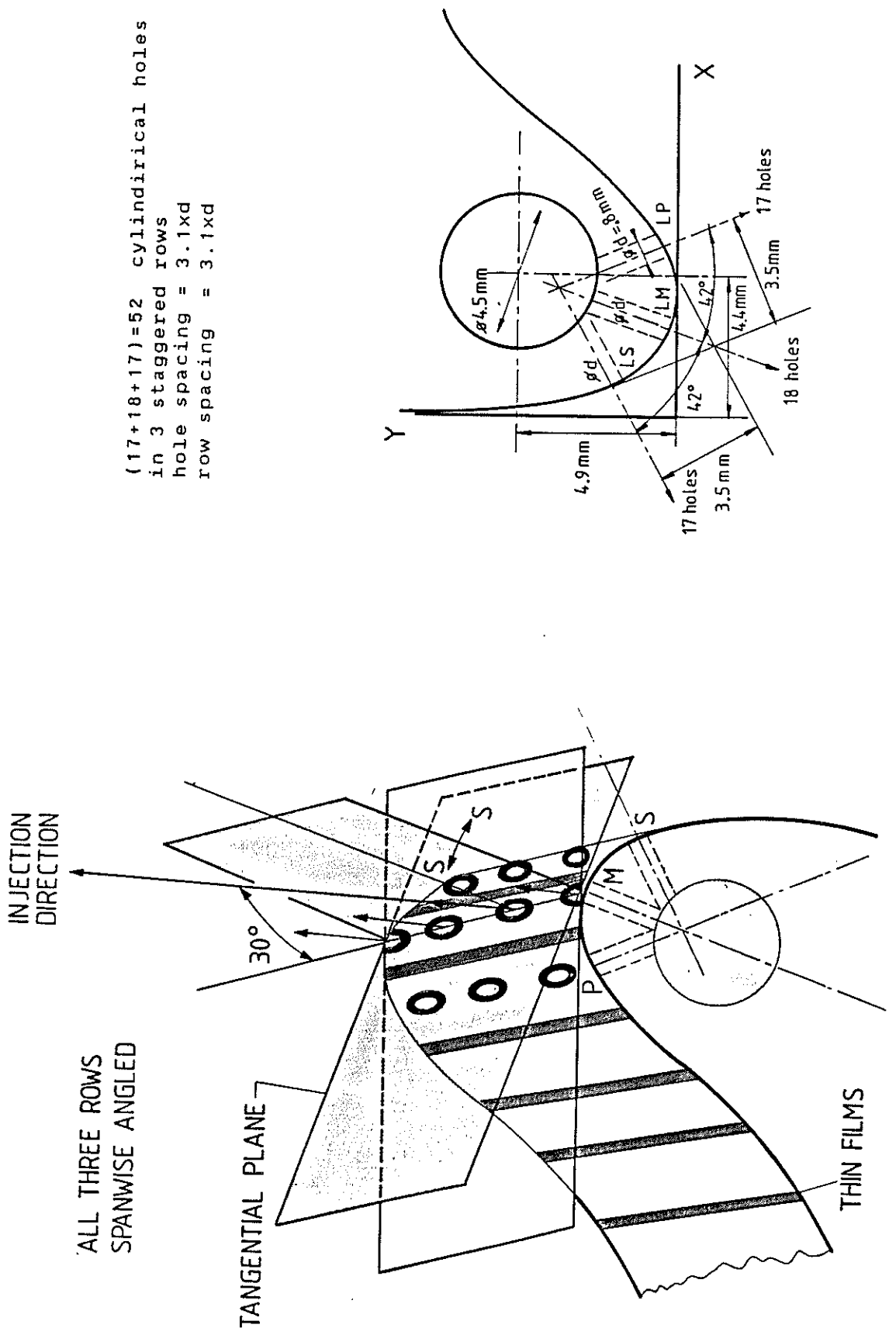


Fig. 86 The geometrical details of the LEADING EDGE ejection site

17 Conically shaped holes
in a single row
hole spacing = $3.15 \times d$

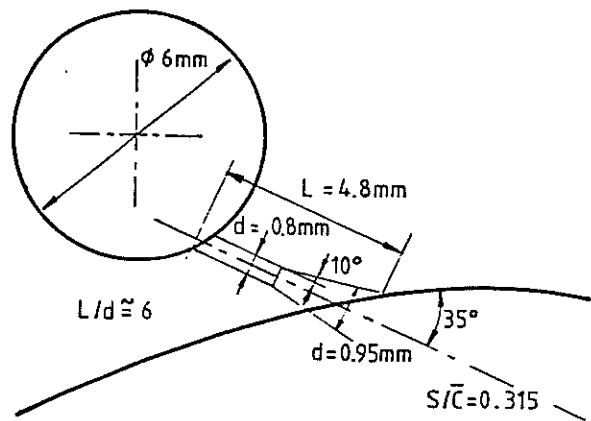


Fig.88 The geometrical details of the PRESSURE SIDE ejection site

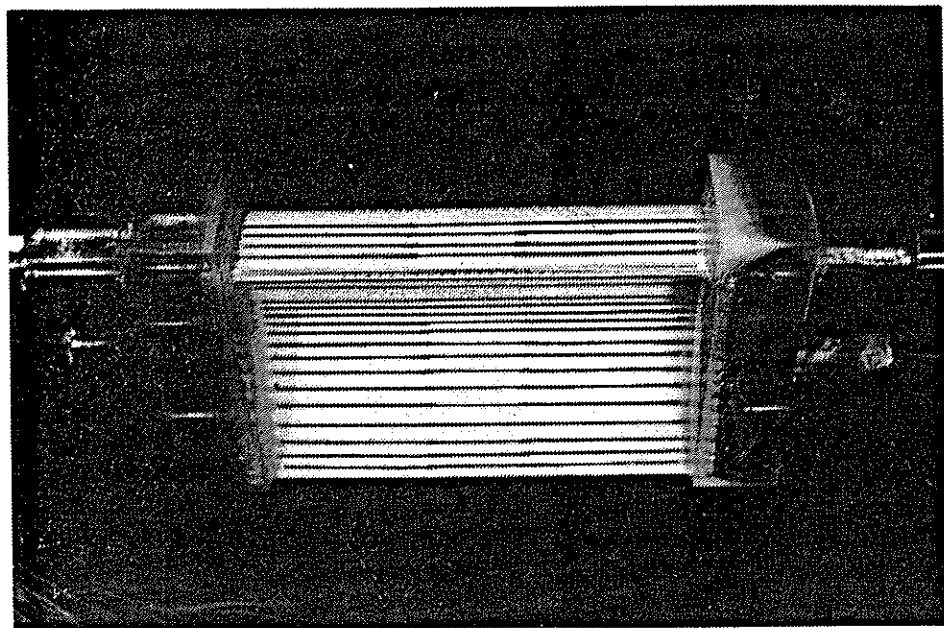


Fig.89 The fully assembled heat transfer instrumented blade

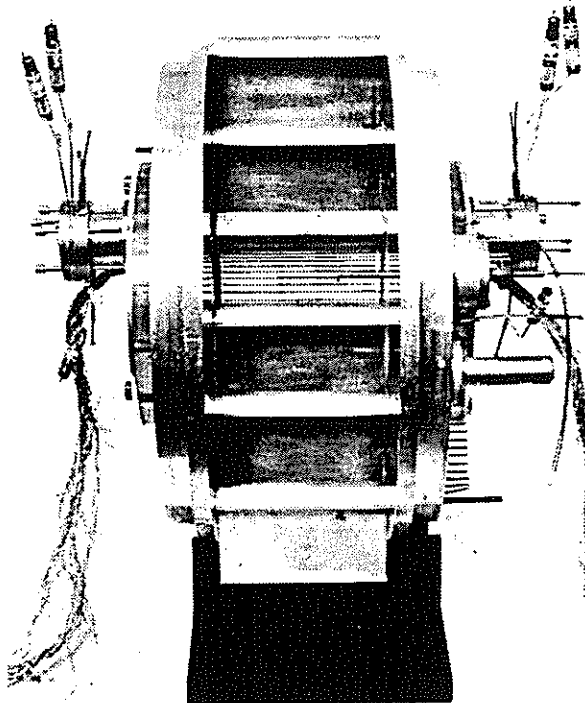


Fig.90 Plenum chamber and side-wall connection details

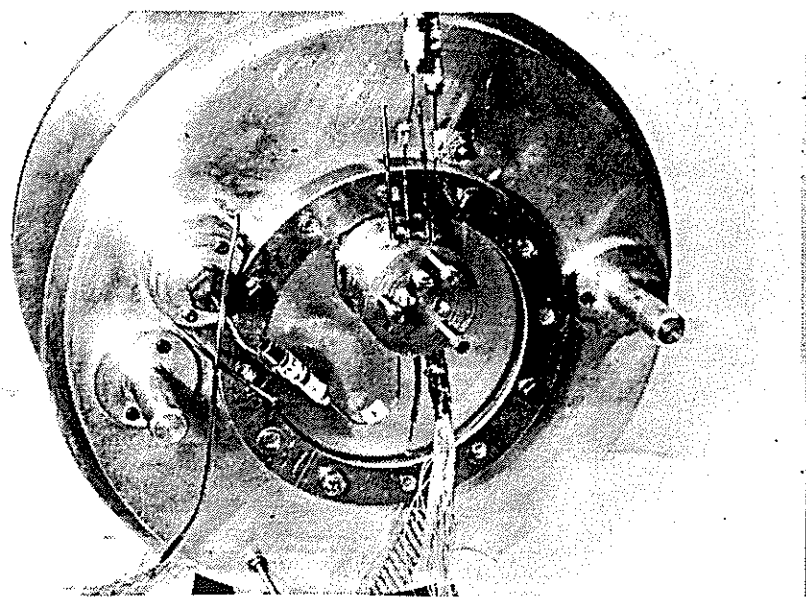


Fig.91 Plenum chamber and side-wall connection details

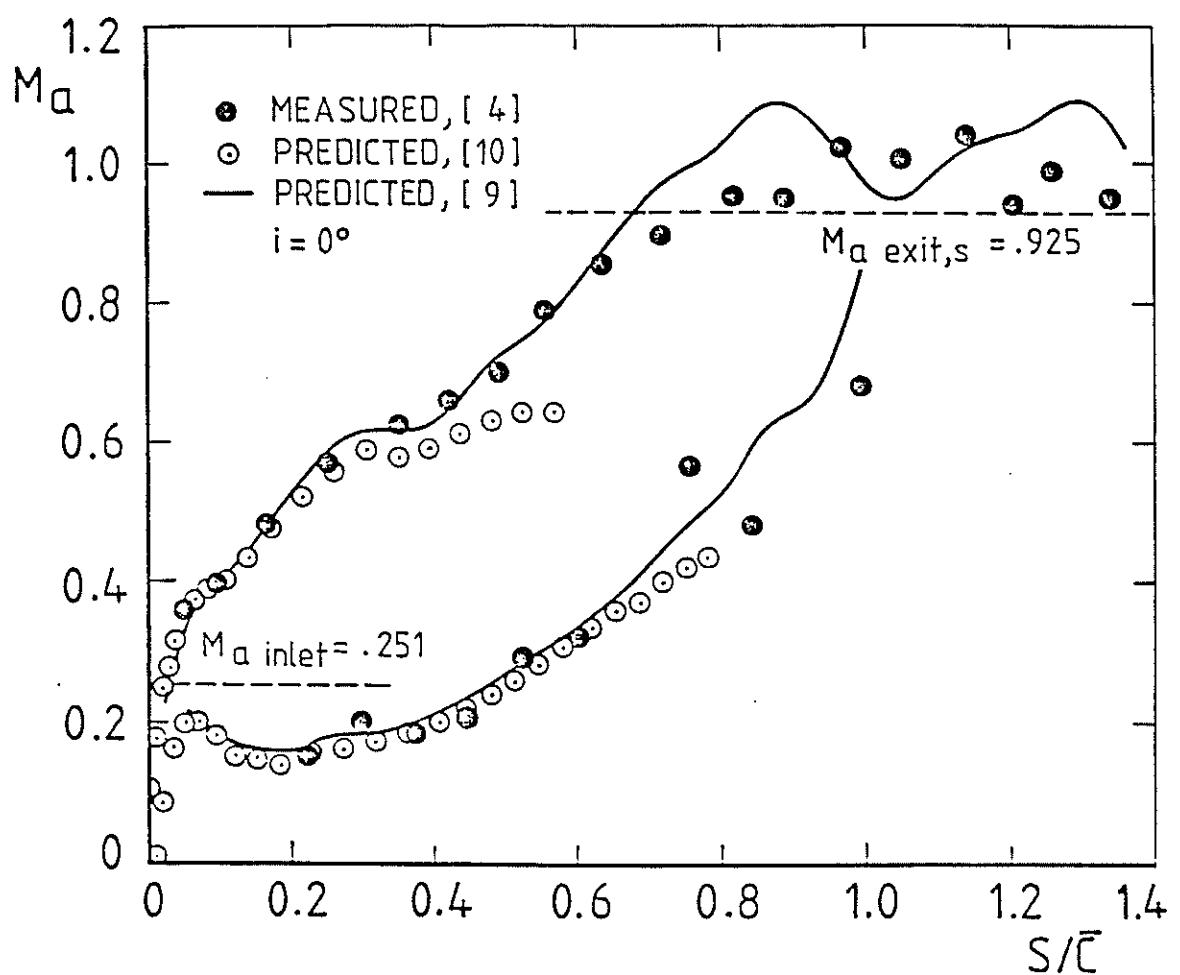


Fig. 92 Blade velocity distribution

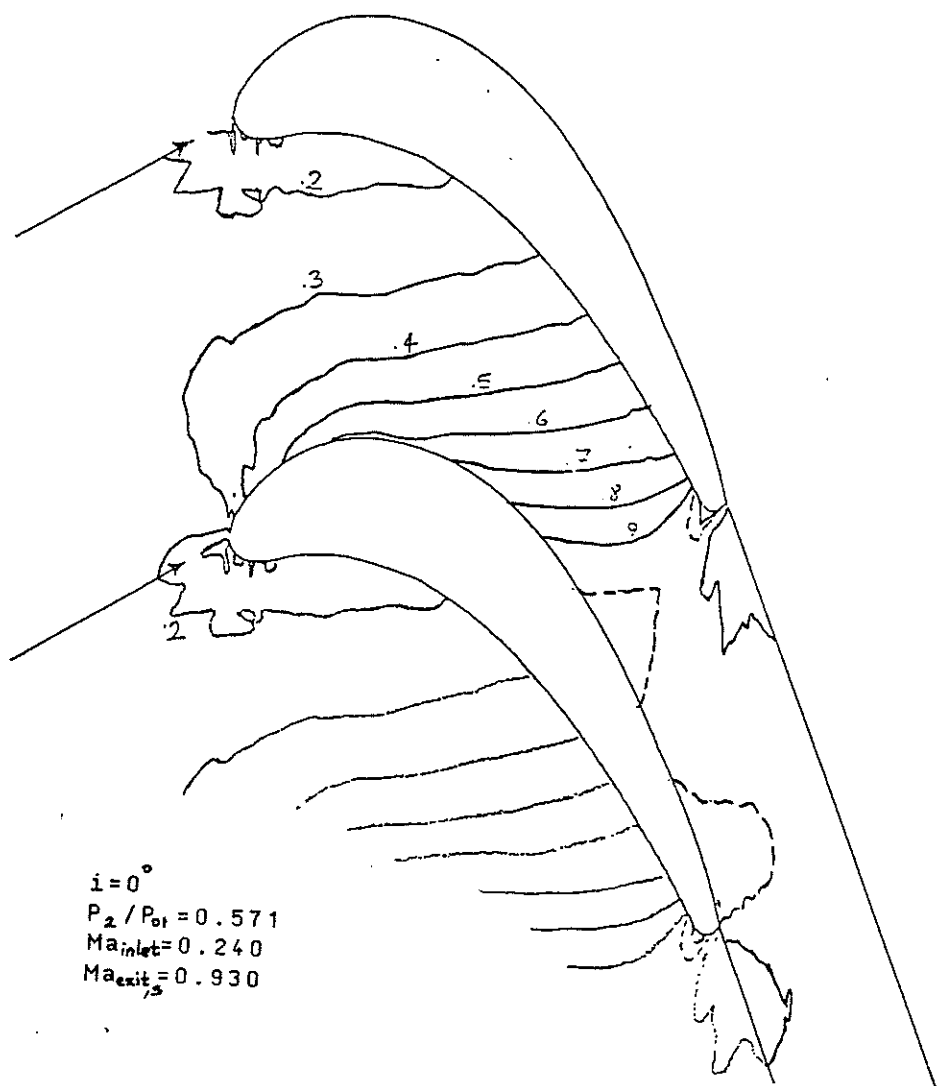


Fig.93 Calculated iso-Mach number lines in the turbine passage

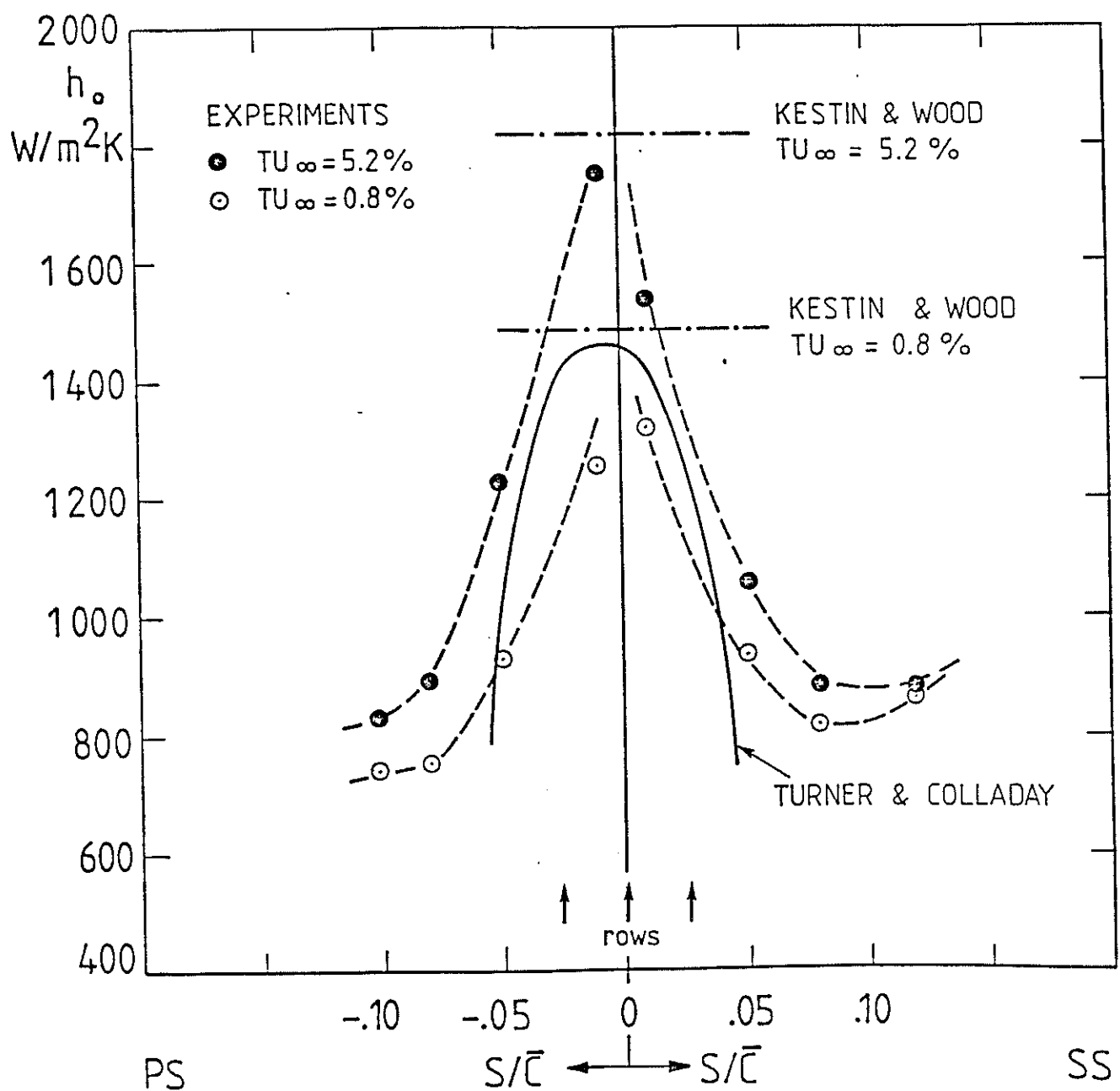
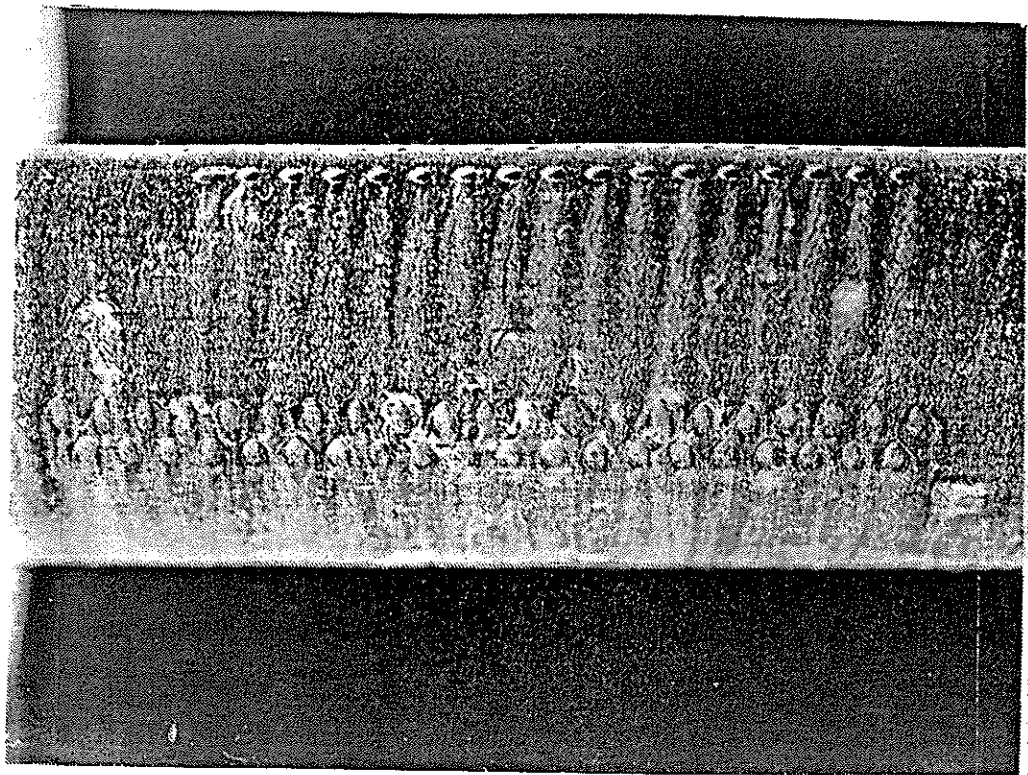
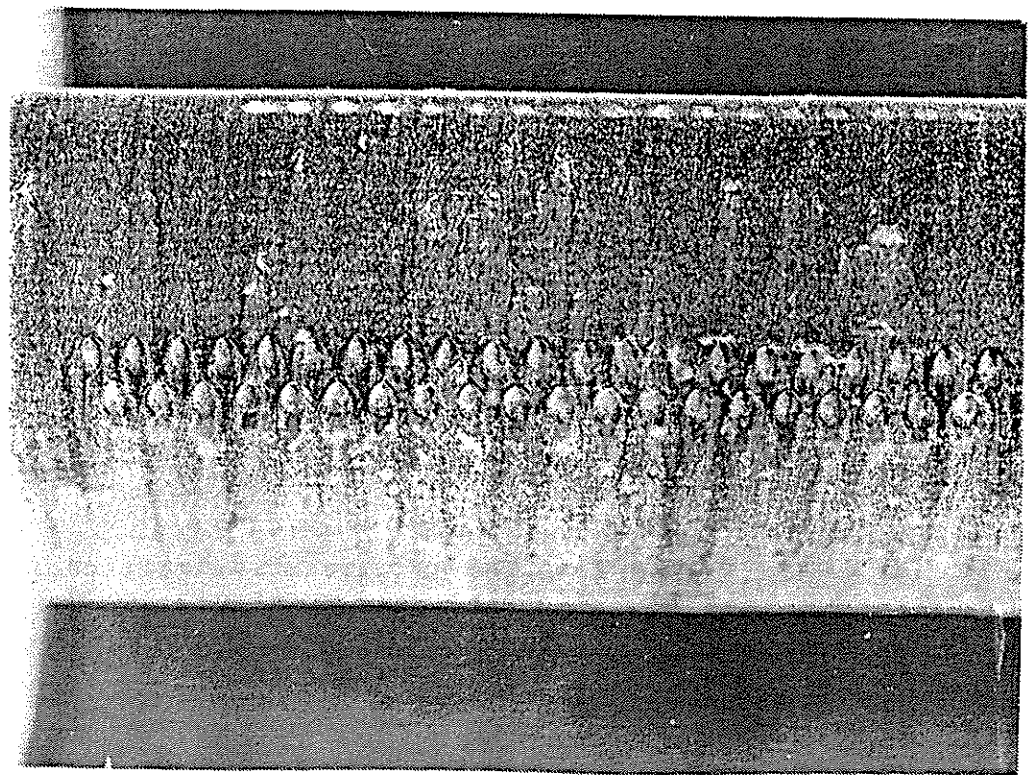


Fig. 94 Leading edge heat transfer without cooling
, effect of TU_{∞}



a. Leading edge holes are not blocked



b. Leading edge holes are blocked

Fig.95 Influence of unblocked leading edge holes
($\dot{m}_e/\dot{m}_\infty = 1.4 \%$ and $U_\infty = 7.7 \text{ m/sec}$)

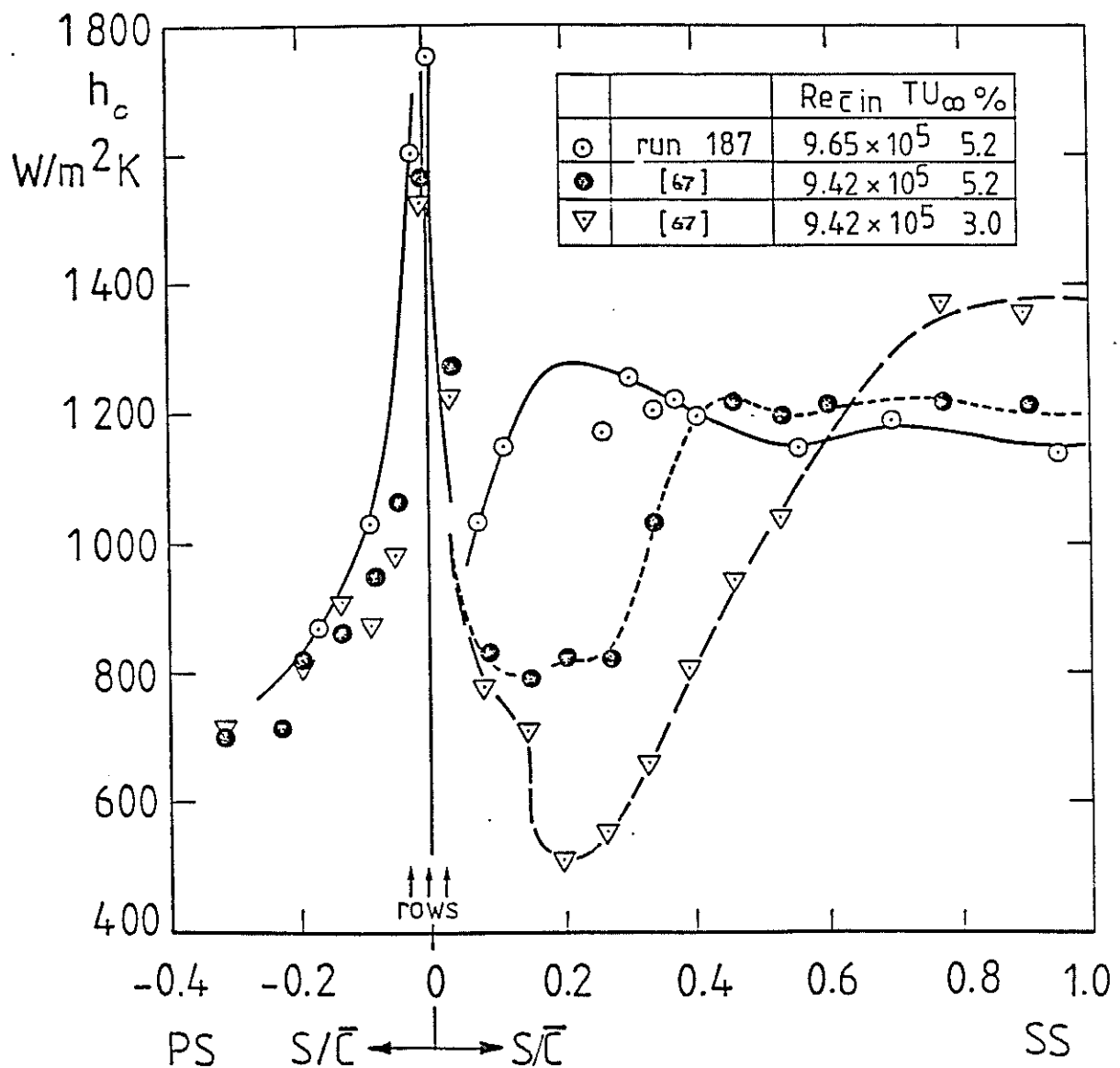


Fig. 96 Leading edge heat transfer without cooling
effect of holes existence

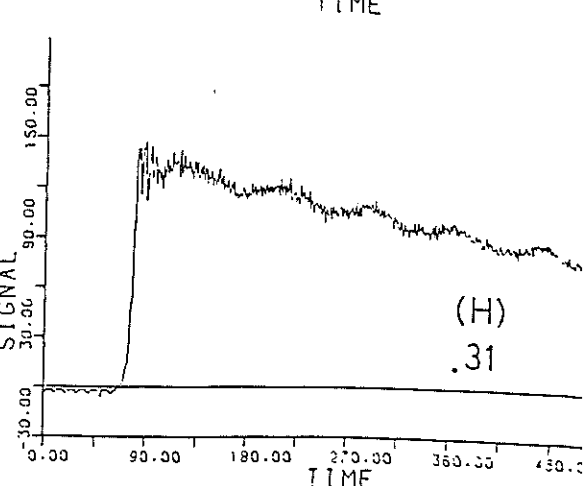
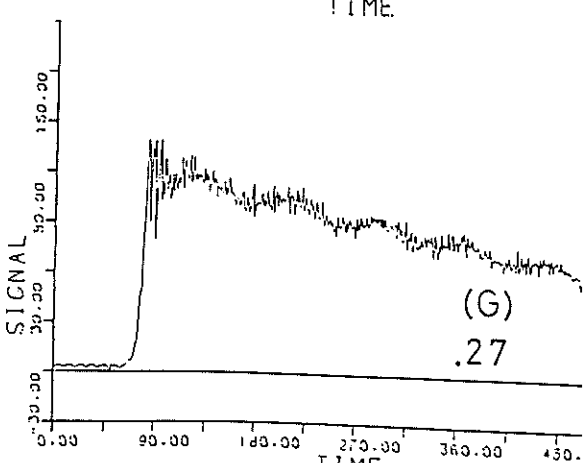
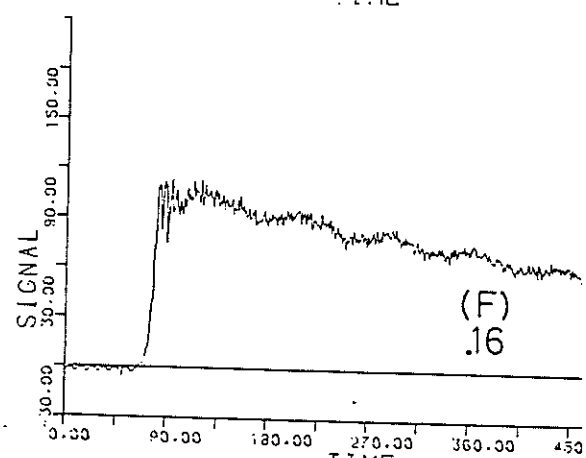
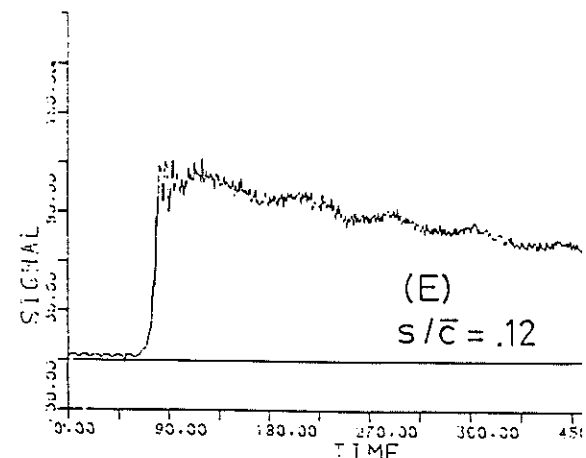
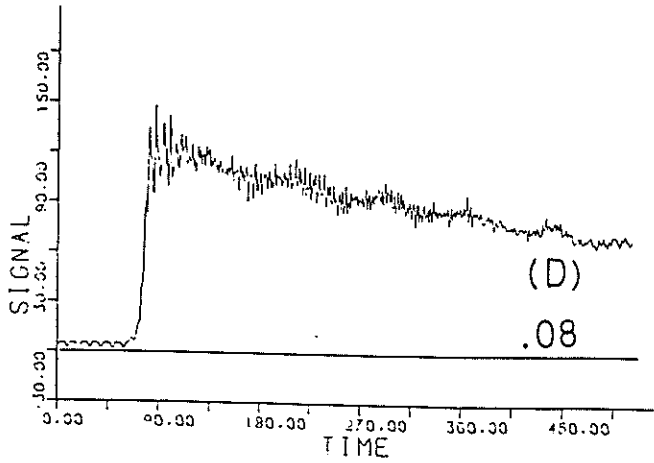
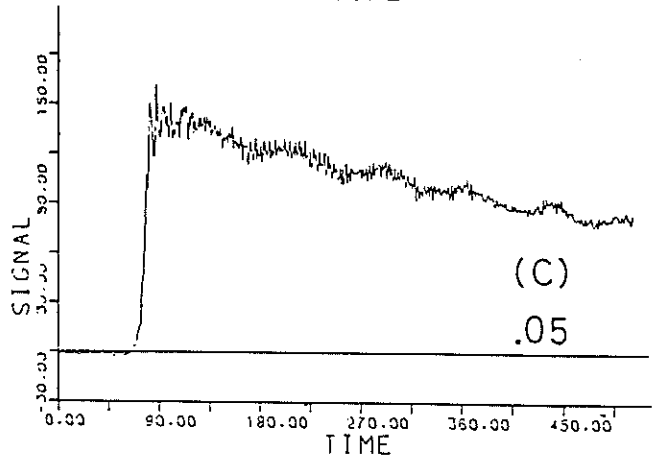
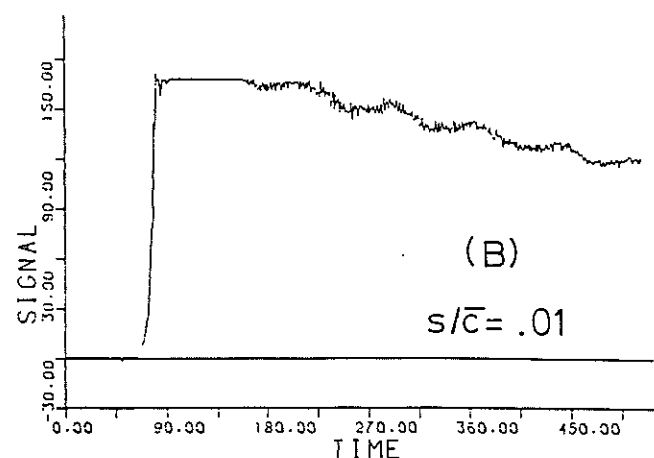


Fig. 97

Wall heat flux signals

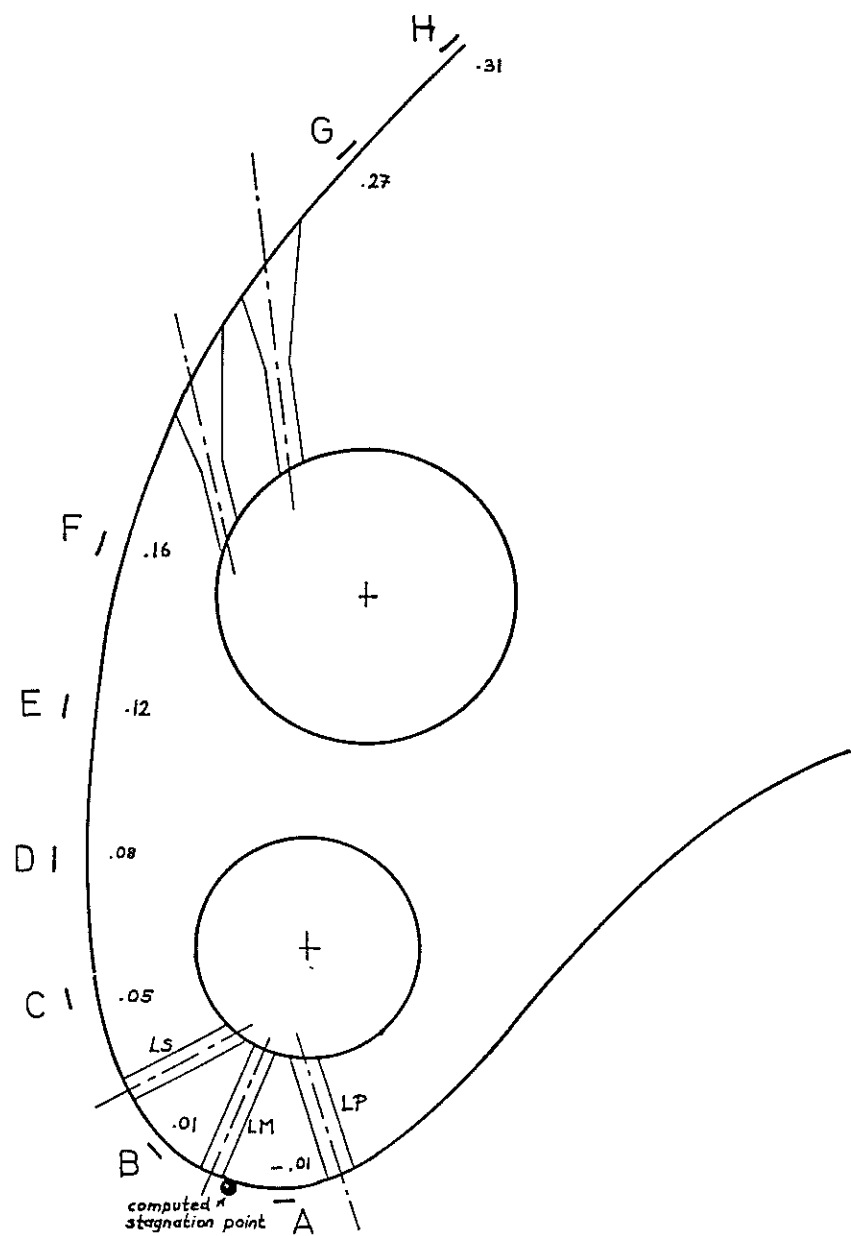


Fig.98 Heat flux gauge locations on the suction side

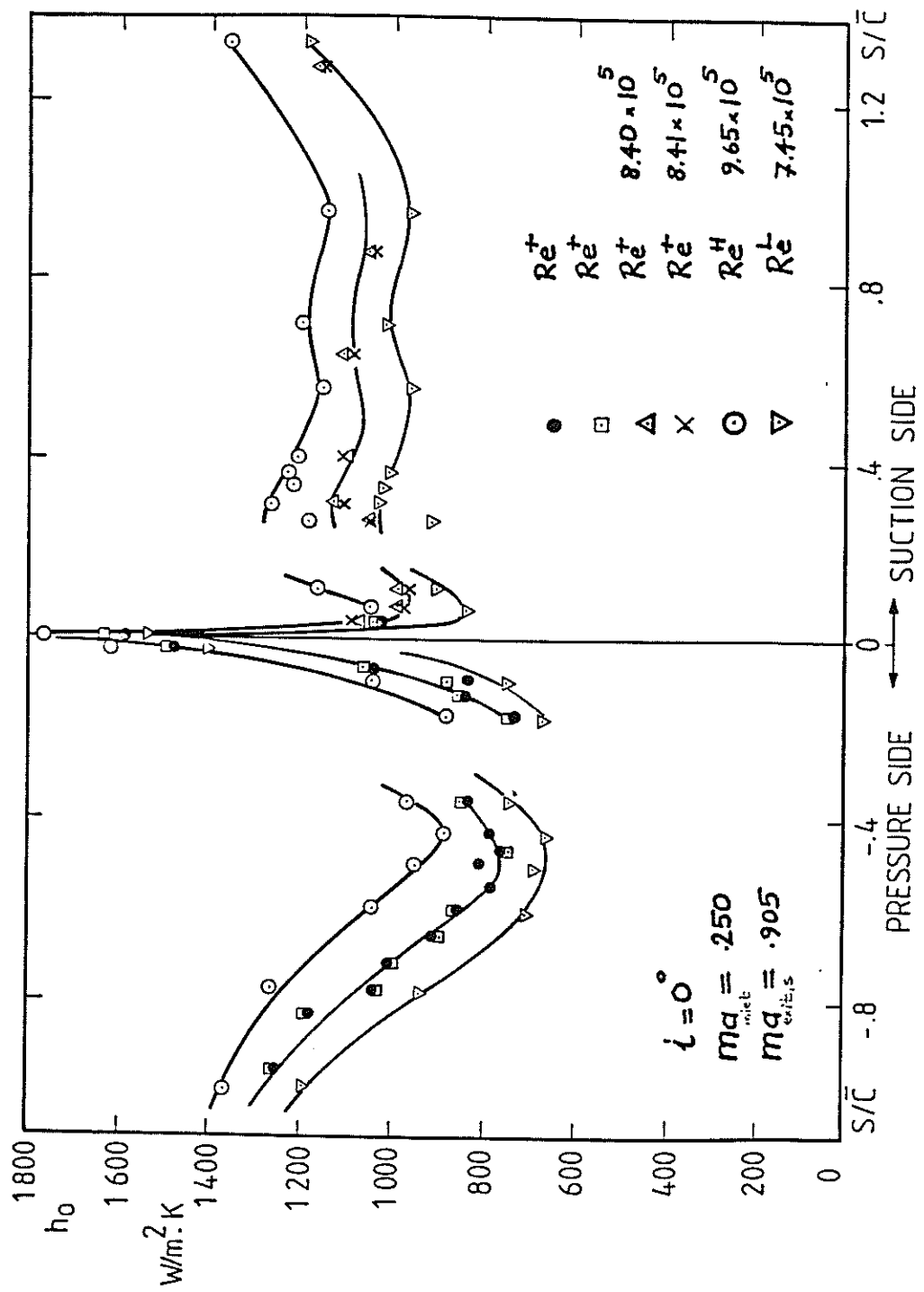


Fig. 99 Effect of local Re number on heat transfer

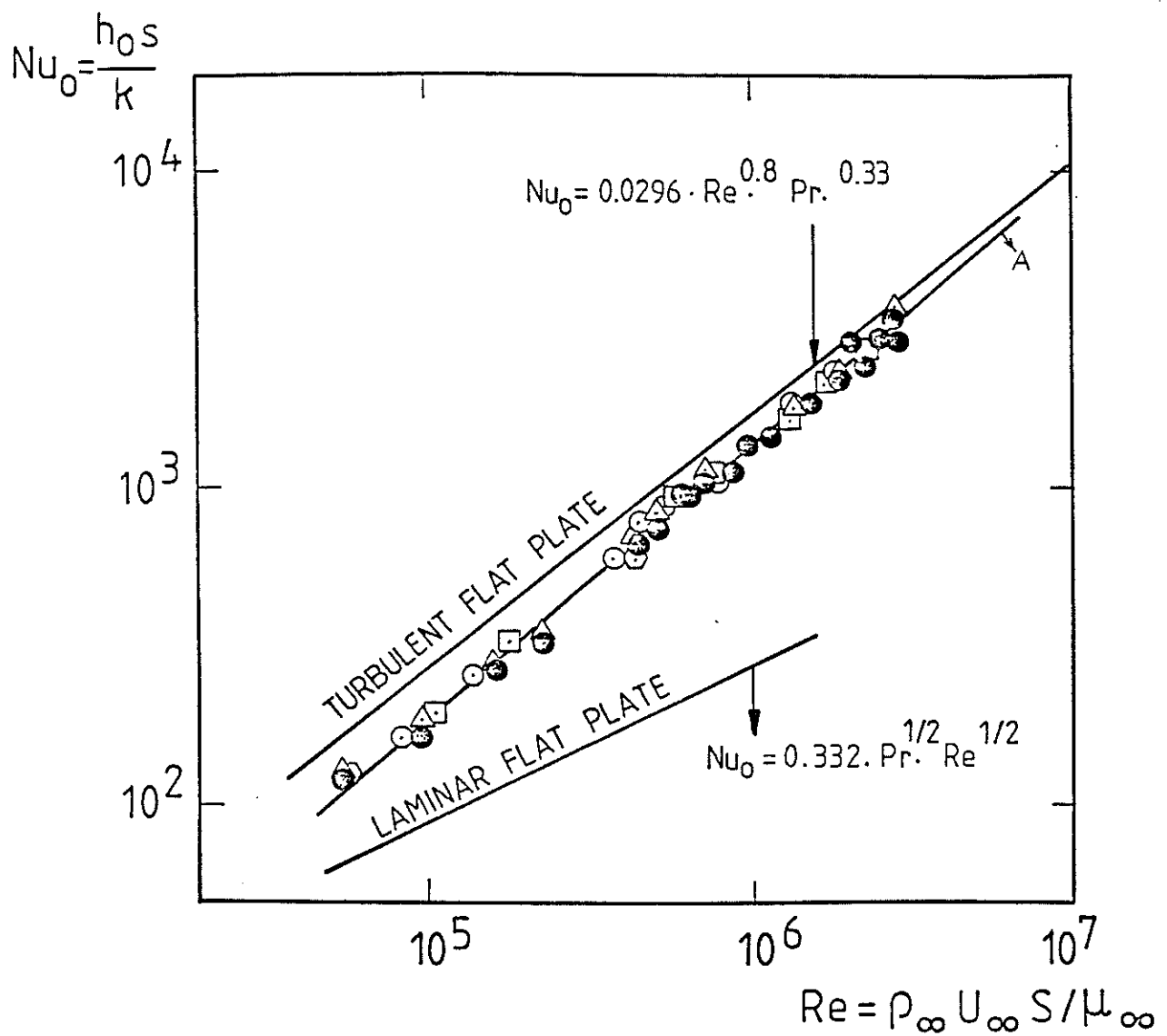


Fig.100 Suction side heat transfer without cooling

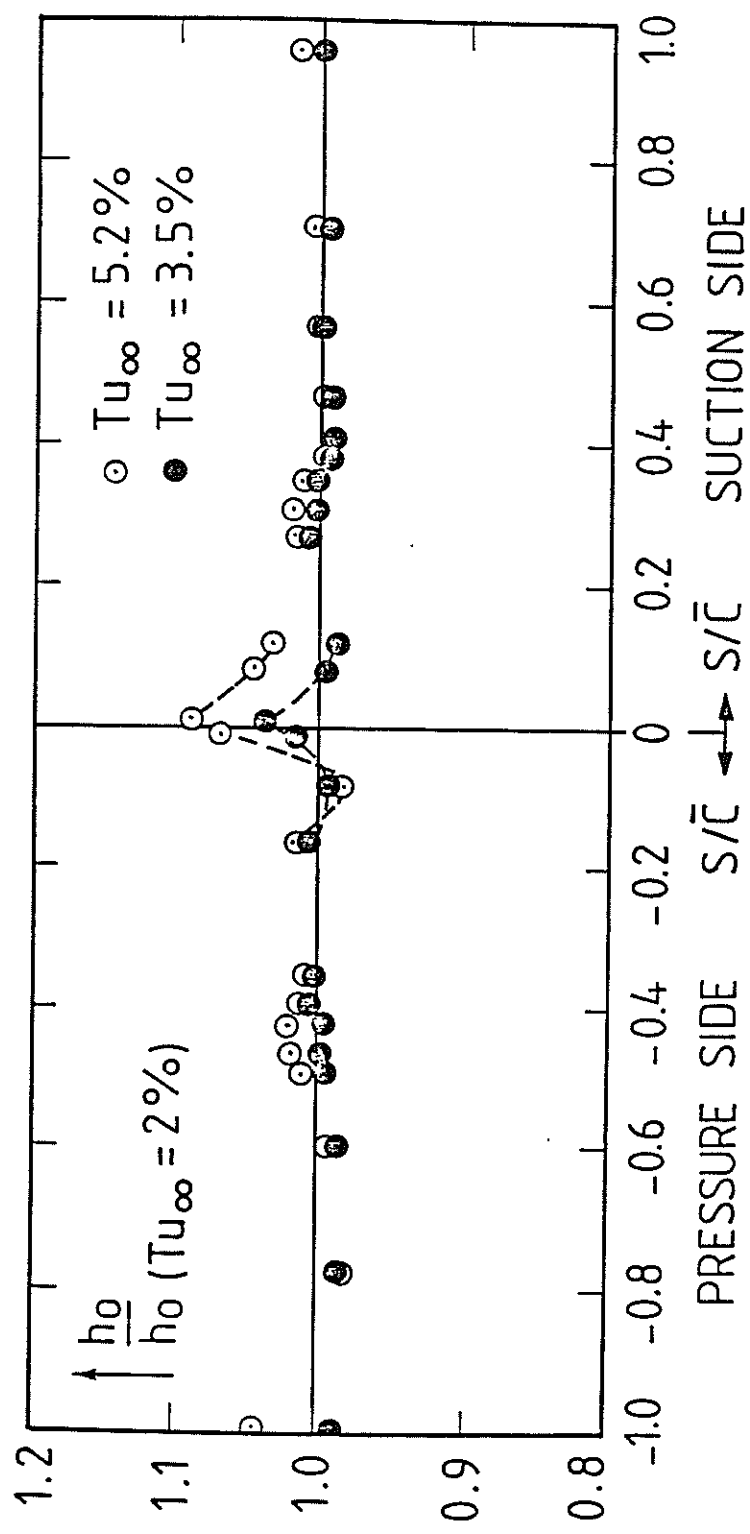
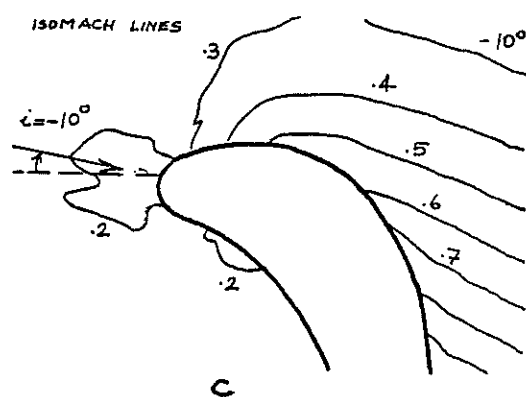
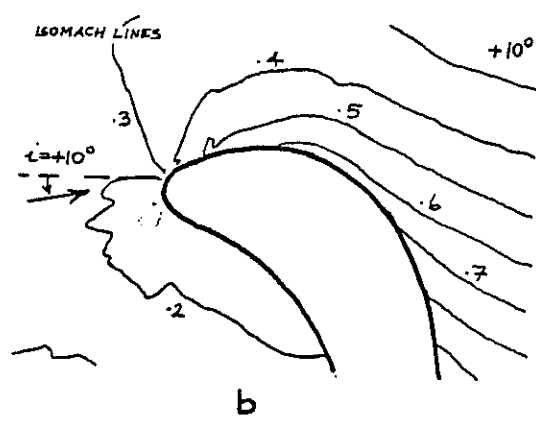
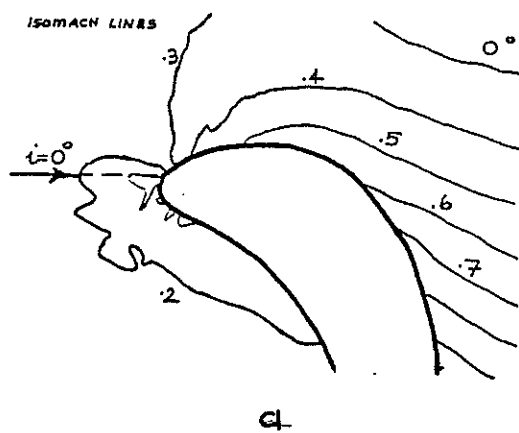


Fig. 101 Heat transfer at different $T_{U\infty}$ levels,
(no coolant ejection)



$Ma_{in} = 0.25$
 $P_1 / P_{\infty} = 0.571$

Fig.102 Effect of inlet flow direction on Mach number distribution around the leading edge

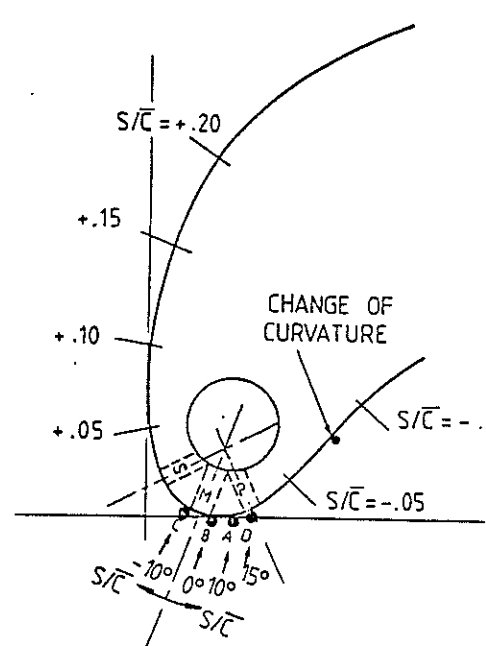
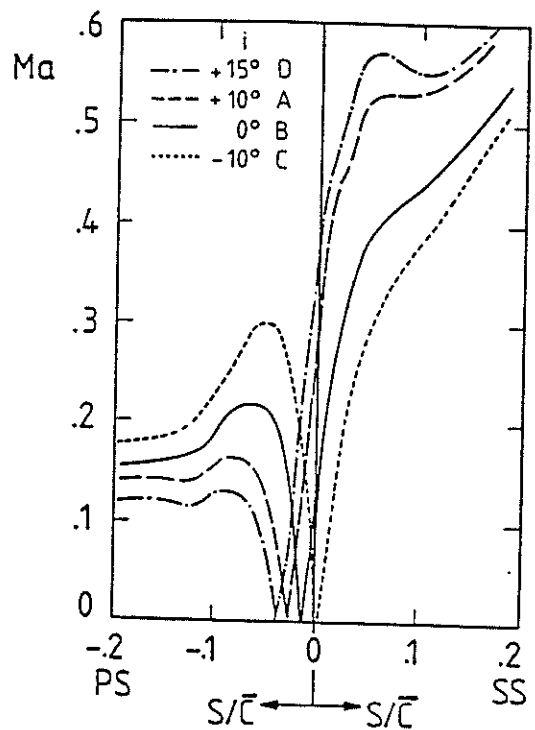


Fig.103 Leading edge velocity distribution,
effect of incidence
(calculations with a singularity method)

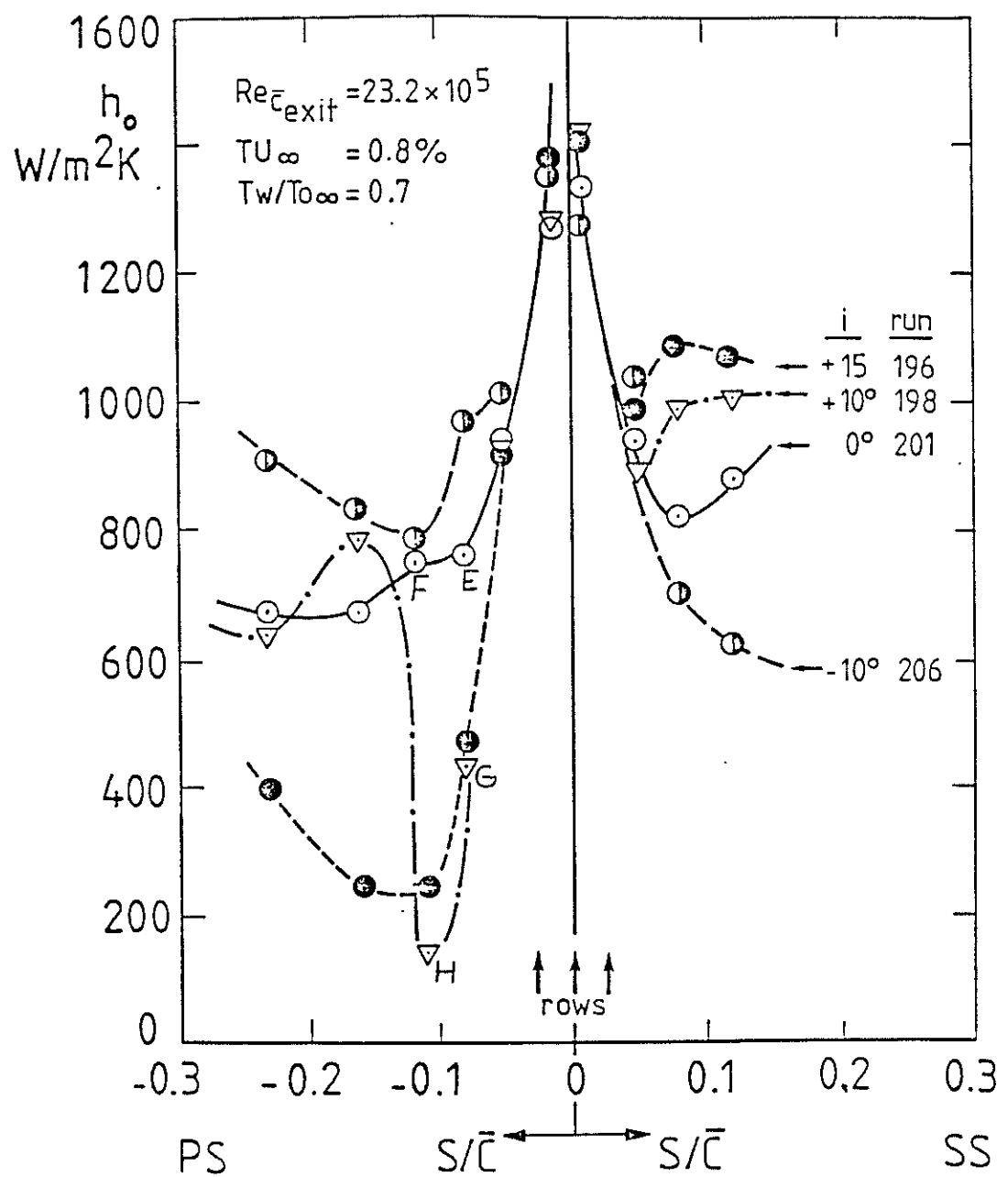


Fig.104 Leading edge heat transfer without cooling,
effect of incidence

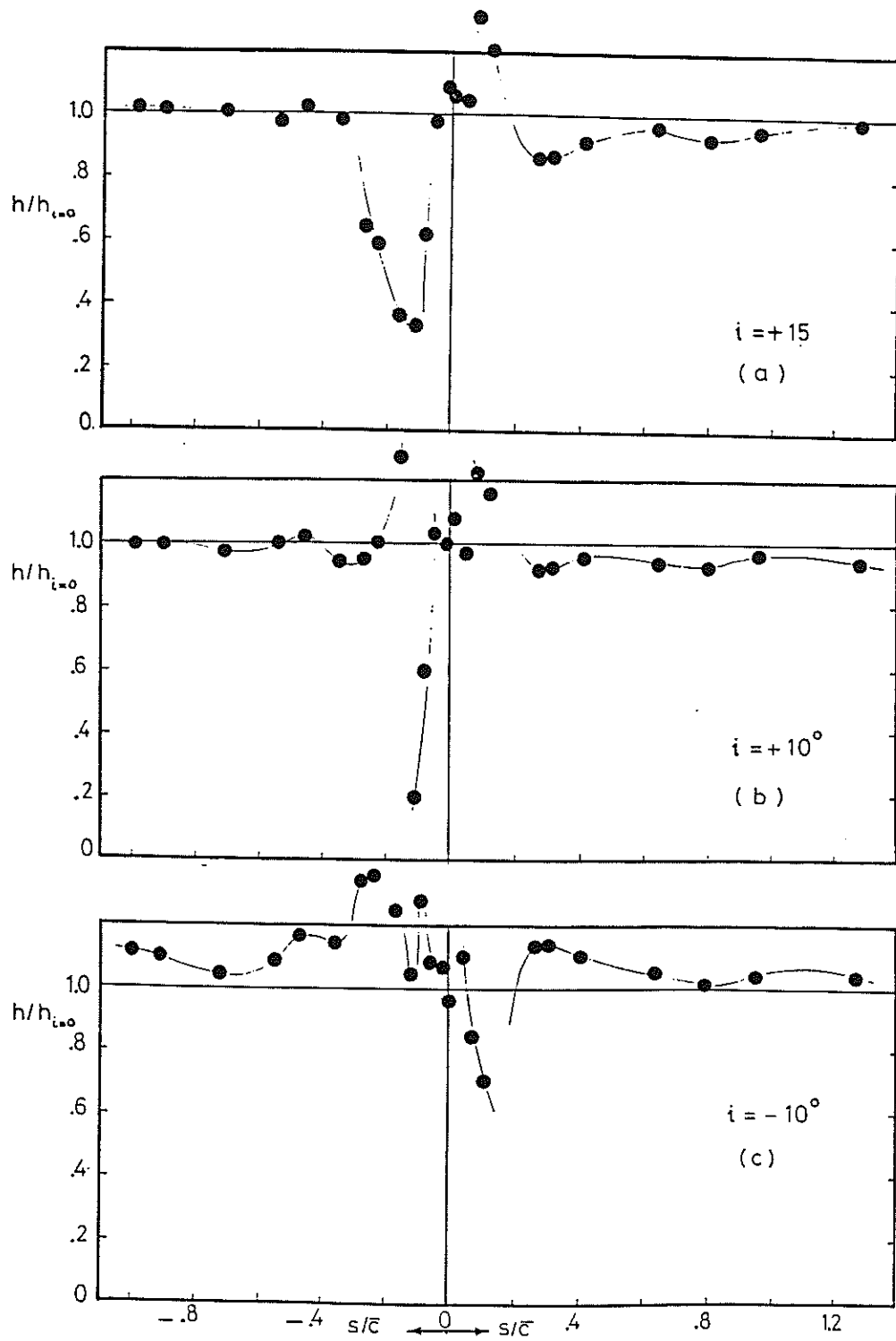


Fig.105 Influence of incidence angle on heat transfer without ejection

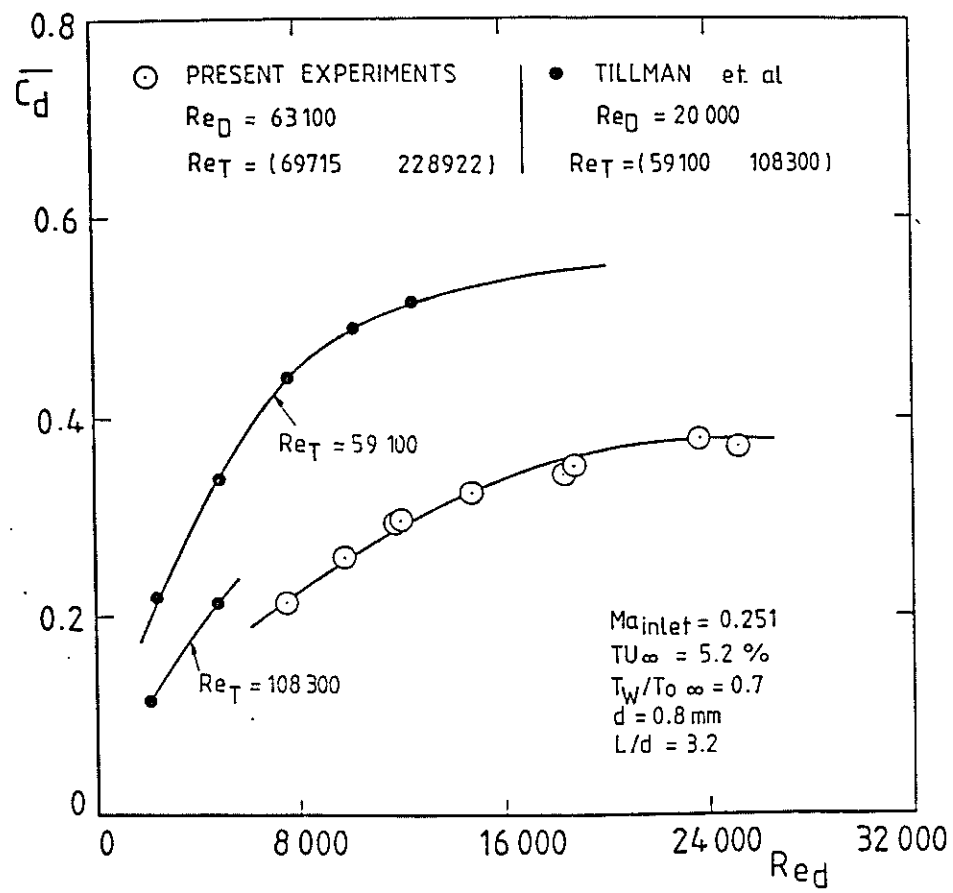


Fig.106 Cooling holes discharge coefficients

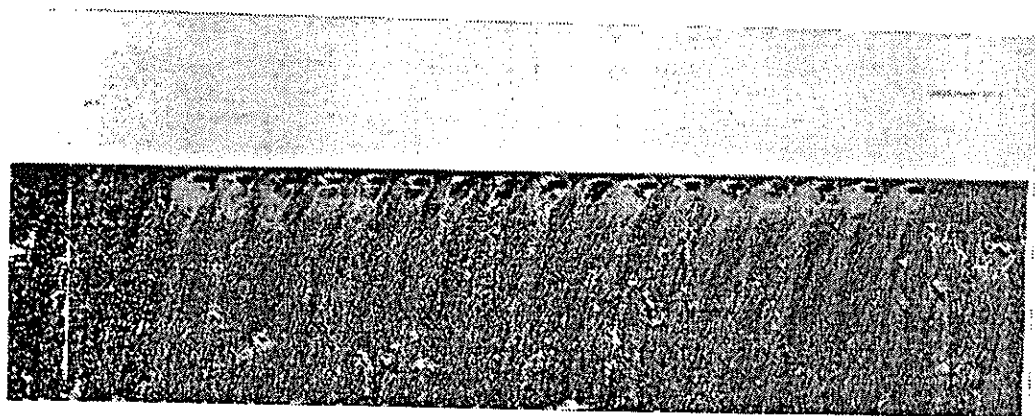


Fig.107 Oil flow vizualisation
leading edge ejection
 $m_e/m_\infty = 1.4 \%$ and $U_\infty = 7.7 \text{ m/sec}$
_{inlet}

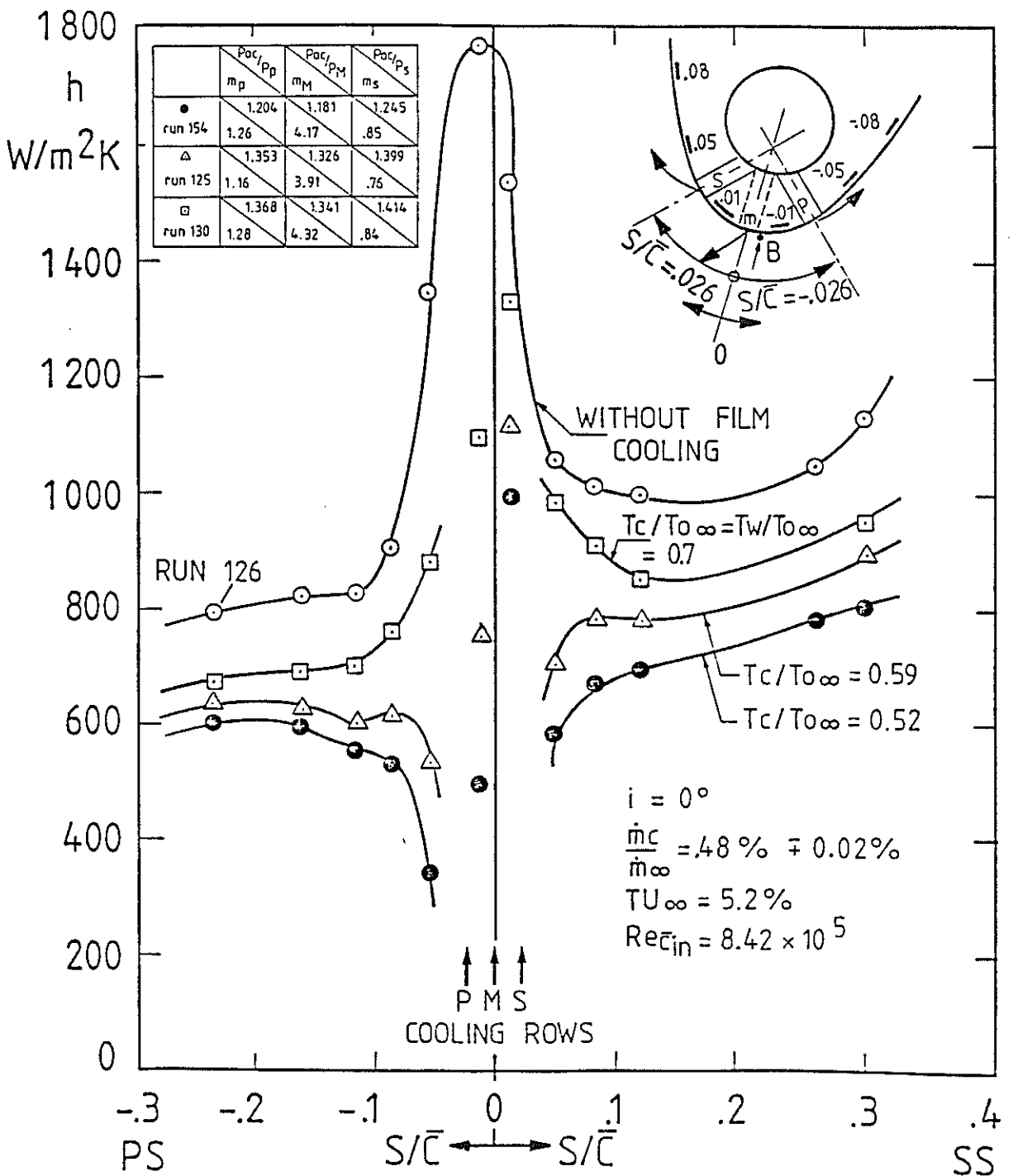


Fig. 108 Leading edge heat transfer with film cooling,
effect of temperature ratio

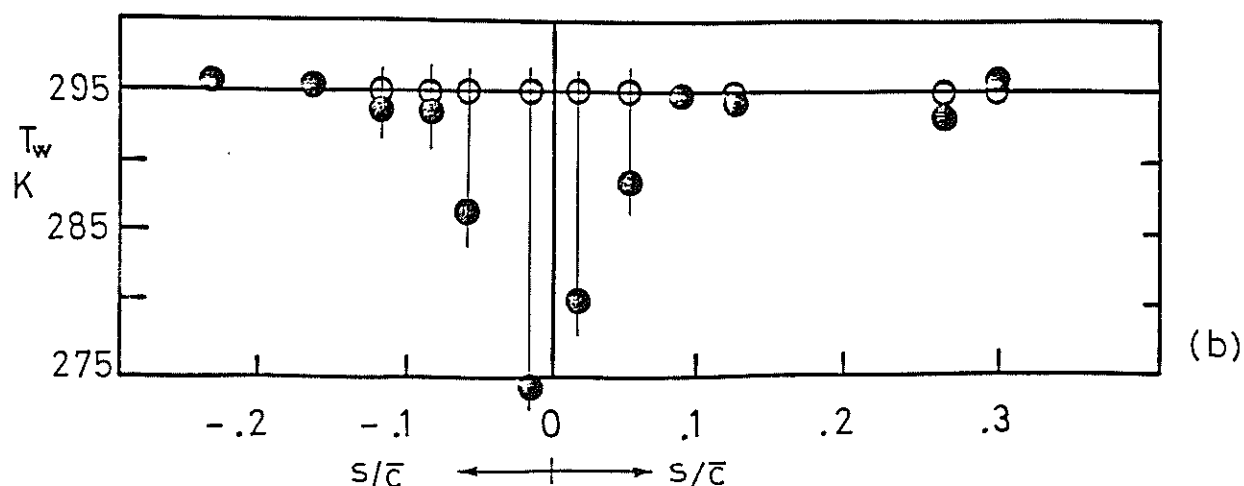
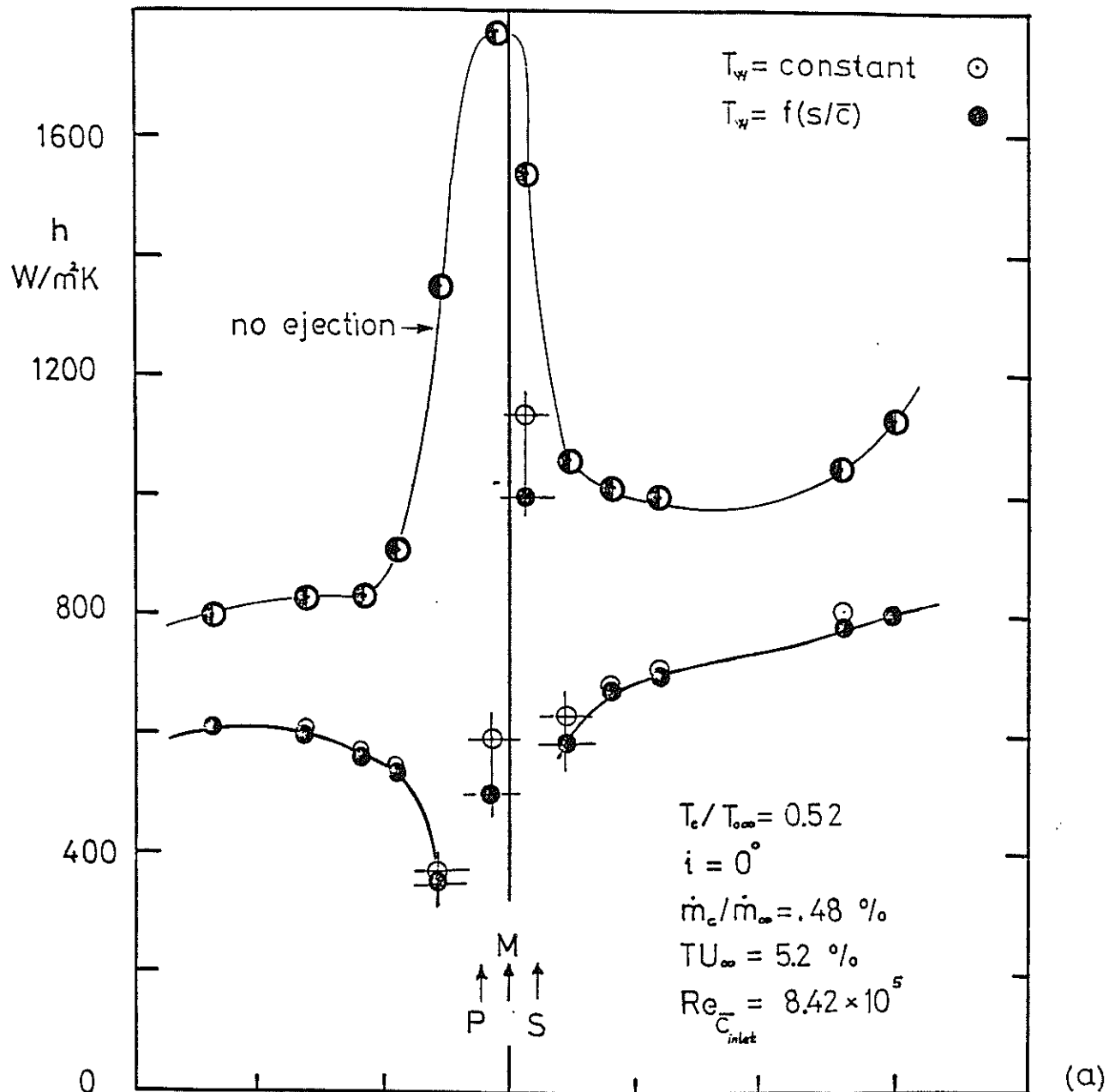


Fig. 109 Effect of wall temperature deviations from an isothermal value on h

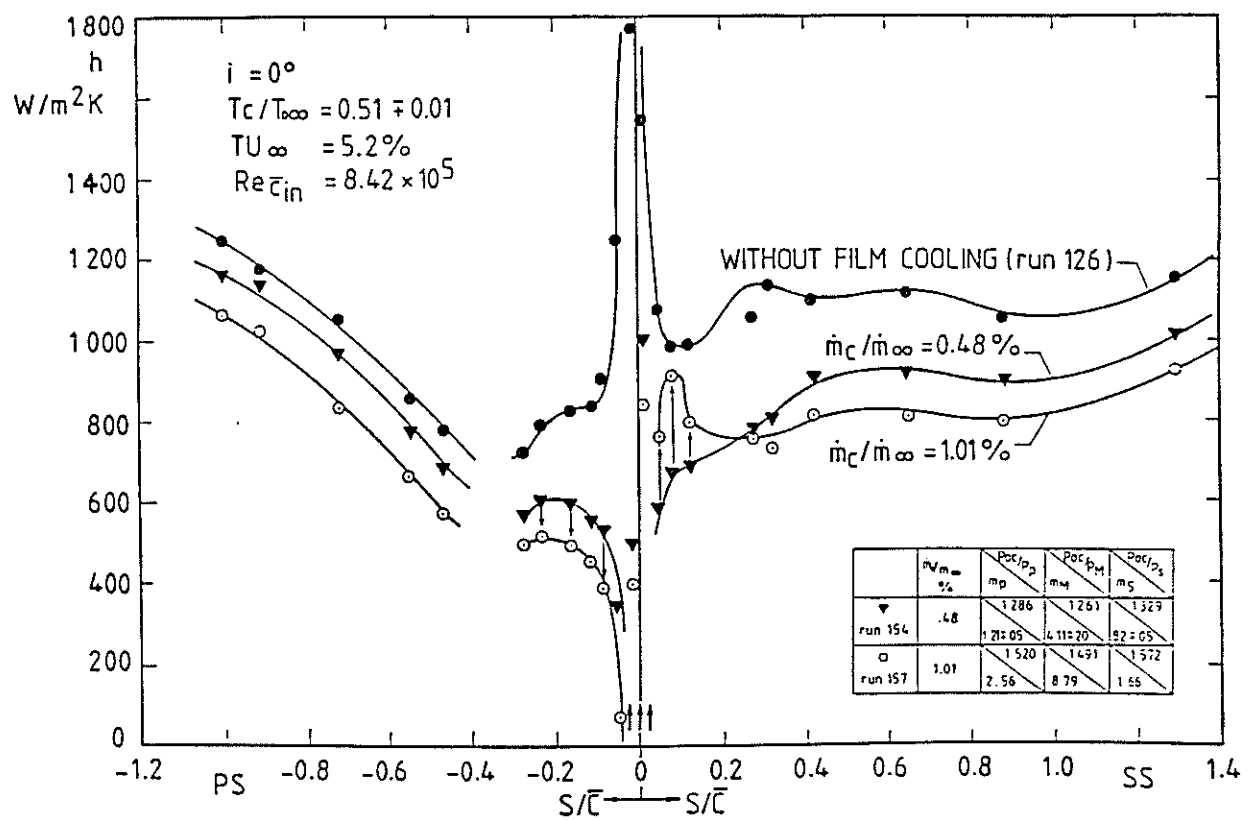


Fig.110 Leading edge heat transfer with film cooling,
effect of mass weight ratio

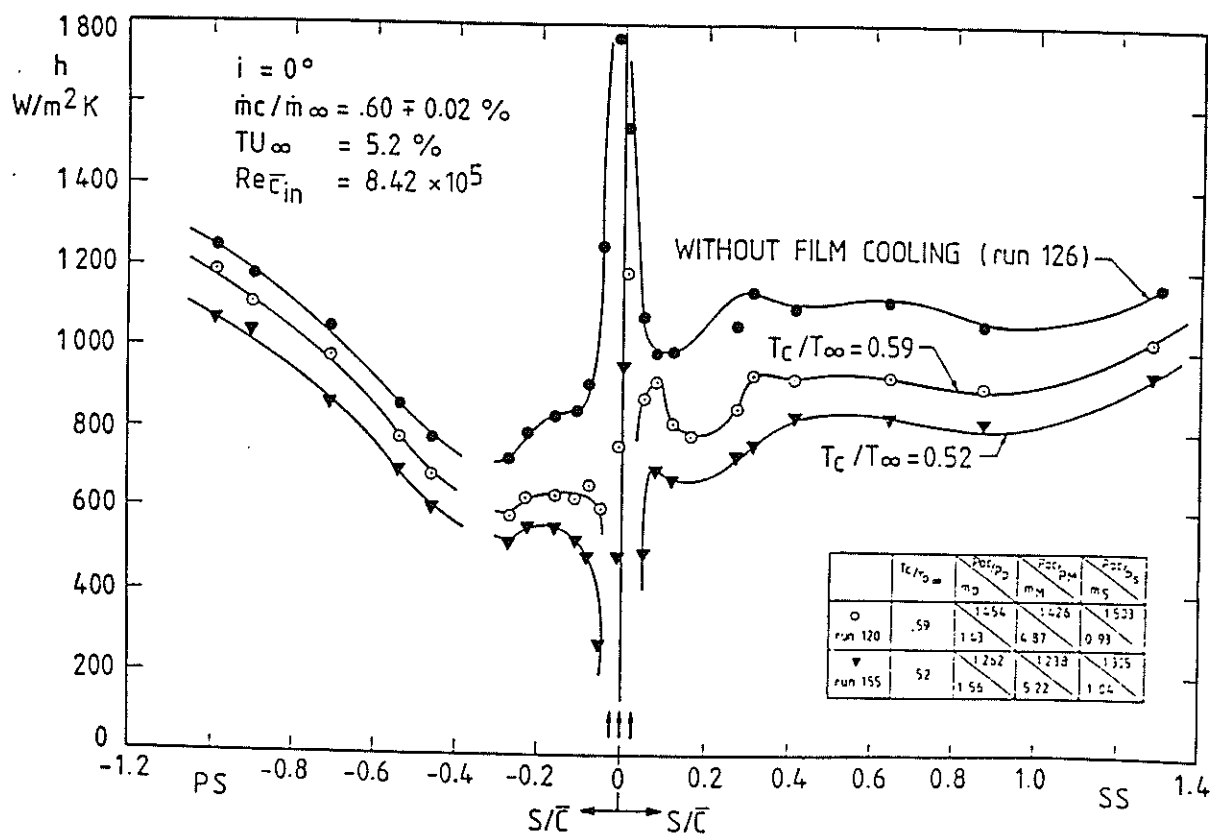


Fig. 111 Leading edge heat transfer with film cooling,
effect of coolant temperature

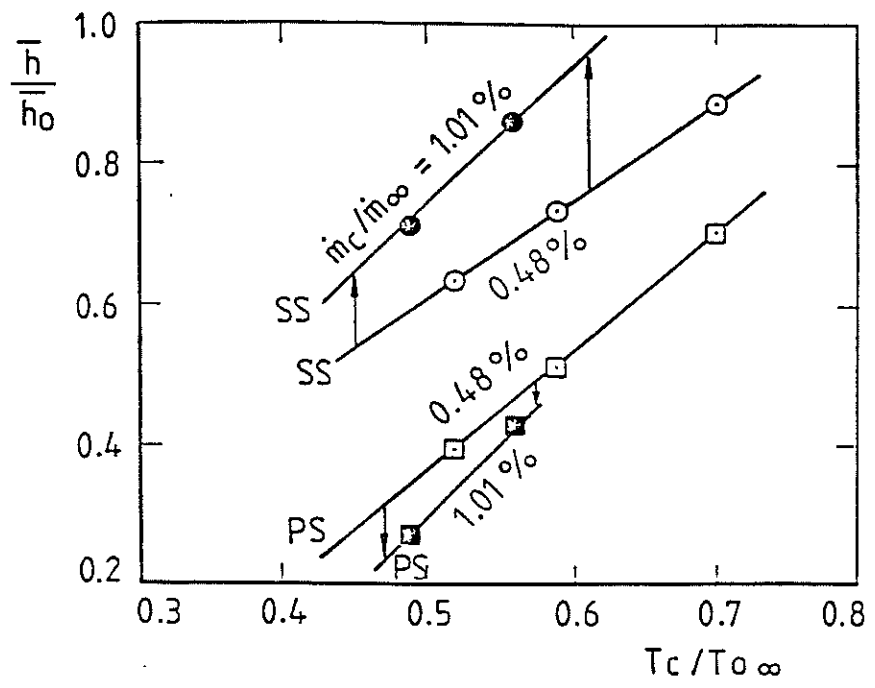


Fig.112 Averaged leading edge heat transfer

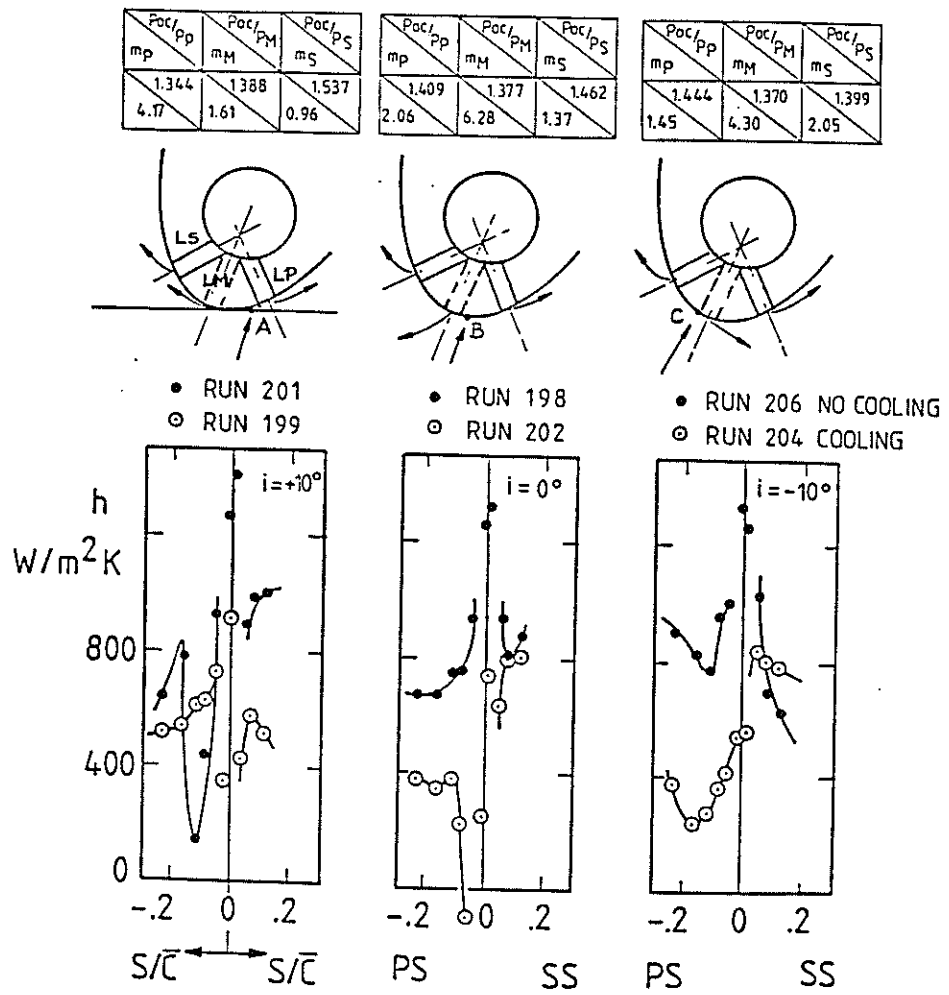


Fig. 113 Leading edge heat transfer with film cooling,
effect of incidence, ($TU_\infty = 0.8\%$)

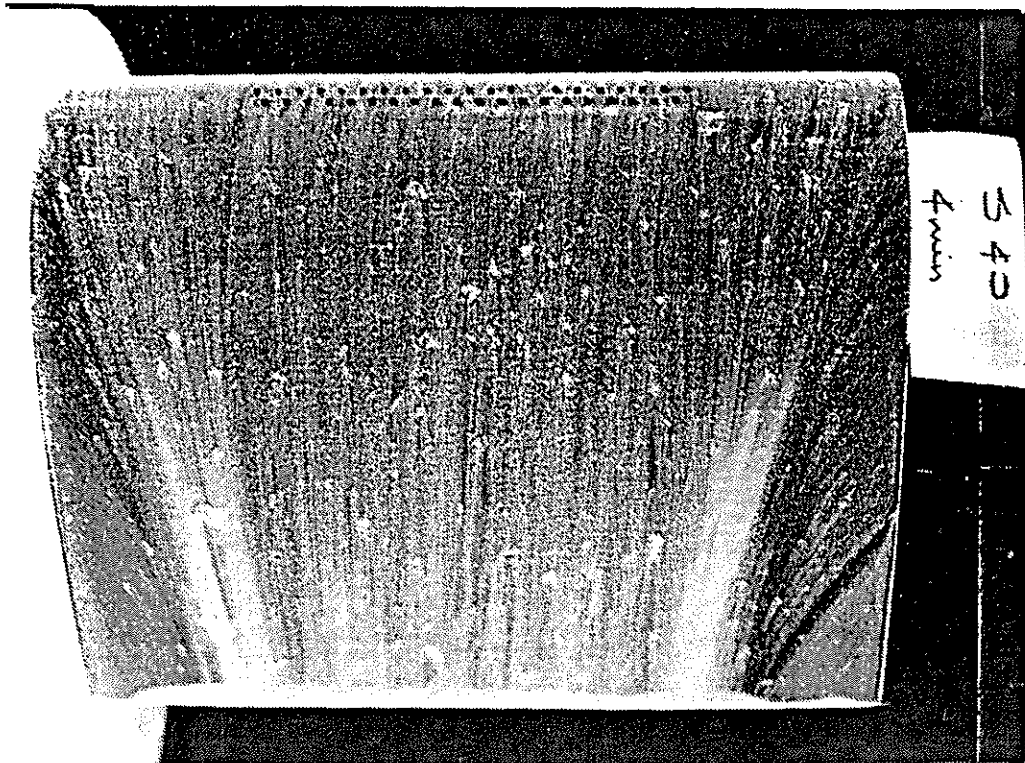


Fig.114 Oil flow vizualisation
suction side ejection
 $\dot{m}_e / \dot{m}_\infty = 1.4 \%$ and $U_\infty = 7.7 \text{ m/sec}$
Inlet

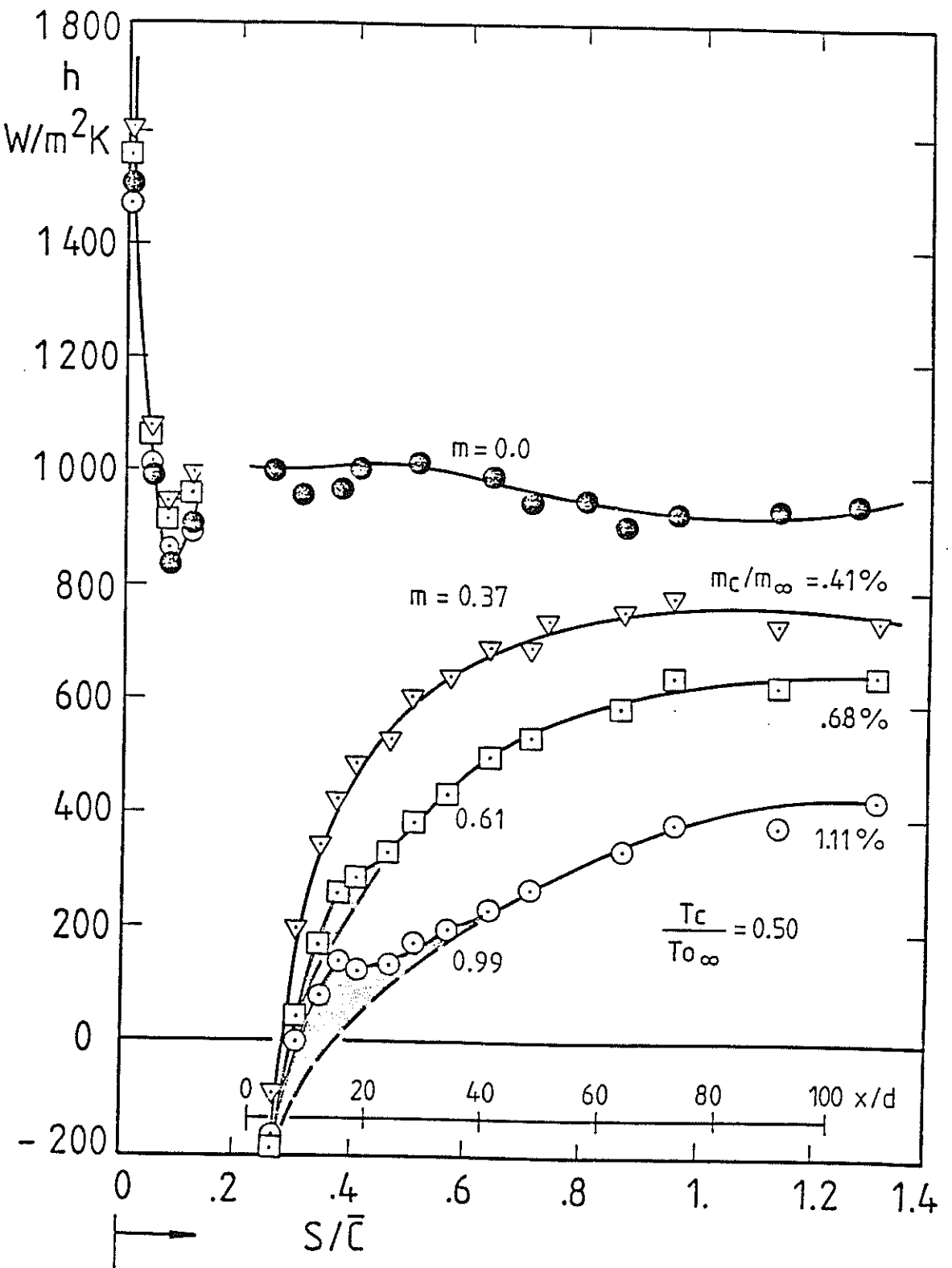
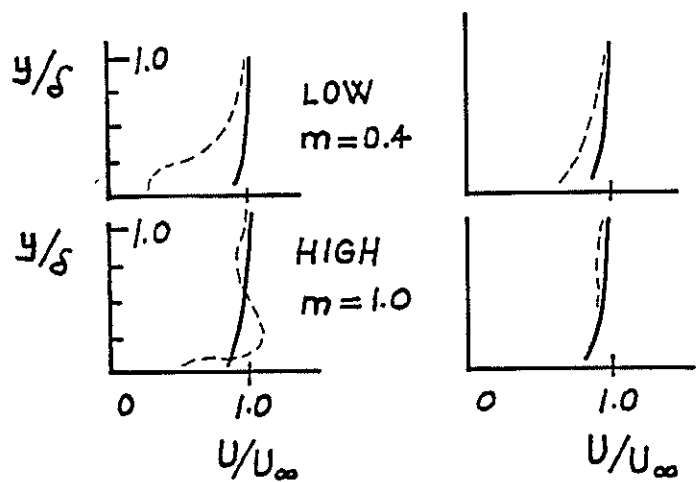


Fig.115 Suction side heat transfer with film cooling,
effect of blowing rate
($i=0^\circ$, $TU_\infty=5.2\%$, $Re_\infty=8.42\times 10^5$, $T_w/T_{0\infty}=0.72$, $T_{0\infty}=408\text{ K}$)

————— $1/7$ power profile
 - - - - film cooling profile



$$x/d \approx 10 \quad x/d \approx 60$$

Fig. 116 Typical velocity profiles,
downstream of double rows of cooling holes

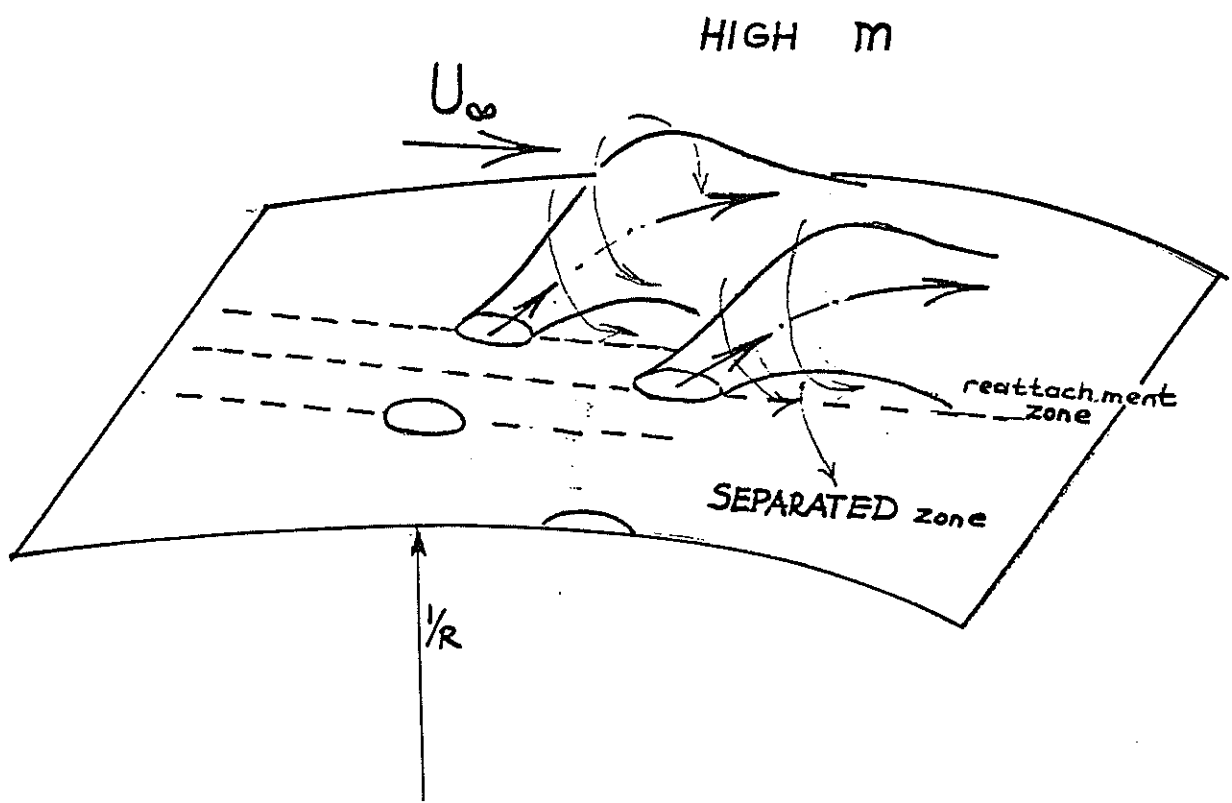


Fig.117 Jet penetration into the mainstream at high blowing rates

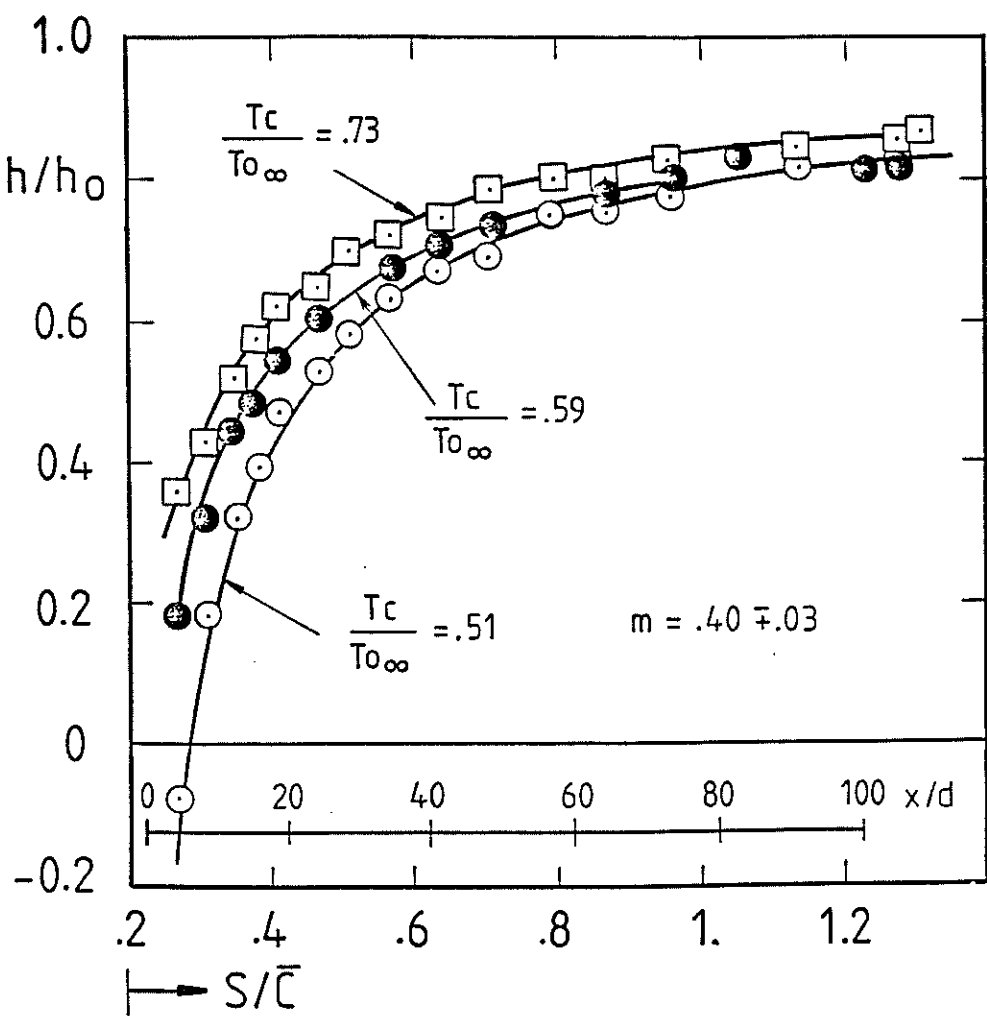


Fig.118 Suction side heat transfer with film cooling,
low blowing rate

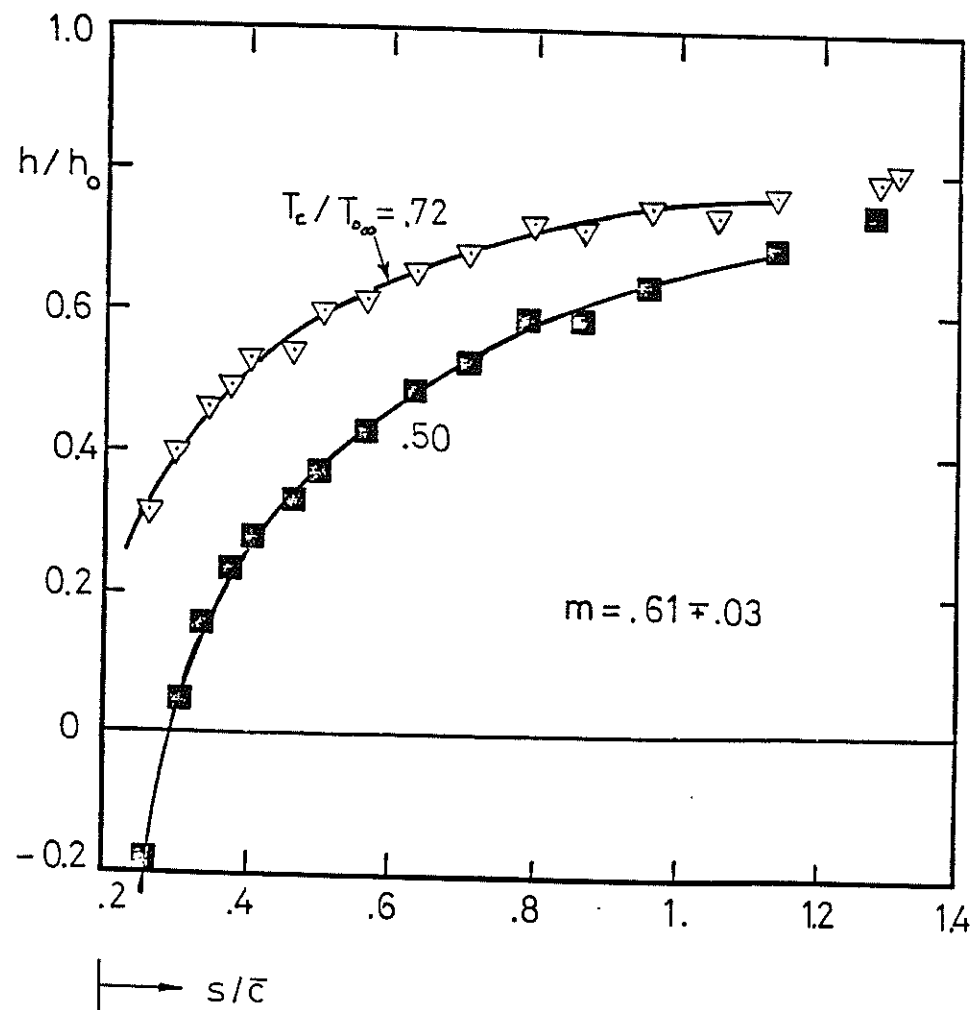


Fig.119 Suction side heat transfer with film cooling,
medium blowing rate

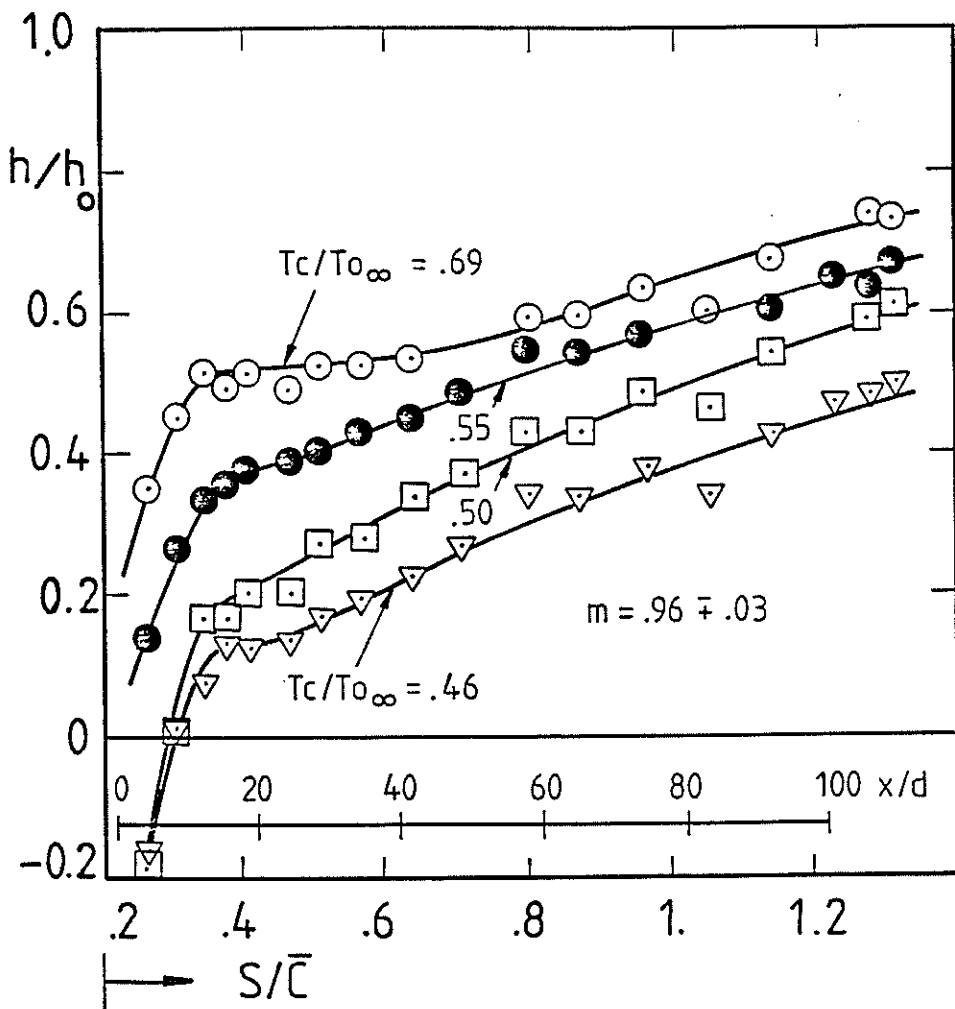


Fig.120 Suction side heat transfer with film cooling.
high blowing rate

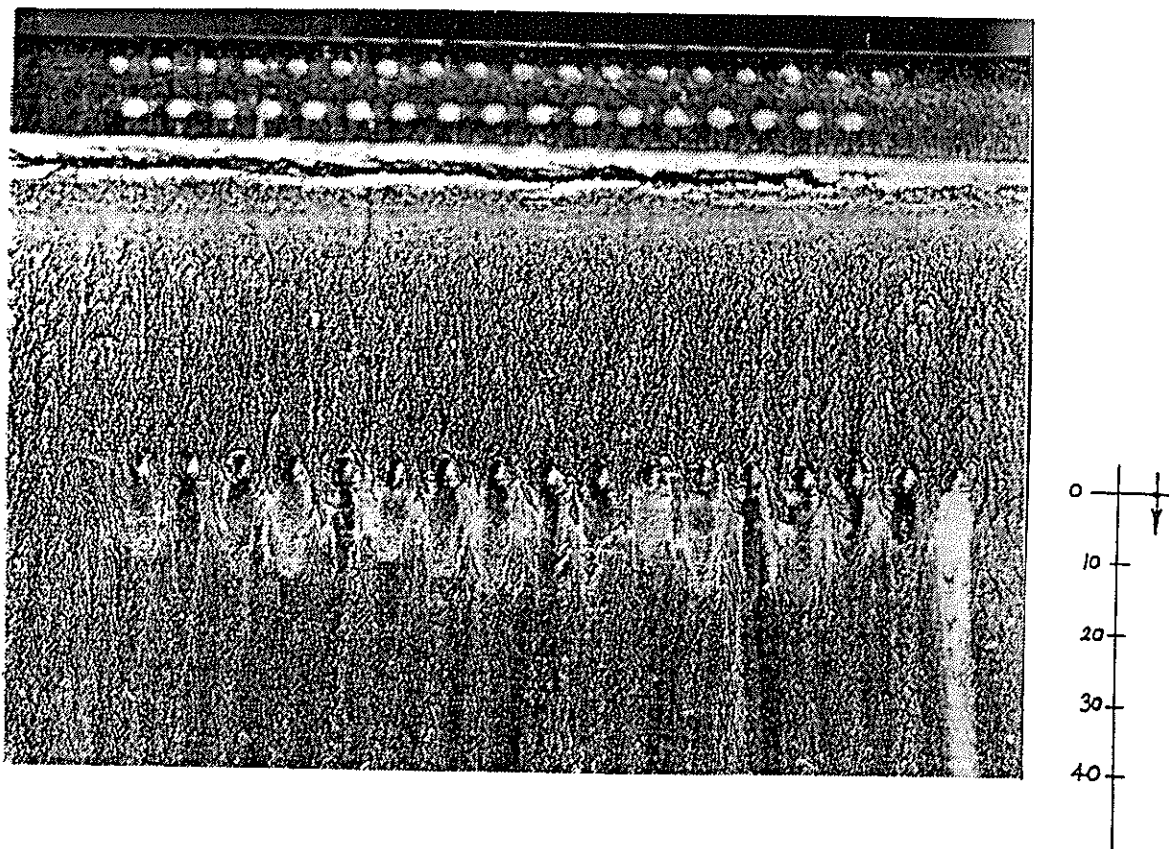


Fig.121 Oil flow vizualisation
pressure side ejection
 $\dot{m}_e / \dot{m}_{\infty} = 1.1 \%$ and $U_{\infty} = 7.7 \text{ m/sec}$
_{inlet}

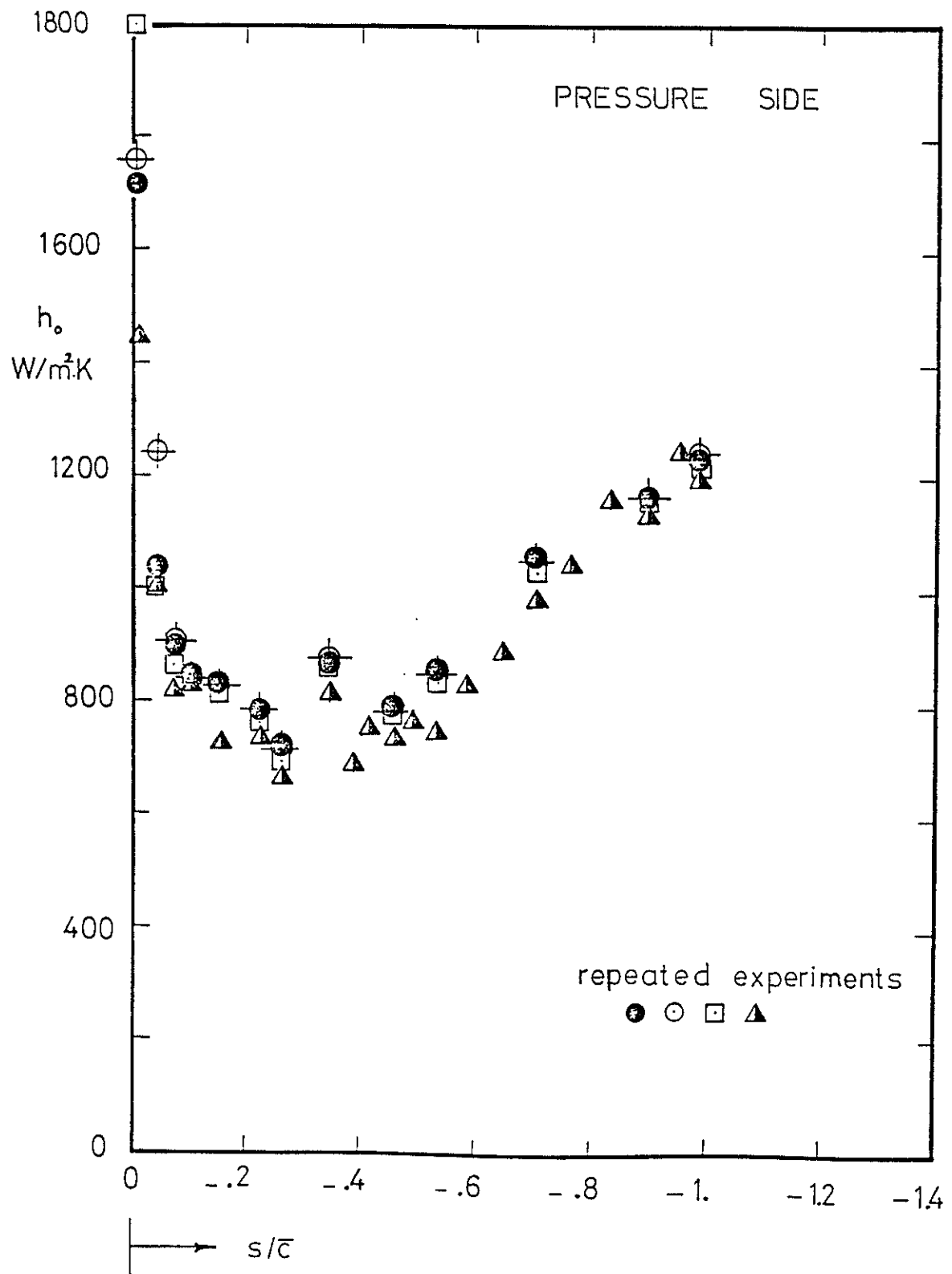


Fig. 122 Heat transfer coefficient, h_o , no coolant ejection
 $(i=0^\circ, T_{U\infty}=5.2\%, Re_{\frac{c}{2}}=8.4 \times 10^5, T_w/T_{\infty}=0.70, T_{\infty}=409\text{ K})$

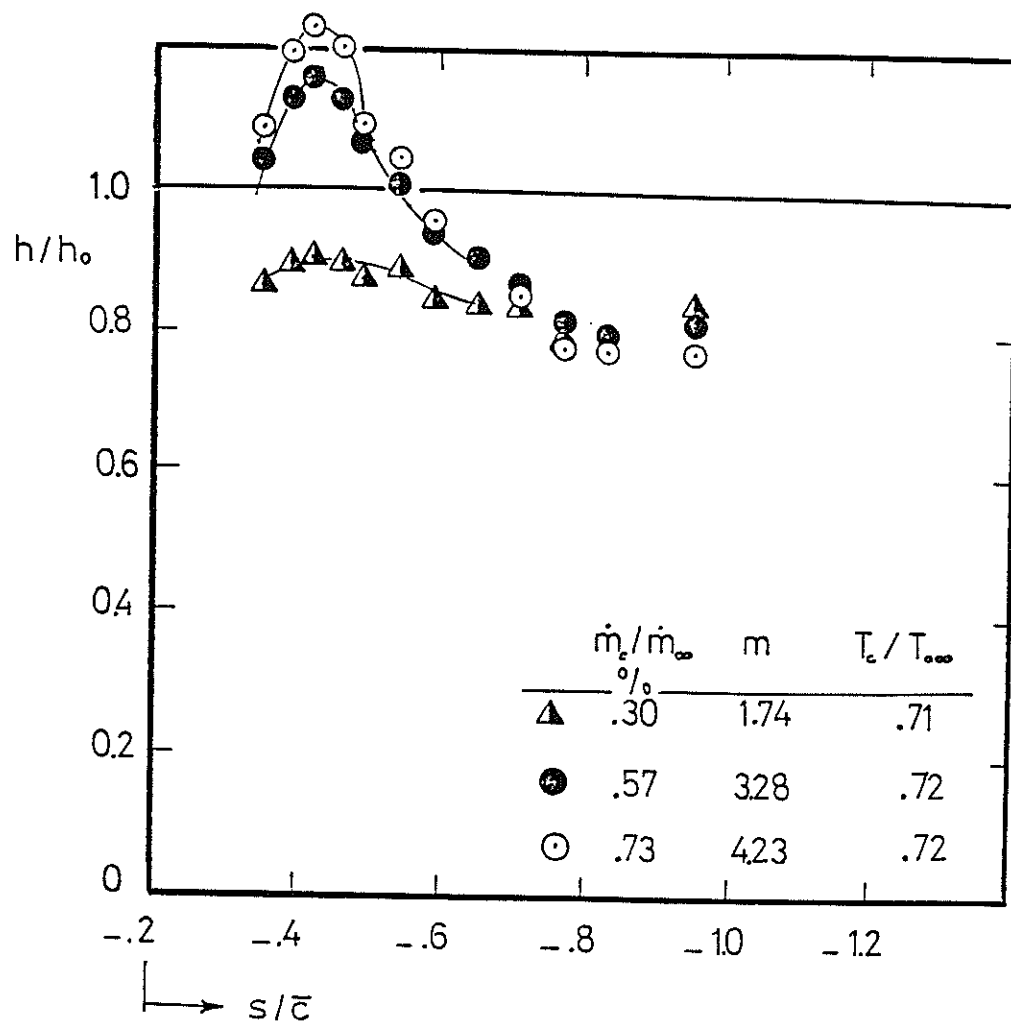


Fig. 123 Film cooling on the pressure side,
coolant at wall temperature, ($T_e/T_{\infty}=0.70$)

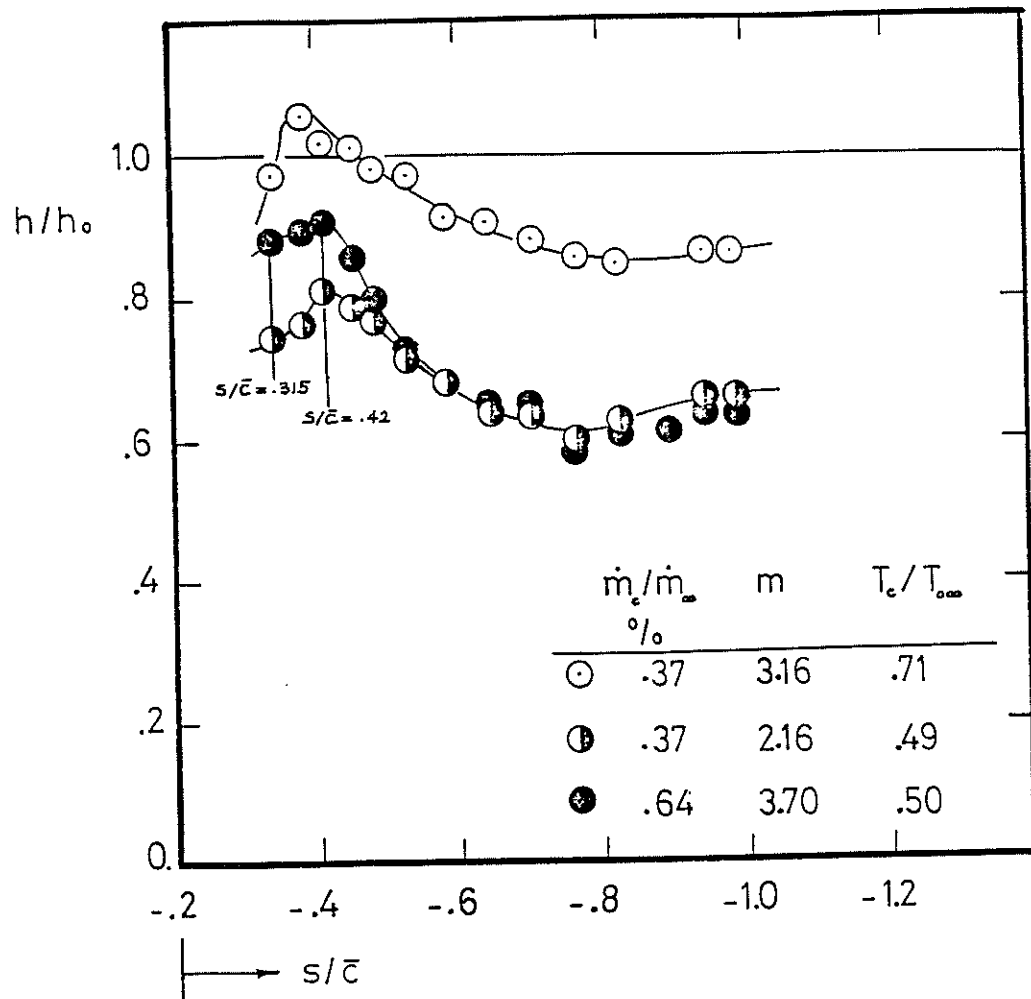


Fig.124 Film cooling on the pressure side
 h/h_0 reductions due to lowered coolant temperature level
 $(T_c = 0.5 \times T_\infty)$

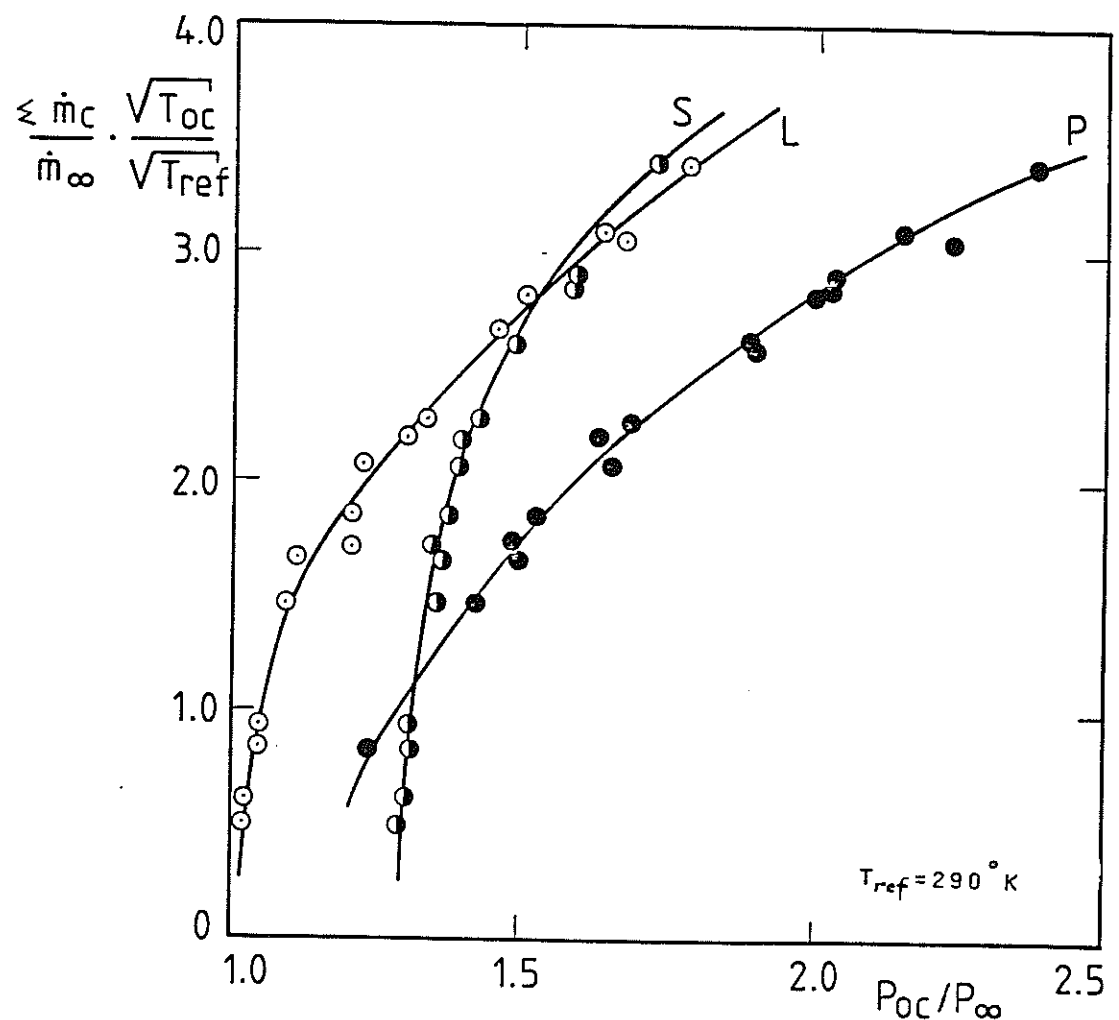


Fig. 125 Total normalized coolant mass weight ratio versus plenum chamber pressure

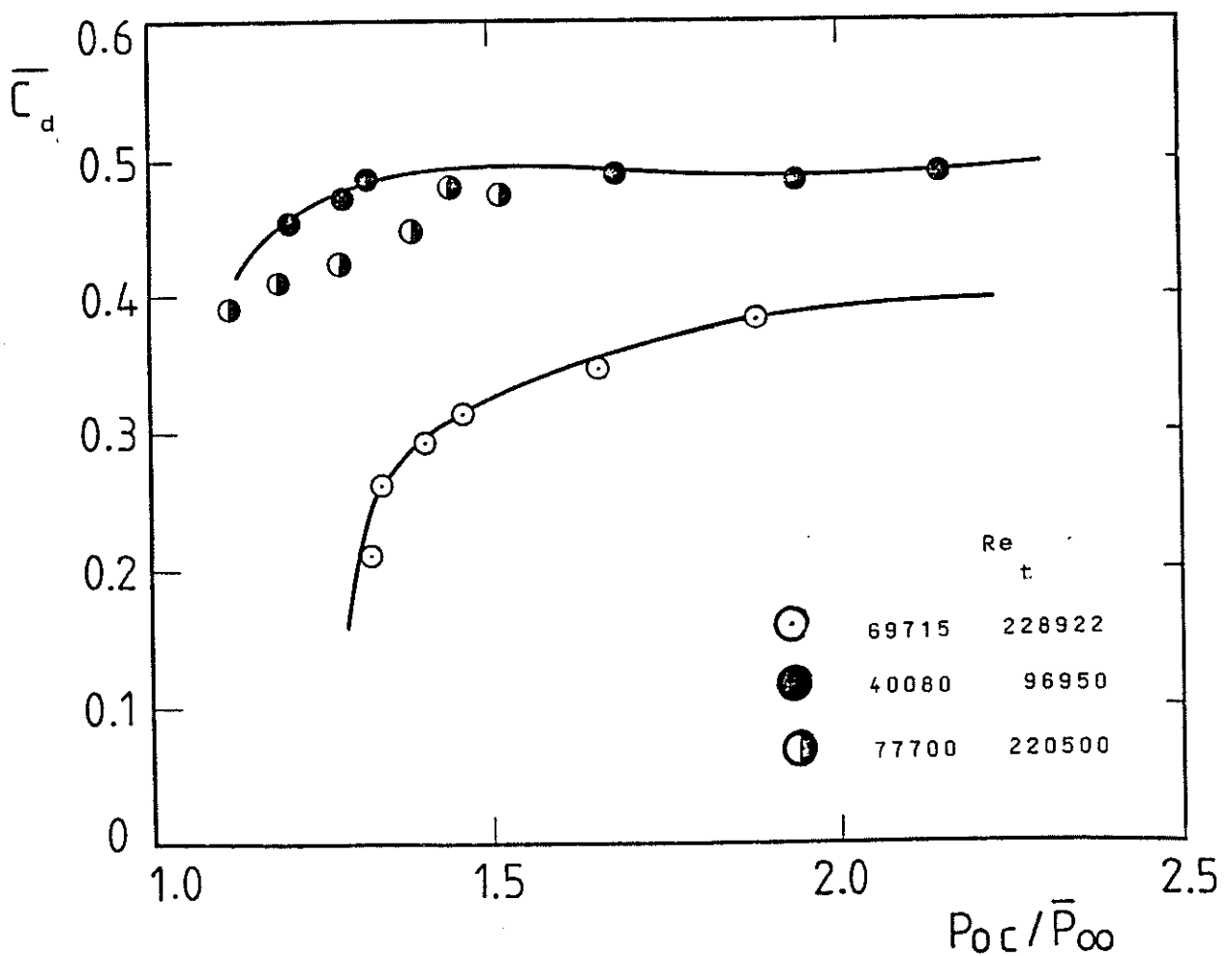
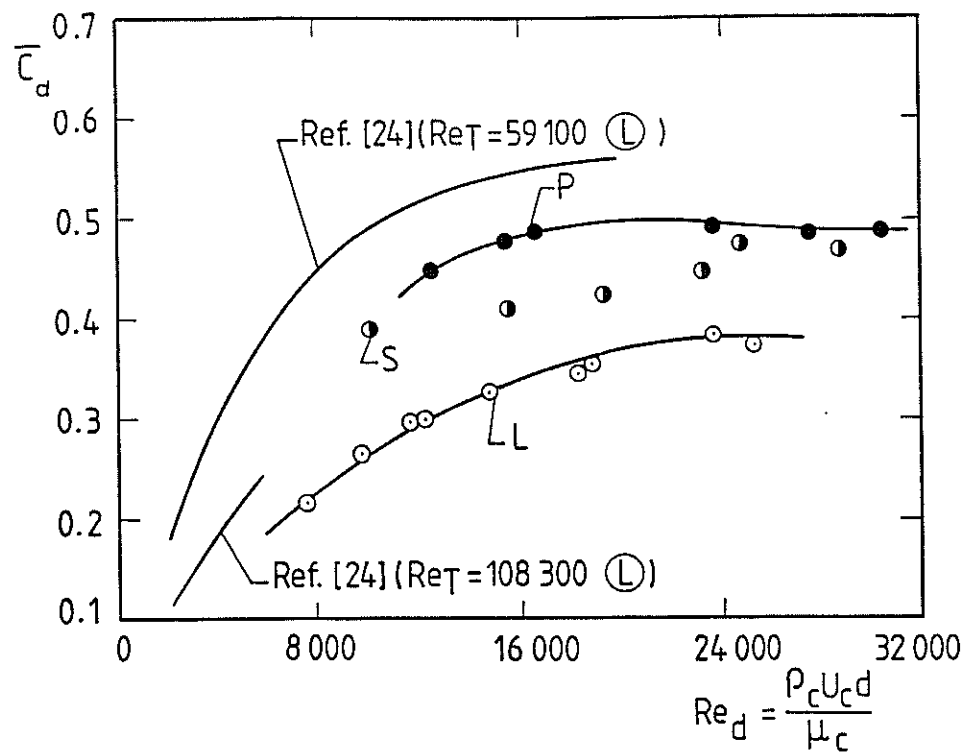


Fig.126 Discharge coefficients of ejection sites

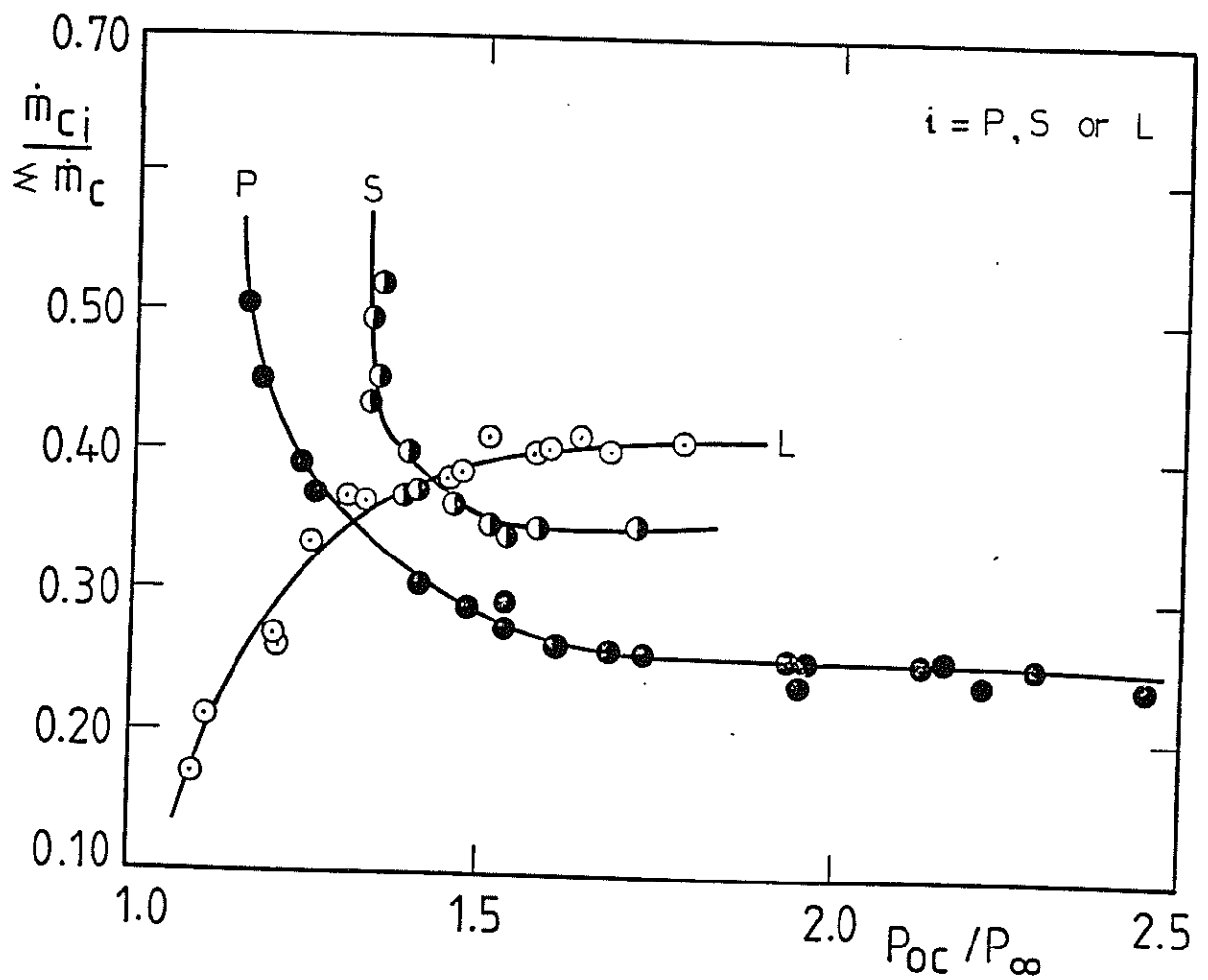


Fig. 127 Coolant split in between plenum chambers
($i=P, S$ or L)

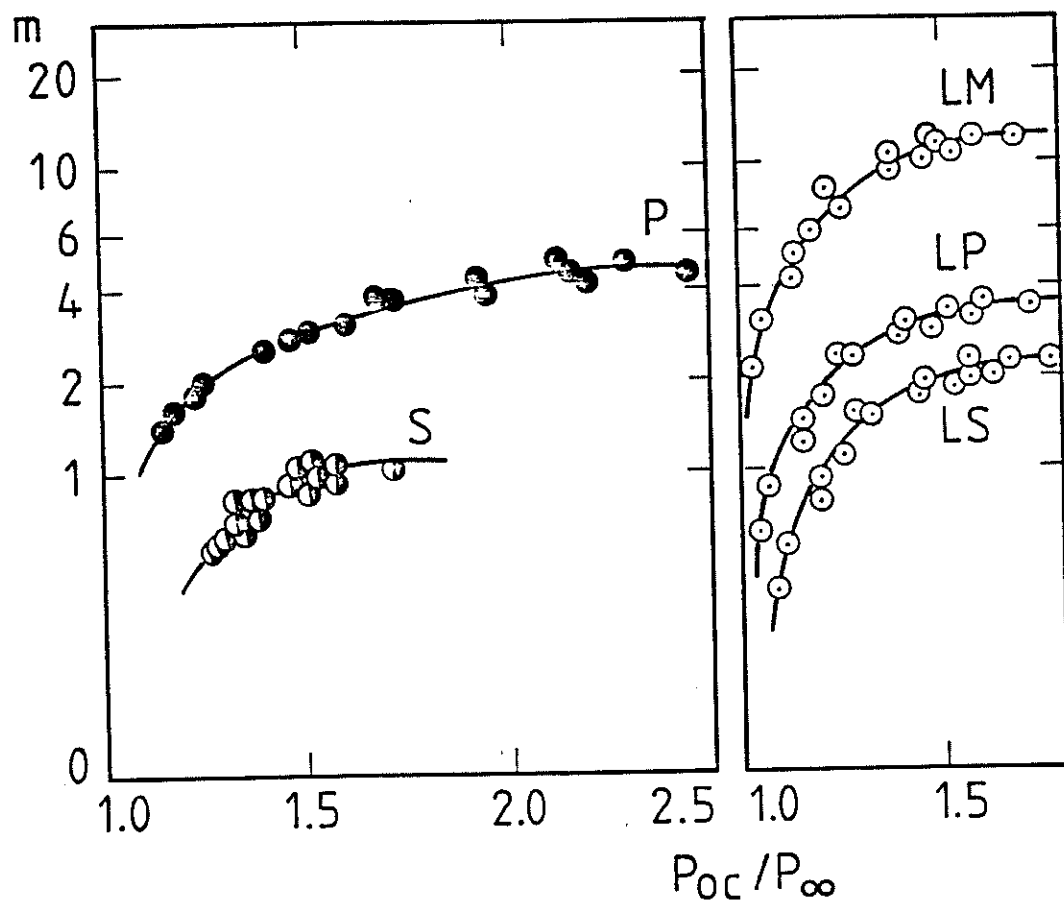


Fig.128 Local blowing rates of the ejection sites

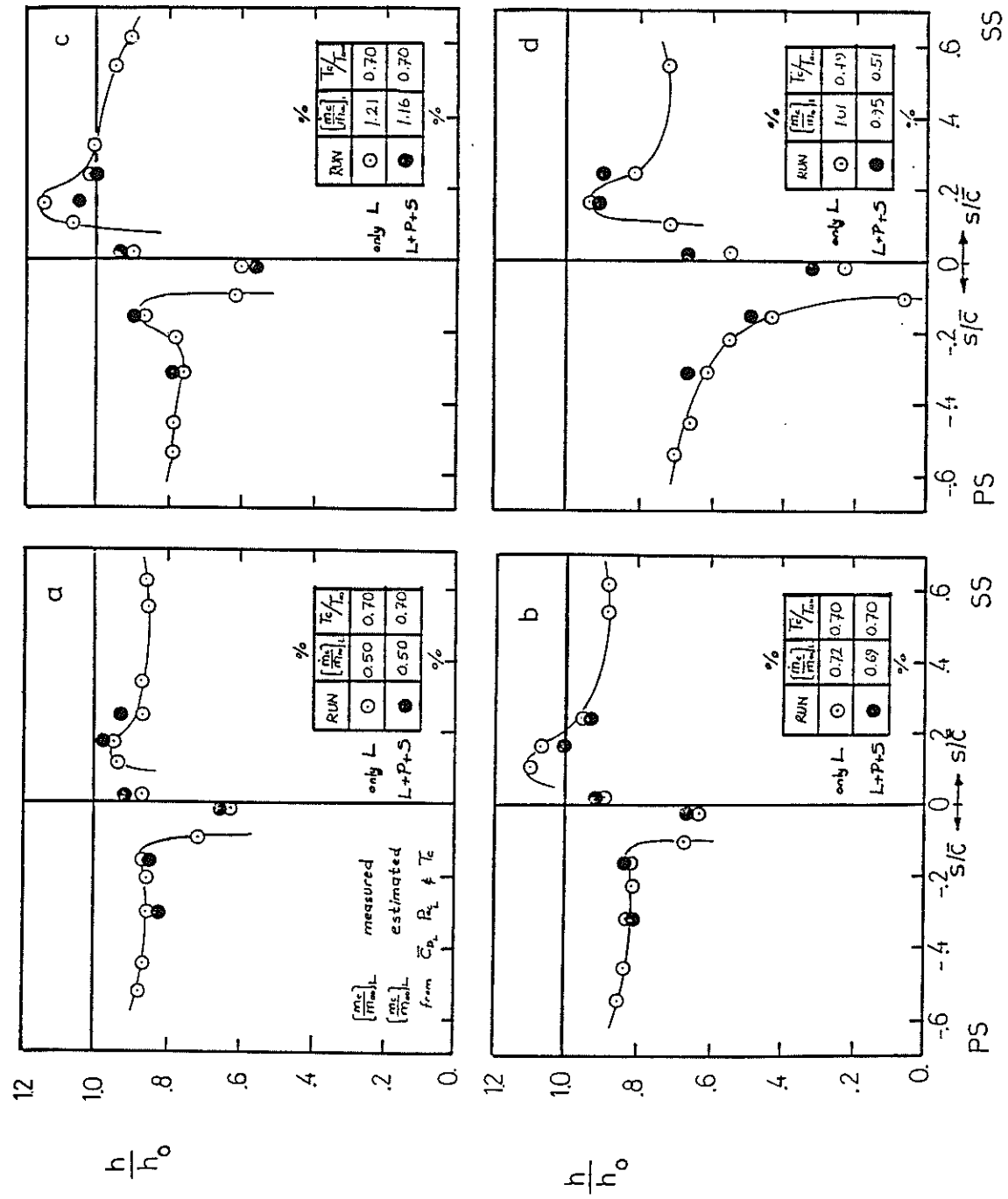


Fig. 129 Leading edge film cooling heat transfer,

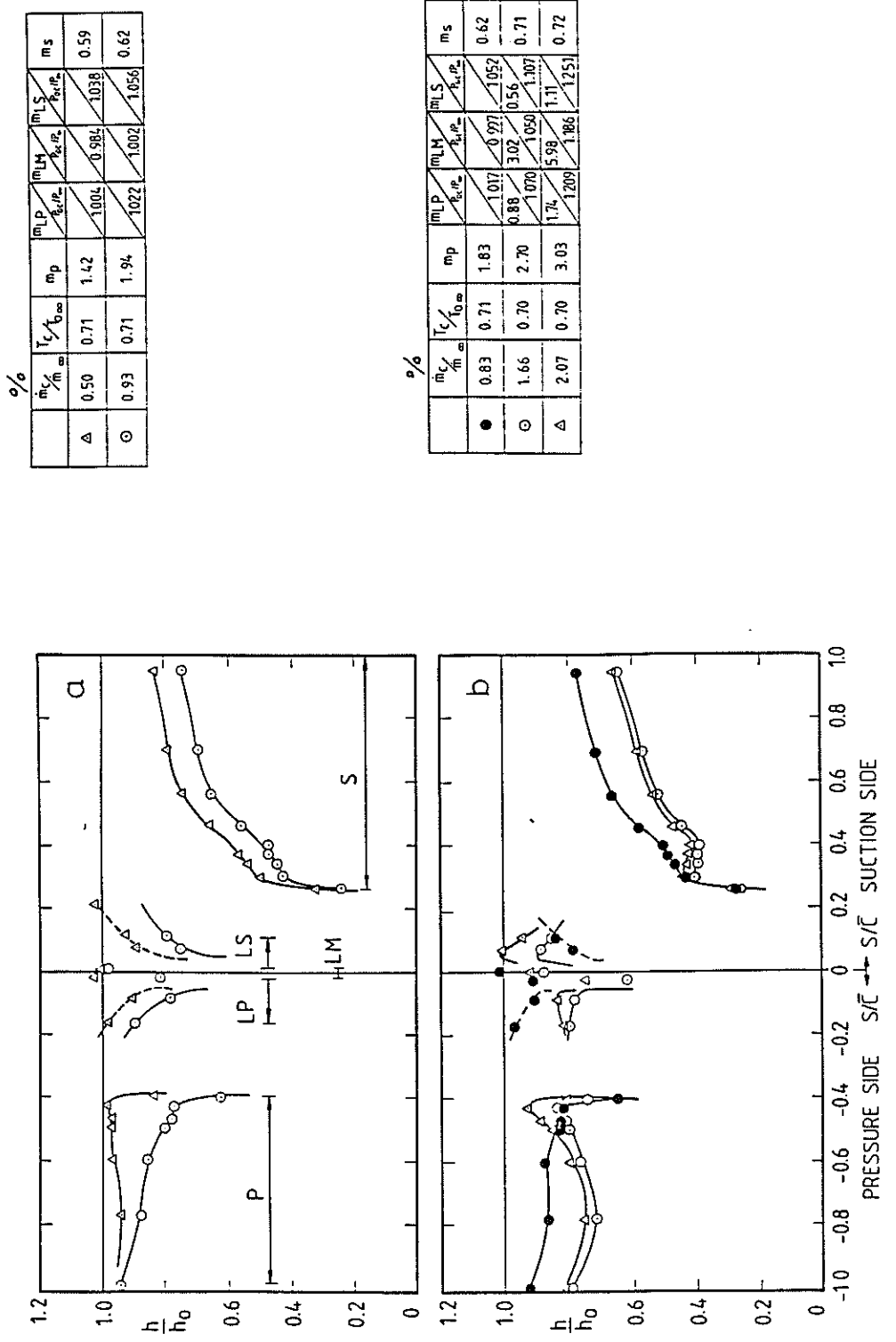


Fig. 130 Simultaneous coolant ejection from L, P and S
($T_e/T_{\infty} = T_w/T_{\infty} = 0.71$)

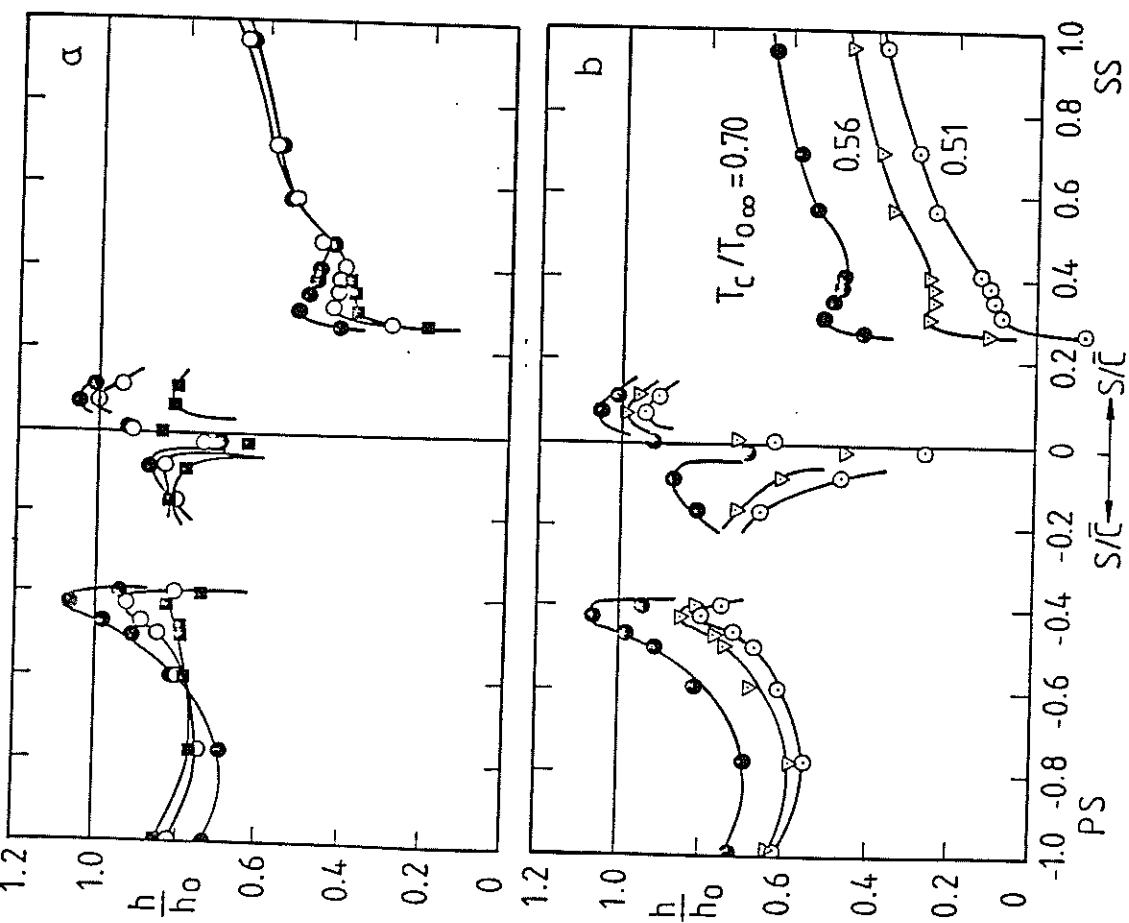


Fig. 131.a Effect of blowing rate
on film cooling neat transfer

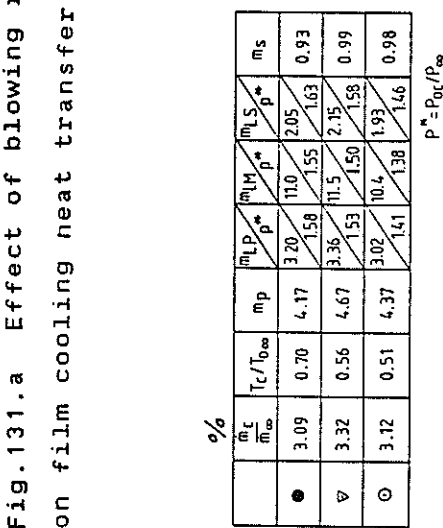
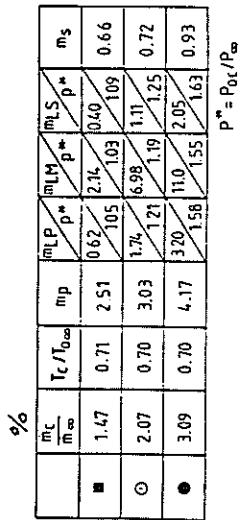


Fig. 131.b Effect of coolant
temperature on film cooling
heat transfer

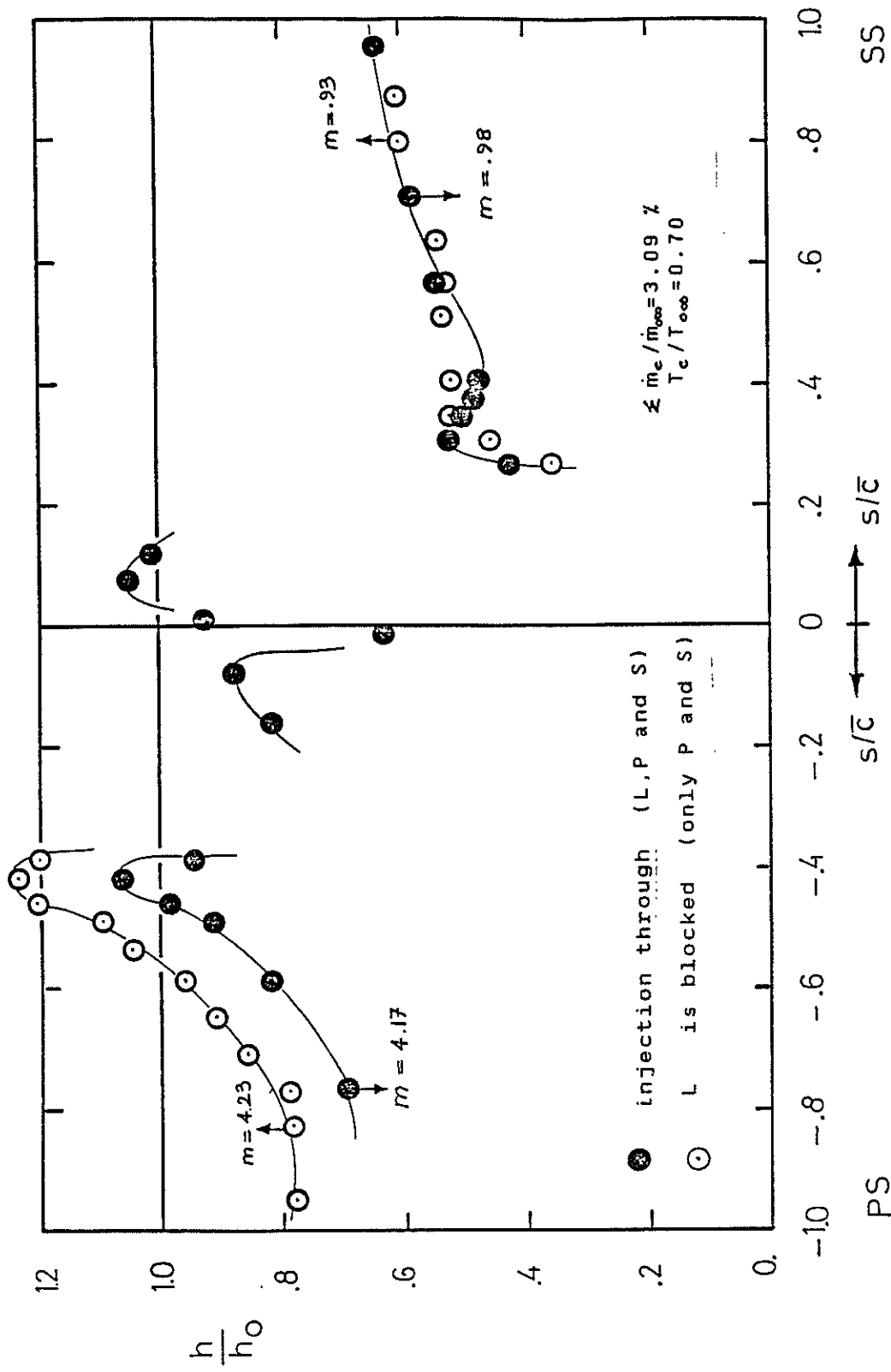


Fig. 132 Influence of leading edge ejection on downstream coolant layers (P and S)

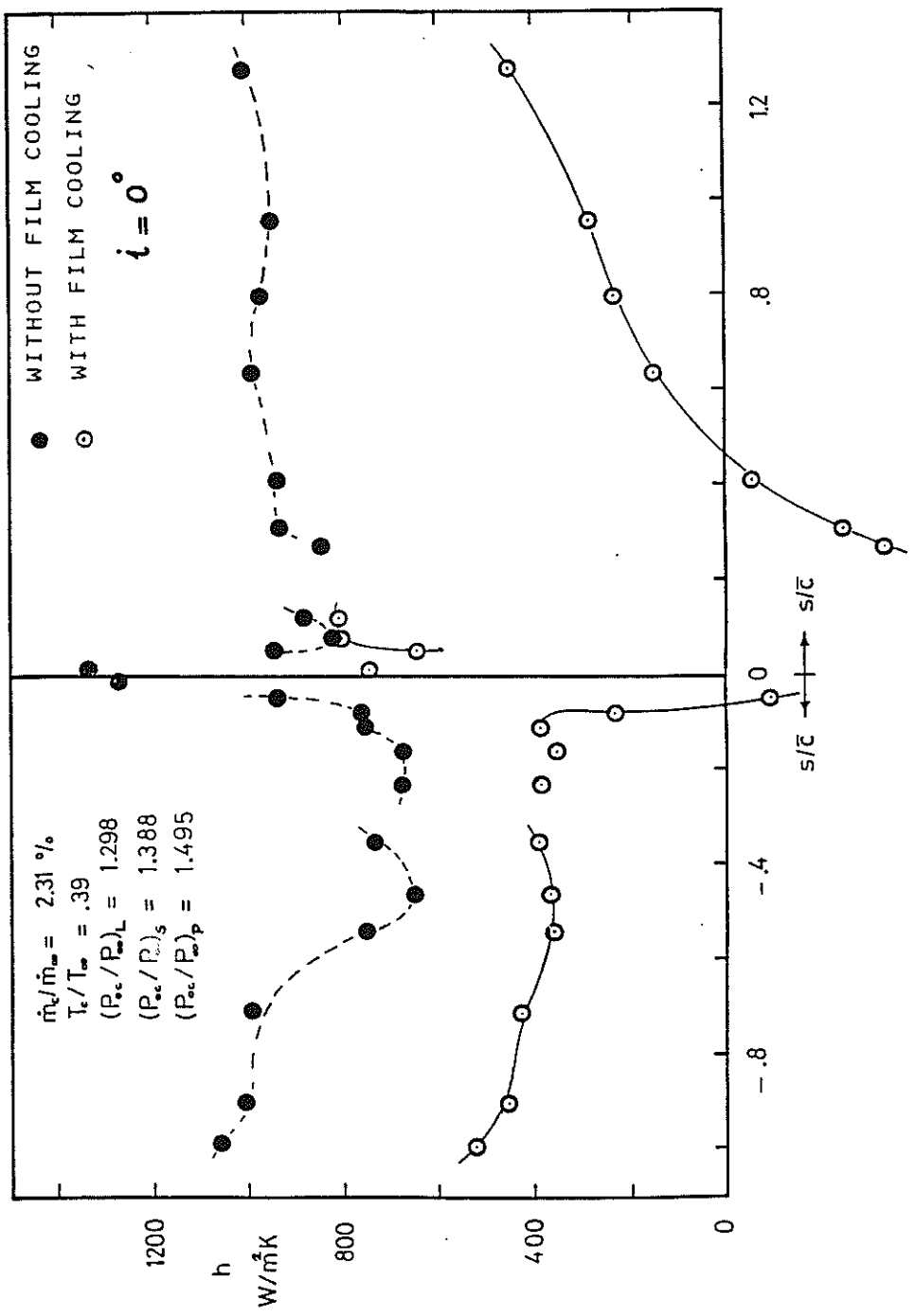


Fig. 134 Effect of incidence angle on film cooling heat transfer

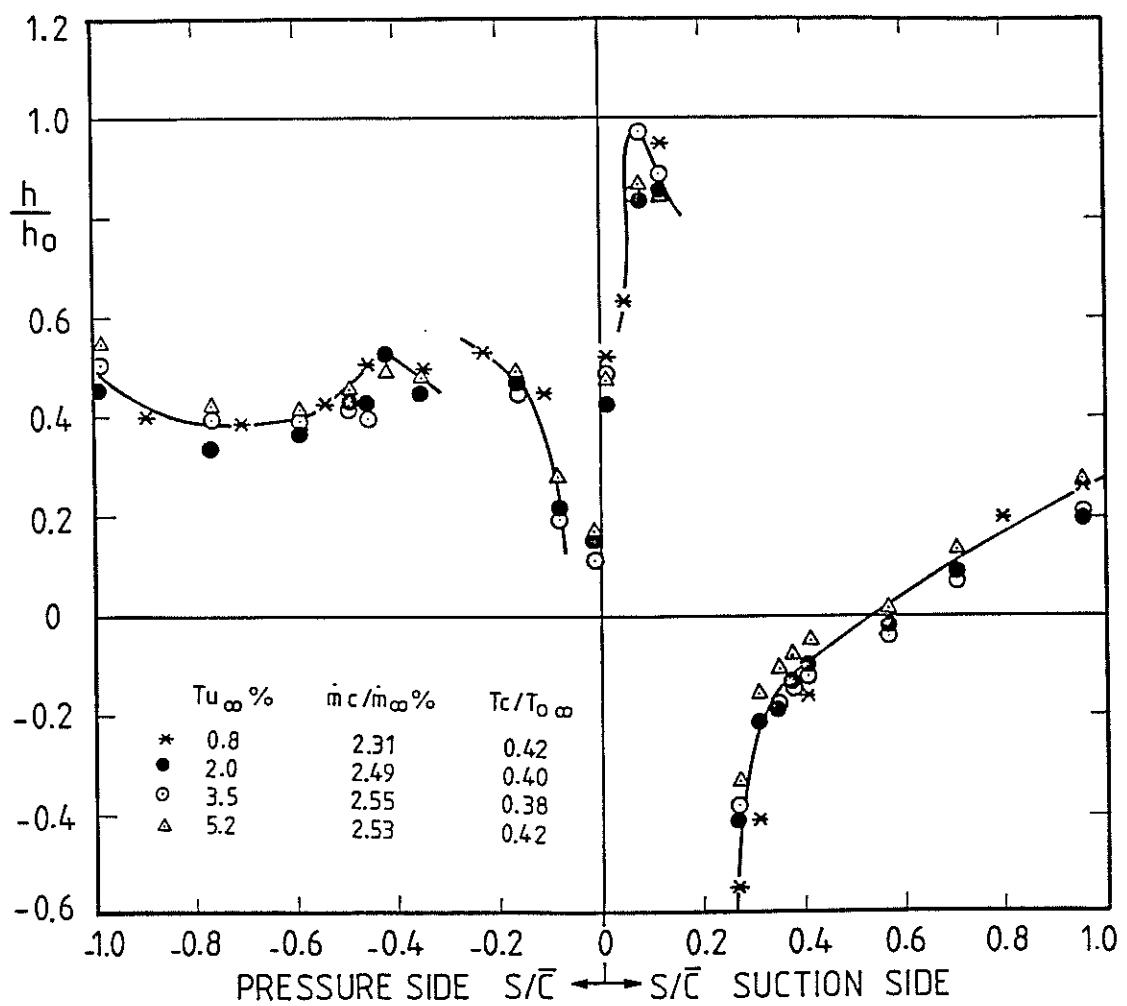


Fig.133 Effect of free stream turbulence intensity on film cooling heat transfer

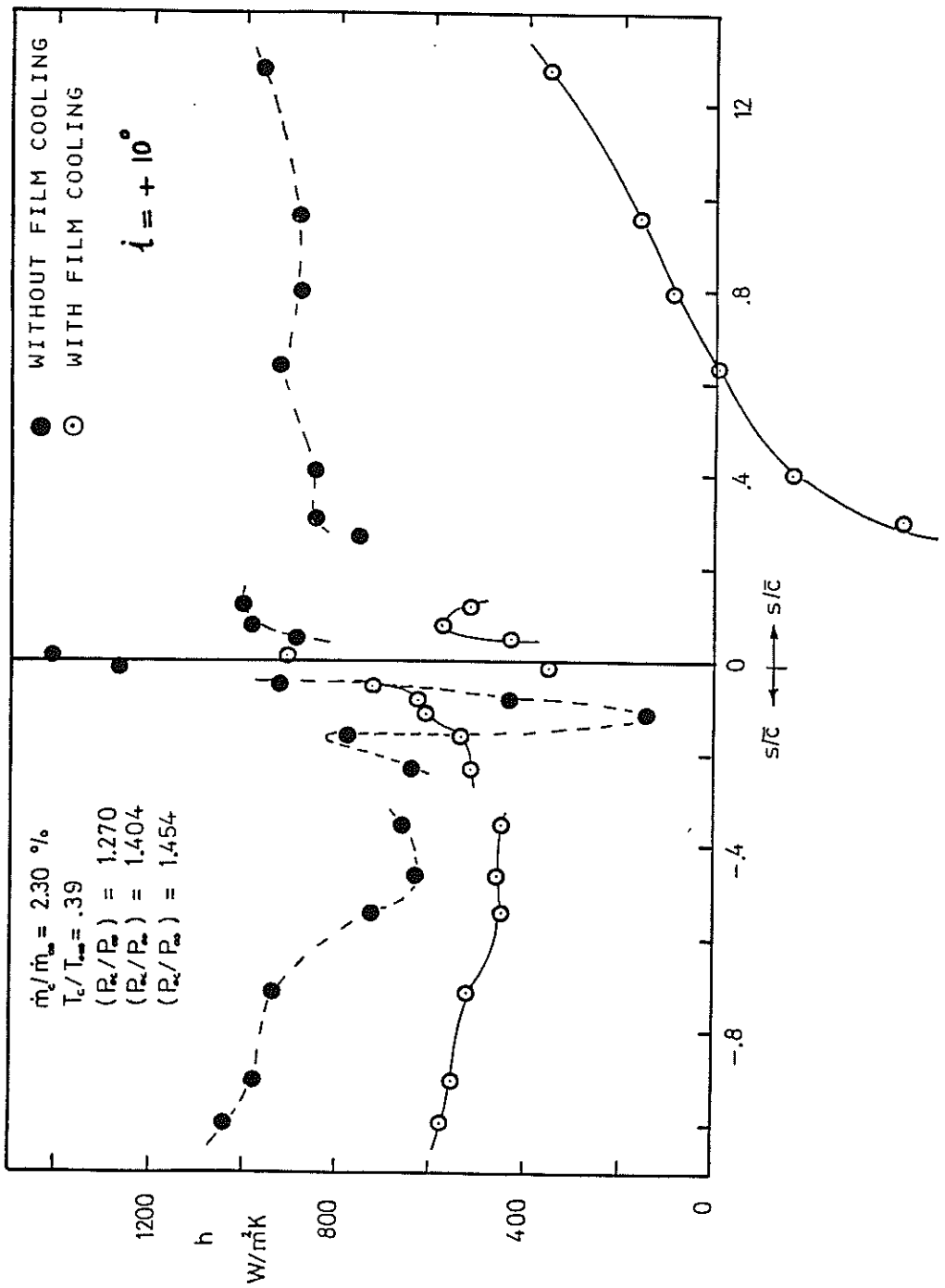


Fig. 135 Effect of incidence angle on film cooling heat transfer, $i = +10^\circ$

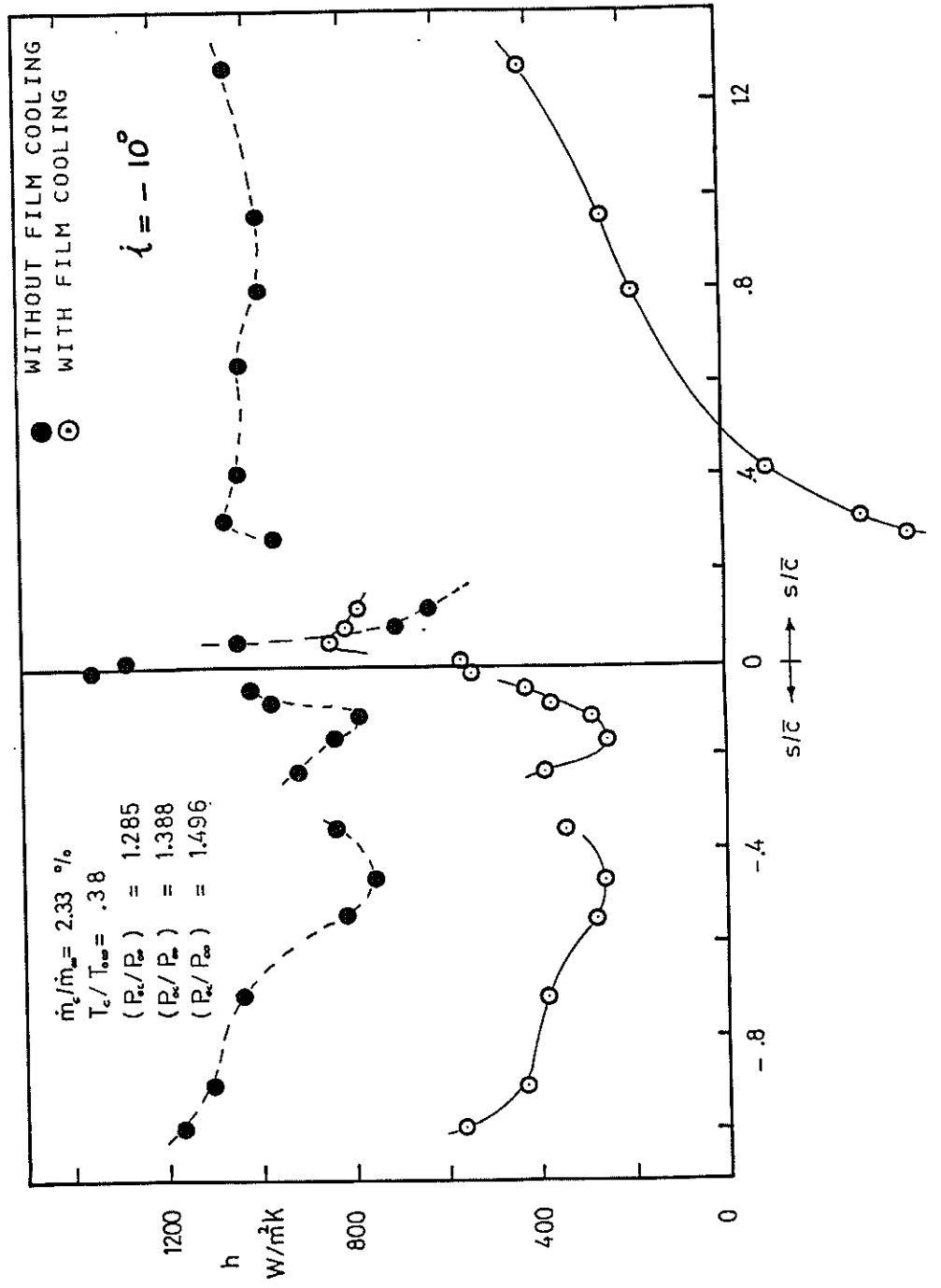


Fig. 136 Effect of incidence angle on film cooling heat transfer, $i = -10^\circ$

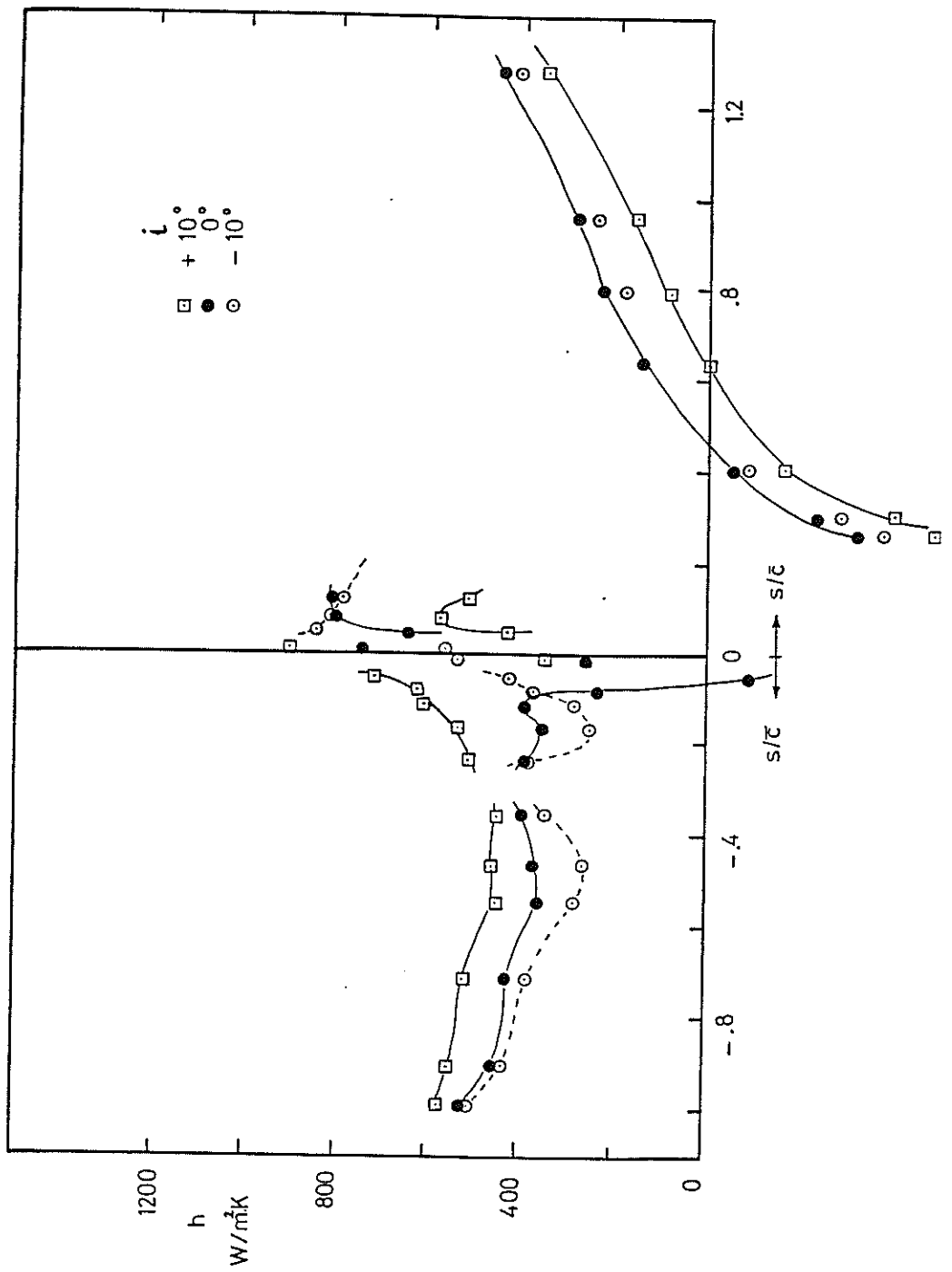


Fig. 137 Comparison of film cooling heat transfer data taken at various incident angles $i_i = 0^\circ \pm 10^\circ - 10^\circ$, $q'' = 10^6 \text{ W/m}^2 \text{ K}$

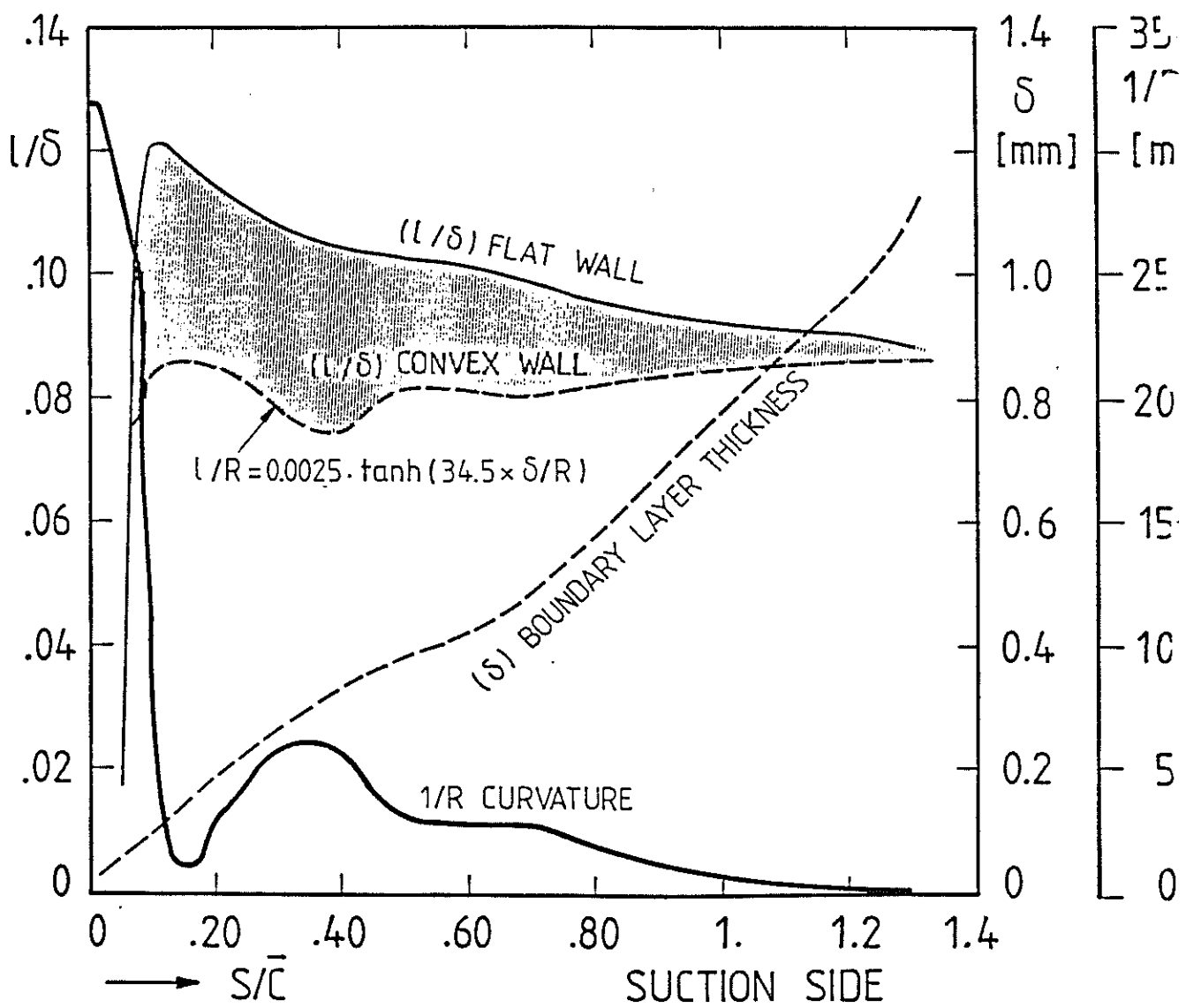


Fig. 138 Outer layer mixing length, curvature and boundary layer thickness on the suction side

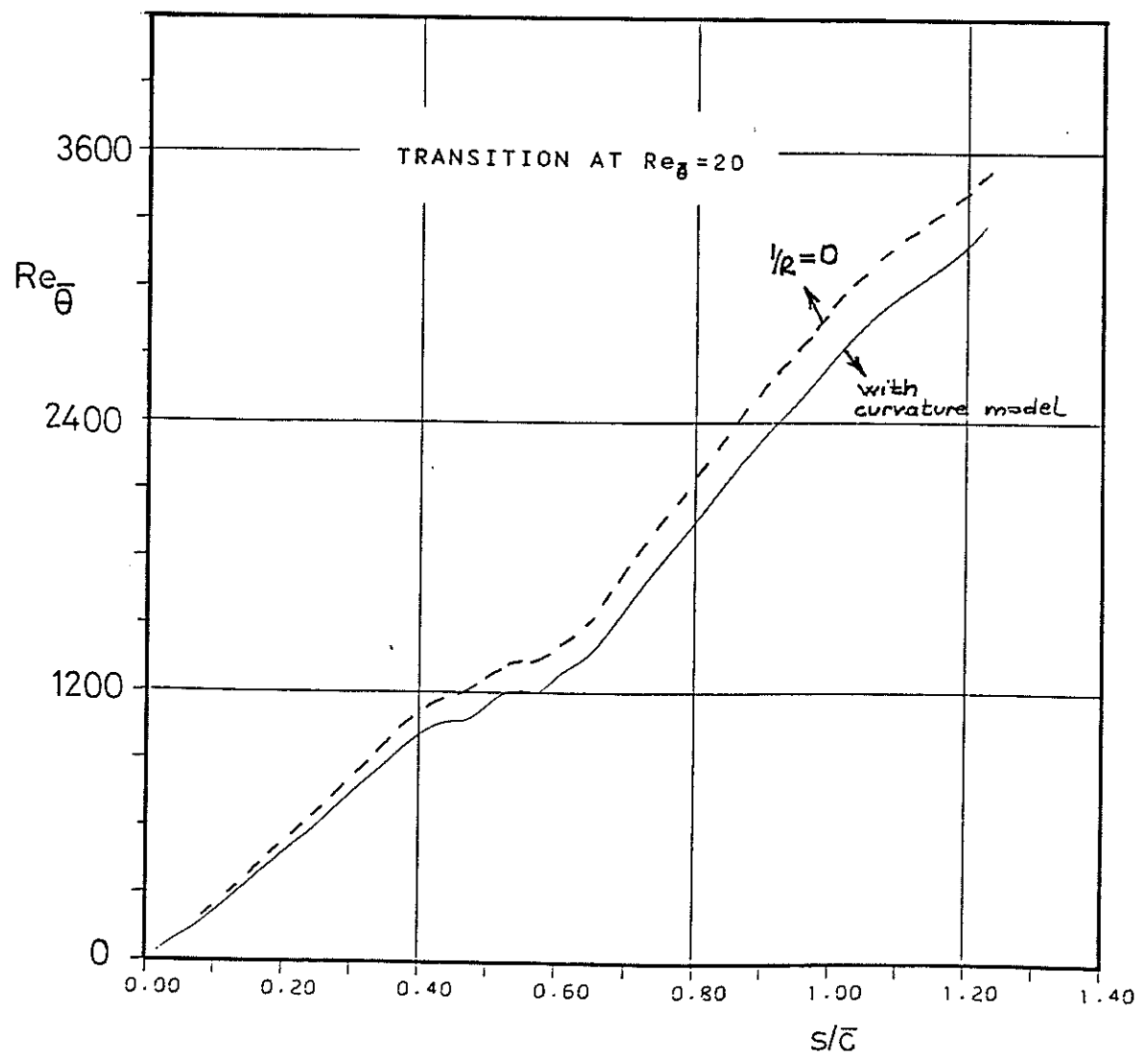


Fig.139 Momentum thickness Reynolds number,with and without curvature effect

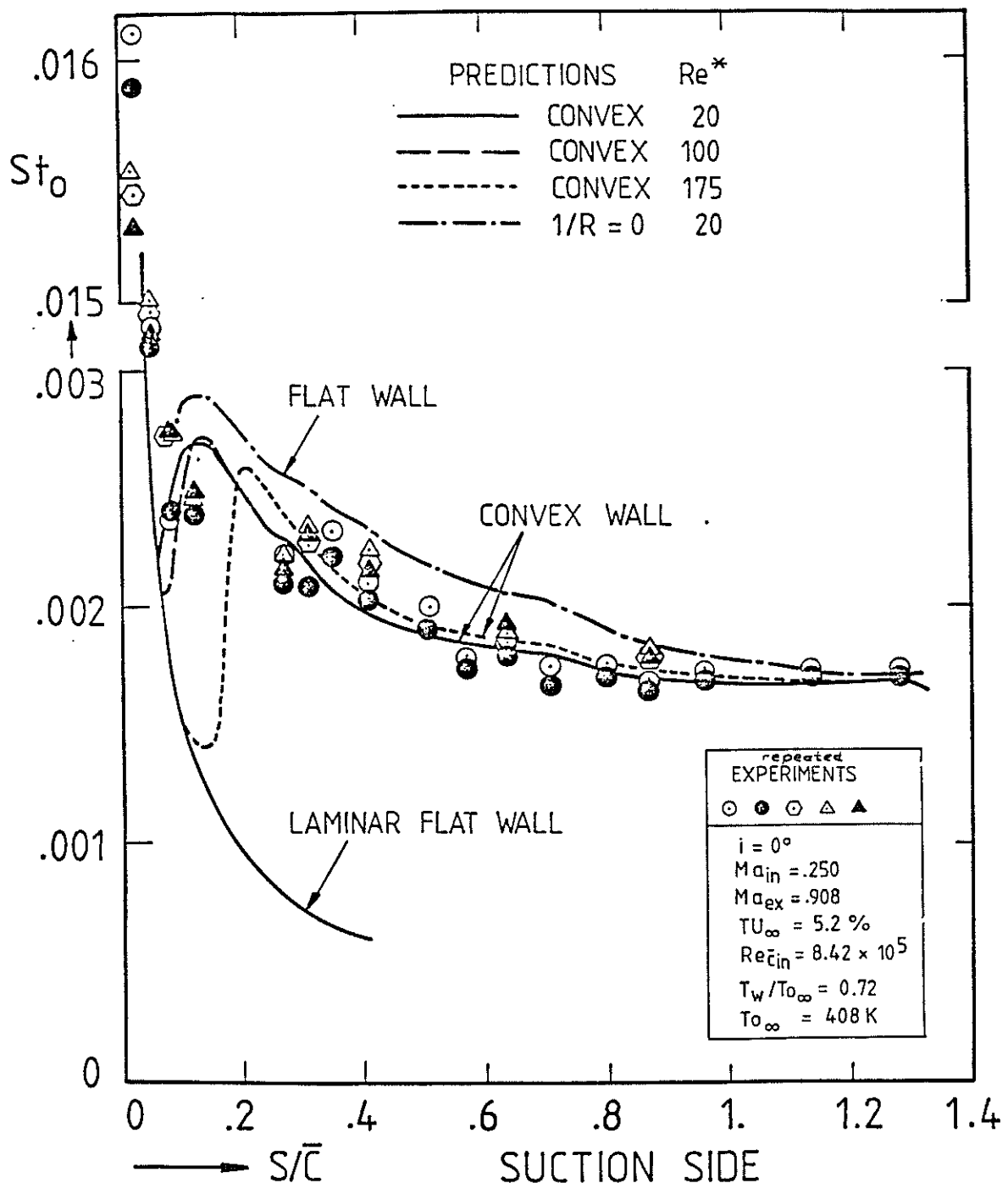


Fig. 140 Measured St_0 number distribution and predictions without cooling

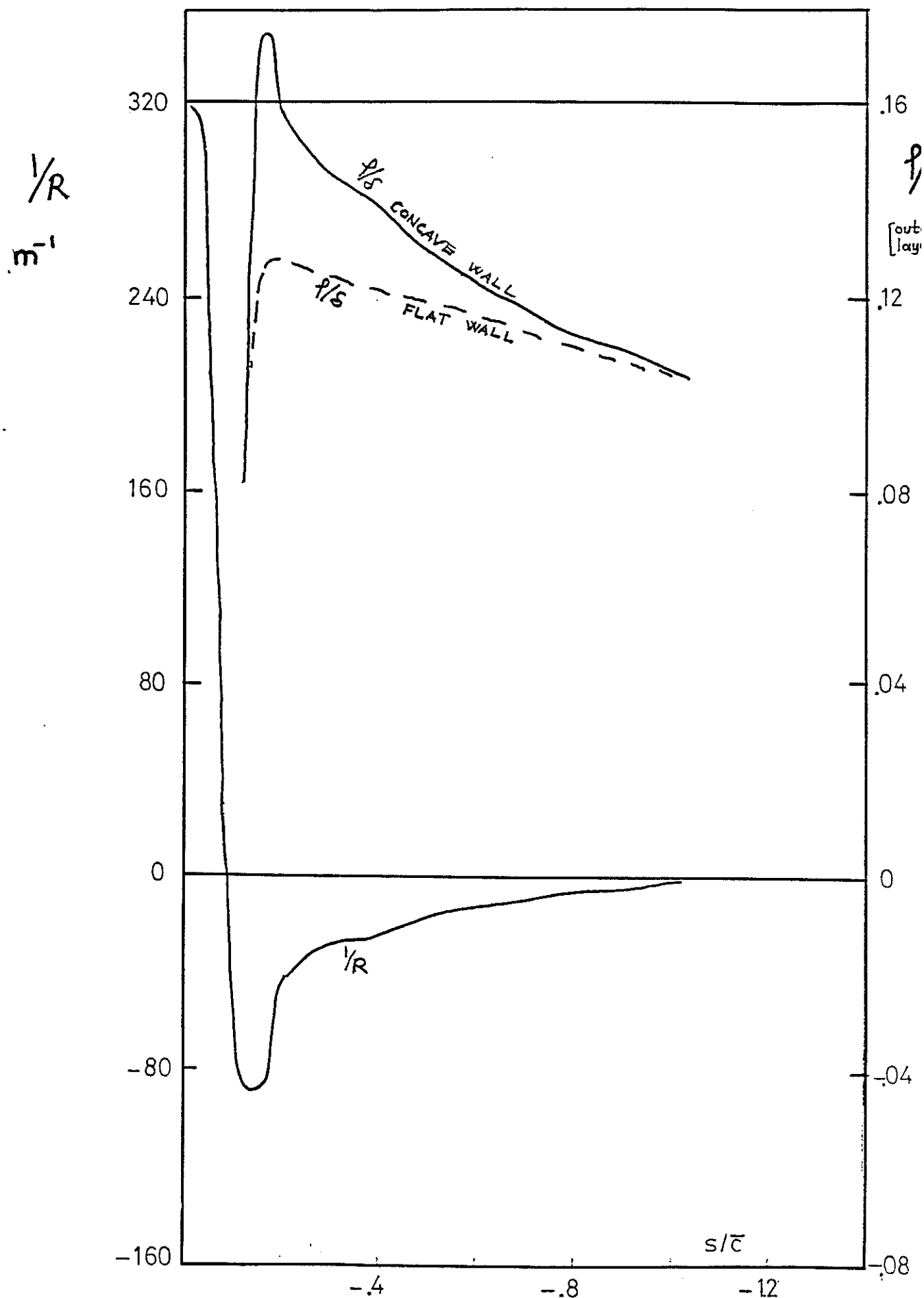


Fig.141 Curvature and outer layer mixing length variation

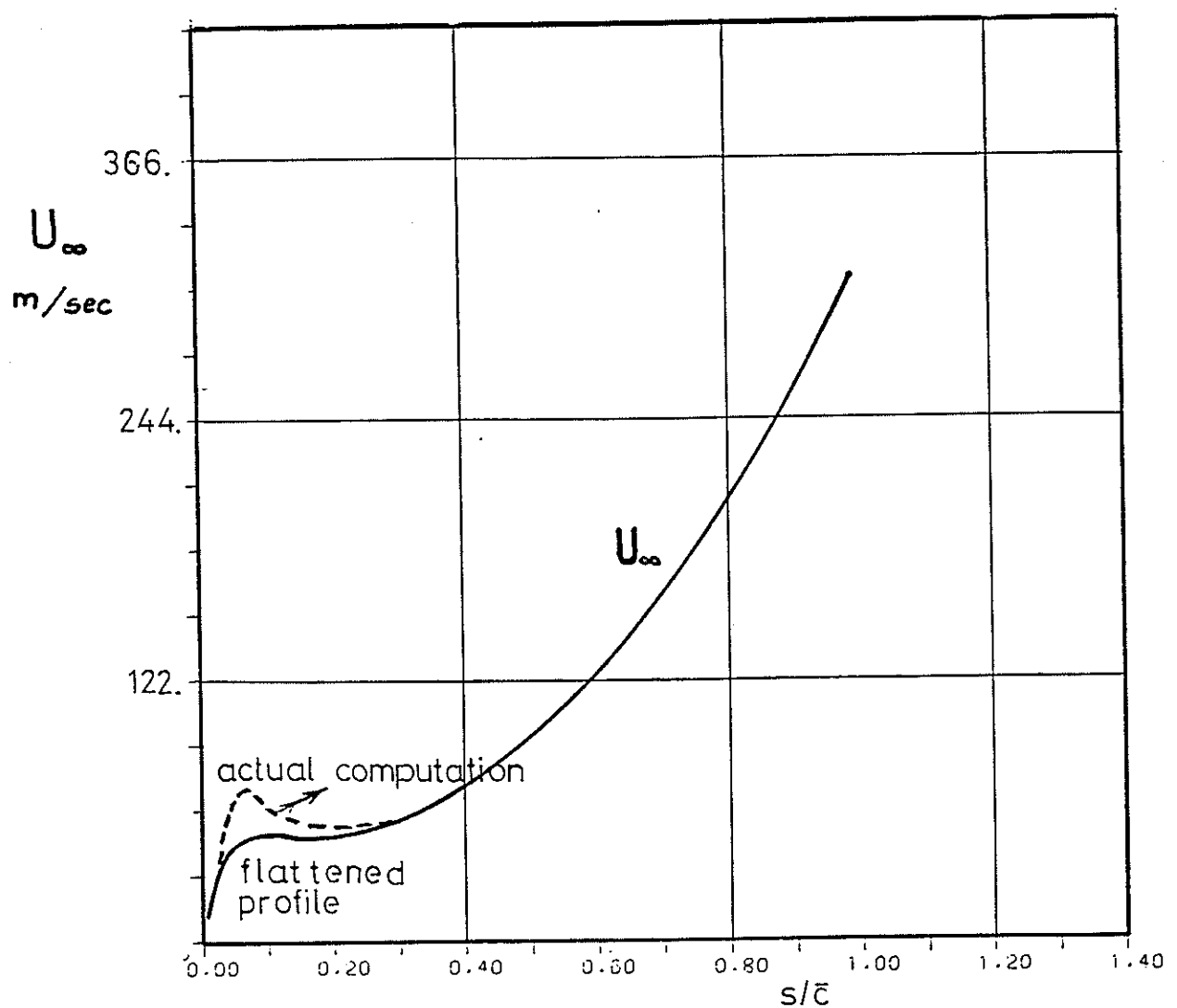


Fig.142 Free stream velocity profile on the pressure side

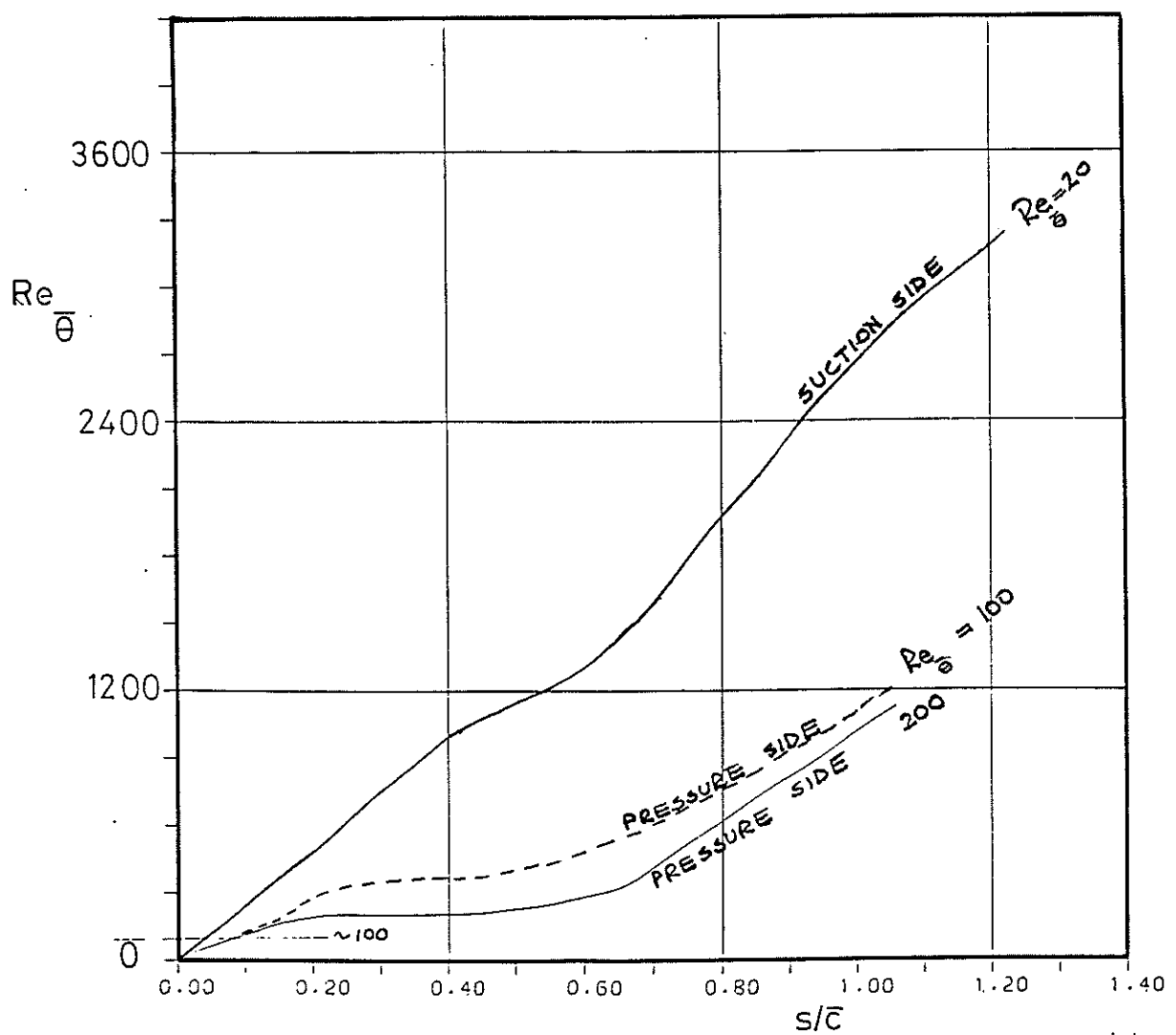


Fig.144 Momentum thickness Re variation on the pressure side and comparison with the suction side data

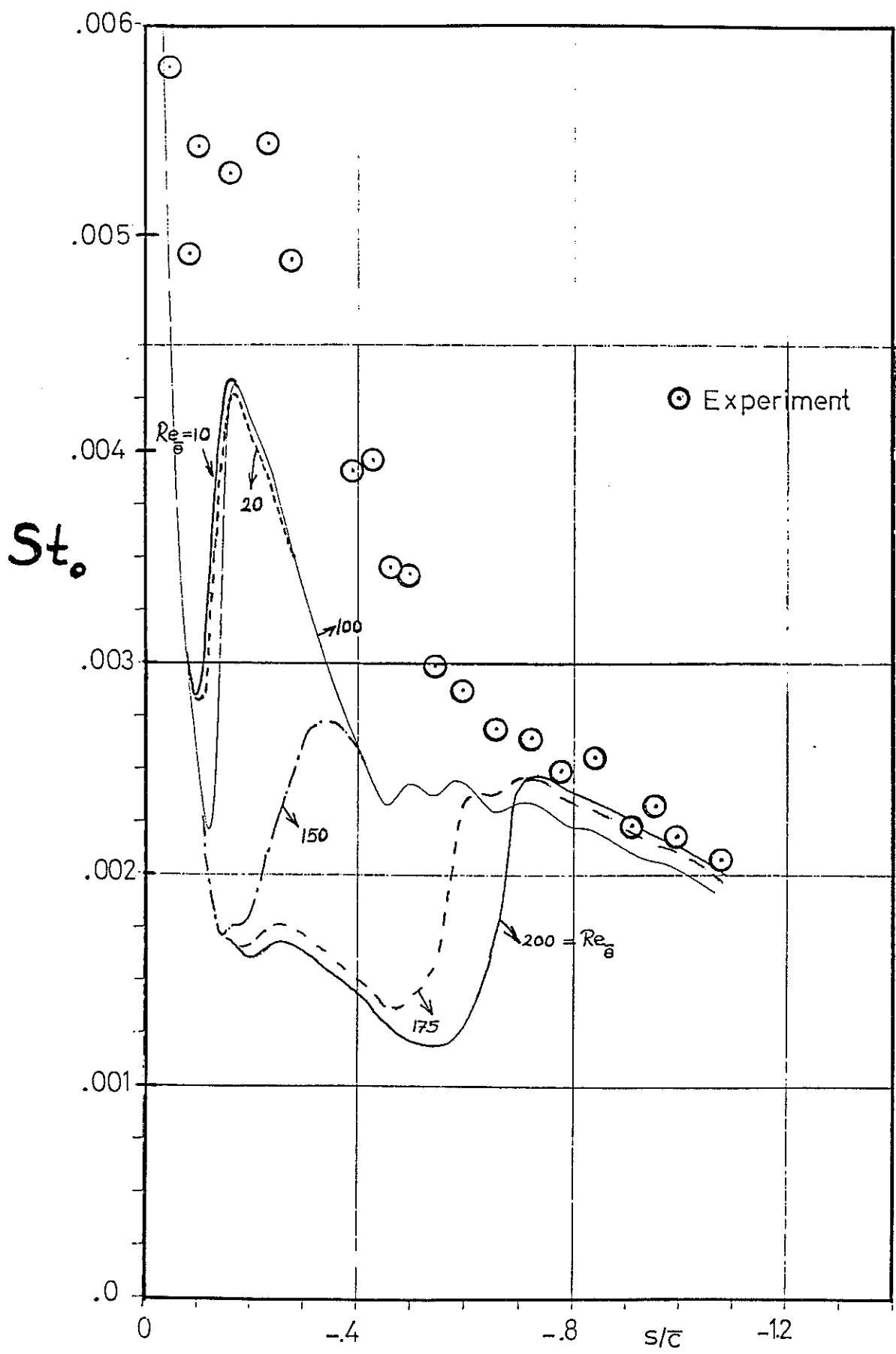


Fig. 143 Measured St_0 distribution and comparison with predictions on the pressure side,
 $(i=0^\circ, Ma_{inlet}=0.25, Ma_{exit}=0.908, TU_{\infty}=5.2\%, Re_{init}=8.4 \times 10^5, T_{\infty}=410\text{ K}, T_w=300$

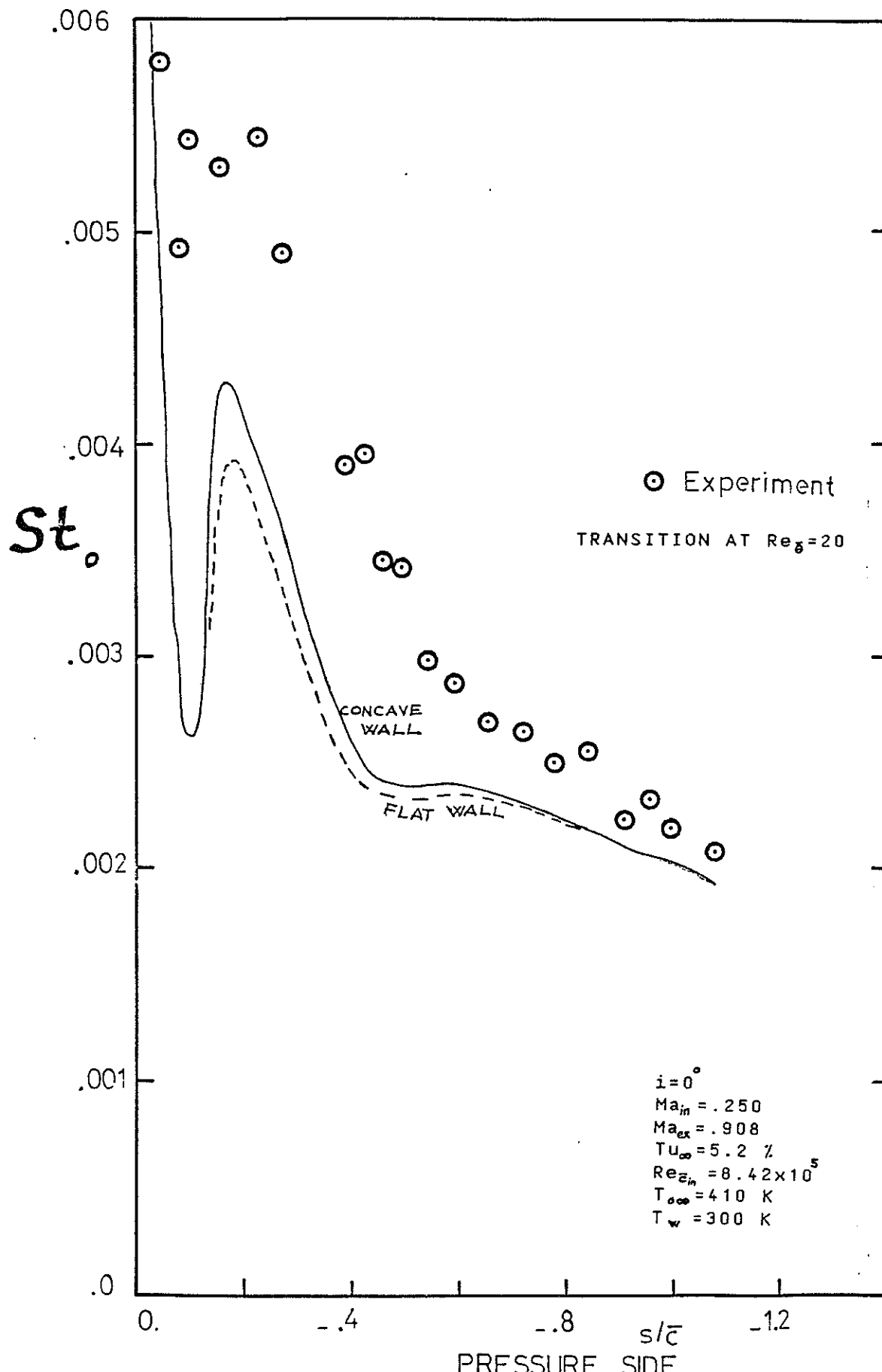


Fig. 145 St_0 predictions on the pressure side

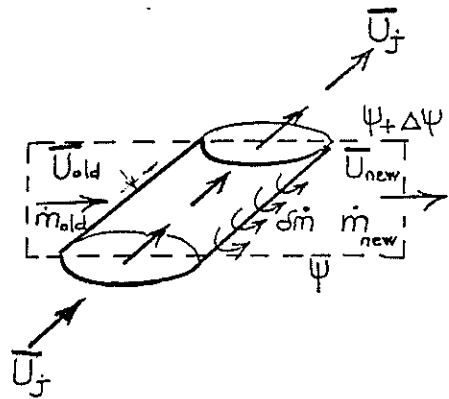
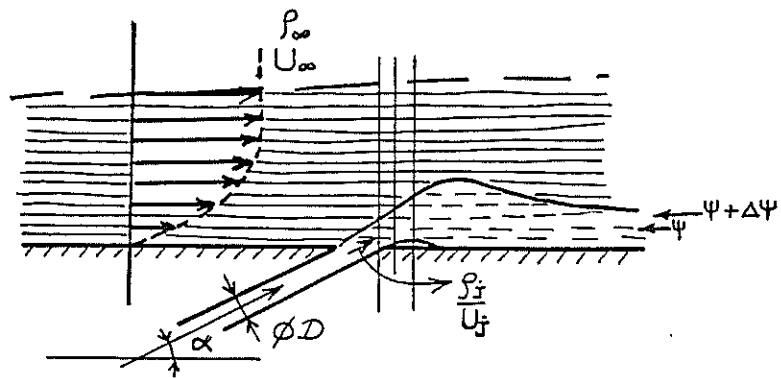
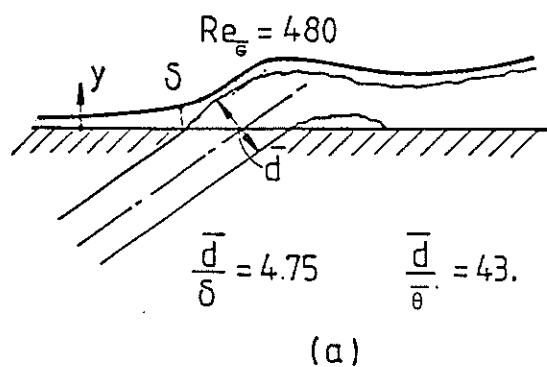


Fig.146 Coolant boundary layer interaction in a typical control volume

PRESENT STUDY
FILM COOLED TURBINE
BLADE



[133]'S GEOMETRY

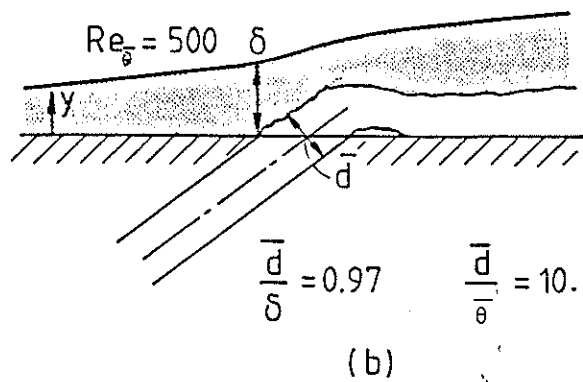


Fig. 147 Boundary layer scaling in the presence
of film cooling

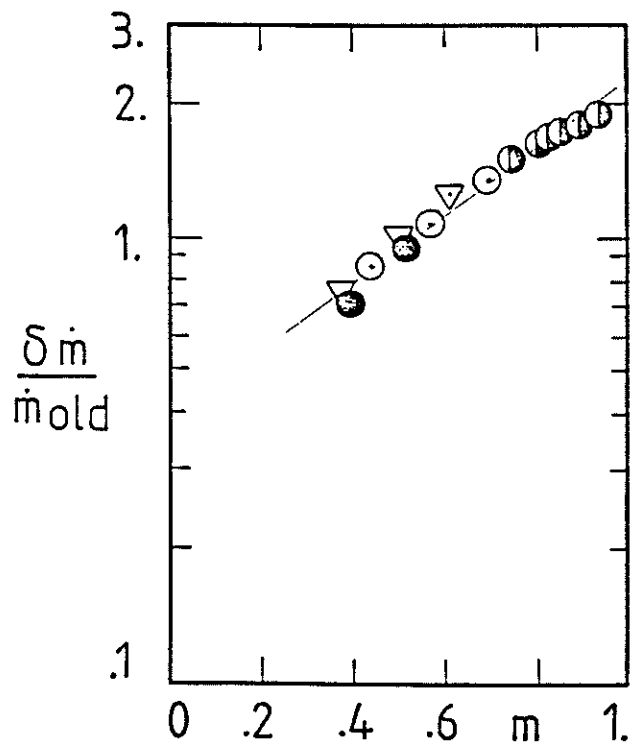


Fig. 148 Mass shed ratio versus blowing rate

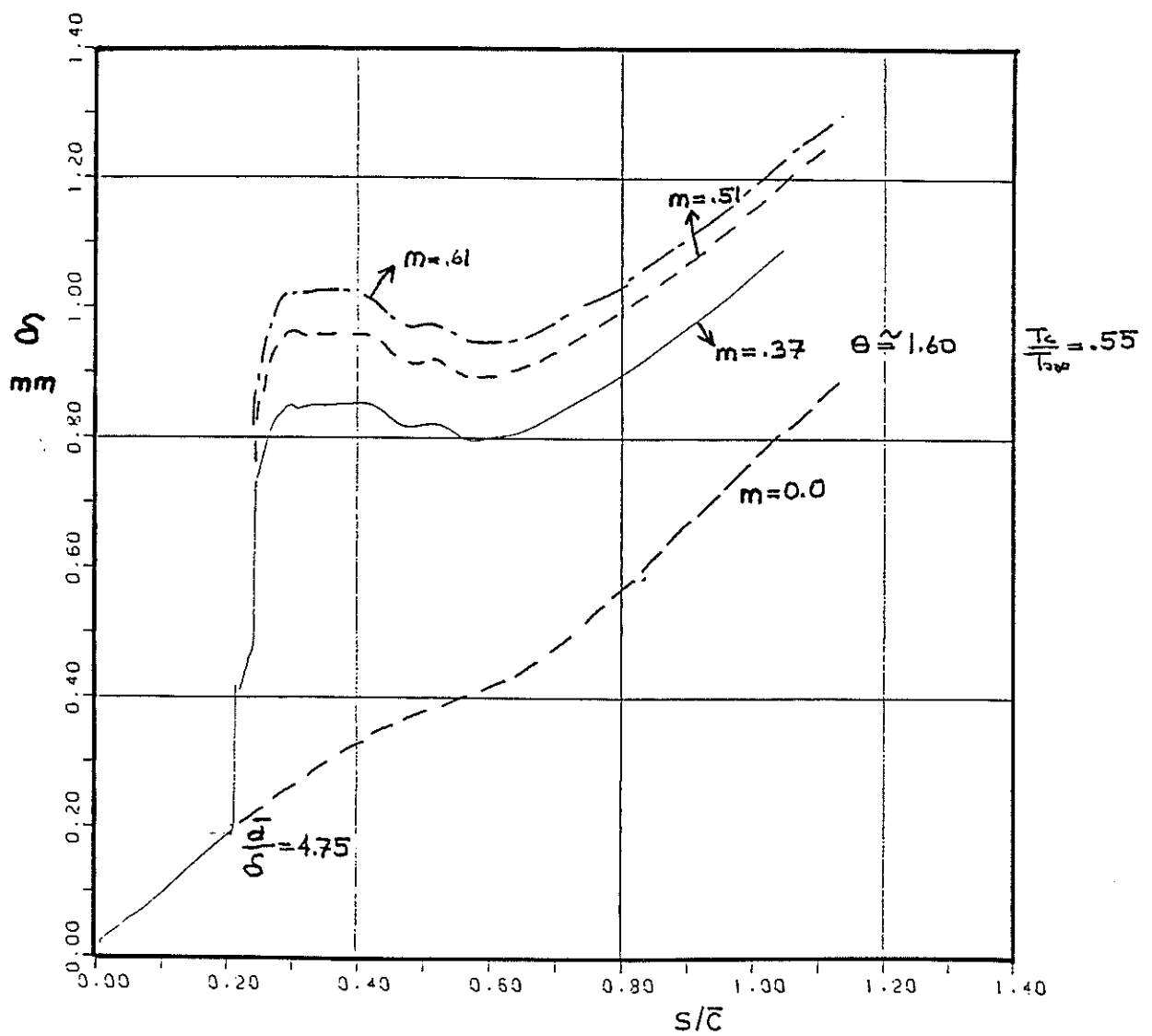


Fig. 149 Boundary layer thickness variation on the suction side with film cooling

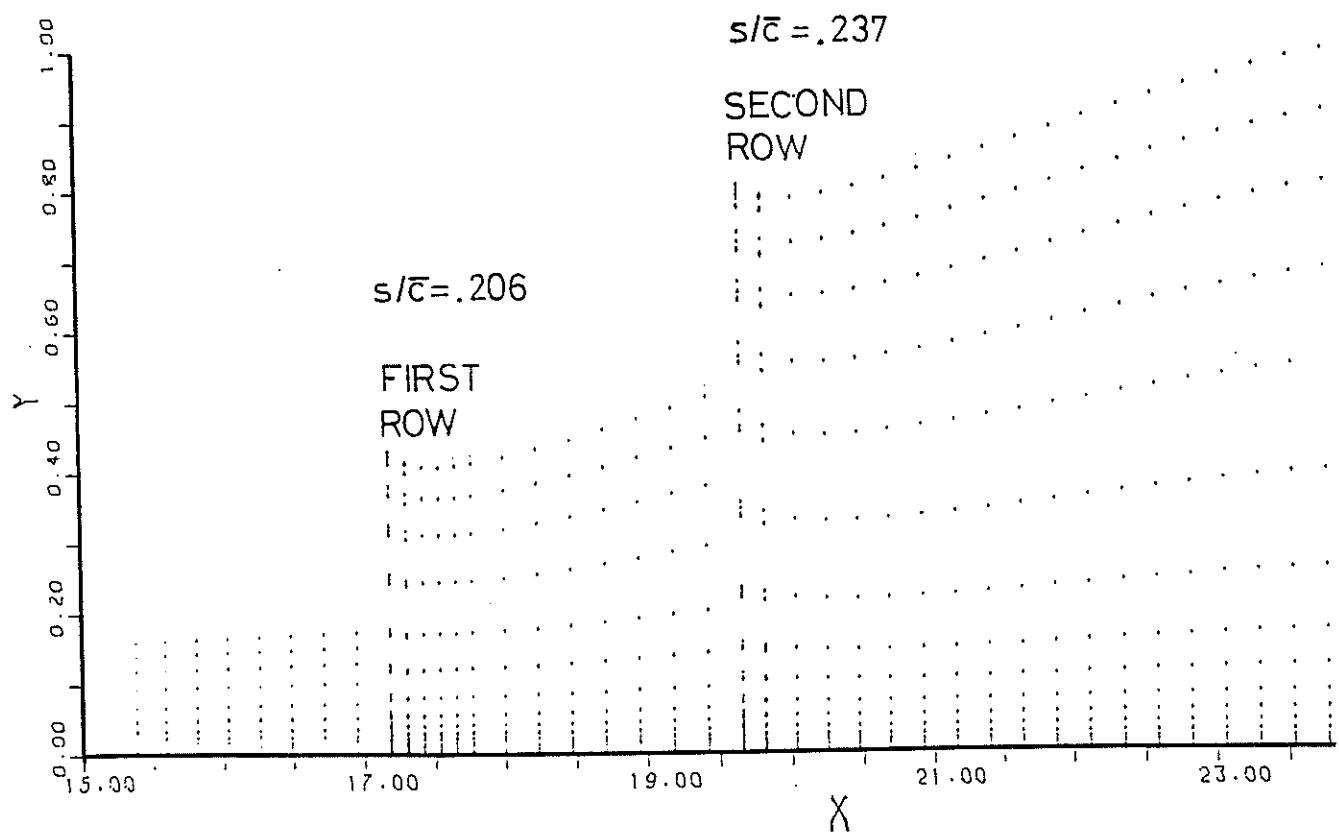


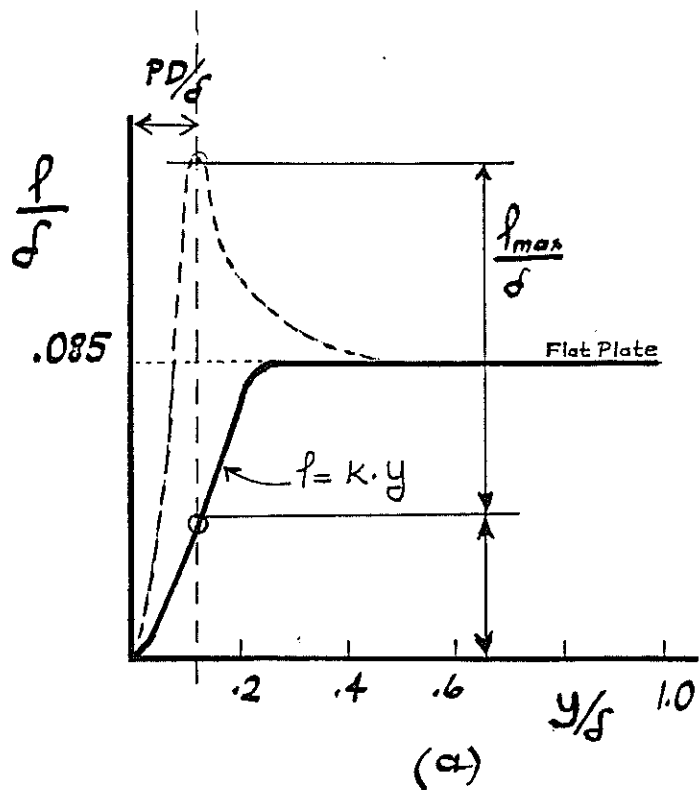
Fig.150 Finite difference mesh near suction side
ejection rows

$$m=0.51$$

$$\Theta = 1.66$$

$$\bar{\rho}_{\max} = .56$$

$$\delta \dot{m}/\dot{m} = 1.01$$



(a)

$$l_{max} = \bar{l}_{max} \cdot \bar{F}$$

$$\bar{F} = 2.718 \left(\frac{y}{\bar{P}D} \right)^2 \exp \left[- \left(\frac{y}{\bar{P}D} \right)^2 \right]$$

$$\bar{P}D = 0.8 \times \delta$$

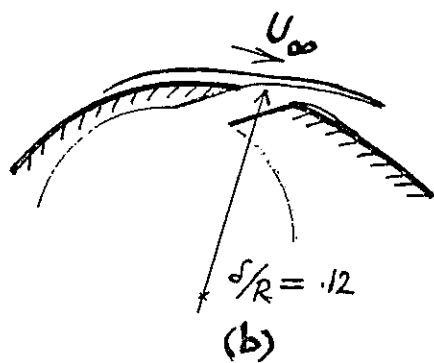
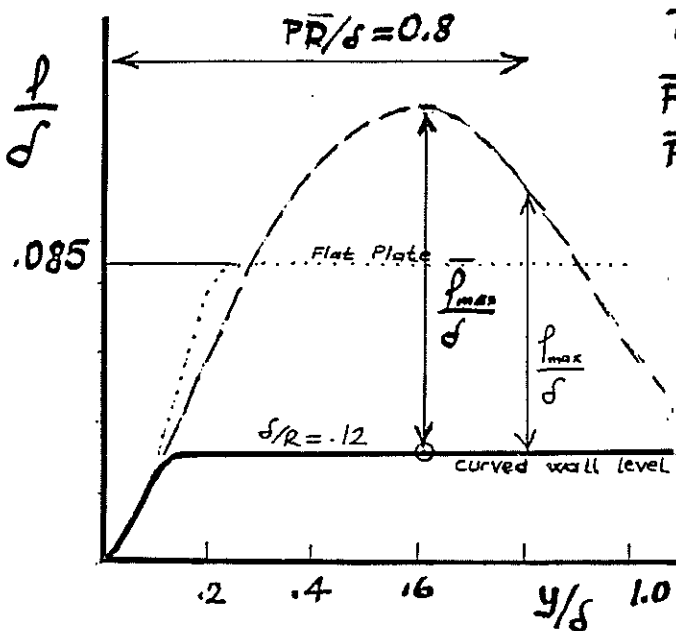


Fig. 151 Mixing length augmentation due to coolant ejection on the suction side

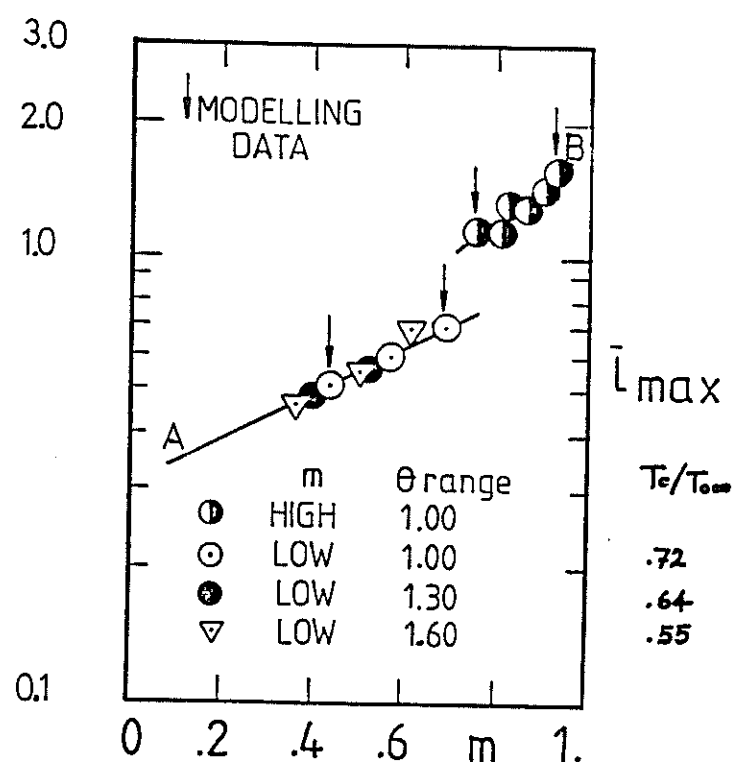


Fig.152 Augmented mixing length versus blowing rate

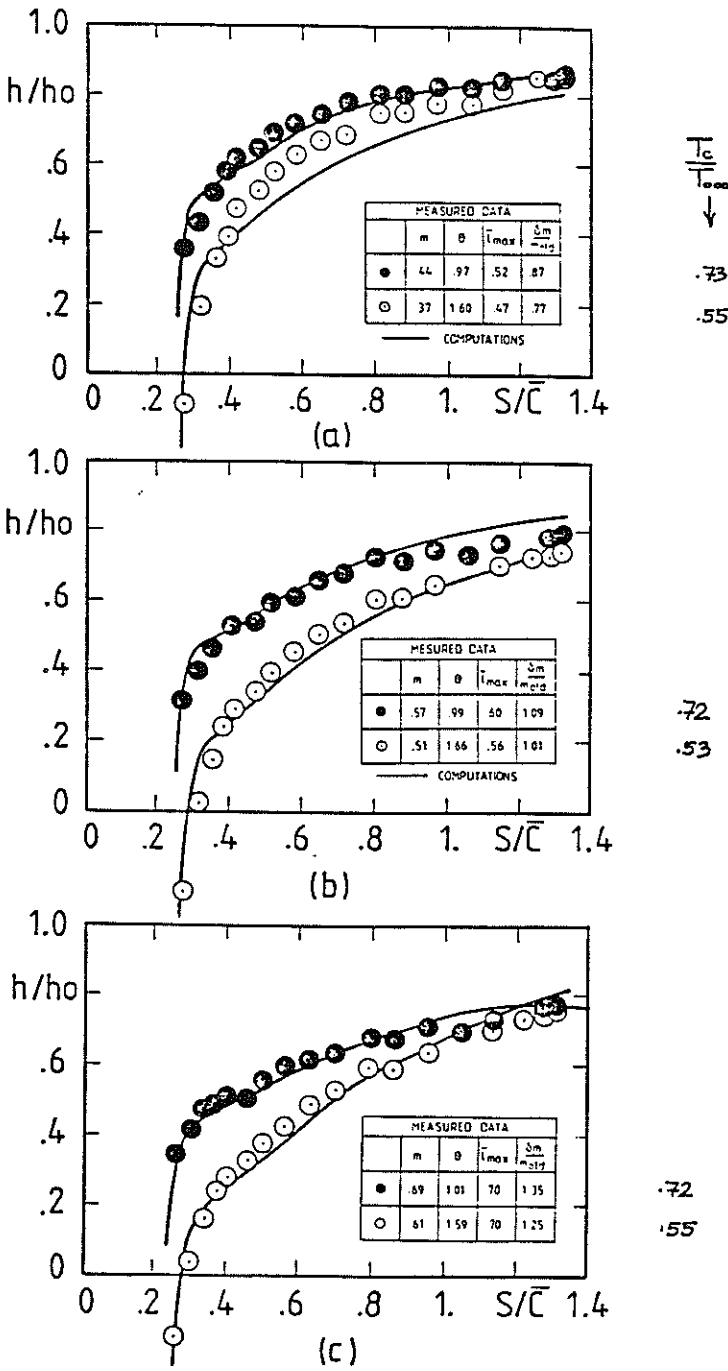


Fig.153 Film cooling heat transfer,predictions, $m < 0.69$

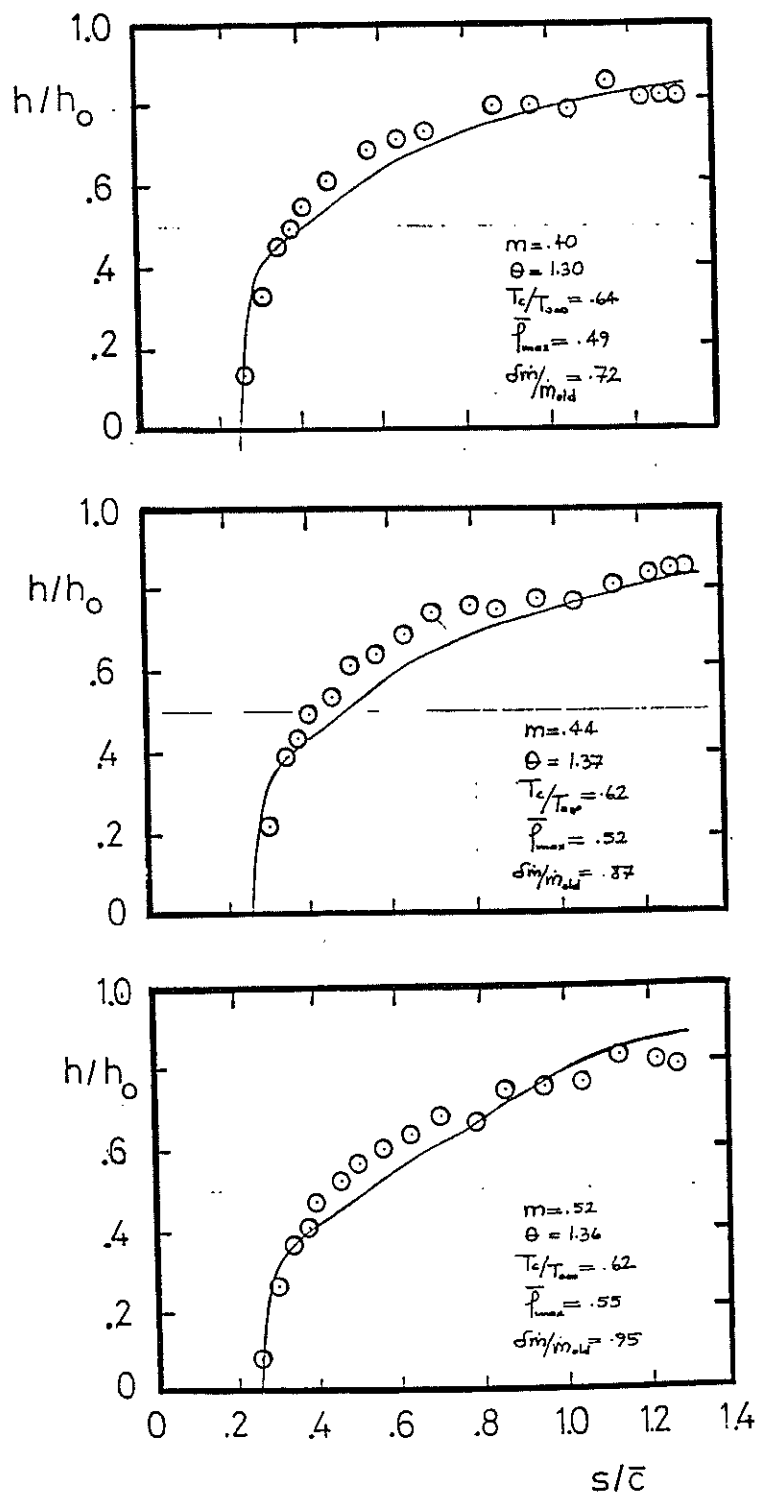


Fig.154 Film cooling heat transfer,predictions

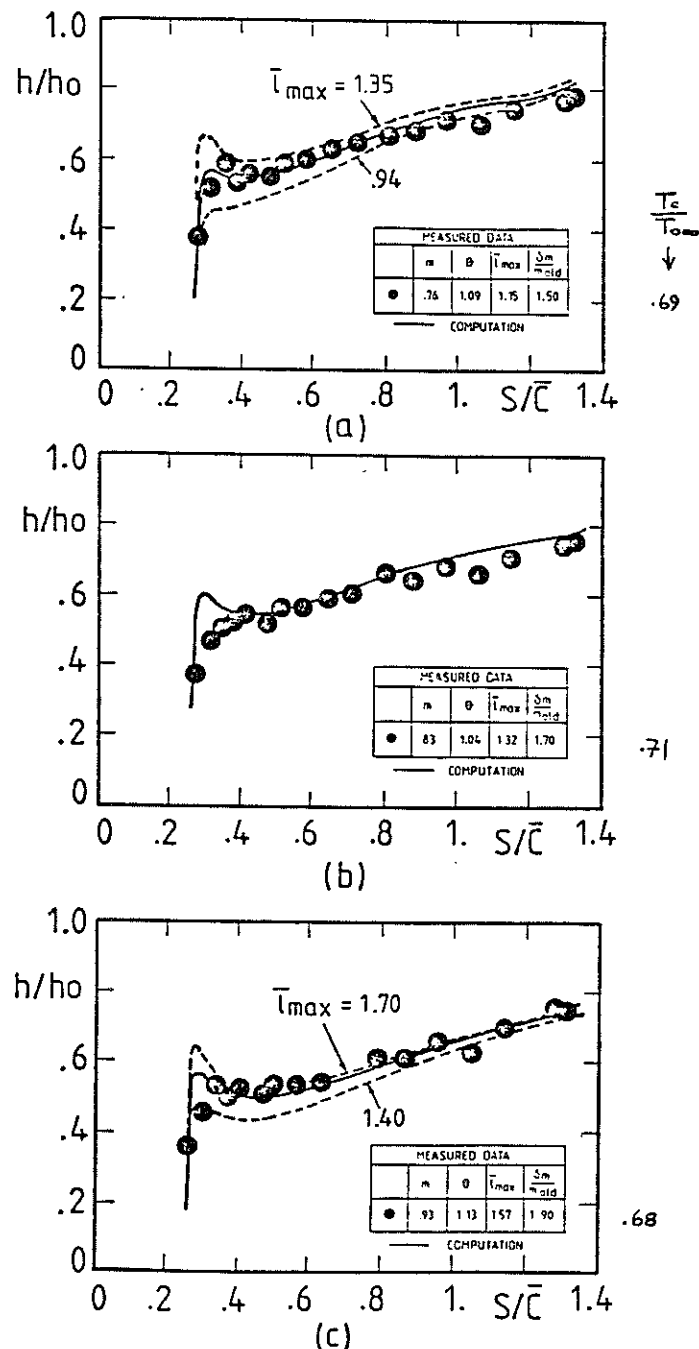


Fig.155 Film cooling heat transfer,predictions, $m>0.76$

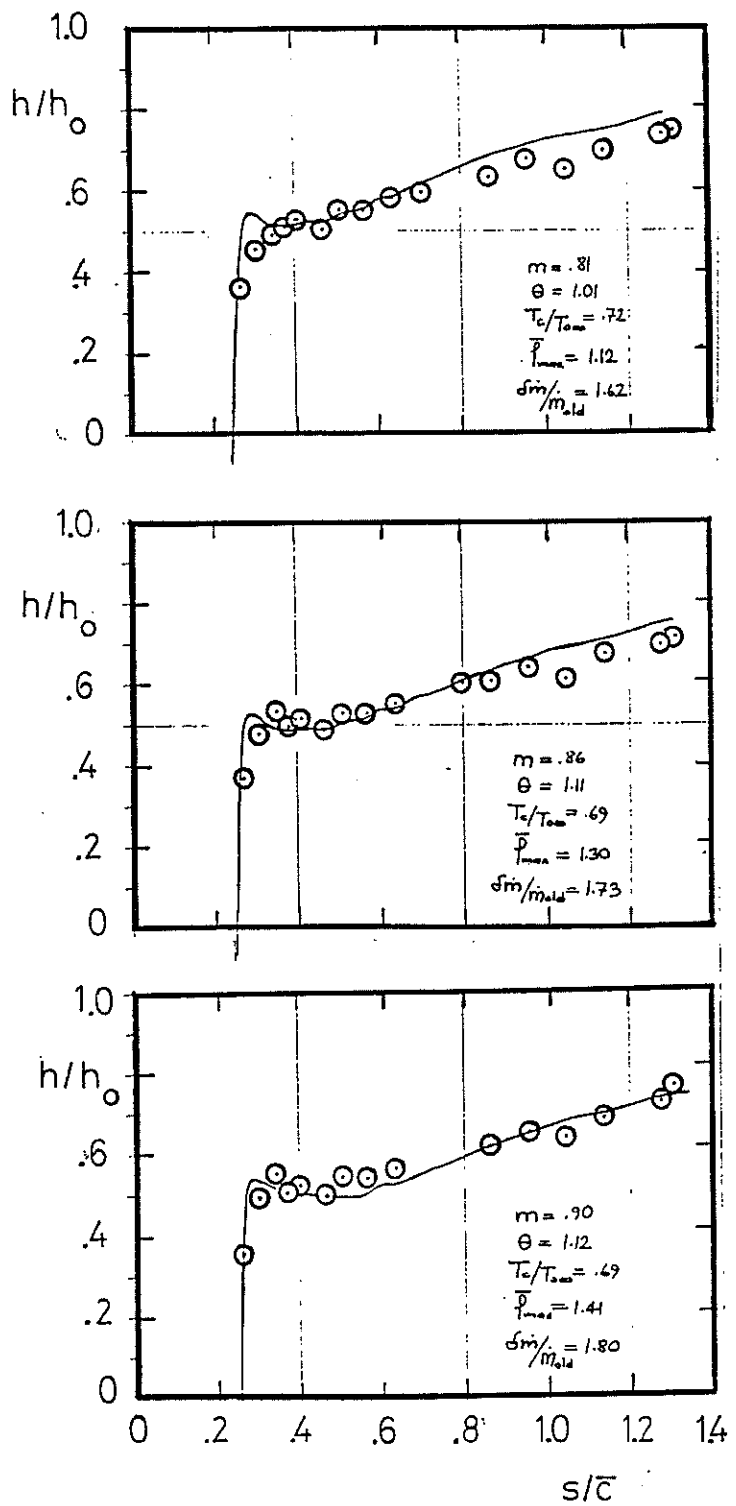


Fig. 156 Film cooling heat transfer, predictions

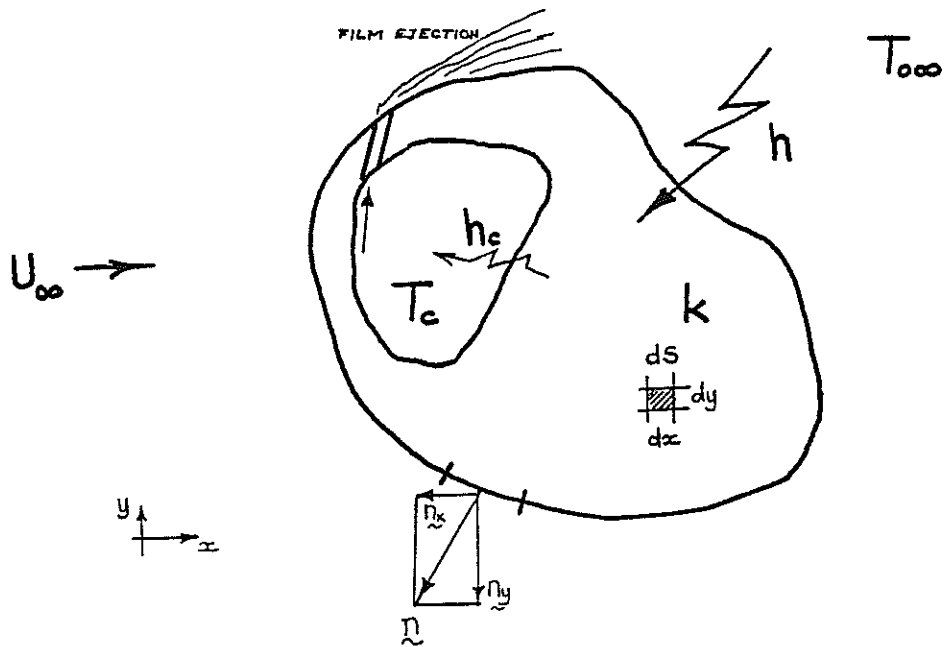


Fig.158 A solution domain and the boundaries for the heat conduction problem

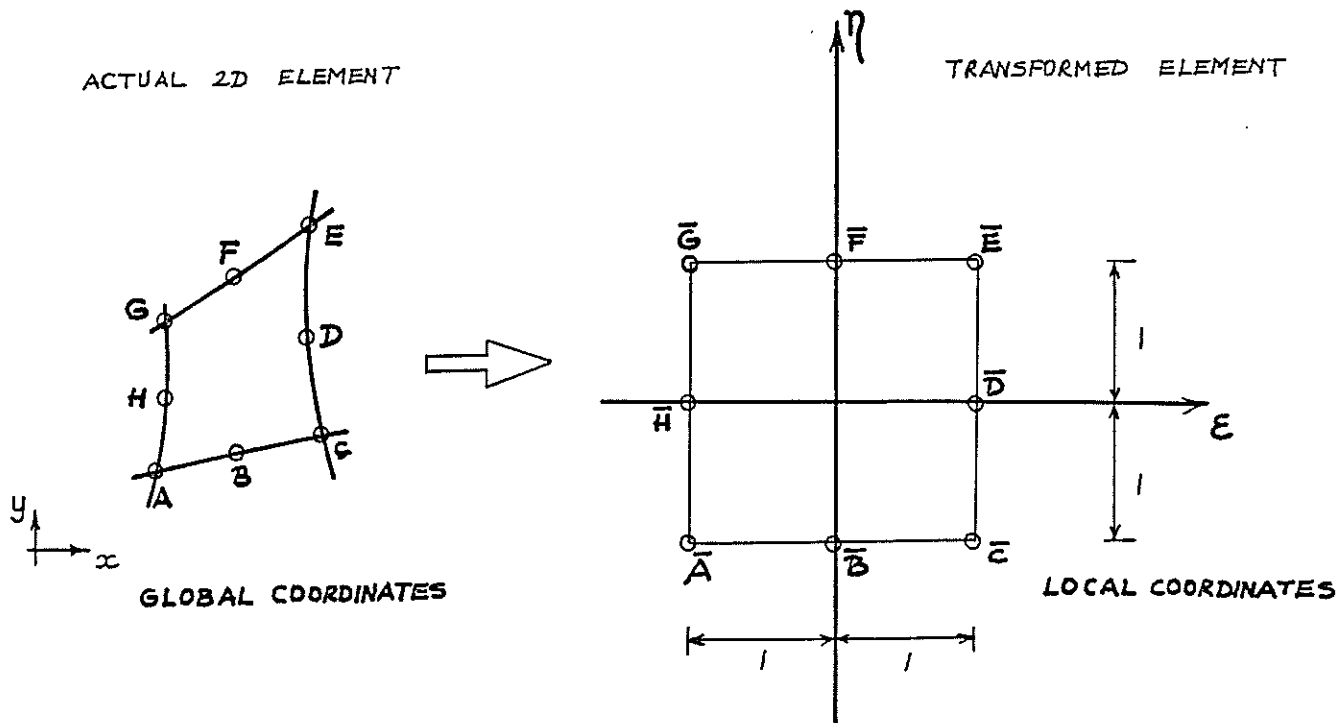


Fig.159 Second order curved and isoparametric finite elements

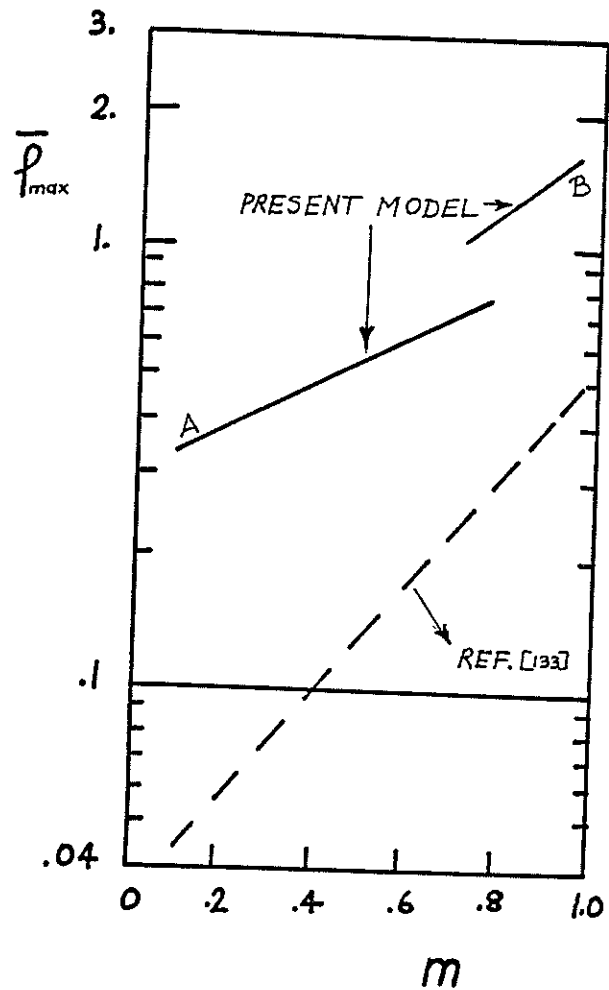


Fig.157 Comparison of $\bar{\rho}_{\max}$ with ref.[133]'s slant angle ejection data

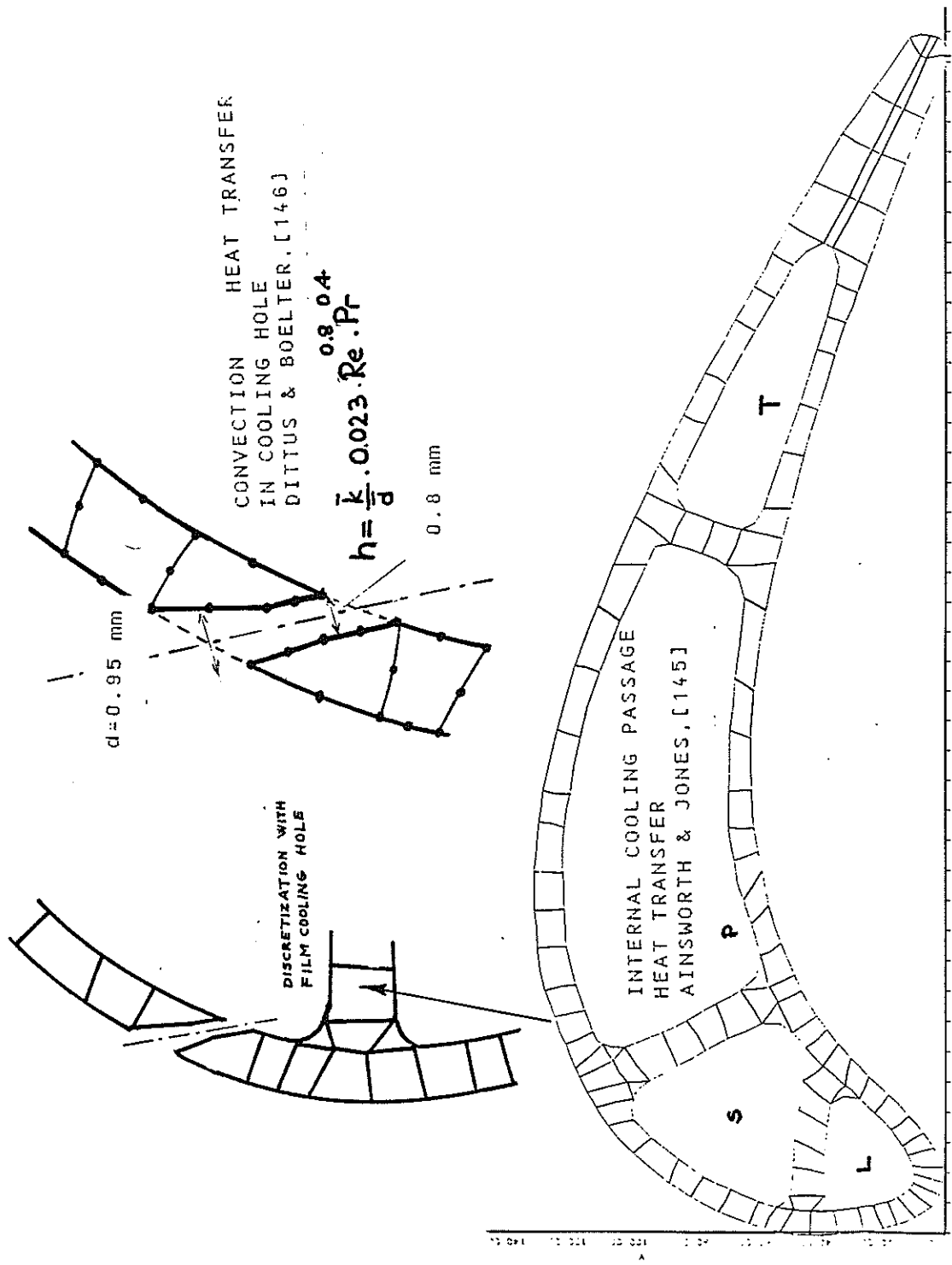
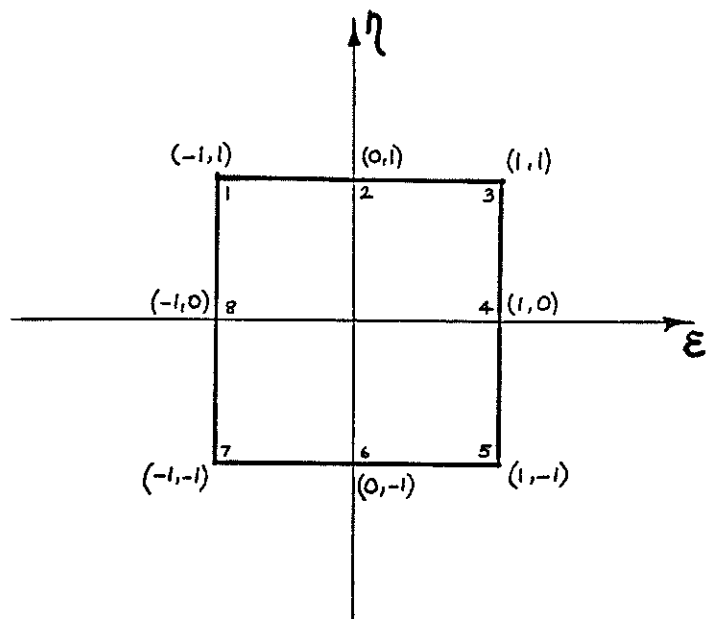


Fig. 161 The discretization of the film cooled blade



$$N_1 = \frac{1}{4} (1-\xi)(1+\eta)(\eta-\xi-1)$$

$$N_2 = \frac{1}{2} (1-\xi)(1+\xi)(1+\eta)$$

$$N_3 = \frac{1}{4} (1+\xi)(1+\eta)(\eta+\xi-1)$$

$$N_4 = \frac{1}{2} (1+\xi)(1-\eta)(1+\eta)$$

$$N_5 = \frac{1}{4} (1+\xi)(1-\eta)(\xi-\eta-1)$$

$$N_6 = \frac{1}{2} (1-\eta)(1-\xi)(1+\xi)$$

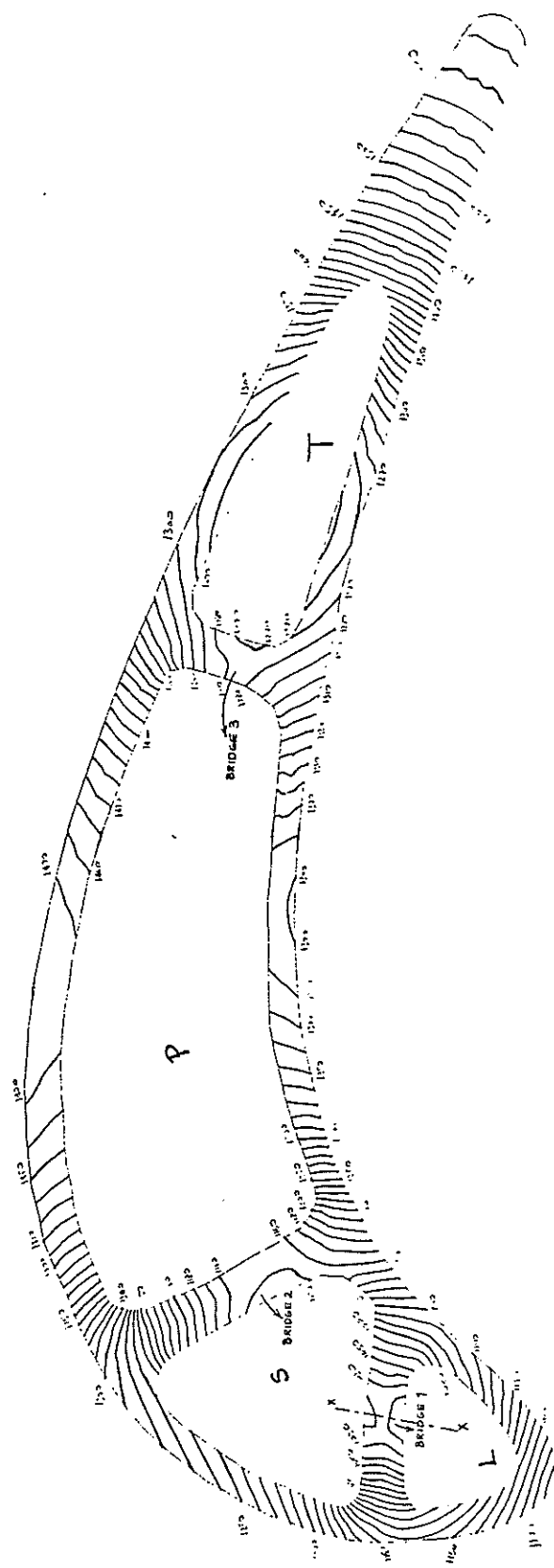
$$N_7 = \frac{1}{4} (1-\xi)(1-\eta)(-\eta-\xi-1)$$

$$N_8 = \frac{1}{2} (1-\xi)(1-\eta)(1+\eta)$$

$$\sum_{i=1}^8 N_i = 1$$

Fig.160 The shape functions

Fig. 163 Isothermal contours in the blade
only internal convection cooling, CASE-1



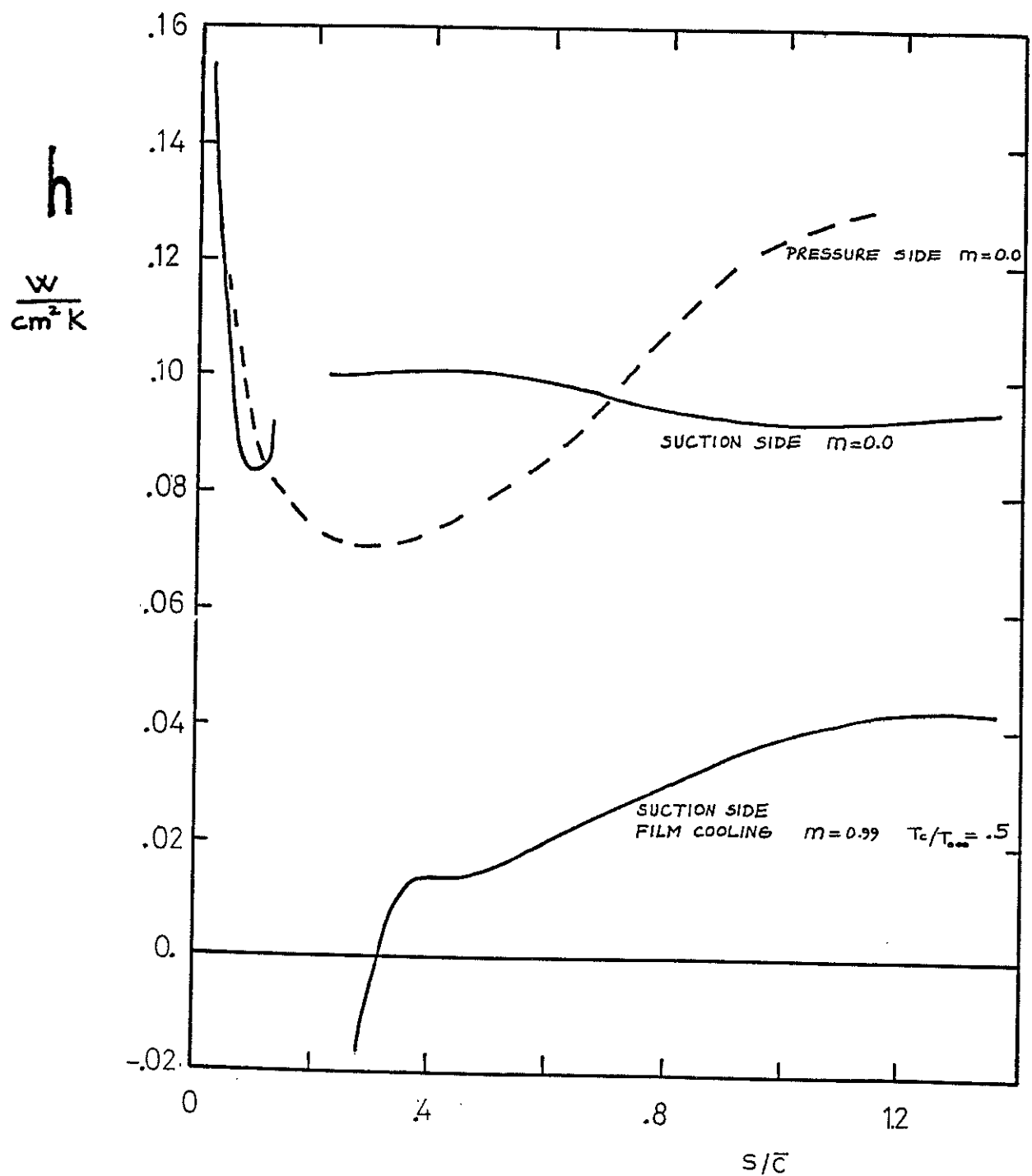


Fig.162 The external convective heat transfer coefficients used in the heat conduction analysis

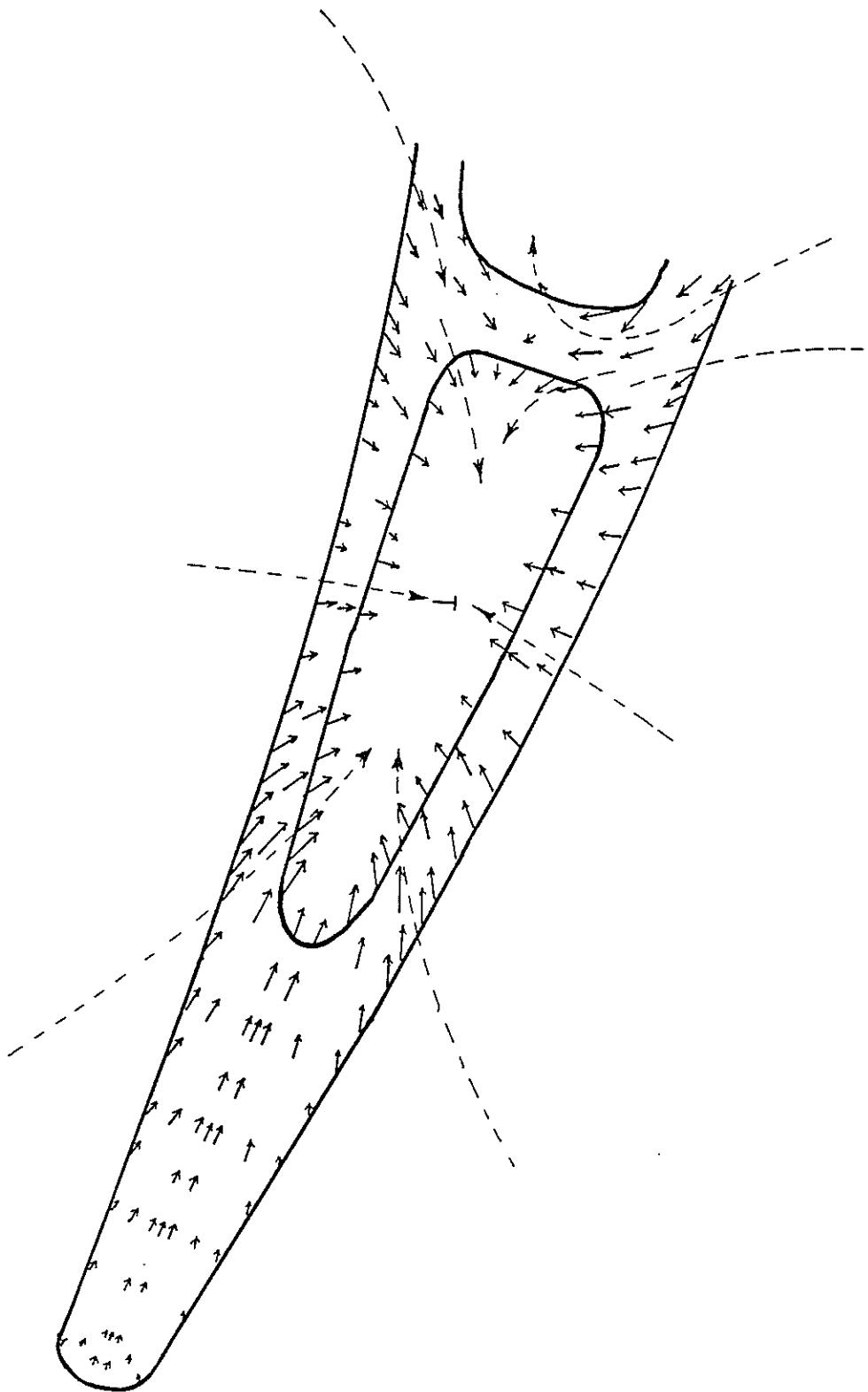


Fig. 164.b Heat flux vectors
only internal convection cooling,CASE-1
near trailing edge region

20 W/cm²

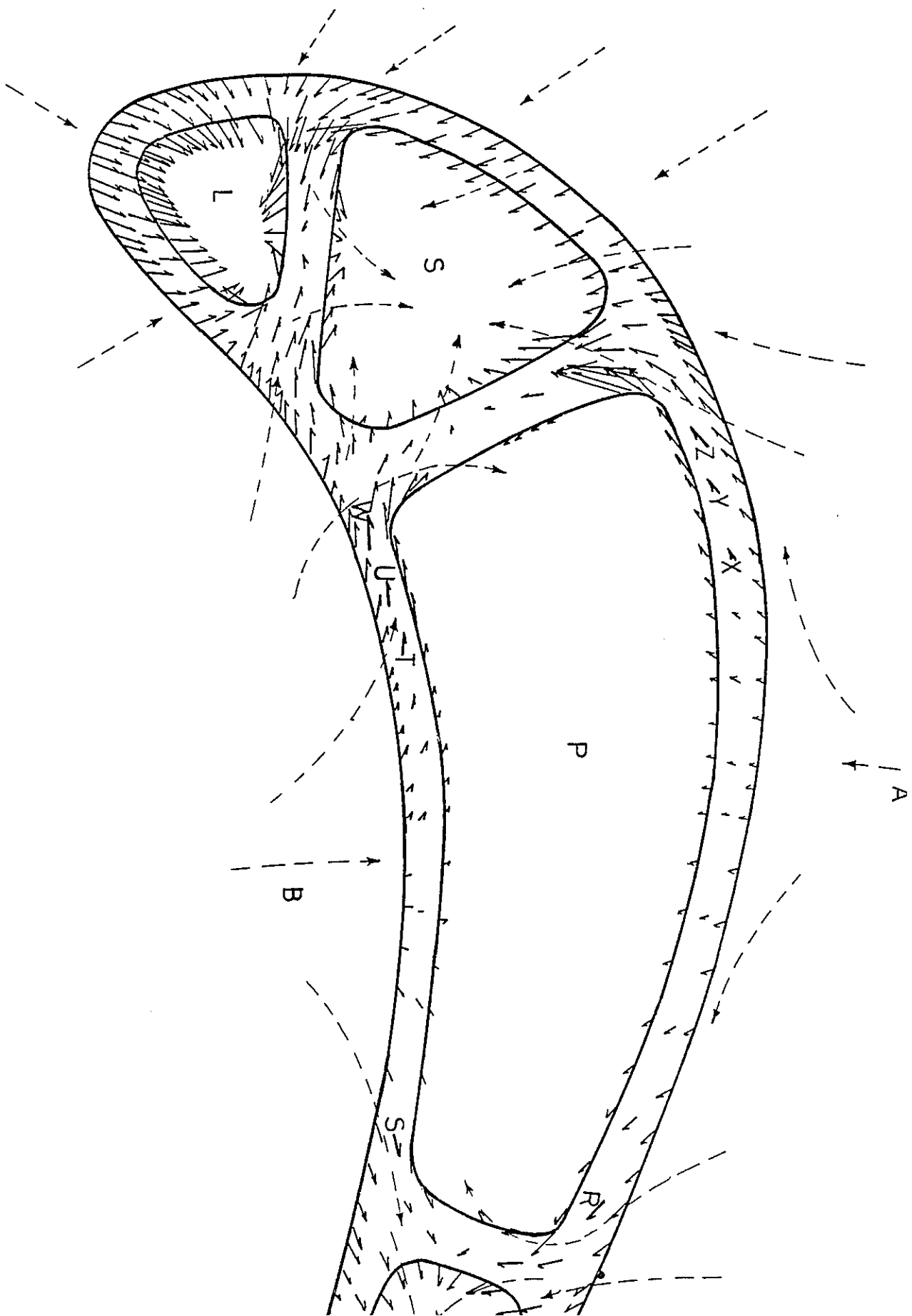


Fig. 164 Heat flux vectors
(a) only internal convection cooling, CASE-1

20 W/cm²

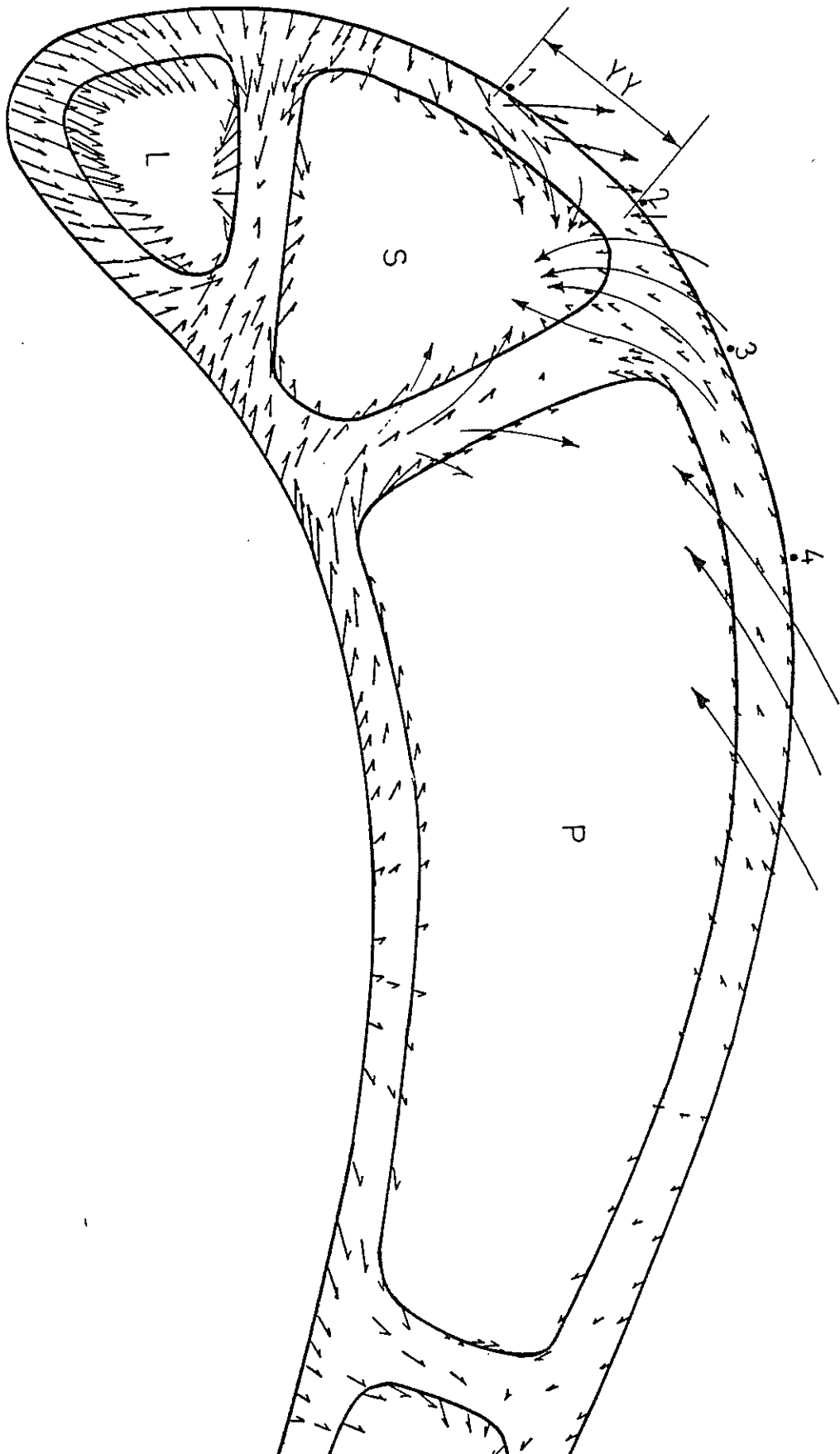


Fig. 166 Heat flux vectors
Internal convection + film cooling
film cooling hole effect is not included,CASE-2

20 W/cm²

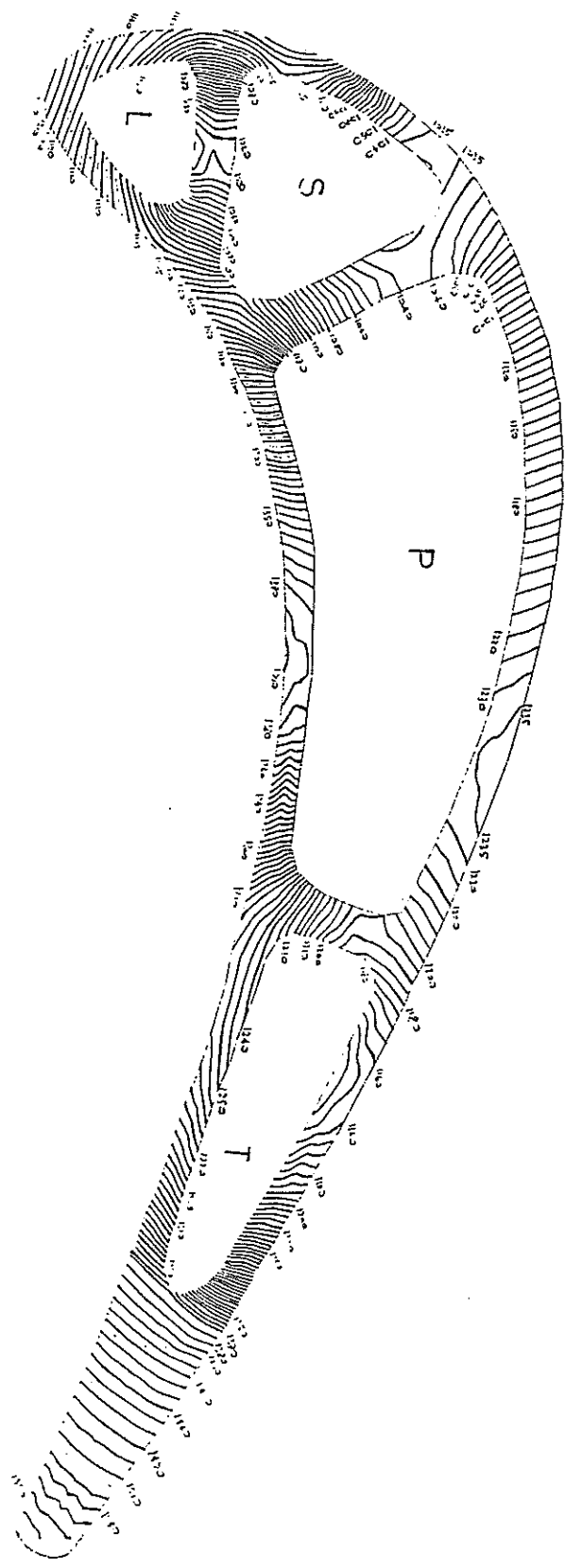


Fig. 165 Isothermal contours in the blade
Internal convection + film cooling
film cooling hole effect is not included, CASE-2

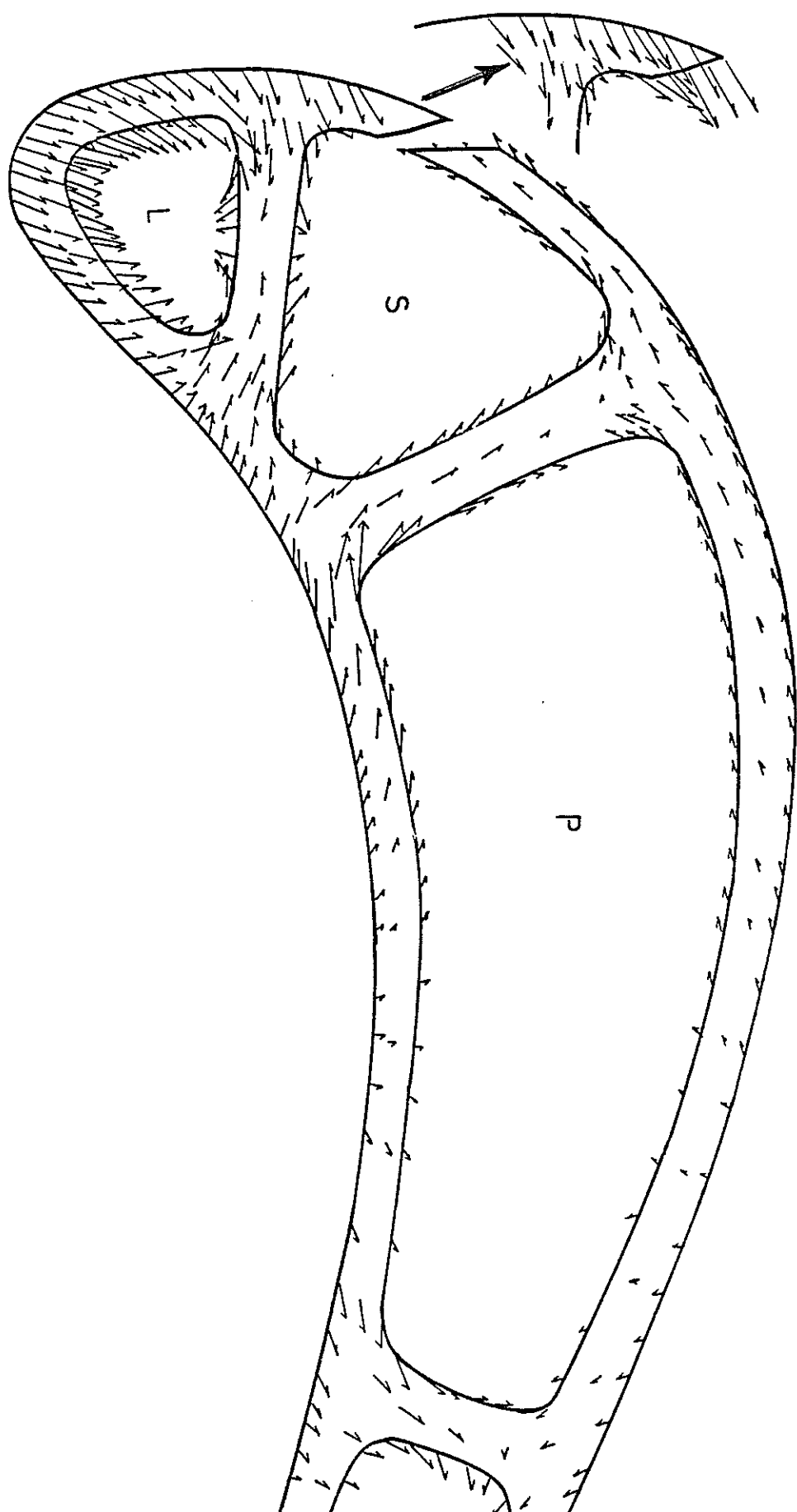


Fig. 168 Heat flux vectors
Internal convection + film cooling
film cooling hole effect is included, CASE-3

20 W/cm²

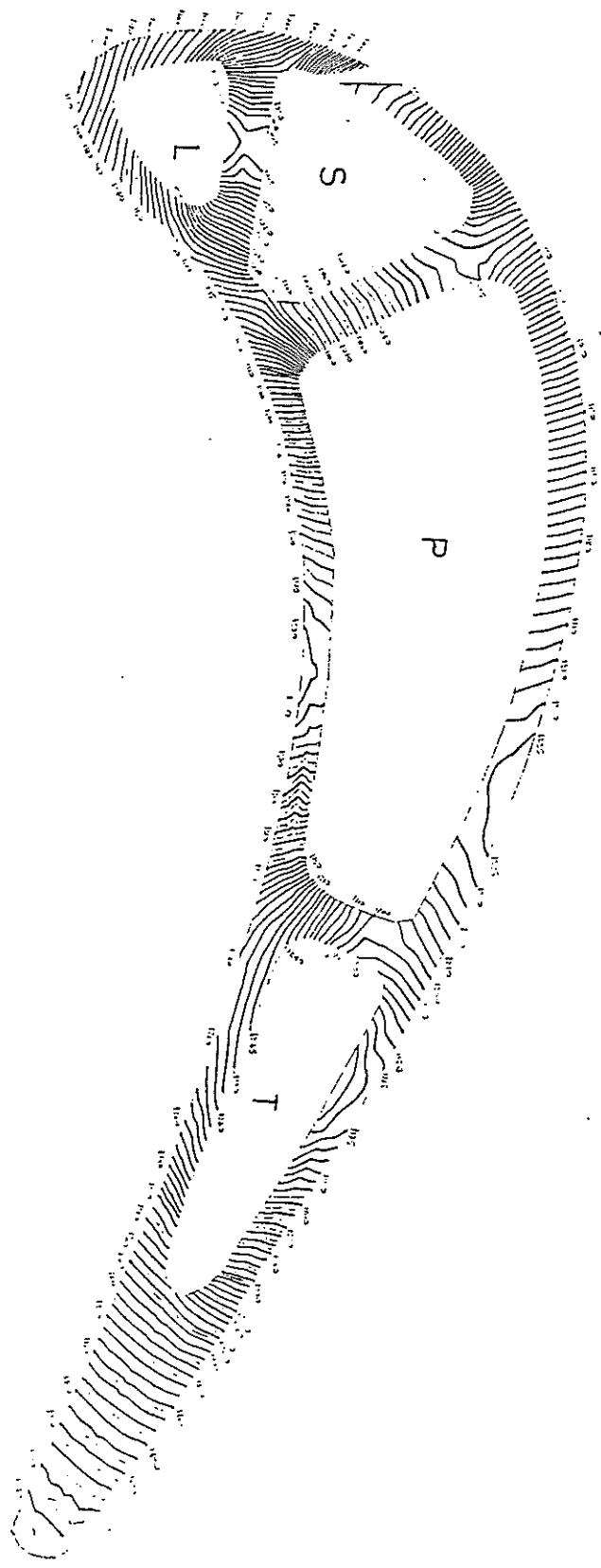
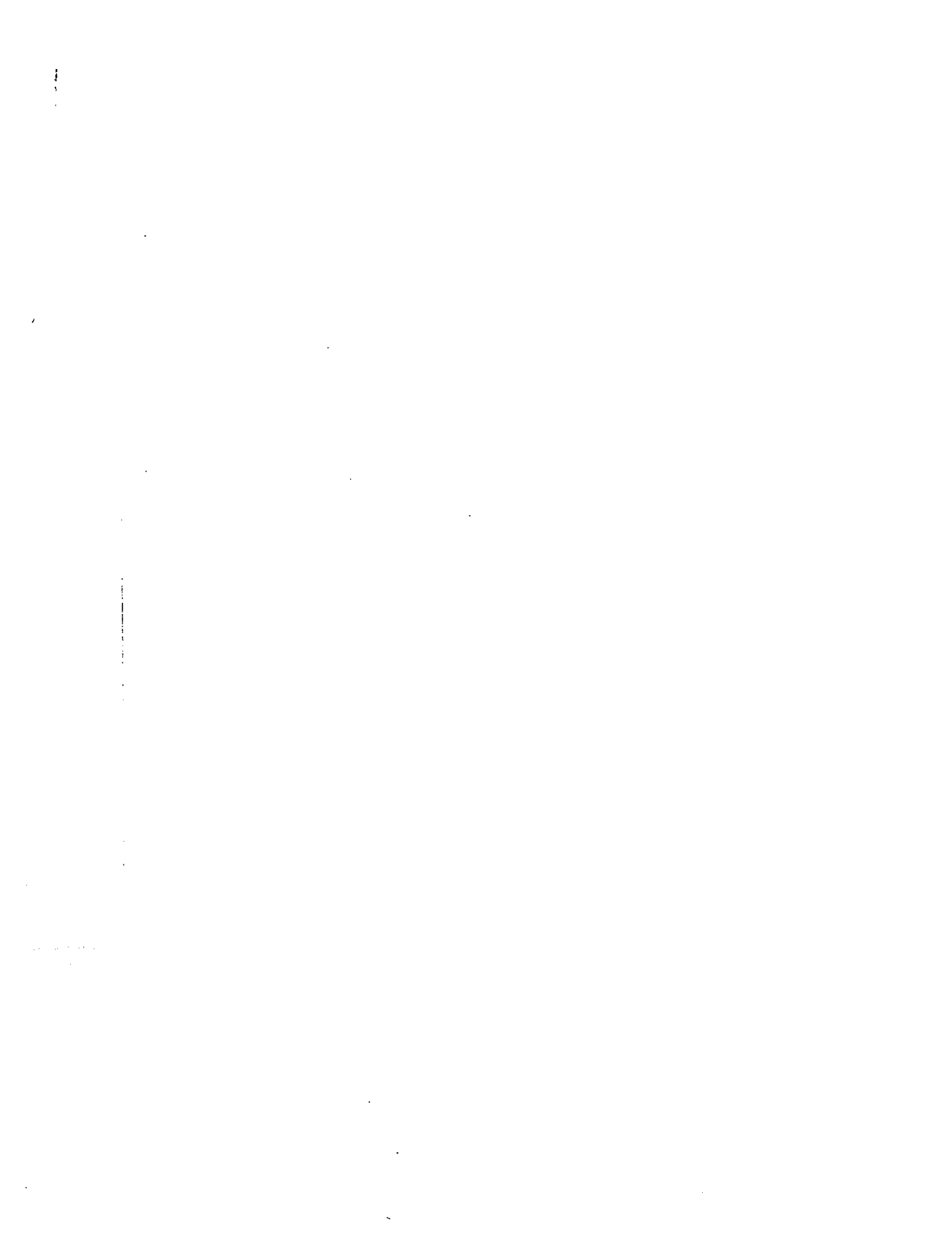


Fig. 167 Isothermal contours in the blade
Internal convection + film cooling
film cooling hole effect is included, race-3



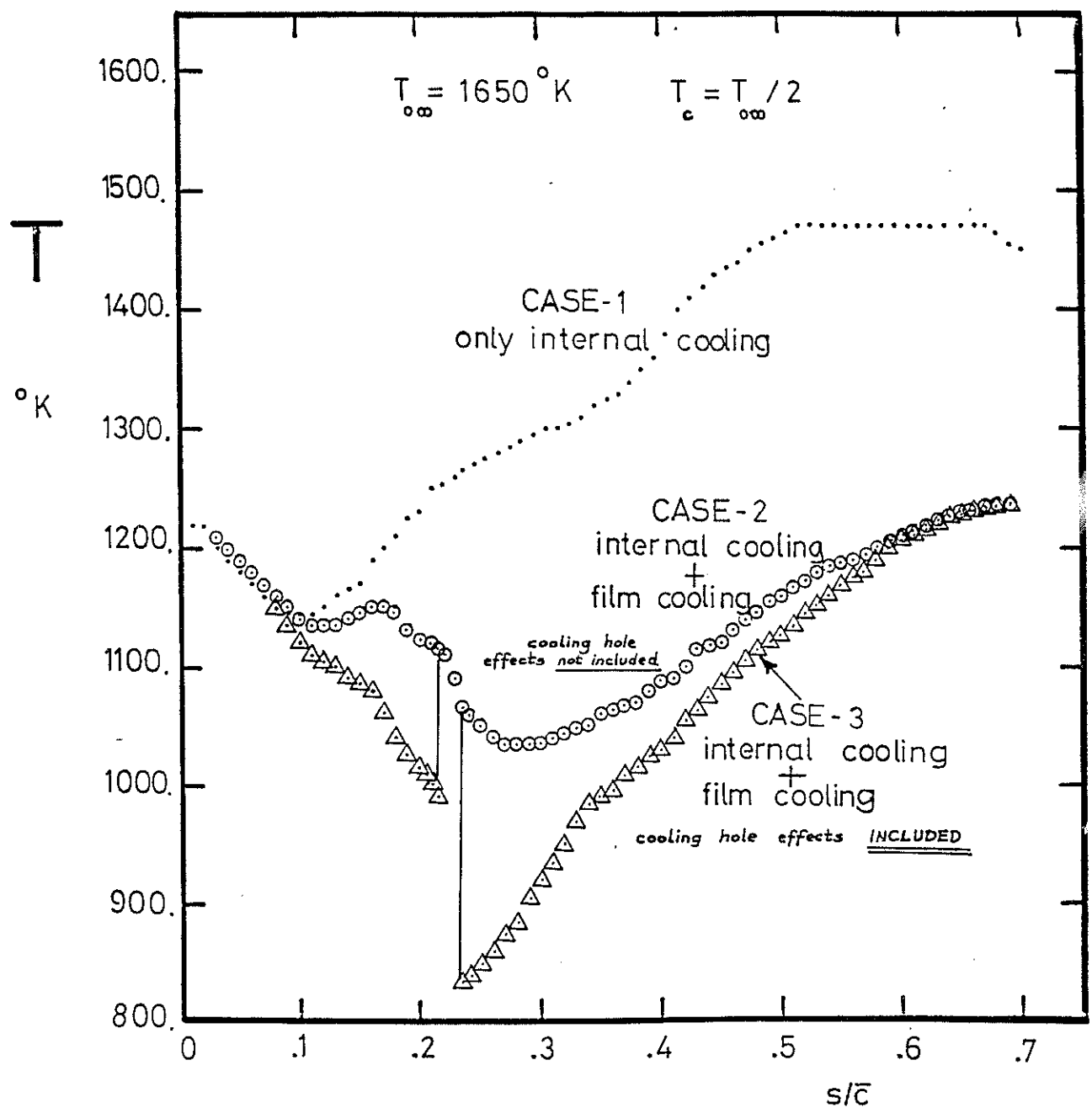


Fig.169 Computed surface temperature distribution on the suction side; comparison of CASE-1 , - CASE-2 and CASE-3.